Aerodynamics of Low Pressure Steam Turbine Exhaust Systems

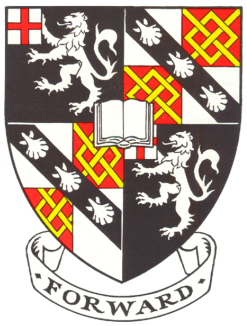

Bowen Ding

Department of Engineering
University of Cambridge

This dissertation is submitted for the degree of
Doctor of Philosophy

Churchill College November 2018

Abstract

The low pressure (LP) exhaust system presents a promising avenue for improving the performance of large steam turbines. For this reason, LP exhaust systems have attracted the attention of the research community for decades. Nevertheless, we still lack understanding of the flow physics and loss mechanisms in the exhaust system, especially at part-load conditions. It is also unclear how the exhaust system should be designed when its required operating range widens. This thesis provides solutions to these aerodynamic issues through experimental and numerical investigations, and provides tools that could contribute to better designs of LP exhaust systems.

Firstly, the Computational Fluid Dynamics (CFD) solver ANSYS CFX was validated against experiments performed on a scaled test rig under representative part-load flow conditions. This validation exposed the weakness of Reynolds-averaged Navier–Stokes (RANS) CFD when there is a highly swirling flow and large separation regions in the exhaust diffuser.

To facilitate the numerical studies, a series of tools were also developed. A design suite, *ExhaustGen*, was used to automate the pre- and post-processing of CFD calculations. The exhaust diffuser was parametrised using "Minimum Energy Curves", which reduce the dimension of parameter space. Further, a suitable stage-hood interface treatment (Multiple Mixing Planes) was chosen to predict the circumferentially non-uniform flow in the exhaust hood at low computational cost.

Numerical investigation of the baseline geometry provided insights into the key flow features and loss mechanisms in the exhaust system, over a wide range of operating conditions. In particular, the bearing cone separation was identified as a key source of loss at part-load conditions. The effect of stage-hood interaction on the performance and design of the exhaust system was studied by varying the rotor blade design, which can positively influence system performance.

Finally, a global sensitivity study was performed to identify the most influential design parameters of the exhaust hood. These findings allow, for the first time, LP exhaust hood performance maps to be constructed, so that the benefits of choosing a suitable hood geometry and blade design can be revealed. The thesis also offers contribution towards formulating LP exhaust system design guidance for a wide operating range.

Preface

The work described in this dissertation was carried out in the Whittle Laboratory, University of Cambridge between October 2014 and November 2018. Except where specific reference is made to the work of others, the contents of this dissertation are original and have not been submitted in whole or in part for consideration for any other degree or qualification in this, or any other university. This dissertation is my own work and contains nothing which is the outcome of work done in collaboration with others, except as specified in the text and Acknowledgements. This dissertation contains approximately 43,000 words including bibliography, tables and equations and has 91 figures.

The work contained within this thesis has, to date, produced the following publications:

- Ding, B., Xu, L., Yang, J., Yang, R. and Dai, Y. (2018). The Effect of Stage-Diffuser Interaction on the Aerodynamic Performance and Design of LP Steam Turbine Exhaust Systems. In *ASME Turbo Expo 2018: Turbomachinery Technical Conference and Exposition*. GT2018-75375.
- Ding, B. and Xu, L. (2017). Designing Steam Turbine Exhaust Diffusers Using Minimum Energy Curves. In *Shanghai 2017 Global Power and Propulsion Forum*. GPPS2017-0060.

Bowen Ding
November 2018

Acknowledgements

Unlike many others, I went full circle before embarking on my PhD journey. My father named me "Bo" which means "doctorate" in Chinese, expecting that I would pursue knowledge through advanced degrees. Against his wishes, I worked for an investment bank after graduation. Having spent an exhausting year working 90 hours a week, I started to ask myself what I truly wanted to do with a degree in Mathematics. To that end, I should really thank those who provided me with the inspiration and motivation for academic research, including Dr. Tristan Gilet and Dr. Lydia Bourouiba who supervised my UROP at MIT's Fluids Lab during my exchange year, my undergraduate Director of Studies Prof. Christopher Tout who encouraged me to return to Cambridge for the Part III Maths course, and Prof. John Hinch, who supervised my Part III project.

I am indebted to Dr. Liping Xu, who kindly accepted me as his PhD student despite my bare knowledge of engineering, not to mention turbomachinery. He entrusted me with full independence to explore research ideas, whilst always challenging me to deliver work of both academic interest and industrial relevance. His office door was always open to me, and I have learnt so much through our meetings.

I would like to thank Shanghai Turbine Works Co. Ltd for funding this project, and the useful discussions with Dr. Jiandao Yang, Mr. Rui Yang and Mr. Yuejin Dai from the R&D team, with whom I undertook a summer placement in 2015, learning valuable lessons about steam turbine design.

The experimental work in this thesis would not have been possible without the support from the Whittle Lab. Special thanks goes to chief technician John Saunders, technical staff members Ian Thornton and Josh Firman. My colleagues Dr. Konstantinos Pantelidis and Dr. Andrew Melzer also taught me so much when designing and building the test rig. I also want to thank Alistair Ross from the CUED workshop, as well as Mark Huntsman and Paul Pedersen from the CUED Electronics Development Group.

I need to thank Dr. David Warren and Mr. Peter Benie for providing the lab IT support. Mr. Stuart Rankin from the Cambridge HPC Service has also helped me numerous times with setting up CFD calculations on the cluster.

I would not have survived the PhD life without my colleagues and friends. I am particularly grateful to Nishad Sohoni, Martin Chilla, Kiran Auchoybur, Teng Cao, and Tim Williams from the lab, and also Raghabendra Pratap, Zhen Rao, Meng Zhang, and

David Driver from Churchill College. I also thank Jack Mainwaring for proofreading this thesis.

Thank you to Mom and Dad for your support throughout my education and my life.

Finally, I would like to thank my wife, Jessie Li. Thank you for all your love, support and understanding over the past four years.

I would like to dedicate this thesis to my wife Jessie Li

Table of contents

List of figures

List of tables

Nomenclature

Roman Symbols

$\dot{m}$	Mass flow rate
$\dot{Q}$	Internal heat source
$\dot{s}_{\text{gen}}$	Irreversible entropy generation rate per unit volume
$\mathbf{q}$	Heat flux vector
$\mathbf{u}$	Velocity vector
$\mathbf{w}$	Weighted average vector
$\mathbf{x}$	(1) Coordinate vector; (2) Vector of design variables
A	Area
C_{p0}	Non-dimensional total pressure coefficient
C_{ps}	Non-dimensional pressure coefficient
C_h	Static enthalpy rise coefficient
C_P	Specific heat capacity at constant pressure
C_p	Static pressure recovery coefficient
C_V	Specific heat capacity at constant volume
D	Depth
D_1, D_2	Dimensional cubic Bezier curve control point parameters
d_1, d_2	Non-dimensional cubic Bezier curve control point parameters
H	(1) Boundary layer shape factor ($\frac{\delta^*}{\theta}$); (2) Height
h	Enthalpy per unit mass

h_0	Stagnation enthalpy per unit mass ($h + \mathbf{u}^2/2$)
k	Turbulent kinetic energy
L	Length
LL	Leaving loss or leaving kinetic energy
M	Mach number
N_{step}	Number of time steps
P	Total power output
p	Pressure
p_0	Stagnation or total pressure
Pr_t	Turbulent Prandtl number
q	Quasi-orthogonal
$r; R$	Radius
r_c	Radius of curvature
s	Entropy per unit mass
T	Temperature
U	Blade velocity
V	Absolute velocity
W	(1) Relative velocity; (2) Width
y^+	Non-dimensional wall distance
Y_p	Total pressure loss coefficient
G-0; L-0	Last stage nozzle and rotor rows, respectively
G-1; L-1	Penultimate stage nozzle and rotor rows, respectively
NI; NJ; NK	Number of grid points in axial/radial/circumferential directions, respectively

Greek Symbols

δ^*	Boundary layer displacement thickness

η	Efficiency
γ	Heat ratio (C_P/C_V)
κ	Curvature
λ	Thermal conductivity
λ_t	Turbulent thermal conductivity
μ_t	Turbulent or eddy viscosity
ω	Turbulent eddy frequency
Φ	Irreversible entropy production
ψ	Flow guide turning angle
ρ	Density
τ	Viscous stress tensor
θ	(1) Absolute swirl angle; (2) Flow guide turning angle; (3) Circumferential angle; (4) Boundary layer momentum thickness
ξ	Residual kinetic energy

Subscripts

θ	Circumferential component
$i; j; k$	Index
m	Meridional component
0	Stagnation
1; 2; 3	Station number at stage (or diffuser) inlet, stage (or diffuser) exit and exhaust hood exit respectively
abs	Quantity in the absolute (stationary) frame of reference
avg	Averaged value
design	Design condition
dyn	Dynamic head

is	Isentropic process
ref	Reference value
rms	Root mean square
s	Static
t-s	Total-to-static
t-t	Total-to-total

Other Symbols

$\mathbb{R}$	Real space
$\mathcal{E}$	Non-dimensional strain energy
D/Dt	Material derivative ($\partial/\partial t + \mathbf{u} \cdot \nabla$)

Acronyms / Abbreviations

1-D; 2-D; 3-D	One-, two-, three-dimensional
AMG	Algebraic Multigrid
AR	Aspect Ratio
BPF	Blade Passing Frequency
CCGT	Combined Cycle Gas Turbine
CDA	Controlled Diffusion Airfoils
CFD	Computational Fluid Dynamics
FFT	Fast Fourier Transform
FR	Frozen Rotor
GA	Genetic Algorithm
HP	High pressure
HPC	High Performance Computing
IAPWS	International Association for the Properties of Water and Steam
IP	Intermediate pressure
LES	Large Eddy Simulation

LHS	(1) Left hand side; (2) Latin hypercube sampling
LHV	Lower Heating Value
LP	Low pressure
MEC	Minimum Energy Curves
MMP	Multiple Mixing Planes
MP	Mixing Plane
MTS	Miniature Traverse System
NEMA	National Electrical Manufacturers Association
NLH	Non-linear Harmonics
PCA	Principal Component Analysis
PIV	Particle Image Velocimetry
PR	Pressure ratio
RANS	Reynolds-averaged Navier-Stokes
RHS	Right hand side
SAS	Scale-Adaptive Simulation
SST	Shear Stress Transport
URANS	Unsteady Reynolds-averaged Navier-Stokes
USC	Ultra-supercritical

Chapter 1

Introduction

1.1 International energy outlook 2020 - 2040

The global power generation market is currently in a paradigm shift, with increasing proportion of electricity being generated by renewables. Nevertheless, around 60% of the world electricity will still come from fossil power plants (coal, oil and natural gas) by 2040, as presented in Fig. 1.1 from the International Energy Outlook [17]. Due to the intermittent nature of solar and wind energies, thermal plants have to vary their load more frequently throughout the day (Fig. 1.2). Therefore, operational flexibility and high efficiency have become the key requirements for large steam turbines (in coal, CCGT and nuclear plants), in the age of electrification amidst concerns over global warming.

Modern steam turbines for power generation have been around for over 130 years since Sir Charles Parsons' invention in 1884 and today they are still one of the most important prime movers for power generation, responsible for over 60% of global electricity supply [77]. Initially, Parsons' turbine could only deliver 7.5 kW of electricity [48]. Nowadays, with advanced design and manufacturing capabilities, steam turbines have become much

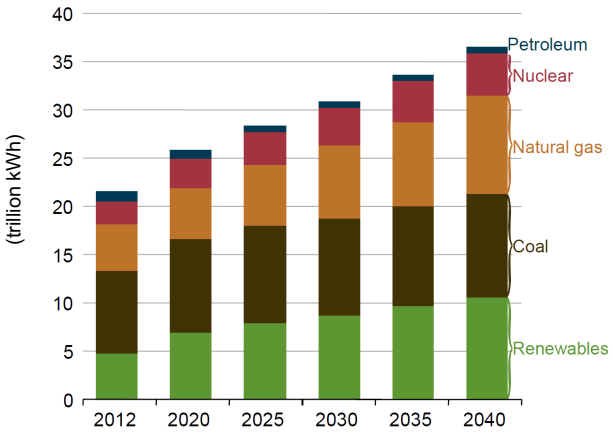

Fig. 1.1 World net electricity generation by fuel type, 2012–40 (in 10^{12} kWh) from the International Energy Outlook 2016 [17]

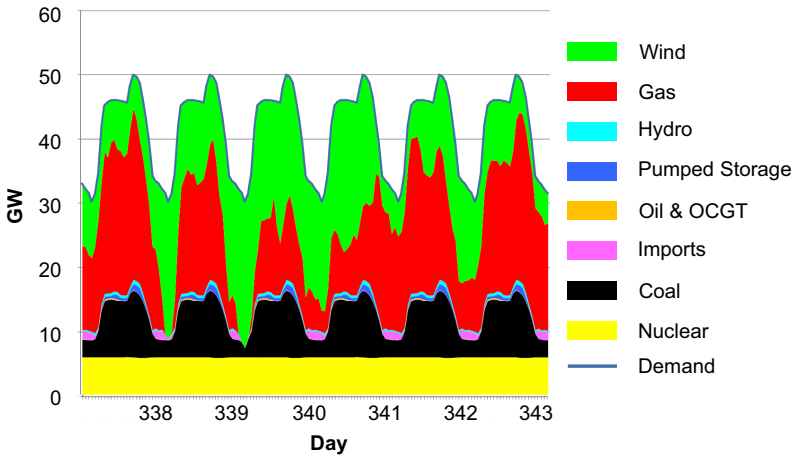

Fig. 1.2 Simulated UK electricity generation by fuel type in 2020, from Rogers [63]

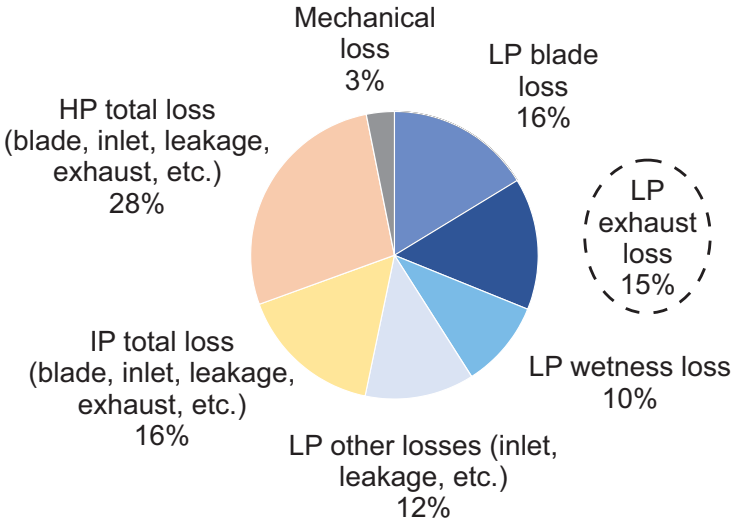

Fig. 1.3 Loss breakdown in a steam turbine, adapted from Tanuma et al. [77]

more powerful and efficient: a single-shaft turbine can now deliver at least 1000 MW of power, with electrical efficiency exceeding 46% (LHV) in some recently built double-reheat ultra-supercritical (USC) coal fired power plants [57].

In order to further improve the efficiency of a large steam turbine, it is important to understand the sources of loss from various components. The loss breakdown in a typical large steam turbine is shown in Fig. 1.3. It is clear that both the high pressure (HP) and intermediate pressure (IP) cylinders attain high aerodynamic efficiencies. Most importantly, LP blading loss and exhaust loss are the top two sources of loss in the entire steam turbine, each contributing approximately 15% of the total loss. In the past few decades, much effort has been made to improve the blading design [75, 46]. This is a rather challenging task since both mechanical integrity and thermal (wetness) effect need to be taken into account when redesigning the blade. In contrast, the LP exhaust system has rather simple structures, so designers can focus on its aerodynamic performance alone.

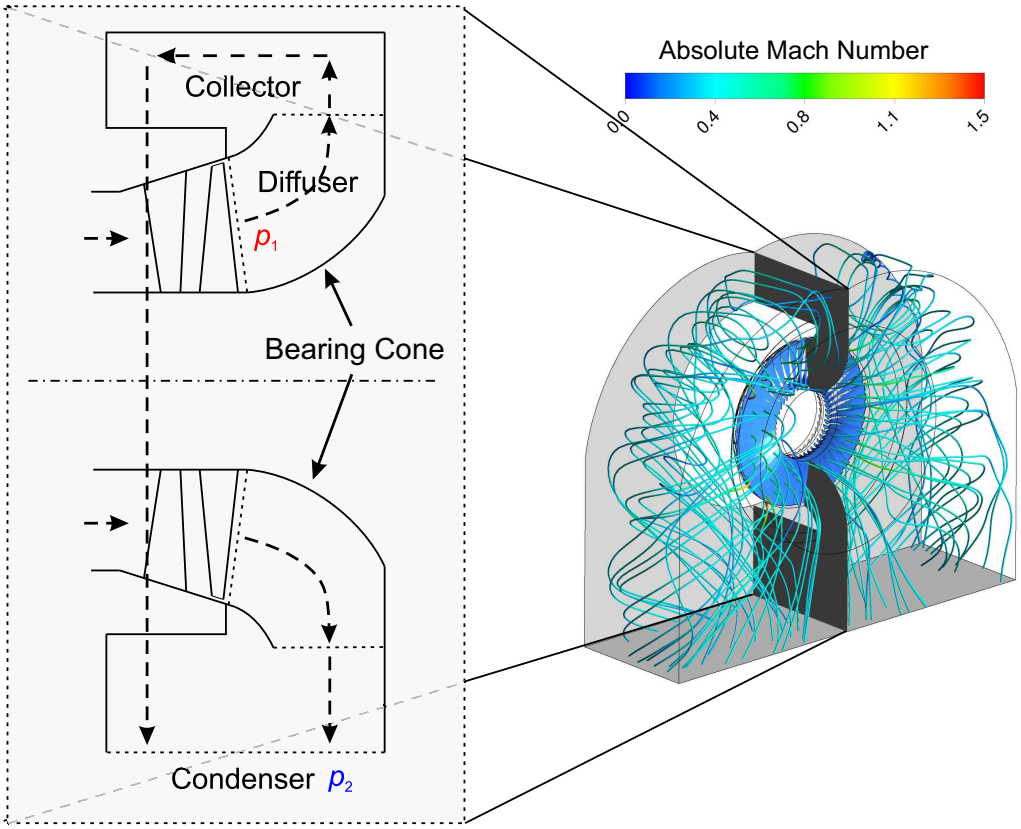

Fig. 1.4 LP steam turbine exhaust system. Left: side view of the exhaust system. Right: streamtubes starting from the diffuser inlet at design condition, with colours indicating Mach number levels

1.2 LP steam turbine exhaust system

A typical down-flow type LP exhaust system for large steam turbines, as illustrated in Fig. 1.4, consists of an axial-radial diffuser and an asymmetric collector that directs the flow downwards to the condenser. The exhaust system recovers the LP leaving energy, reduces the back pressure of the last stage and increases its power output.

The flow physics inside the LP exhaust system is rather complex, as illustrated by the streamtubes in Fig. 1.4. The wet steam flow field is transonic (supersonic near the diffuser outer casing), unsteady and vortical. The flow in the last stage is strongly coupled with that in the exhaust hood and experiences a circumferentially non-uniform back pressure due to the presence of the collector. Finally, as the turbine operates at part-load conditions, the flow becomes highly swirling and the size of flow separation regions grows significantly, which not only impacts the system performance but also makes numerical simulations difficult.

Despite the challenges in dealing with such complex flow, there is great incentive to design a better exhaust system. Keller was one of the first to recognise the importance of careful LP exhaust system design, demonstrating that as much as 0.5% gain in thermal efficiency could be realised for a fossil fuel power turbine by adding a diffuser to the exhaust

hood [40]. More recently, Burton reported that recovering a third of the leaving kinetic energy in the LP cylinder, which is as much as 30 MW for a 750 MW steam turbine, leads to a 2.5% increase in LP turbine power output [10].

The potential for performance improvement has motivated the research community to study the LP exhaust system for many decades. However, there are still some gaps in our knowledge and this thesis aims to address these issues:

1. There has been a lack of attention to the part-load operation of LP exhaust systems and very little validation of numerical tools at such flow conditions. Moreover, it is not well understood what the key flow features and loss mechanisms are in the exhaust system, as the operating condition changes.

2. The two components in the LP exhaust system, *i.e.* the blading and the exhaust hood, are strongly coupled, although they were often designed and optimised in isolation. It is also unclear how much each component is responsible for the overall loss generation, and how much benefits could blading and exhaust hood redesigns bring to the system.

3. It is not yet clear how the exhaust system should be designed to cope with a wide range of operating conditions. And there is a lack of understanding of the sensitivities of exhaust hood design parameters, due to the high dimensionality of the parameter space and high cost of numerical and experimental investigations.

1.3 Thesis outline

In this thesis, **Chapter 1** provides background and motivation for this research, followed by a literature survey in **Chapter 2**. **Chapter 3** describes the experimental method and the validation of the CFD solver based on a scaled test rig. **Chapter 4** concerns actual size LP exhaust systems and the associated numerical methods. **Chapter 5** investigates the key flow features and loss mechanisms in the LP exhaust system (last stage and exhaust hood) with particular attention paid to its part-load performance. In addition, the effect of stage-hood interaction on system performance is studied by restaggering the last stage rotor blade. **Chapter 6** explores ways to reduce the parameter space dimension for the exhaust diffuser, by introducing the concept of "Minimum Energy Curves". This is later used in **Chapter 7**, together with the recently emerged idea of "active subspace", to study the sensitivity of key design variables of the LP exhaust system with relatively low computational cost. Finally, major findings and suggested future work are summarised in **Chapter 8**.

Chapter 2

Literature Review

LP steam turbine exhaust systems have attracted the attention of the research community for decades, with early published work dating back to the late 1960s. There are two literature reviews that provide excellent summaries of relevant works, by Keller [40] and Burton et al. [14]. Keller's review in 1986 relates conventional diffuser theory and relevant data to the commercial design of LP steam turbine exhaust systems [40]. Until then, studies on diffusers and LP exhaust system had very much been theoretical and experimental, and were mainly concerned with 1-D performance metrics, such as pressure recovery and loss coefficients, rather than detailed flow features. Moreover, Keller commented that conventional diffuser data could not be directly applied to the LP exhaust design, and there was a lack of "consistent and reasonably complete approach to the optimization" of turbine exhaust diffusers. Nevertheless, "every endeavour should be made to improve the aerodynamic performance of the exhaust system", since the potential for plant efficiency improvement was estimated to be around 1% in heat rate.

Since then, the research community has been equipped with more detailed measurement techniques and advanced computational tools such as 3-D CFD, which enable deeper insights into the flow physics and loss mechanisms in the LP exhaust system. The review by Burton et al. in 2013 provides a good summary of the key flow structures inside the exhaust hood, factors influencing the exhaust hood performance, as well as numerical and experimental methods applied to study the flow in the exhaust hood [14].

This chapter is not meant to be repetitive of the above-mentioned reviews, but to highlight the work done to help fill the gaps in our knowledge that were identified in Section 1.2. The first section of this chapter introduces metrics used to evaluate the performance of LP exhaust systems. The second section focuses on the part-load operation of exhaust systems, and the validity of prediction tools in comparison with experiments. The third section concerns stage-hood interactions and compares different interface treatments used in turbomachinery CFD. The final section reviews work on the sensitivities of exhaust system design parameters and introduces the recently emerged idea of "active subspace" for dimension reduction and global sensitivity analysis.

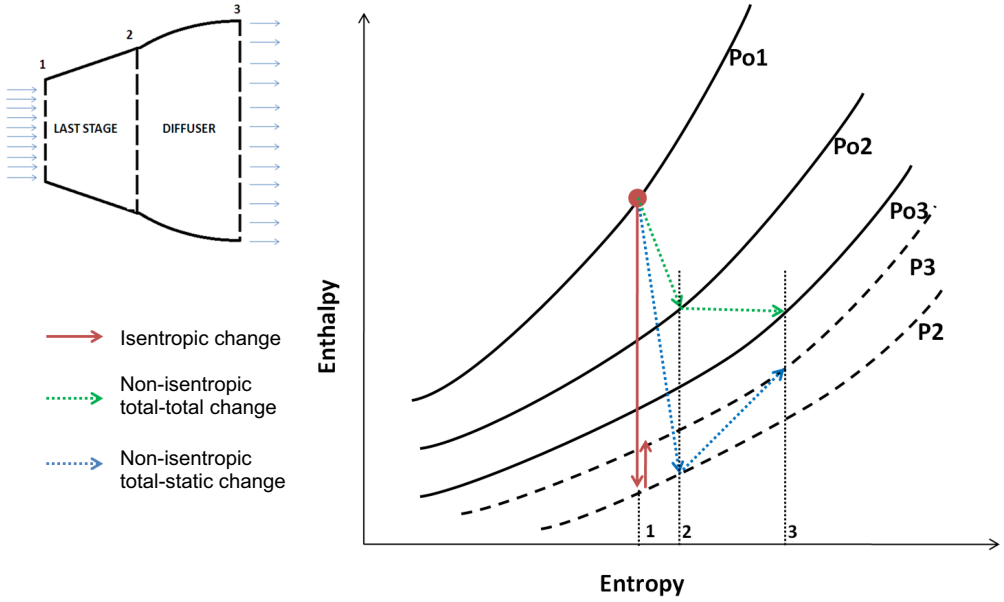

Fig. 2.1 Thermodynamic process in the last stage and exhaust diffuser, from Singh [68]

2.1 Performance metrics of LP exhaust systems

Before delving into the details of complex flow features and loss mechanisms, it is important to recognise the metrics that are suitable for evaluating the merits of an exhaust system against another. Depending on the objective of the design or optimisation, the performance metrics could be component-specific, such as the last stage or the exhaust hood, or one is concerned with the overall system performance that considers the last stage and the exhaust hood as a whole.

For the sake of simplicity, it shall be assumed the LP exhaust system consists of two components: the last stage and the exhaust hood, the latter consisting of an axial-radial diffuser and a collector. Fig. 2.1 plots the thermodynamic process inside the system: steam expands from the inlet to the outlet of the last stage generating work ($1 \rightarrow 2$), and then compresses in the diffuser by raising its static pressure ($2 \rightarrow 3$).

When considered in isolation, the last stage's performance can be evaluated by its total-total efficiency since the leaving energy can still be recovered by the downstream exhaust hood, as commented by Singh [68]:

$$\eta_{\text{t-t, stage}} = \frac{h_{01} - h_{02}}{h_{01} - h_{02s}}. \tag{2.1}$$

The performance of the downstream exhaust hood is typically judged by its capability to recover static pressure and to minimise drag (or total pressure loss). Pressure is used instead of energy (enthalpy) since it can be more directly measured in the experiment.

Following the derivation by Hirschmann et al. [35], we have:

$$\frac{p_3 - p_2}{p_{\text{dyn, 2}}} + \frac{p_{02} - p_{03}}{p_{\text{dyn, 2}}} + \frac{p_{03} - p_3}{p_{\text{dyn, 2}}} = 1 \tag{2.2}$$

where $p_{\text{dyn, 2}} = p_{02} - p_2$ is the dynamic head at diffuser inlet (station 2 in Fig. 2.1). The three terms on the LHS of Eq. 2.2 are the static pressure recovery coefficient:

$$C_p = \frac{p_3 - p_2}{p_{\text{dyn, 2}}}, \tag{2.3}$$

the total pressure loss coefficient:

$$Y_p = \frac{p_{02} - p_{03}}{p_{\text{dyn, 2}}}, \tag{2.4}$$

and the dimensionless residual kinetic energy:

$$\xi = \frac{p_{03} - p_3}{p_{\text{dyn, 2}}}. \tag{2.5}$$

As commented by Hirschmann et al. [35] and also widely accepted in the research community, an exhaust hood should be designed so that C_p is maximised. Assuming p_3 is fixed (which is usually at condenser pressure level), an increase in C_p reduces the stage back pressure p_2 and hence increases the enthalpy drop across the turbine. What is missing sometimes in literature is that the total pressure loss, Y_p, also plays an important role in evaluating diffuser performance, since it directly relates to the irreversible entropy generated inside the diffuser and contributes to the total lost work. When C_p is maximised and Y_p is minimised, the residual kinetic energy at diffuser (or hood) exit, ξ, is minimised and the diffuser design is considered optimum. In fact, ξ has a lower limit for a given diffuser area ratio based on the conservation of mass.

When the last stage and the exhaust hood are considered as a system, the system total-static efficiency should be used instead:

$$\eta_{\text{t-s, sys}} = \frac{h_{01} - h_{02}}{h_{01} - h_{3s}} = \frac{\text{Actual work}}{\Delta h_{\text{is}}}, \tag{2.6}$$

where Δh_{is} is the isentropic enthalpy drop from the last stage inlet (total) to exhaust hood exit (static) condition [90].

As shall be discussed in Chapter 5, the system total-static efficiency is considered a more appropriate performance metric over C_p. In certain situations, an increase in C_p does not necessarily result in performance improvement for the *system*, even though it is considered beneficial for the *component*.

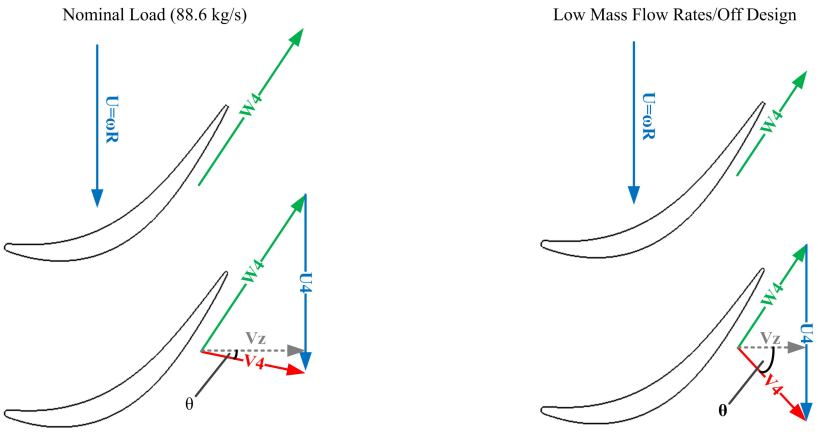

Fig. 2.2 Last stage exit absolute swirl angle at nominal and part-load, from Burton [10]

2.2 LP exhaust system at part-load conditions

As commented in Section 1.1, due to the increasing use of renewable energy sources, steam turbine plants nowadays operate over a much wider range of flow conditions. This means more frequent part-load operations with lower flow rates than the design value. Therefore, it is important to understand how the system behaves at part-load conditions, and whether the numerical tools used are capable of predicting system performance at part-load conditions. It is worth mentioning that part-load in this study refers to approximately $30-85\%$ of the design mass flow rate. This thesis does not concern very low flow conditions (less than 30% flow rate), at which the structural integrity of the last stage blades becomes important due to the so-called ventilation effect.

2.2.1 Overall performance and flow features

Gray et al. [28] used simple velocity triangles to demonstrate the effect of running an LP turbine at part-load conditions. Fig. 2.2 shows that as the flow rate reduces, the last stage exit (or diffuser inlet) absolute swirl angle θ increases. The effect of swirl (or spin) on the diffuser's performance was first recognised as early as 1970, discussed in a comprehensive report on exhaust diffuser and hood design for turbomachines [19]. In particular, according to experiment results, total pressure loss was found to increase as the swirl level increases beyond 30° for axial-radial diffusers, which corresponds to the machine operating at low flow rate conditions. The reason for the reduction in performance was attributed to the flow separation on the internal surface of the diffuser, *i.e.* the bearing cone. This was later observed experimentally by Owczarek et al. in the late 1980s using lamp-black oil visualisation technique [58].

Since the early 1990s, 3-D RANS CFD has become more affordable and numerical methods have been used to quantify the effect of swirl on the exhaust system performance, to better understand the associated flow physics. For instance, using the commercial CFD

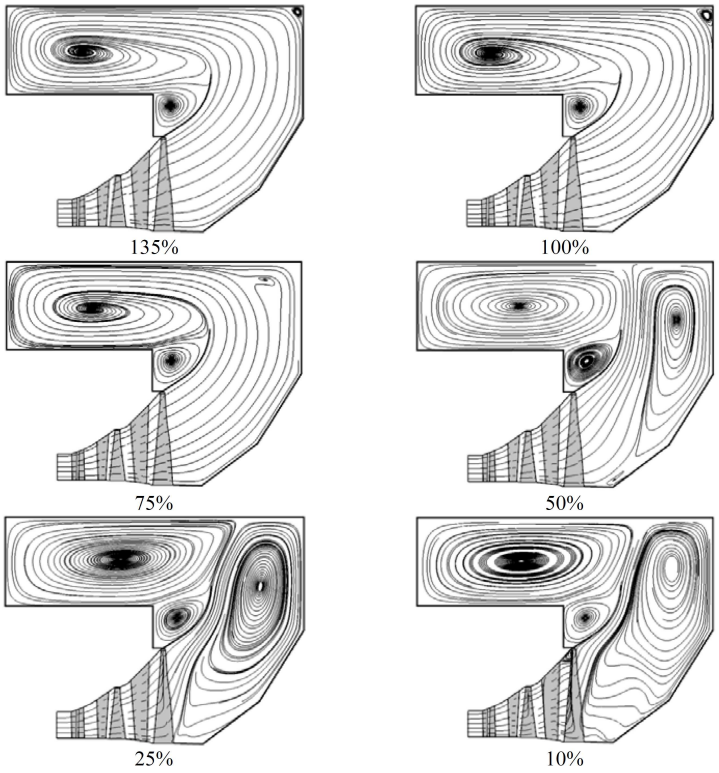

Fig. 2.3 Exhaust hood meridional streamlines at different flow rates, from Liu et al. [44]

solver FLUENT in conjunction with experiment, Stastny et al. [73] found the bearing cone separation, asymmetric flow features in the exhaust hood, as well as the increased level of pressure losses are associated with diffuser inlet swirl. A decade later, more detailed CFD simulations were performed by coupling single or multiple last stage passages with the exhaust hood geometry [65, 10, 44]. Fig. 2.3 shows that as the mass flow rate drops below 75% of its design value, the bearing cone separation size grows, which would lead to pressure loss and increased blockage. A fair amount of research has been undertaken that concerns the association between the bearing cone separation and the deterioration of exhaust hood performance [79, 86, 23]. Nevertheless, the exact loss mechanism and for how much loss the bearing cone separation is responsible are still unclear, not to mention how the exhaust system can be redesigned to minimise such loss. These issues shall be addressed in Chapter 5 in which an energy based analysis quantifies the sources of loss at different flow conditions, and blading changes are proposed to improve the part-load performance.

2.2.2 Experimental validation

3-D RANS CFD has been used to understand the flow physics of LP exhaust systems and to predict system performance since the early 1990s. At first, simulations were mostly performed at or near the design condition of the exhaust system, which achieved some success when comparing numerical results to those obtained from on-site measurements

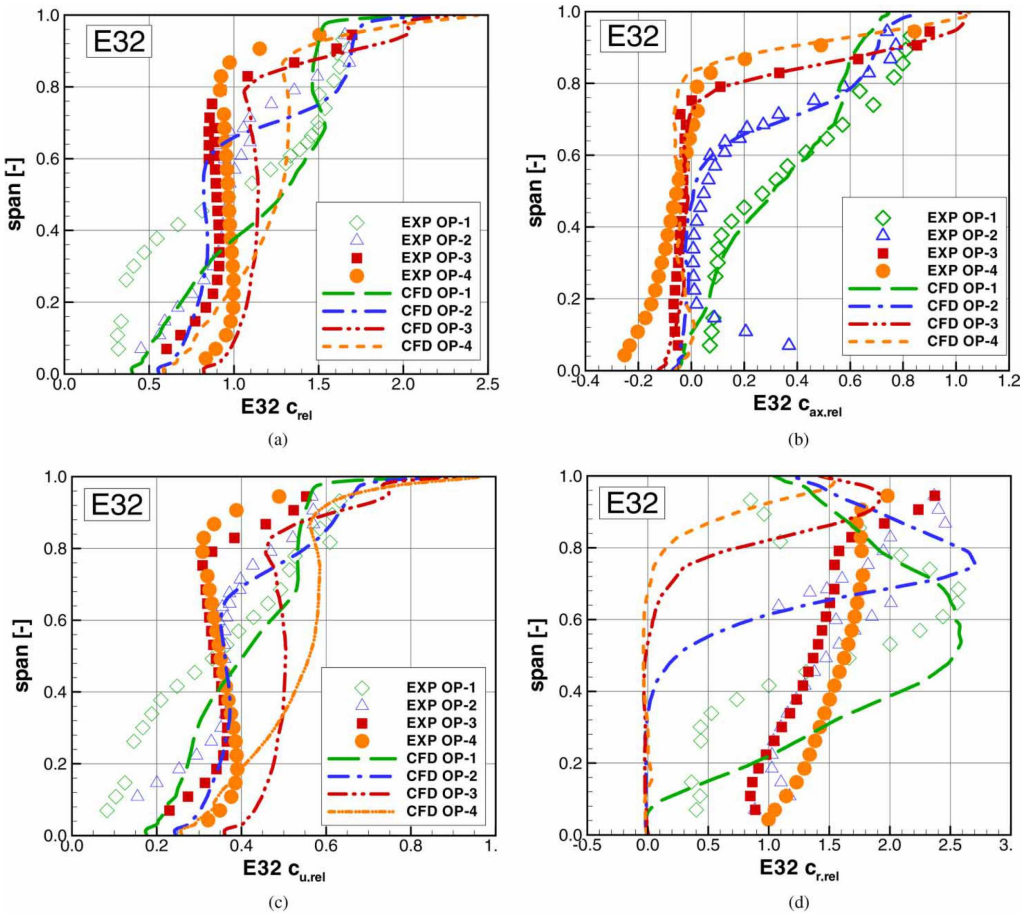

Fig. 2.4 Radial traverses of velocity (a), axial velocity (b), circumferential velocity (c) and radial velocity (d) downstream of last stage rotor, from Sigg et al. [66]. OP-1: 34% $\dot{m}_{\text{design}}$; OP-2: 23% $\dot{m}_{\text{design}}$; OP-3: 14% $\dot{m}_{\text{design}}$; OP-4: 5% $\dot{m}_{\text{design}}$

[39] and scaled test rigs [45, 7, 8, 69]. At such operating conditions, the size of flow separation inside the exhaust hood is small, so close agreement between experiment and CFD results would be expected.

As steam turbine plants are now required to operate much more flexibly, attention has been drawn to operational safety at very low loads, also known as *windage*. At such flow conditions, highly unsteady and three-dimensional flow may lead to blade excitations and it is therefore vital to correctly predict the flow field using numerical tools. For instance, Sigg et al. carried out detailed experimental and numerical investigations on the LP model steam turbine at the Institute of Thermal Turbomachinery and Machinery Laboratory (ITSM), University of Stuttgart [66]. Their instrumentation included traverses at several streamwise locations in the exhaust diffuser using a seven-hole pneumatic probe so that flow reversals could be detected. Fig. 2.4 presents the measured and calculated velocity components at the diffuser inlet at four different mass flow rates. Of interest is OP-1, or 34% of design mass flow rates, at which CFD significantly overpredicts the absolute

velocity level. This is due to an overprediction of the circumferential velocity, which is also observed in the experimental validation in Chapter 3.

Megerle carried out experiments on ALSTOM's (now GE Power) air and steam model turbines at very low flow rate conditions, and compared results to RANS CFD of various geometry configurations and turbulence models for his PhD thesis [49]. Although the focus of the work was on the ventilation phenomenon and its effect on non-synchronous aerodynamic excitations, it is interesting to note the advantage of a hybrid RANS-LES approach, such as the SAS-SST model [51], over eddy viscosity models such as the $k-\omega$ SST model [50] when it comes to resolving large-scale turbulence with limited computational effort.

Between the design condition and the very low flow rate condition, there seems to be a gap (*e.g.* $30-85\%$ of design flow rate) over which many large steam turbine plants nowadays frequently operate. This motivates the current study to validate the CFD solver at representative flow conditions (corresponding to approximately 40% and 60% flow rate) and to understand the limit of RANS CFD.

2.2.3 Design and optimisation for flexible operation

The design and optimisation of LP exhaust systems using 3-D CFD has become possible thanks to advances in computational power. Most previous studies focused on single objective optimisations, *i.e.* the performance at design condition [82, 56, 88]. The fact that steam turbine plants frequently operate at part-load conditions requires multi-objective optimisations be performed, so that the system performance at different operating conditions is weighted and evaluated. The only relevant study to the author's knowledge was done by Verstraete et al. [81], in which a weighted average static pressure recovery coefficient is used as the objective function. Indeed, the optimisation objective should be adjusted based on the actual operating profile (number of hours operated over different operating conditions) of the power plant throughout the year.

What is missing in most of these optimisation studies, however, are the linkage between expensive computations and the understanding of what is driving the performance of the exhaust system, and how the knowledge obtained can be applied to a different design task. To do so, sensitivities of key design parameters must be understood, which will be covered in the final section of this chapter.

2.3 Stage-hood interaction

It is well known that the exhaust hood is strongly coupled with upstream stages, in particular the last stage [28, 45]. This section reviews studies on the interaction mechanism, together with treatment applied to the stage-hood interface in numerical simulations.

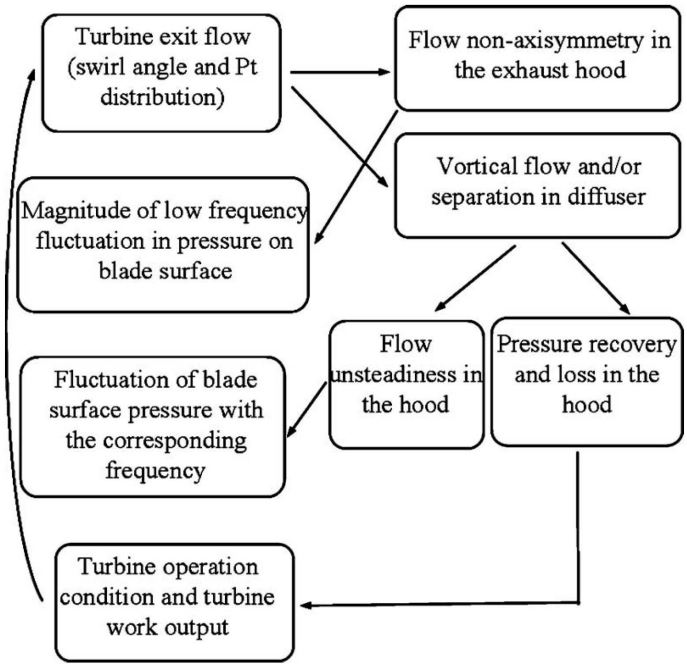

Fig. 2.5 Flow interactions between turbine and exhaust hood, from Fu et al. [27]

2.3.1 Interaction mechanism

In one of the earliest pieces of literature that focused on the flow interaction between the last stage and the exhaust hood (Gray et al. [28]), two different blade designs were compared in terms of the associated hood performance. It was suggested the lower value of total pressure near the hub of the rotor exit is associated with higher exhaust losses. The paper also addressed the need to integrate the optimisation process for the last stage and the exhaust hood, although no design changes to the blading were proposed.

In a recent study by Fu et al. on the unsteady interaction between the turbine and exhaust hood, experiments and simulations on a scaled rotating test rig revealed the interaction mechanism between the two components [27]. As summarised in Fig. 2.5, the operating condition of the last stage is influenced by the downstream exhaust hood (downstream $\rightarrow$ upstream), while the stage exit flow condition, in terms of total pressure and swirl distribution (in radial direction), affects the flow field and the performance of the exhaust hood (upstream $\rightarrow$ downstream). This is consistent with findings by Gray et al. [28], and can be considered a **quasi-steady** interaction via radial flow profiles at the stage-hood interface. Details on how the flow profile influences the diffuser performance will be provided in Section 2.3.2.

In addition, the two components interact with each other **unsteadily**. Fast Fourier Transform (FFT) performed on the pressure signals on the blade surface and at the turbine exit indicates that the vortical and asymmetric flow in the hood is inherently unsteady, and also influences the pressure field on the blade surface at very low frequency (< 50Hz)

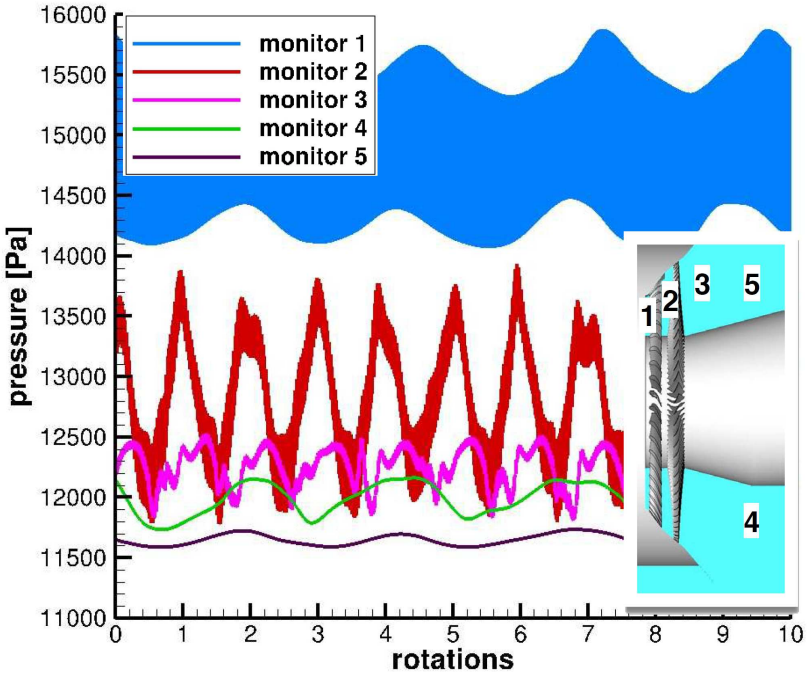

Fig. 2.6 Unsteady pressure monitoring points, from Stanciu et al. [72]

compared to blade passing frequencies (> 2kHz) [27]. This is corroborated by the full annulus unsteady RANS (URANS) simulations performed on an actual half-speed nuclear steam turbine [72]. The unsteady pressure monitored at various locations fluctuates at very different length scales (Fig. 2.6), which are related to the large vortical flows and separation regions inside the exhaust hood (Fig. 2.3). This leads to the question of whether steady RANS CFD can accurately predict the system performance compared to the much more expensive URANS CFD (typically 500 times more expensive). In Section 4.3, full annulus URANS simulations will be compared against various types of steady simulations, and the so-called Multiple Mixing Planes approach [74] will be shown to be capable of capturing most of the flow features at relatively low computational cost.

2.3.2 Effect of inlet flow profile on exhaust hood performance

The exhaust hood performance is known to be sensitive to its inlet boundary conditions, including spanwise total pressure and swirl distributions, rotor tip leakage jet, boundary layer blockage, turbulence levels, Mach number, Reynolds number, etc. Amongst these factors, the total pressure and swirl distributions are strongly influenced by both stage-hood interactions and the turbine operating condition, and hence become the focus of discussion in this section. The effect of the tip leakage jet for unshrouded rotor blades will be mentioned in Chapter 6. For the remainder of the effects, readers may refer to [70, 40, 26].

Keller commented that up to a certain limit, swirling flows help the adhesion of the boundary layer on upward concave surfaces. However, they may also have detrimental

effects concerning static pressure recovery on the bearing cone [40]. Tindell et al. performed CFD calculations for both full scale and 1/36 scale models, in which uniform and non-uniform inlet total pressure and swirl distributions were studied. Calculations showed that the hood performance was highly dependent on its inlet flow conditions, which even inverted the relative merit of their candidate flow guides. It was also reported that the non-uniformity of inlet flow caused $5-9\%$ of total pressure loss in the exhaust system.

More recently, Fu and Liu numerically investigated the influence of inlet swirl and total pressure distributions [26]. They demonstrated that the swirl at the hub of the diffuser inlet causes the separation region to grow near the bearing cone. Moreover, total pressure profiles with a negative gradient in the radial direction lead to the highest C_p and the lowest Y_p values inside the diffuser. Nevertheless, it was not stated whether the flow rate was fixed for the different profiles studied, and a mechanism to achieve such favourable profiles through blading design was not suggested.

In contrast to imposing artificially generated flow profiles at the diffuser inlet, it was decided to vary the diffuser inlet conditions by making minor variations to the blading design, as shall be seen in Section 5.3. The resultant flow profile variations are considered more realistic that those artificially imposed in [26].

2.3.3 Modelling stage-hood interaction

Liu et al. used guide vanes and screens to generate representative turbine exit conditions for their scaled exhaust hood test rig, and found diffuser performance to be strongly influenced by its inlet flow conditions [45]. This makes it necessary to include the last stage in numerical simulations, so that realistic boundary conditions can be passed from the upstream stage to the downstream exhaust hood.

In the literature, methods with various levels of fidelity were used to model the stage-hood interaction. Burton's thesis provides a comprehensive summary of both sequential and bi-directional coupling approaches used until the early 2010s [10], and hence is not repeated here. Since then, new methods have been proposed and are reviewed here in chronological order, as a complement to Burton's work.

Non-linear harmonic method (NLH)

Burton et al. applied the Non-Linear Harmonic (NLH) method by He and Ning [32] to capture the unsteady rotor-stator and rotor-hood interactions at significantly lower computational cost compared to full annulus URANS CFD [11]. By assuming that the largest unsteady disturbances are due to blade passing frequency (BPF), the NLH method decomposes unsteady flow variable $U(\mathbf{x}, t)$ into time-averaged and unsteady components:

$$U(\mathbf{x}, t) = \bar{U}(\mathbf{x}) + \sum_{i=1}^{M} U_i'(\mathbf{x}, t), \tag{2.7}$$

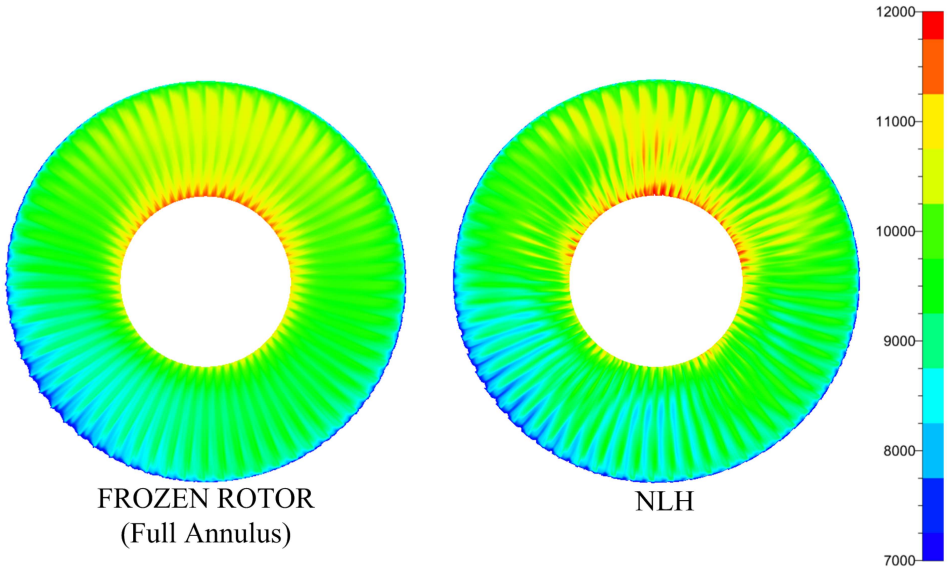

Fig. 2.7 Rotor exit static pressure (in Pa) based on frozen rotor (left) and Non-linear Harmonic (right) methods, from Burton [10]

where M is the total number of unsteady disturbances. The periodically unsteady component $U_i'(\mathbf{x}, t)$ can be further decomposed using Fourier series:

$$U_i'(\mathbf{x}, t) = \sum_{k=1}^{N} A_{i,k} \cos(k\omega t) + B_{i,k} \cos(k\omega t), \tag{2.8}$$

where N refers to the number of frequencies per perturbation.

This way, $U(\mathbf{x}, t)$ can be written as:

$$U(\mathbf{x}, t) = \bar{U}(\mathbf{x}) + \sum_{i=1}^{M} \sum_{k=1}^{N} A_{i,k} \cos(k\omega t) + B_{i,k} \cos(k\omega t), \tag{2.9}$$

Compared to full annulus URANS simulations, the NLH method only needs to model a single passage of the last stage, provided there are sufficient number of cells in the circumferential direction [83]. Its accuracy, however, depends on the number of harmonics (N) and perturbations (M) used. Burton et al. set N to 3 and M to 2, which resulted in a computational cost of around seven times that of mixing plane simulations on the same mesh [11]. In their subsequent publication [13], comparisons were made between frozen rotor and NLH methods. As shown by the rotor exit pressure contours in Fig. 2.7, the circumferentially non-uniform flow field can be well captured by the NLH method, which requires 75% less computational cost than the frozen rotor approach.

Although considered a promising method to capture asymmetric flow field in the exhaust hood, currently the NLH method has not been validated against full annulus URANS simulations, so its ability to approximate unsteady flows has not been verified.

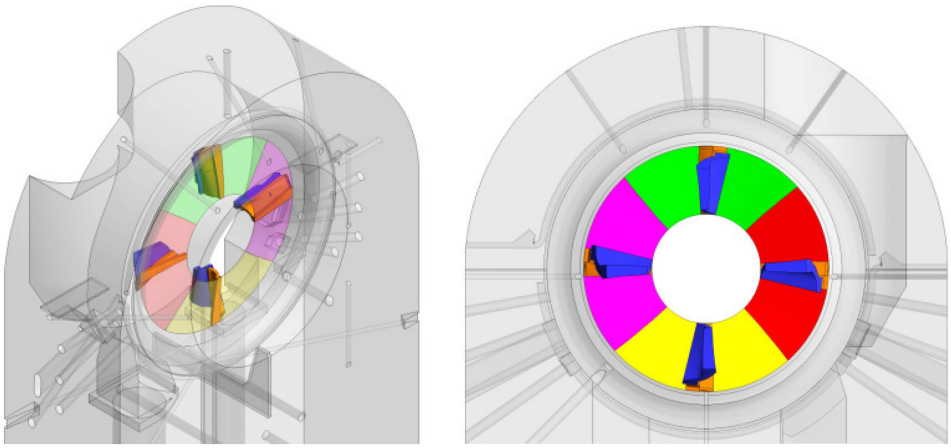

Fig. 2.8 CFD setup of last stage and diffuser using Multiple Mixing Planes (MMP) approach, from Stein et al. [74]

Multiple mixing planes (MMP)

Stein et al. proposed a stage-hood coupling method called "Multiple Mixing Planes" (MMP) [74]. In the MMP setup, multiple (typically four) isolated blade passages are equidistantly placed around the annulus, each coupled to a sector of the diffuser inlet via a mixing plane type of interface, as illustrated in Fig. 2.8. The predicted flow field using MMP was in close agreement with experiment measurement, and the predicted exhaust hood performance also agreed well with full annulus URANS simulations. More details of this interface treatment can be found in Appendix A.

The greatest advantage for the MMP method is its low computational cost compared to the frozen rotor approach (approximately 5 times lower), which makes full annulus simulations affordable for design and optimisation. In Chapter 4 of this thesis, detailed comparisons will be made between MMP, frozen rotor and full annulus URANS simulations to assess the capability of MMP to simulate asymmetric flow fields in the LP exhaust system.

Throughflow-boundary layer coupled solver

Most recently, Zhang et al. came up with a low order performance prediction algorithm based on a 2-D streamline curvature throughflow code ("Haze") coupled with an axi-symmetric boundary layer solver [91], which was similar to an algorithm proposed by Musch et al. [56]. The novelty lies in the geometry-modification treatment of the diffuser for off-design conditions. As shown in Fig. 2.9, the diffuser lip and hub shapes can be modified should the flow be predicted to separate by the boundary layer solver. This algorithm, together with an in-house hood loss model (HLM), can be used to quickly optimise the diffuser geometry during the tendering phase of retrofit projects. Despite

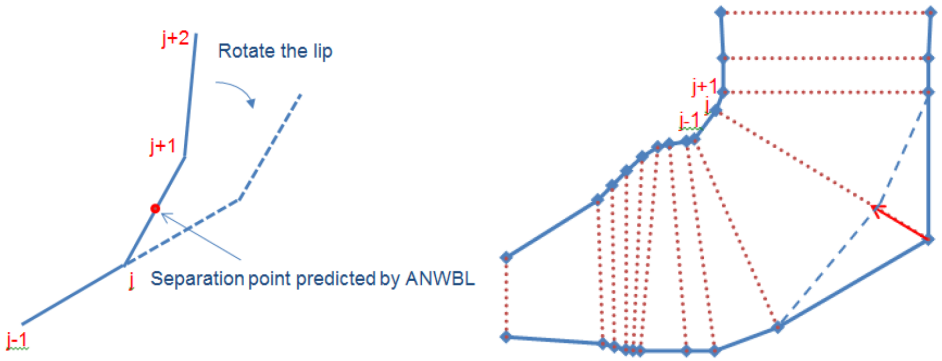

Fig. 2.9 Geometry modifications for diffuser lip (left) and hub (right), from Zhang et al. [91]

that, a more accurate algorithm based on flow physics is still required to model the large scale flow separation at part-load conditions.

2.3.4 System-based design and optimisation

In the conclusion of his paper, Keller stressed that selecting a geometry on the basis of the optimisation of an isolated parameter nearly always means a deterioration in overall performance [40]. Therefore, it is important to consider all components of the exhaust system in the process of design and optimisation. This was echoed by Tindell et al., who commented that the design of the exhaust hood and the last stage of blading should be developed as an integrated system, given the significant sensitivity in the LP exhaust system to the variations in turbine discharge conditions [79].

Nevertheless, the idea of system-based, integrated design and optimisation has only been employed since 2010. To the author's knowledge, the only related works in the public domain are by Musch et al. [56] and Cremanns et al. [18]. Musch et al. used a throughflow code coupled with a boundary layer solver to optimise the last stage together with the exhaust diffuser [56]. In their study, the last stage rotor blade angles were adjusted to minimise the leaving loss at the diffuser exit. Although the numerical model was unlikely to be able to deal with asymmetric and large scale separations inside the exhaust diffuser, especially at part-load, the results were in good agreement with 3-D RANS CFD and the optimised design was predicted to be around 3% higher in efficiency compared to the datum. The researchers did comment that it was questionable whether such a design could be put into manufacturing practice as no structural tests were carried out.

Cremanns et al. used 3-D RANS CFD for the optimisation by varying both blading and diffuser designs [18]. It was demonstrated that some 1.8% increase in system efficiency can be achieved through coupled rather than sequential optimisation. However, it was not mentioned what flow physics led to such performance improvement.

Section 5.3 will focus on the effect of rotor blade restaggering on the exhaust system performance, although such modification is restricted to the hub region. This is due to the incidence sensitivity of the supersonic airfoil shapes in the upper blade sections.

2.4 Sensitivity of exhaust hood design parameters

Previous sections have revealed the sensitivity of LP exhaust system performance to both its operating condition and the stage-hood interaction. In this section, the focus is shifted towards the sensitivity to exhaust hood design parameters. This is of great practical value to the industry, since there is a lack of relevant literature on how exhaust hoods should be designed, especially when the turbine operates over a wide range of flow conditions.

2.4.1 Lessons from conventional diffuser design

Sovran and Klomp were amongst the first to investigate rectilinear diffusers experimentally [70]. The authors determined the optimum diffuser geometries for straight-walled annular diffusers by varying two key parameters: the non-dimensional diffuser length ratio and area ratio. They demonstrated that the optimum lines of the three different diffuser types (rectangular, conical or annular) are very similar to each other on a non-dimensional basis, so long as bending is not significant. They were also able to correlate the performance of optimum and near-optimum diffuser geometries with non-uniform inlet velocities and area blockage. However, their results cannot be directly applied to curved diffusers due to the streamline curvature effects.

Compared to rectilinear diffusers, 90° curved diffusers more closely resemble the geometry of steam turbine exhaust diffusers. Fig. 2.10 presents the contours of pressure recovery ratio, C_p, against the diffuser's non-dimensional radius ratio and area ratio, based on experiments performed with annular bent diffusers [76]. Rather disappointedly, as Keller pointed out, the diffuser data for low radius ratio (under 4) and area ratio is contradictory to other publications, which is more relevant for steam turbine exhaust diffusers [40].

2.4.2 Parametric studies on exhaust hood design parameters

Compared to conventional diffusers, a steam turbine exhaust diffuser (or hood) requires many more parameters to fully define its geometry. As shall be presented in Chapter 4, a minimum of eight parameters are required in this study. Such high dimensionality (compared to two for straight diffusers) makes parametric studies very expensive. Only in the past decade have a few parametric studies on exhaust hood design parameters been published, owing to the improved test facilities and increased computational power. The

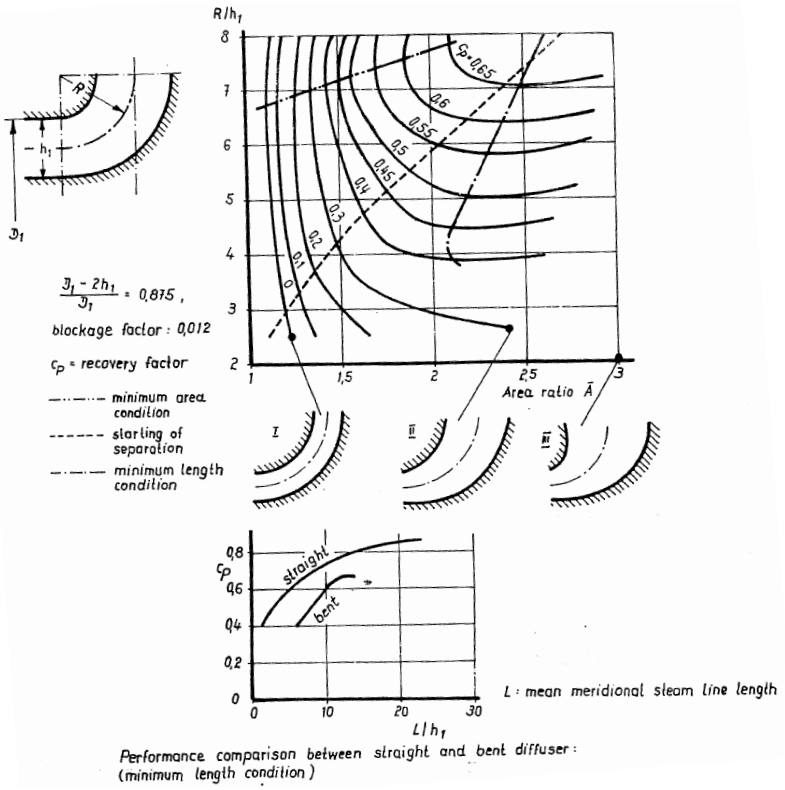

Fig. 2.10 Performance map of 90° curved annular diffusers [76], extracted from Keller [40]

bulk design parameters investigated include the diffuser axial length ratio, diffuser area ratio, exhaust hood height ratio and hood exit area ratio, defined in various forms.

Hoznedl et al. investigated the effect of diffuser axial length and divergence (area) ratios [38]. It was found that a longer diffuser is associated with lower pressure loss, while an optimum choice of diffuser divergence (around 1.4) exists to minimise the pressure loss in both the diffuser and the hood.

Finzel et al. carried out extensive experimental investigations into the scaled exhaust system test rig at ITSM Stuttgart, which operates at full-scale Mach numbers and near design flow conditions for both shrouded and unshrouded rotor tip configurations [24]. The design parameters of interest included the exhaust hood area and the horizontal joint plane area, as depicted in Fig. 2.11. The half joint area ratio, A_{JP}, was identified as the most sensitive parameter, and has a positive impact on diffuser performance. The hood area, A_{hood}, is related to the exhaust hood height, and its optimum choice depends on the tip Mach number. This was later corroborated by Munyoki et al. in their detailed analysis of the effect of hood height variation on exhaust hood performance [54].

Burton's numerical investigation found that exhaust hood performance is strongly impacted by the diffuser axial length ratio [10]. Moreover, the circumferential non-uniformity of the flow field increases as the diffuser becomes shorter, which makes it necessary to choose a proper interface treatment that can capture such asymmetry.

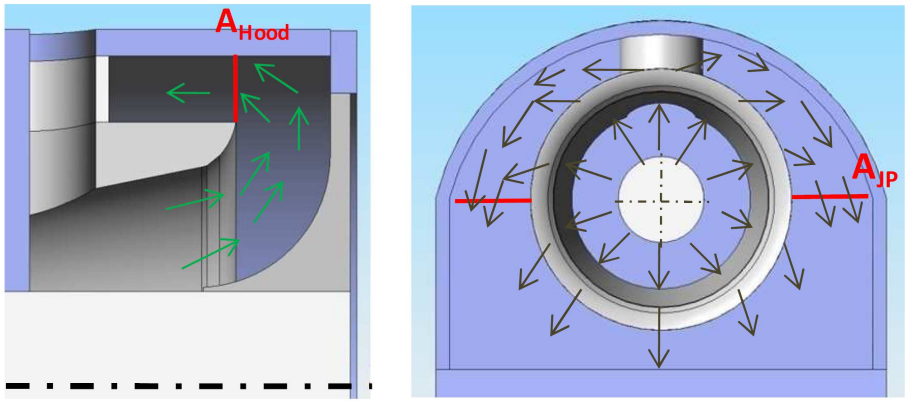

Fig. 2.11 Definition of hood area A_{hood} (left) and half joint area A_{JP} (right), from Finzel et al. [24]

Most recently, Taylor et al. carried out experimental and numerical studies on a scaled rotating LP rig at GE Power in Rugby, UK [78]. The interchangeable components in the test rig enabled many design parameters to be varied, which include the exhaust hood height and width, the diffuser length, the hub cone angle, etc. The power output of the rig was used to quantify the hood performance, consuming much less time and cost compared to probe traverses. The limitation of their approach, as for others, was that the sensitivities were only assessed at a *local* level; each time only one parameter was varied while the rest were fixed. The effect of each parameter on the *global* level cannot be easily evaluated, not to mention the interaction between the parameters.

2.4.3 Dimension reduction using active subspaces

The high dimensionality of the exhaust hood parameter space (typically at least eight) makes it very expensive to assess the sensitivity of system performance towards design parameters, and to identify the most influential parameters. Recently the concept of "active subspaces" has emerged [16] and has started to be used in turbomachinery design [64].

Mathematically, the design parameters of the exhaust system can be represented by some vector $\mathbf{x} = (x_1, x_2, .., x_n)$ where n is the number of parameters, or the dimension of the parameter space. For a given input vector $\mathbf{x}$, through experimental measurement or CFD simulations, some output variable of interest y can be obtained. y can be the system total-static efficiency as defined in Eq. 2.6, the last stage power output, or the static pressure recovery coefficient of the exhaust hood. This would construct a map $y = f(\mathbf{x})$ between the n-dimensional parameter space in $\mathbb{R}^n$ and the output values in $\mathbb{R}$. From a black box perspective, f is the experimental facility, or the non-linear mathematical model (in this case, the discretised Navier-Stokes equations).

When there is only one design parameter, *i.e.* $n = 1$, one could approximate the representation map f using various regression techniques on the samples of x_1 and the

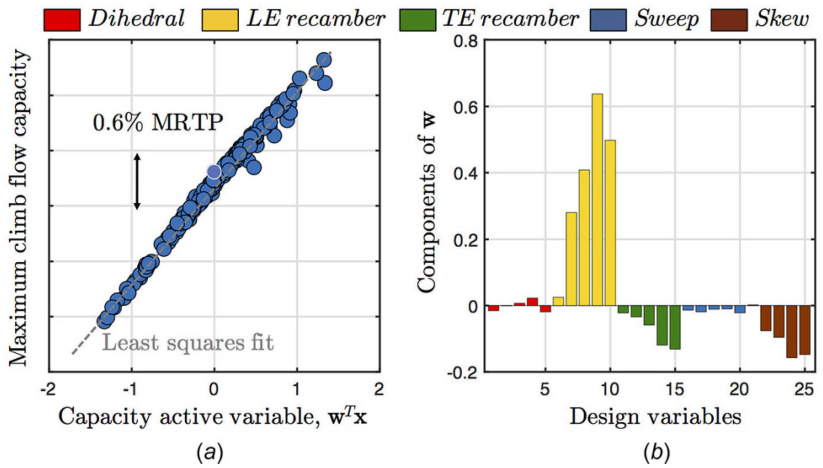

Fig. 2.12 Scatter plot of maximum climb flow capacity using the 1-D active subspace (a), with the components of **w** shown in (b), from Seshadri et al. [64]

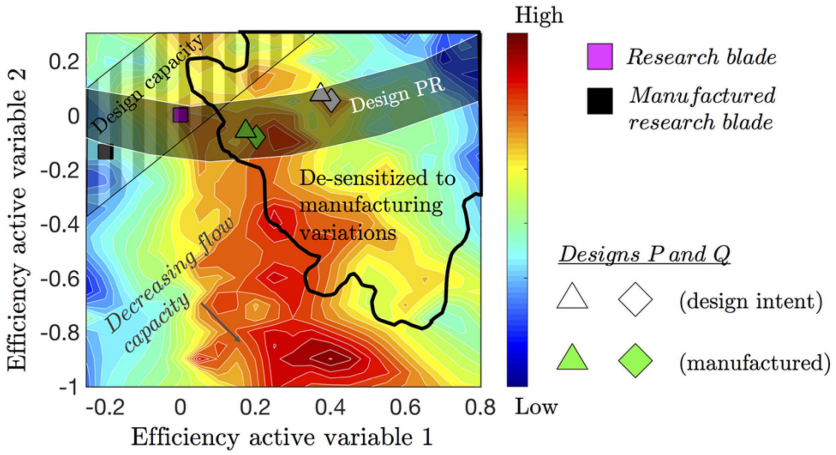

Fig. 2.13 Fan active subspace performance map in terms of pressure ratio, maximum climb flow capacity, efficiency, and efficiency–sensitivity, from Seshadri et al. [64]

corresponding outputs y. When $n = 2$, one could still construct 2-D contours of output y against the two design parameters (x_1 and x_2), as has been done for conventional diffusers in terms of length and area ratios. As n goes beyond 2, it becomes very difficult to visualise in three and even higher dimensions. Under such circumstances, active subspaces are devised to reduce the parameter space dimension down to 1 or 2, so that designers can focus on the directions along which the output y varies most significantly. In other words, active subspace is an output-based Principal Component Analysis (PCA), as commented by Seshadri et al. [64].

Seshadri et al. used active subspaces to construct performance maps for fan blades [64], which were parameterised using 25 design variables $\mathbf{x} = (x_1, x_2, .., x_{25})$ as shown on the right hand side of Fig. 2.12. By applying the algorithm outlined in [16], the 25-dimensional parameter space can be reduced down to just one single active variable

$\mathbf{w}^T\mathbf{x}$, some linear combination of the design variables $\mathbf{x}$. The scatter plot on the left hand side of Fig. 2.12, based on Latin Hypercube Sampling (LHS), clearly demonstrates the linear relation between the maximum climb flow capacity against this capacity active variable. This is an example of 1-D active subspace.

Quadratic active subspaces were also created for efficiency and pressure ratio, so that 2-D contours could be constructed [64]. For instance, Fig. 2.13 overlays the efficiency contour with regions for design pressure ratio (PR) and flow capacity, as well as regions where blade performance is relatively insensitive to manufacturing variations. This way, it would be easier for designers to make decisions, by balancing different requirements.

However, one limitation of active subspaces is the lack of physical interpretation of the active variables. A special case would be the 1-D active subspace. Assuming a linear relation between the output (*e.g.* system total-static efficiency) and the active variable, the coefficients of the linear combination, such as those shown in Fig. 2.12, can be interpreted as the global sensitivity of each design variable. Further details of how such 1-D active subspace can be constructed will be presented in Chapter 7.

2.5 Summary and research questions

This chapter has reviewed relevant works relating to the study of LP exhaust system aerodynamics. The part-load performance of the exhaust system has become increasingly important. Previous studies have attributed the drop in system performance to the enlarged separation region size inside the exhaust hood, due to the increased swirl angle at the diffuser inlet. Although such flow phenomenon has been captured in both experimental and numerical studies, there has been limited experimental validation of numerical tools, and the limit of RANS CFD is not understood. Moreover, the design and optimisation of LP exhaust systems typically focus on the design point performance. There is clearly a lack of design guidance for exhaust systems that frequently operate under part-load conditions.

The interaction between the last stage and the exhaust hood has been recognised across the literature. Downstream exhaust hood performance is strongly influenced by the flow conditions at the stage-hood interface, which are dependent on the upstream blading design. The upstream stage operating condition is influenced by the exhaust hood design and performance. Models of various fidelities have been proposed for the stage-hood interface treatment, which requires a careful balance between accuracy and cost. Moreover, the design and optimisation of LP exhaust systems must take both components (stage and hood) into account, given the strong interaction between the two, although not much work has been published with this in mind.

Finally, the chapter also reviewed the effect of various design parameters on the exhaust hood performance, for both conventional diffusers and steam turbine exhaust hoods. Some successes have been made in assessing the *local* sensitivity of design variables, but there

is a clear lack of understanding of the *global* sensitivity and the relative importance of all design parameters. The notion of "active subspaces" has recently emerged, and has been successfully applied to fan blade design to significantly reduce the parameter space dimension, and to identify dominant directions in which system performance varies the most.

In response to the gaps in our understanding identified in the literature review, the author would like to address the following research questions in the rest of this thesis:

1. How much trust can we place in RANS CFD when predicting the flow field and performance of exhaust hoods? Where is the limit beyond which RANS CFD would likely fail, when compared to experimental results? These questions will be answered in **Chapter 3**, in which experiments and simulations on a scaled test rig at representative part-load flow conditions will be compared. This will help to identify the causes of the failure of RANS CFD.

2. How does the stage-hood interaction affect LP exhaust system performance? What are the key flow features and loss mechanisms in the exhaust hood, at different operating conditions? How could last stage blading be redesigned to improve overall system performance? These questions shall be addressed in **Chapter 5**, using numerical methods described in **Chapter 4**.

3. What are the sensitivities of each design parameter of the LP exhaust system? How should the exhaust hood be designed to achieve good performance over a wide range of flow conditions? These questions will be considered in **Chapter 7** where the parameter space dimension is reduced using the so-called "active subspace" method, along with tools developed in **Chapter 6** to parametrise the exhaust diffuser using a minimal set of variables.

Chapter 3

Experimental Methods and Validation of CFD Solver

Large steam turbines nowadays frequently operate under part-load conditions, due to the increasing use of intermittent renewable energy sources. In order to accurately predict a machine's part-load performance, it is important to validate the numerical tool used at representative flow conditions, and to understand the limitations of RANS CFD, which is currently routinely used by the industry.

The challenges of part-load simulations originate from the complex flow features inside the exhaust hood at low flow rates. Fig. 3.1 presents the meridional streamlines in a typical LP exhaust hood as the mass flow rate varies between 50% to 100% of its design value. As flow rate decreases, the stage exit absolute swirl angle increases and the size of the separation region near the bearing cone grows, making it increasingly difficult for RANS CFD to accurately predict the flow field and the level of losses in the exhaust hood.

Throughout the literature there seems to be two extremes of experimental validation. At one end, the focus is on the design condition (100% flow rate) at which flow separation in the exhaust hood is small. At the other end, the concern is operational safety when the flow rate becomes very low (typically under 30% flow rate) or even zero, also known as *windage*, when the last stage starts to operate like a compressor and experiences oscillations due to rotating instability [66, 92]. There has been a lack of research on the part-load aerodynamic performance of the LP exhaust system, despite many large steam plants nowadays typically operating at low flow rate conditions (around $30 - 85\%$ flow rate).

For the current project, a low speed air test rig was built at the Whittle Laboratory to validate the CFD solver used. An overview of the test rig will first be given, followed by an introduction of the instrumentation and numerical setup. Comparisons between experiment and CFD results will be made in order to answer the following research questions:

1. How much trust can we place in RANS CFD when predicting the flow field and performance of exhaust hoods, especially at part-load conditions?

2. What is causing RANS CFD to deviate from the experiment results?

3.1 Experimental methods

A suitable test rig is needed to provide the data required to answer the questions above. In this study, representative exhaust diffuser and hood geometries were used while the Reynolds number and the diffuser inlet swirl angle were set to values as close to those in an actual machine as possible. The test rig had two configurations, the building and testing of which were carried out in two phases. The first configuration was an axi-symmetric axial-radial diffuser. In the second configuration a collector was added to the same diffuser so that the effect of circumferential non-uniformity could be studied.

3.1.1 Test facilities

Axi-symmetric diffuser

Fig. 3.2 illustrates a side view of the diffuser, with a photograph of the actual rig in Fig. 3.3. The test rig consisted of a square-to-round transition from the exit of a wind tunnel, followed by a row of stationary guide vanes to generate swirling flows, a key flow feature at low flow conditions. Details of the guide vane design will be introduced in Section 3.1.2. An axial-radial diffuser, at approximately 1/10 scale of a 1000 MW steam turbine, was located at approximately half the blade height downstream of the guide vanes. The diffuser outlet was extended by two parallel discs with an outer diameter of around 10 times the blade height. The key geometric parameters are listed in Table 3.1.

Table 3.1 Geometric parameters of the axi-symmetric diffuser (Configuration 1)

Parameter	Value
Inlet height (L_0)	97 mm
Hub-tip ratio	0.552
Axial length ratio (L_1/L_0)	1.394
Area ratio (A_1/A_0)	1.335
Total angle turned ($\Delta\theta$)	60°

L_0 and A_0 are the height and area at diffuser inlet E1 respectively, and L_1 and A_1 are the width and area respectively at diffuser outlet E2. The diffuser's hub-to-tip ratio was approximately 0.55, close to that found in typical large LP turbines ($0.4 - 0.5$). The axial-radial diffuser consisted of an inner casing (bearing cone) and an outer casing (flow guide), both machined using Green M945 modelboards. The extension discs were made from acrylic sheets so that flow visualisation could easily be performed and observed.

The experiment was carried out at the same wind tunnel fan speed for two guide vane designs, which essentially acted as throttles to the fan, resulting in different levels of mass flow rates. The Reynolds numbers, based on the height and the inlet velocity of the guide vanes, were around 250,000 and 180,000 for vanes of 40° and 60° of turning respectively.

Full annulus collector

In the second phase of the experiment, a collector made from acrylic tubes and sheets was added to the above-mentioned diffuser, to resemble an actual exhaust hood for a 1000 MW steam turbine plant. This current setup did not include any internal structures such as supporting struts and flanges. The flow guide was extended in the radial direction compared to the first configuration. The design parameters of the exhaust hood are listed in Table 3.2, and were close to those in an actual LP exhaust system. The side and front views of the configuration are illustrated in Fig. 3.4, and Fig. 3.5 is a photograph of the test rig. Note that the rig is inverted so that the flow exits vertically upwards from the exhaust hood.

Table 3.2 Geometric parameters of the exhaust hood (Configuration 2)

Parameter	Value
Diffuser inlet height (L_0)	97 mm
Flow guide outer radius ratio (R_1/L_0)	3.093
Hood vertical height ratio (H_1/L_0)	18.557
Condenser neck height ratio (H_2/L_0)	9.180
Collector depth ratio (D_1/L_0)	3.436
Collector width ratio (W_1/L_0)	10.825
Hood area ratio (A_2/A_0)	3.418

The hood geometry was extended from the condenser neck upwards to the hood exit, as can be seen in Fig. 3.5. The purpose of this was to avoid flow reversal at the hood exit as much as possible, so that the CFD simulation had a well-posed exit boundary condition.

Similar to the first configuration, the same wind tunnel fan speed was used for both guide vanes. The Reynolds numbers, based on the height and the inlet velocity of the guide vanes, were around 270,000 and 190,000 for vanes of 40° and 60° of turning respectively, close to the corresponding values in the axi-symmetric diffuser configuration.

3.1.2 Guide vane design

In order to achieve representative part-load flow conditions in an actual LP exhaust system, two sets of guide vanes were designed and 3D printed to achieve different levels of swirl angle at the diffuser inlet. The blade sections and front view of the guide vanes are presented in Fig. 3.6. Both blades are straight and are of the same axial chord ($0.33L_0$). They are used to represent low flow rate (around 60% of design mass flow rate with an averaged swirl angle of around 40°) and very low flow rate (around 40% of design mass flow rate with an averaged swirl angle of around 60°), and are referred to as "40° vane" and "60° vane" respectively throughout this chapter.

3.1.3 Pressure measurement

Steady pressure measurement was the main instrumentation in the current experiment, and was obtained using *SensorTechnics* transducers with ±25 mbar gauge range. The sensors output amplified analog signals that were acquired and converted to digital signals with *National Instruments* PXIe-6345. The transducers were calibrated against a *Druck* DPI 520 pressure controller (70 mbar gauge range). Before and after each experiment, the zero pressure offset was recorded to account for the temperature drift throughout the course of the experiment. The error in the pressure sensor readings due to non-linearity and thermal drift was within ±0.3% of its full scale.

In this study, measured pressure was non-dimensionalised as:

$$C_{\mathrm{ps}} = \frac{p - p_{\mathrm{s,\ ref}}}{p_{0,\ \mathrm{ref}} - p_{\mathrm{s,\ ref}}}, \tag{3.1}$$

where p is the nominal static or total pressure measured. $p_{0,\ \mathrm{ref}}$ is the total pressure at the inlet traverse location, obtained using pitot probes at 71% of the span and averaged from readings at four equidistant locations around the annulus. $p_{\mathrm{s,\ ref}}$ is the arithmetically averaged wall static pressure at the inlet of the bearing cone and the flow guide (H1 and T1 in Fig. 3.2), again based on four readings around the annulus. By applying the partial differential method as recommended by Abernethy et al. [4], the uncertainty of C_{ps} in wall static measurement is estimated to be within ±0.005 when C_{ps} is above -0.2, and increases to ±0.03 as C_{ps} drops to -0.6, the lowest level measured.

Wall static pressure

As shown in Fig. 3.2, both configurations of the test rig were instrumented with wall static pressure tappings on the bearing cone (H1 to H5) and the flow guide (T1 to T5). In the axi-symmetric diffuser configuration, readings were taken at four equidistant locations around the annulus and averaged arithmetically.

In the exhaust hood configuration, the number of readings within the diffuser increased to 12 around the annulus, so that circumferential non-uniformity could be captured and compared against CFD. In addition, wall static pressure readings were taken around the condenser neck plane, as illustrated in Fig. 3.4.

Pneumatic probe design and calibration

In the axi-symmetric diffuser configuration, line traverses were performed at the inlet and outlet of the diffuser (E1 and E2) using a four hole pneumatic probe for pressure and flow angle measurement. The probe head shape and hole locations were based on the design by Pfau et al. [61], illustrated in Fig. 3.9. The probe was calibrated for the speed range of $25 - 45$ m/s in a free jet, generated in a calibration wind tunnel. The calibration

coefficients were defined as:

$$\text{Yaw Coefficient} = \frac{P_2 - P_4}{P_3 - P_{\text{avg}}}$$
$$\text{Pitch Coefficient} = \frac{P_3 - P_1}{P_3 - P_{\text{avg}}}$$
$$\text{Total Pressure Coefficient} = \frac{P_0 - P_3}{P_3 - P_{\text{avg}}}$$
$$\text{Static Pressure Coefficient} = \frac{P_0 - P_{\text{s}}}{P_3 - P_{\text{avg}}}$$

where

$$P_{\text{avg}} = \frac{1}{2} \cdot (P_2 + P_4)$$

and P_0 and P_{s} refer to the total and static pressure respectively, measured using separate pitot and static probes in the calibration jet.

Fig. 3.10 demonstrates a typical calibration map, showing the effects of yaw and pitch coefficients on contours of yaw and pitch angles, which were similar to those observed by Pfau et al. [61]. The asymmetry of the map is due to the arrangement of top (P1) and centre (P3) hole locations. 5^{th} order polynomials were employed to fit the calibration map. The error in angle measurement was within $\pm 1°$ for yaw angles in the range of $\pm 24°$ and pitch angles between $-24°$ to $+30°$. This level of accuracy was considered acceptable given that the yaw angle varies significantly inside the diffuser, due to the presence of highly swirling flows and large separation regions. The uncertainty of C_{p0}, the total pressure coefficient, is estimated to be within ± 0.008 when C_{p0} is greater than 0.0, and increases to ± 0.03 as C_{p0} drops to around -0.2, the lowest level measured.

A 2-axis miniature traverse system (abbreviated as "MTS" in Fig. 3.2) was designed and built to perform both linear movement and yaw rotation through two NEMA size 8 stepper motors, as shown in Fig. 3.9. The MTS could be attached to any surface through 3D-printed platforms. Encoders were installed to keep track of the probe positioning. Yaw rotation was monitored using an axial magnetic ring (*RENISHAW* RoLin$^{\text{TM}}$ miniature incremental magnetic encoder) glued to the sleeve onto which the probe was screwed, and readings were obtained from the miniature read head mounted below the magnetic ring.

The flow recirculation inside the diffuser made the measurements by the non-nulling pneumatic probes very difficult. To overcome this problem, a rotating mechanism was devised for the four hole probe. To detect the flow angle at each spanwise location, the probe was first rotated 8 times, each time by 40°. The location of the maximum total pressure was considered to be the closest to the actual flow direction. This was followed by a final measurement at the maximum response location to increase the resolution and accuracy of the measurements.

3.1.4 Flow visualisation

In addition to pressure measurement, flow visualisation was used to qualitatively study the flow features inside the exhaust hood. Fluorescent paints mixed with Paraffin were applied to the surfaces of the diffuser and the collector's front wall. The surface flow patterns were then compared with streamline plots obtained from CFD.

3.2 Validation of CFD solver

3.2.1 Numerical setup

In this study, the commercial CFD solver ANSYS CFX 17.0 was used for steady RANS simulations. More details of the solver will be described in Chapter 4. The CFD domain for the axi-symmetric configuration is presented in Fig. 3.7, which included an artificial plenum in order to avoid reverse flows at the CFD outlet. The CFD inlet coincided with the inlet traverse location in Fig. 3.2, and the radial distribution of inlet total pressure was matched to that measured in the experiment. Since the CFD outlet was different from the actual outlet in the experiment, the average static pressure at the CFD outlet needed to be adjusted to match the wall static pressure readings and hence the flow speed at the domain inlet. The blade passage meshes were generated using NUMECA Autogrid 5. The rest of the domain was meshed using multi-block H-meshes with a MATLAB script, the details of which can again be found in Chapter 4. The guide vanes and the diffuser were coupled via a frozen rotor interface, since the radial traverse was performed only in one line, and there was no relative motion between the guide vanes and the diffuser. y^+ was set to be less than 1.0 everywhere on viscous surfaces. Menter's $k-\omega$ SST model was used for turbulence closure, assuming a fully turbulent flow [50]. The single passage domain, representing 1/36 of the annulus, consisted of around 1.5 million grid points.

In the exhaust hood configuration, full annulus blade passages were modelled together with the exhaust hood geometry used in the experiment. The CFD domain is illustrated in Fig. 3.7. Again, in order to avoid flow reversal at the CFD exit the hood domain was extended upwards by another 500 mm or $5.155L_0$ with the same cross-sectional area. The CFD exit pressure was adjusted so that the flow speed at the domain inlet could be matched with the experiment. Compared to the axi-symmetric configuration, a much greater mesh size was used to model all blade passages, as shown in Fig. 3.8. There were 1.1 million grid points per blade passage, and 10 million in the exhaust hood. This resulted in a total mesh count of 45 million, and y^+ was under 1.0 on the vane and diffuser surfaces.

3.2.2 Axi-symmetric diffuser

The numerical results were compared to those obtained in the experiment, in terms of the following: wall static pressure on the bearing cone and flow guide of the diffuser, radial

distributions of total pressure and flow angle at the inlet and outlet of the diffuser, and surface streamlines.

Fig. 3.11 illustrates the static pressure distributions on the bearing cone and the flow guide. The experiment results were arithmetically averaged from the measurement taken at 4 equidistant locations around the annulus. Overall, CFD captured the same trend as the experiment on both surfaces, but with a few discrepancies. On the bearing cone, CFD underpredicted the pressure recovery for the 60° vane, due to the overprediction of the separation size on this surface, as evidenced by the surface streamline comparison in Fig. 3.12. The CFD streamlines were duplicated circumferentially based on the 10° sector's result. CFD overpredicted the radius of the reattachment line on the extension disc by around 26% of diffuser inlet height L_0. On the flow guide, there was close agreement up to $60 - 80\%$ of the arc length. There was greater disagreement towards the end of the flow guide, especially for the 40° vane, for which the CFD value flattened out due to an earlier onset of separation, seen in Fig. 3.13.

Fig. 3.14 shows the radial distributions of total pressure coefficient and absolute swirl angle at the diffuser inlet and outlet. The total pressure coefficient has been defined in Eq. 3.1, referenced to the total pressure at the domain inlet (upstream of the guide vanes) and static pressure at the diffuser inlet. The swirl angle distributions were in close agreement for most of the span, between experiment and CFD. For the 60° vane, there was disagreement in swirl angles in the reversed flow regions at the diffuser inlet, which was below 20% of the span. This can be seen in the surface streamline comparison in Fig. 3.15. CFD overpredicted the circumferential velocity, which was also observed by Sigg et al. [66]. Moreover, the agreement in swirl angle was notably better for the 40° vane, as the flow stayed attached at the inlet (H1) and the outlet (H5) of the bearing cone, with a much smaller separation region, as shown by the surface streamlines in Fig. 3.15. The uncertainties of the CFD prediction at higher swirl (60° vane) was also clear in total pressure plots (Fig. 3.14). Although CFD captured the correct trend, it underpredicted the pressure loss for most of the span. The situation again improved for the 40° vane, apart from the regions near the endwalls.

Overall, the CFD tool was in close agreement with the experiment, particularly for the 40° vane, for which the flow separation region was much smaller. For the 60° vane, there appeared to be some difficulties when using the turbulence model to predict the mixing in large separation regions and highly swirling flows. As shall be discussed in Section 5.2.4, the bearing cone separation is the main loss contributor at part-load conditions. Caution must therefore be taken when one attempts to predict the performance and the flow field of the exhaust system for very low flow rate and high swirl angle.

3.2.3 Full annulus exhaust hood

For the exhaust hood configuration, the focus was on the circumferential and streamwise distributions of wall static pressure in the diffuser, as well as the level of pressure recovery from the diffuser inlet to the condenser neck.

Fig. 3.16 illustrates the streamwise and circumferential variations of static pressure on the flow guide and the bearing cone. The 5 streamwise locations correspond to those plotted in Fig. 3.2 and the 12 circumferential locations are illustrated in Fig. 3.4. Similar to the first configuration, overall close agreement was observed between experiment and CFD results in terms of pressure level and circumferential variation due to the swirling flow and the presence of the asymmetric collector. For low swirl (40° vane) there was greater discrepancy on the flow guide at Locations 2 and 3. CFD underpredicted the pressure level due to its prediction of an earlier onset of flow separation at both the top and bottom of the surfaces, as shown by the streamline plots in Fig. 3.17. This suggests that the SST model might be too pessimistic when predicting the onset of flow separation. For high swirl (60° vane), CFD overpredicted the pressure rise on the bearing cone despite arriving at the same level as the experiment at the diffuser outlet (Location 5). As can be seen in the flow visualisation in Fig. 3.18 and Fig. 3.19, the hub separation zone was much greater at higher swirl angle. As discussed earlier, CFD tended to predict a smaller blockage in the diffuser passage compared to the experiment, leading to a higher level of pressure recovery.

In addition to the flow guide and bearing cone, another region of interest was the condenser neck (Fig. 3.7). Fig. 3.20 and Fig. 3.21 show the static pressure coefficients measured and calculated on the four sides of this plane for 40° and 60° vanes, respectively. To illustrate the flow features, contours of C_{ps} (defined in Eq. 3.1) based on CFD results were plotted along with streamtubes originating from different sectors at the diffuser inlet. This post-processing method has been used in some recent studies [52, 89, 53], and will be applied in Chapter 5 to study the flow features in an actual exhaust hood.

At both flow conditions, an asymmetric pair of vortices appeared at the condenser neck, as shown by the streamline and streamtube plots (Fig. 3.20 and Fig. 3.21), as well as the pressure levels on the side walls. Although CFD correctly captured the asymmetric flow field, it predicted a lower pressure level with larger pressure gradients in the regions where the vortices met the walls. This was thought to be due to the unsteady nature of the vortical flow, which could not be well predicted by steady RANS CFD.

Between the two flow conditions, some differences were observed. With the 60° vane, the pressure distribution along the side walls was much flatter than the 40° vane, shown in Fig. 3.20 and Fig. 3.21. The 2-D contour was more uniform at a higher level of diffuser inlet swirl angle, possibly due to the greater amount of mixing between the streamtubes, smearing out the pressure gradients. This also supports a closer agreement between the experiment and CFD.

Table 3.3 Pressure recovery in diffuser and exhaust hood

Configuration	Coefficient	Experiment	CFD	$C_{\text{p, CFD}} - C_{\text{p, exp}}$
40° vane	$C_{\text{p, dif}}$	0.30	0.27	-0.03
40° vane	$C_{\text{p, hood}}$	0.26	0.21	-0.05
60° vane	$C_{\text{p, dif}}$	0.23	0.28	+0.05
60° vane	$C_{\text{p, hood}}$	0.35	0.34	-0.01

Once the pressure levels were obtained within the diffuser and at the condenser neck, it was possible to evaluate the static pressure recovery levels at each flow condition. Table 3.3 summarises the static pressure recovery coefficients measured in the experiment and predicted by CFD, where

$$C_{\text{p, dif}} = \overline{C}_{\text{ps, Loc 5}} - \overline{C}_{\text{ps, Loc 1}} \tag{3.2}$$

$$C_{\text{p, hood}} = \overline{C}_{\text{ps, cond neck}} - \overline{C}_{\text{ps, Loc 1}} \tag{3.3}$$

with the overbar referring to arithmetical average at all measurement points (in the experiment) at each evaluation station (Location 1, Location 5 and condenser neck). Therefore, $C_{\text{p, dif}}$ measures the pressure recovery from the diffuser inlet to the diffuser outlet, whereas $C_{\text{p, hood}}$ measures the pressure recovery from the diffuser inlet to the condenser neck. The uncertainty in the measured pressure recovery coefficients was within ± 0.004. Although a continuous distribution of pressure was available from CFD results, it was decided to calculate the recovery coefficients in the same fashion as the experiment, for the sake of consistency. The maximum difference between experiment and CFD was 0.05, which was considered good given the complex flow features (large separation regions and highly swirling flows).

For the 40° vane, CFD consistently underpredicted the pressure recovery level, due to the fact that the SST model used was rather conservative on flow separation prediction on the flow guide surface.

For the 60° vane, CFD underpredicted the blockage and mixing in the diffuser passage, supporting the 0.05 overprediction in pressure recovery. As the flow entered the collector in the form of counter-rotating vortices, the much more uniform pressure distribution at the condenser neck explains the higher level of pressure recovery in the exhaust hood, when the swirl level was higher. Moreover, both experiment and CFD results suggested a higher pressure recovery in the exhaust hood compared to the diffuser, *i.e.* pressure continued to rise from the diffuser outlet to the condenser neck. This was because at higher swirl angle the separation size inside the diffuser grew (see meridional streamlines for 60° vane in Fig. 3.15), which reduced the effective diffuser area ratio. This resulted in a lower pressure level at the diffuser outlet, and hence explained the pressure rise from there towards the condenser neck.

Finally, Fig. 3.22 compares the surface streamlines and oil paints on the front wall of the exhaust hood. CFD was in close agreement with the experiment, by correctly capturing the separation lines on the two sides, the surface flow angles, and the reattachment locations on the bearing cone for the 60° vane.

3.3 Concluding remarks

This chapter explained how the commercial CFD solver ANSYS CFX was validated against experiments performed on a low speed air test rig, both quantitatively (steady pressure measurement) and qualitatively (surface streamline and oil paints). Representative part-load operating conditions were achieved through two different guide vane designs.

It was established that the numerical uncertainties in CFD would grow with the size of the separation region. In the axi-symmetric diffuser configuration, the CFD solver agreed with the experiment when there was moderate level of swirl (around 40°). For higher swirl angles and consequently larger separation regions, CFD overpredicted the reattachment radius on the bearing cone, whilst underpredicting the pressure loss and level of mixing inside the diffuser. In the configuration with full annulus exhaust hood, similar conclusions could be drawn for the diffuser domain. Nevertheless, when the entire exhaust hood was considered, a closer agreement in C_p was observed between experiment and CFD for the 60° vane instead, due to a much more uniform pressure field at the condenser neck and a smaller separation region on the flow guide compared to the 40° vane.

In an actual LP exhaust system, especially with unshrouded rotor blades, the leakage jet from the rotor tip helps to suppress the flow separation on the diffuser flow guide. This means more confidence should be placed in the results at lower swirl angles (*i.e.* 40° vane), while caution must be exercised at higher swirl angles (*i.e.* 60° vane). As shall be discussed in Section 5.2.4, the tip leakage jet is more influential on the exhaust system performance near design condition, while the bearing cone separation becomes the dominant loss source at part-load condition. Nevertheless, the tip leakage jet flow feature should be considered in future experimental investigations.

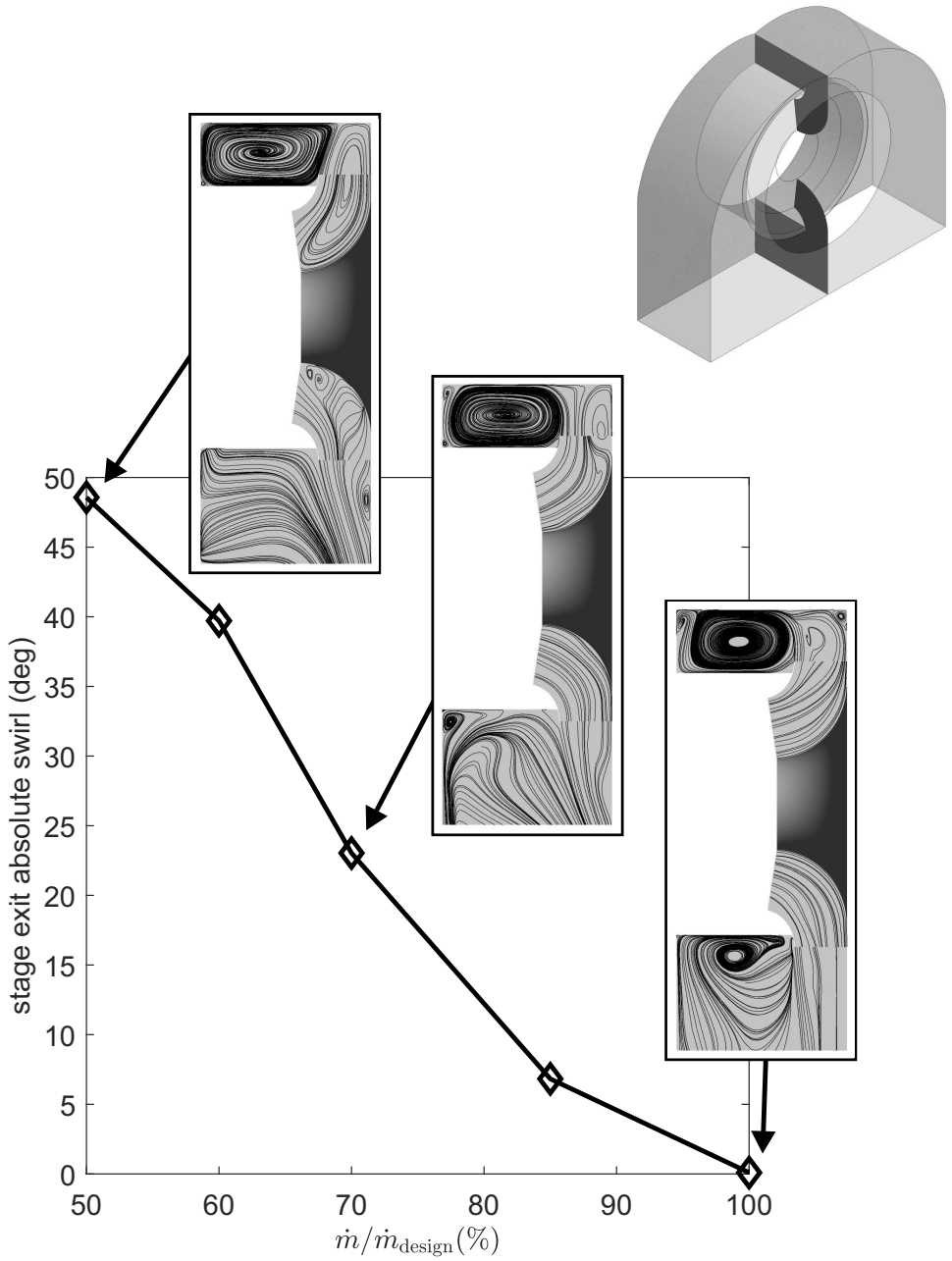

Fig. 3.1 Stage exit absolute swirl angle variation with mass flow rate for a typical LP turbine, with meridional streamlines from CFD

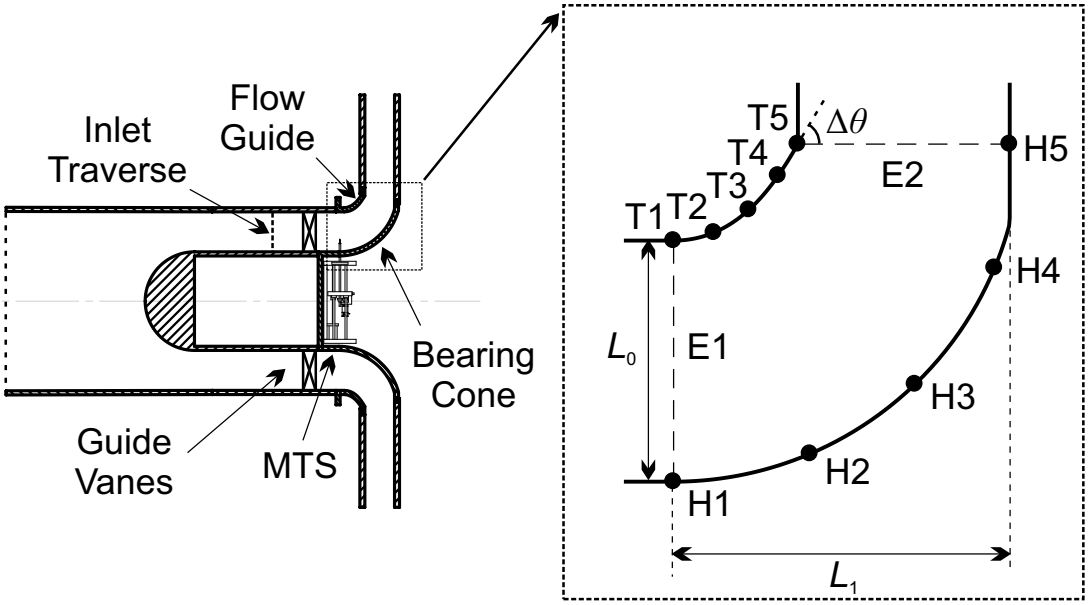

Fig. 3.2 Side view of the test rig (axi-symmetric diffuser configuration)

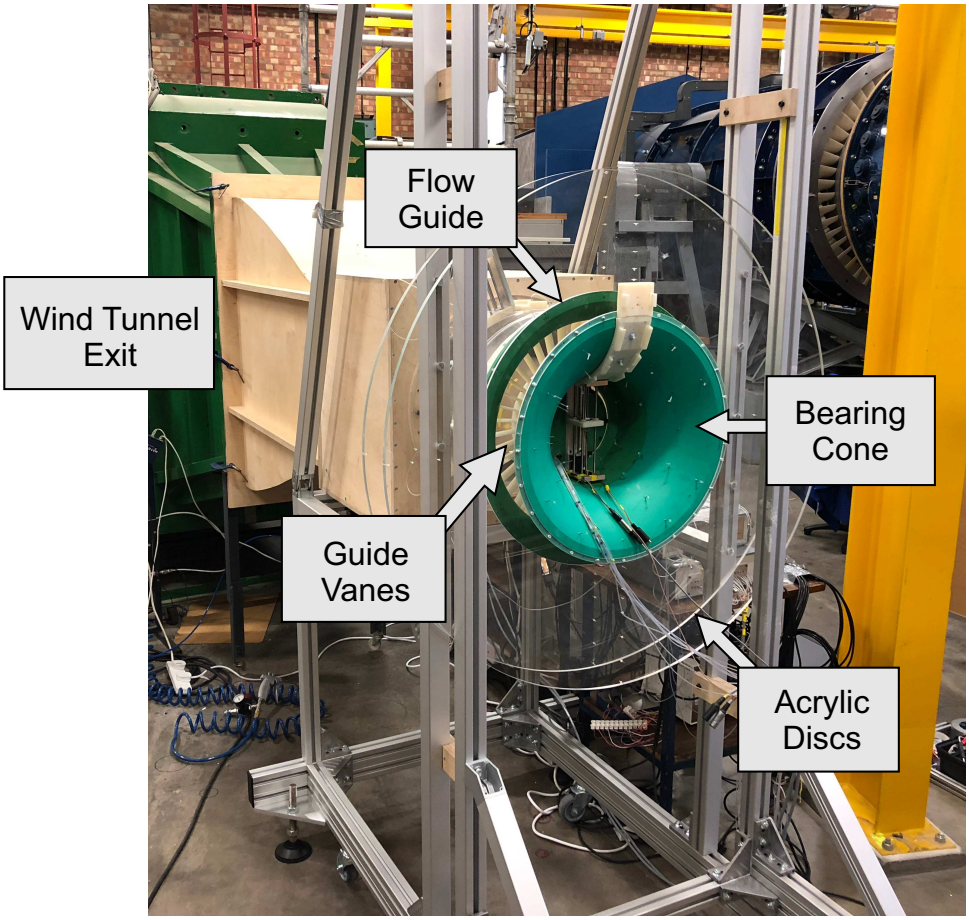

Fig. 3.3 Photograph of the axi-symmetric diffuser configuration

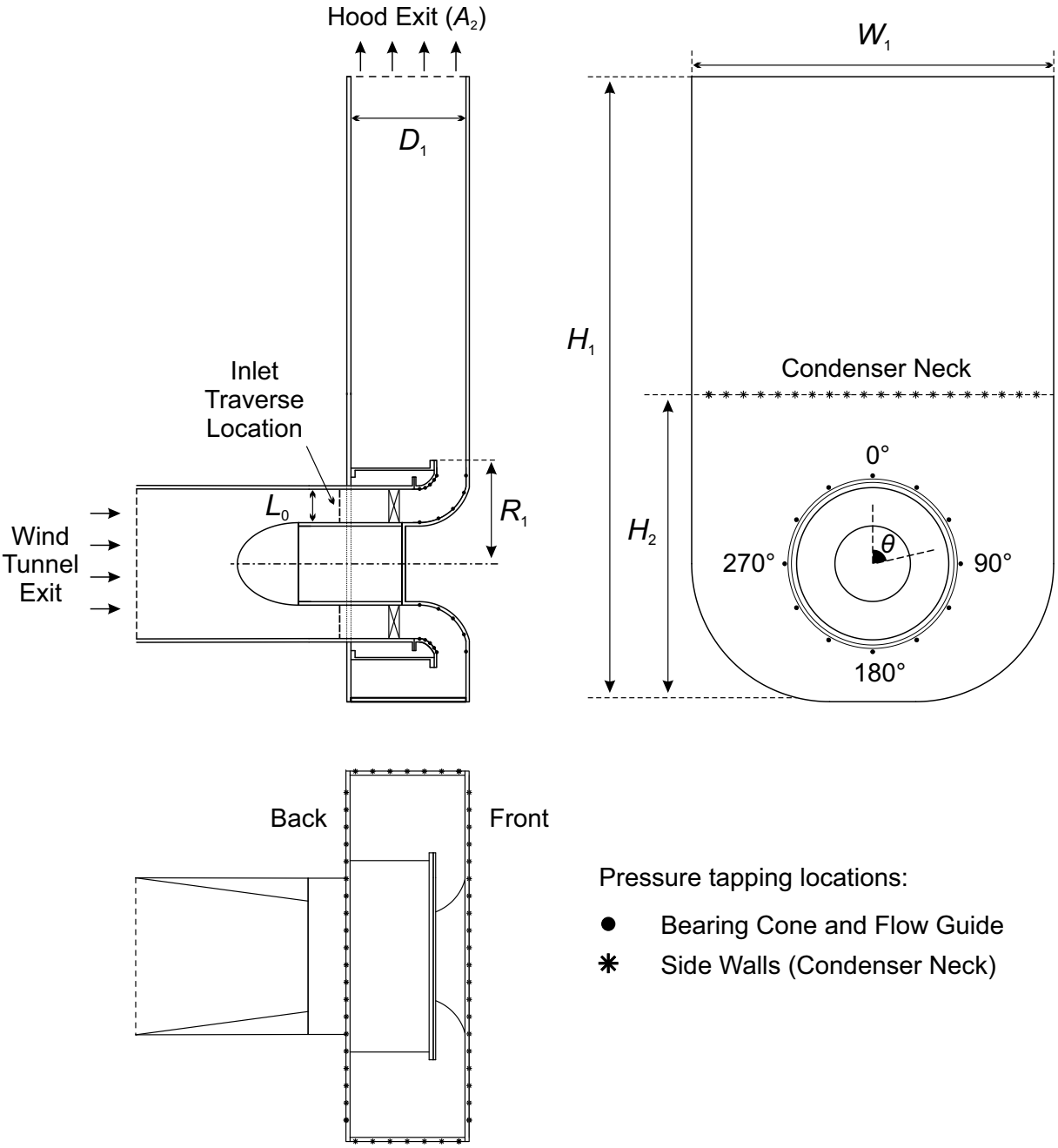

Fig. 3.4 Side, top and front views of the test rig (exhaust hood configuration)

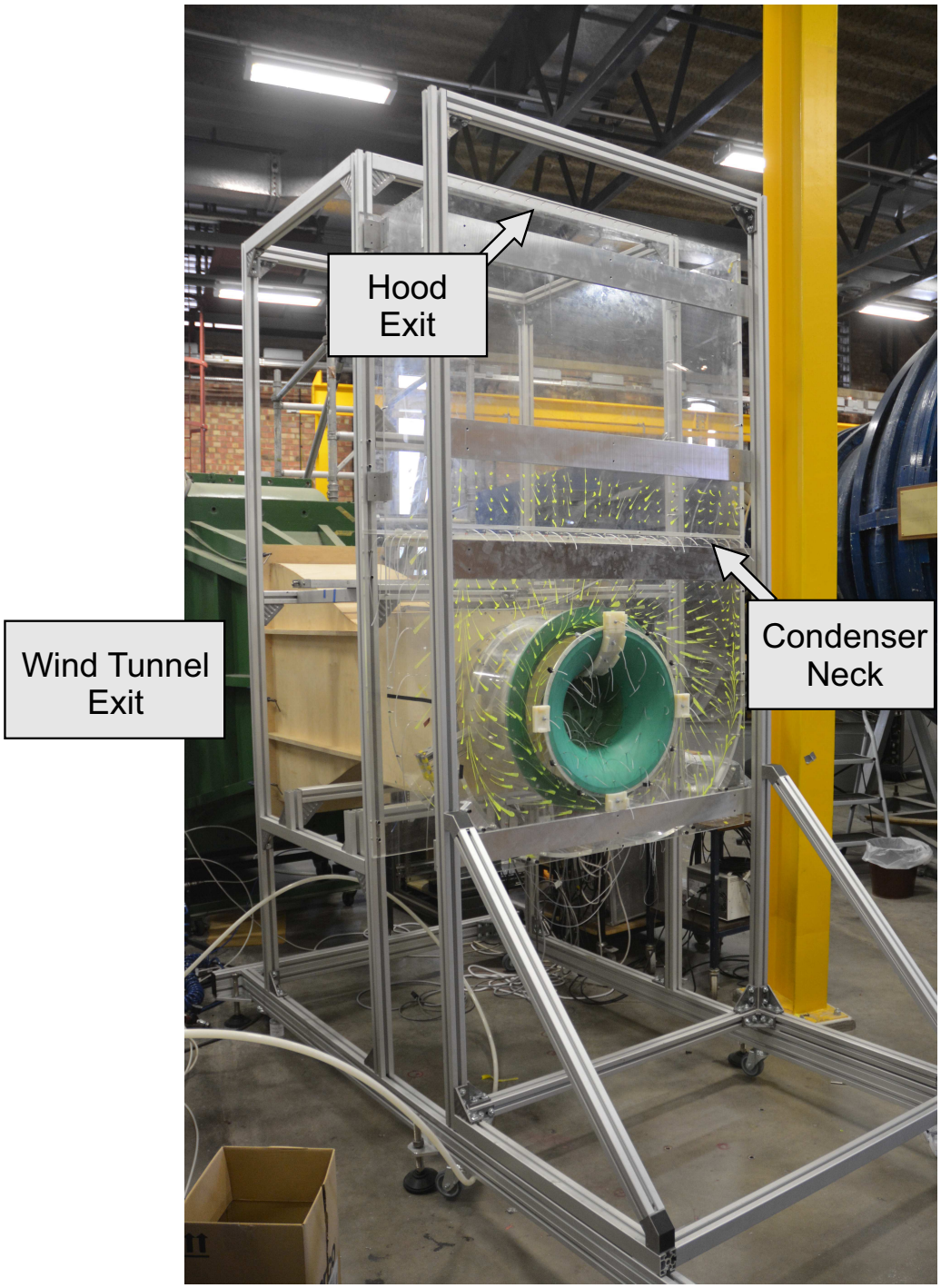

Fig. 3.5 Photograph of the exhaust hood configuration

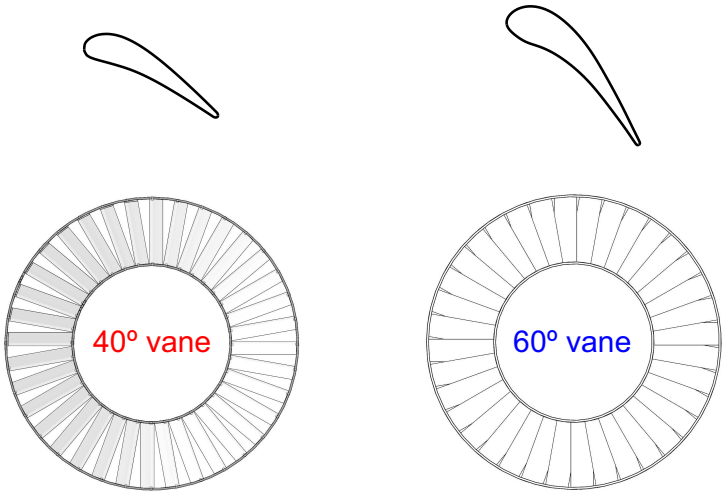

Fig. 3.6 Guide vane designs (left: 40° vane; right: 60° vane)

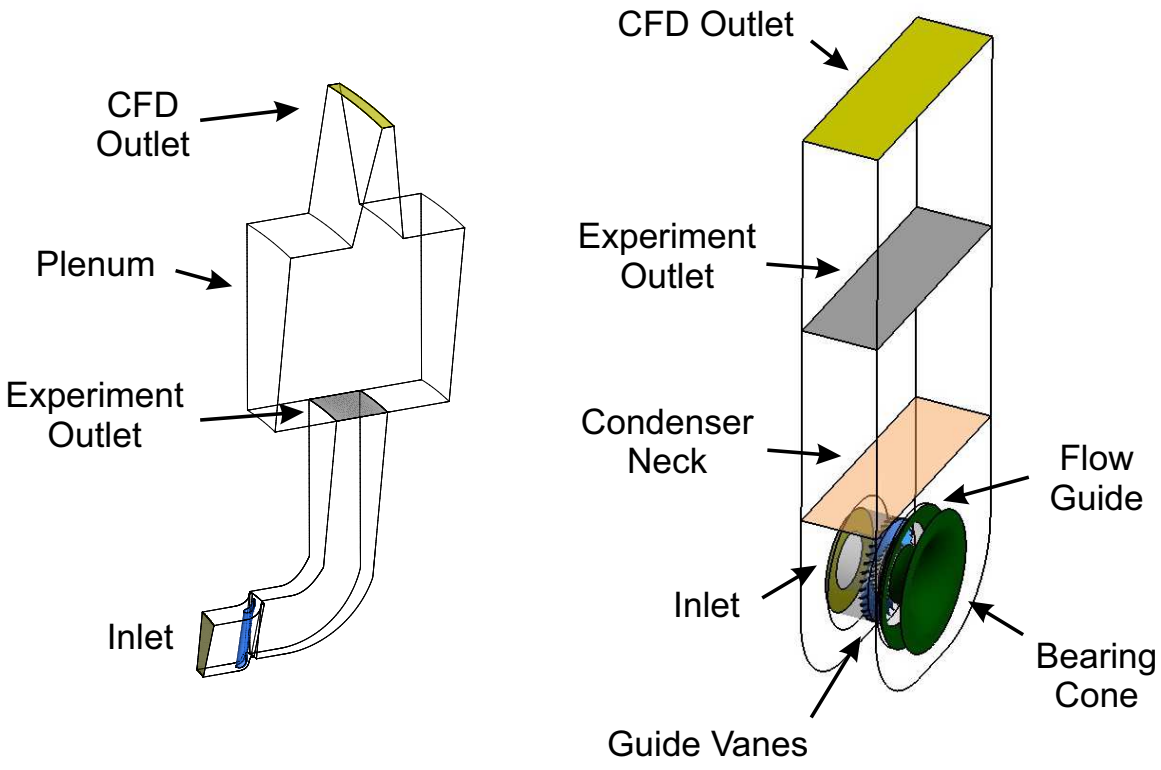

Fig. 3.7 CFD domain of the configurations with axi-symmetric diffuser (left) and exhaust hood (right)

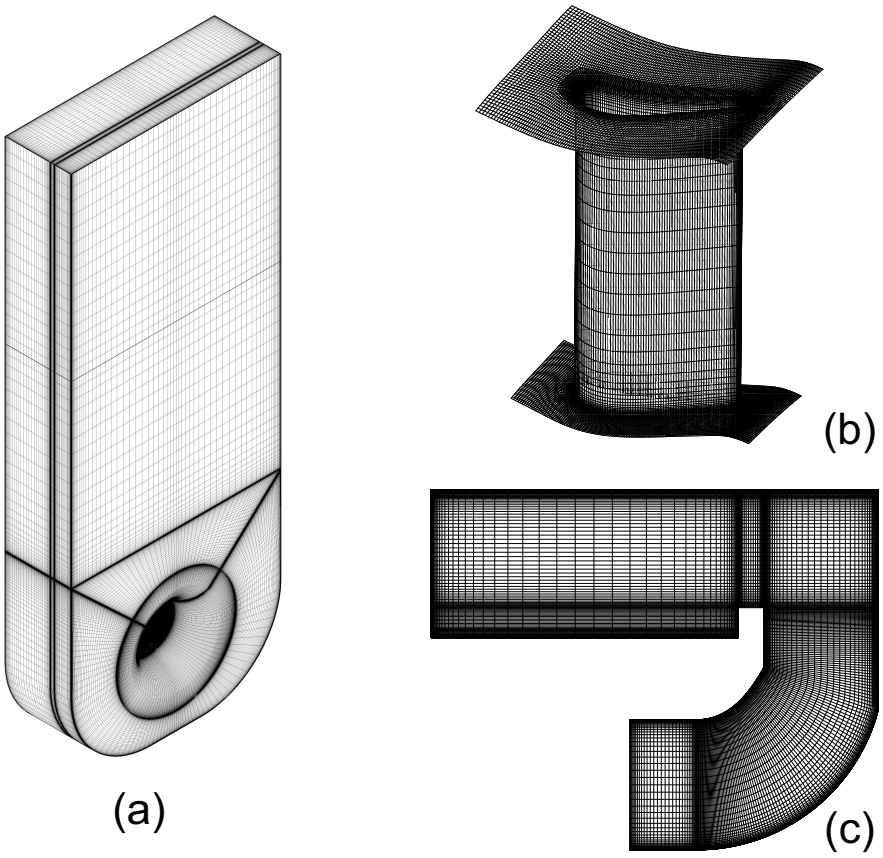

Fig. 3.8 CFD mesh used for the exhaust hood (a), guide vane passage (b) and a cross section in the exhaust hood (c)

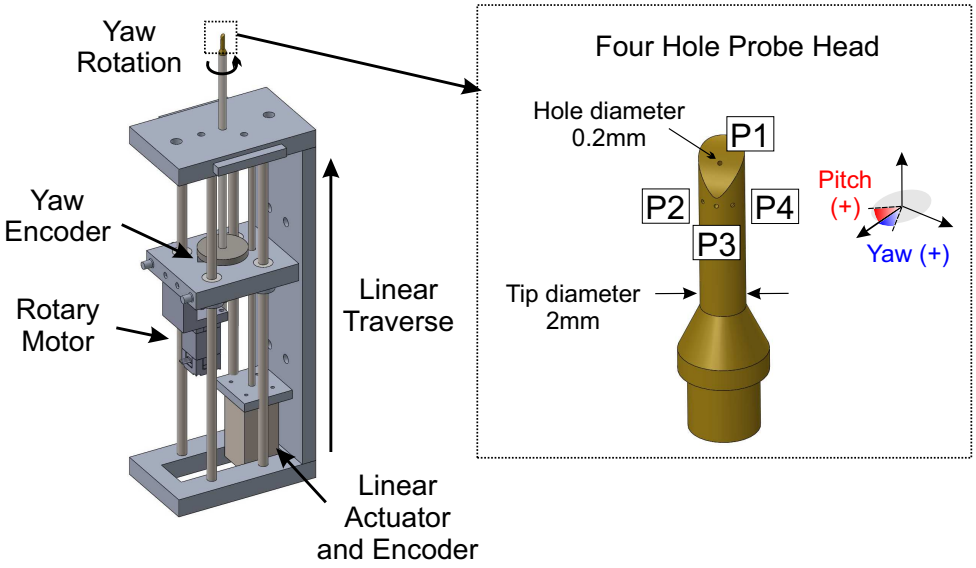

Fig. 3.9 Miniature traverse system (MTS) and four hole probe head

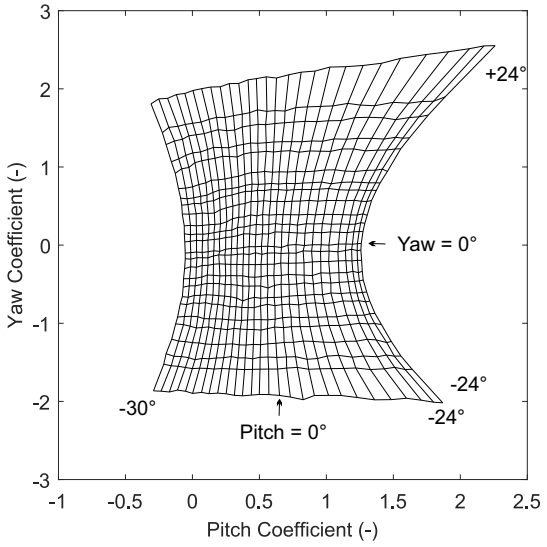

Fig. 3.10 Calibration contours for the four hole probe. Effect of yaw and pitch coefficients on contours of yaw and pitch with 2° intervals

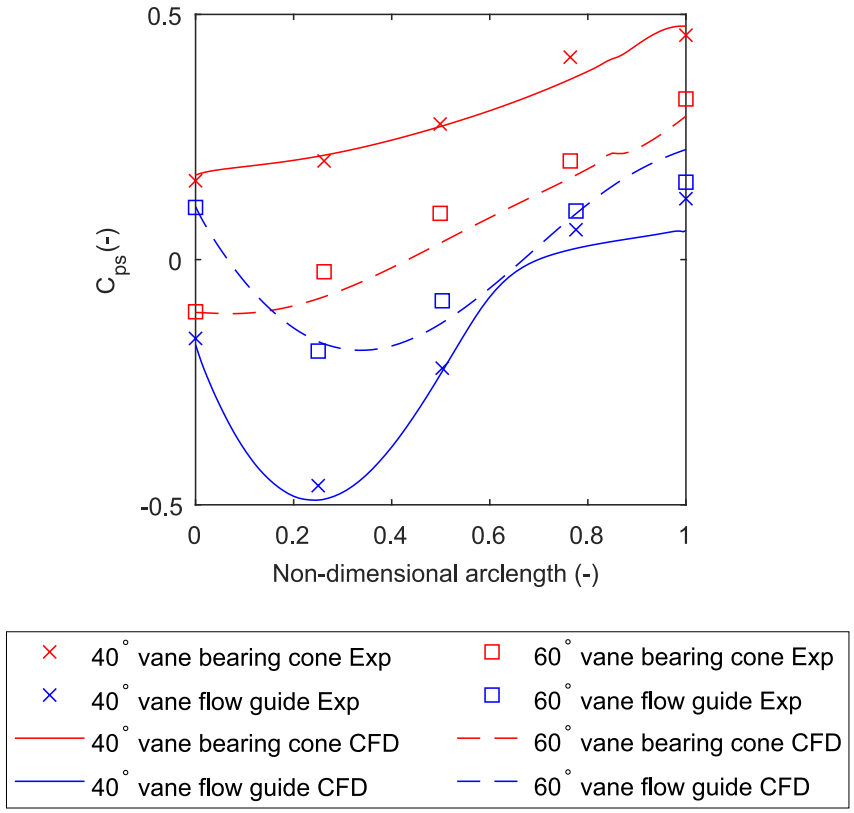

Fig. 3.11 Static pressure distributions on the diffuser bearing cone and flow guide (axi-symmetric diffuser configuration)

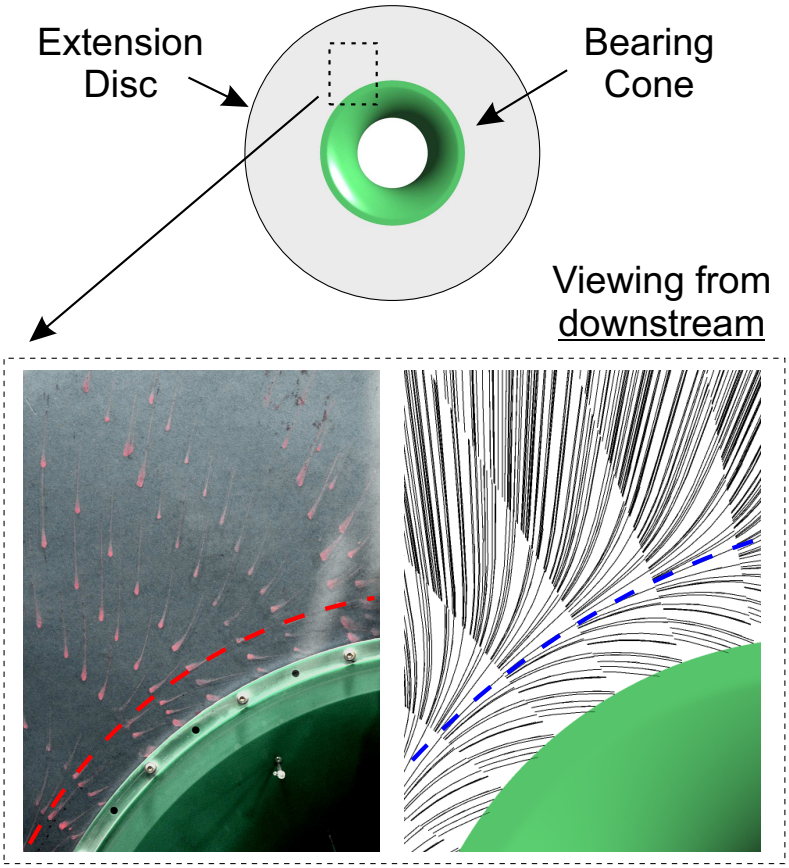

Fig. 3.12 Surface streamlines on the extension disc (60° vane, axi-symmetric diffuser configuration)

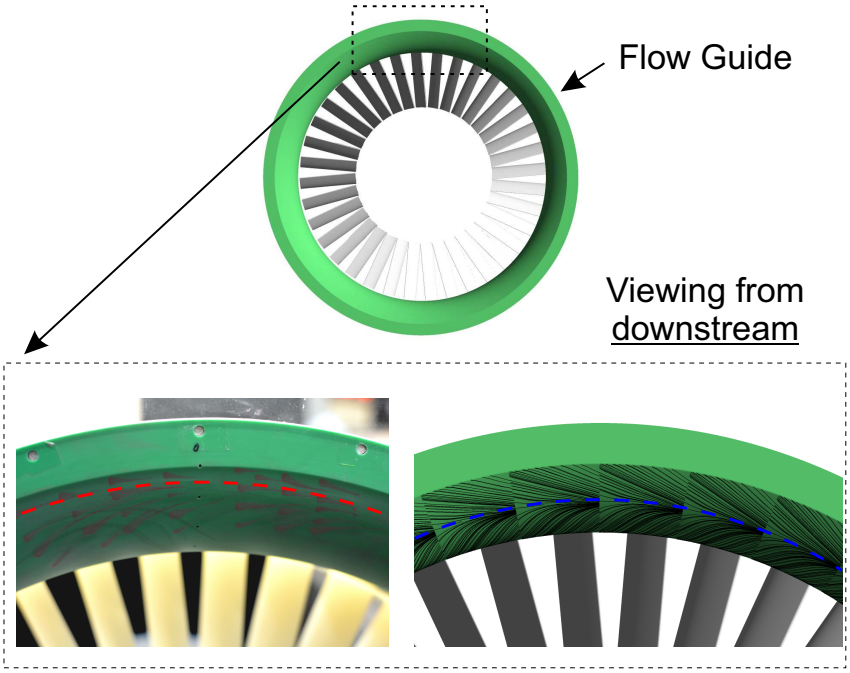

Fig. 3.13 Surface streamlines on the flow guide (40° vane, axi-symmetric diffuser configuration)

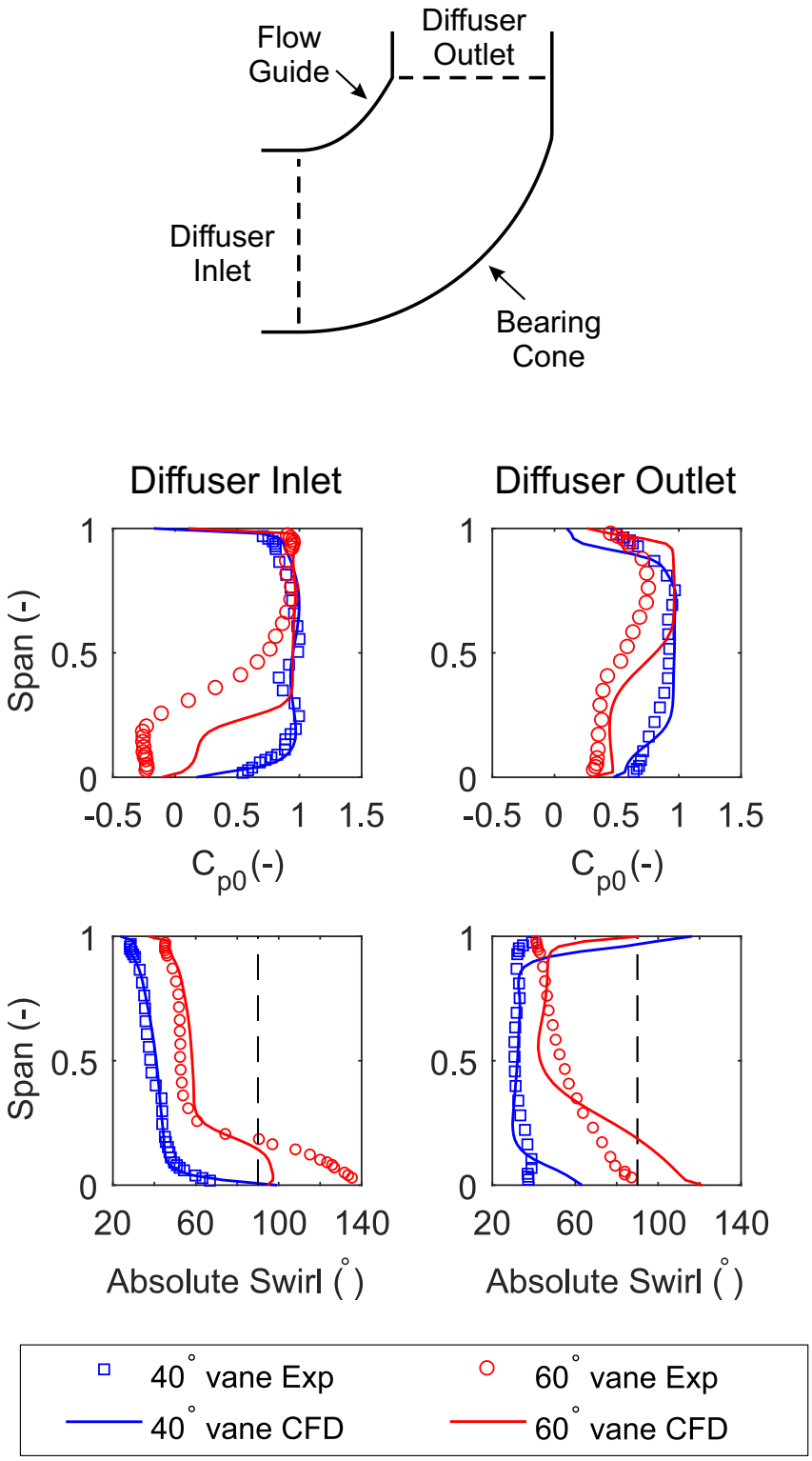

Fig. 3.14 Radial distributions of total pressure and absolute swirl angle at diffuser inlet and outlet (axi-symmetric diffuser configuration). Dashed lines: tangential direction (90° swirl)

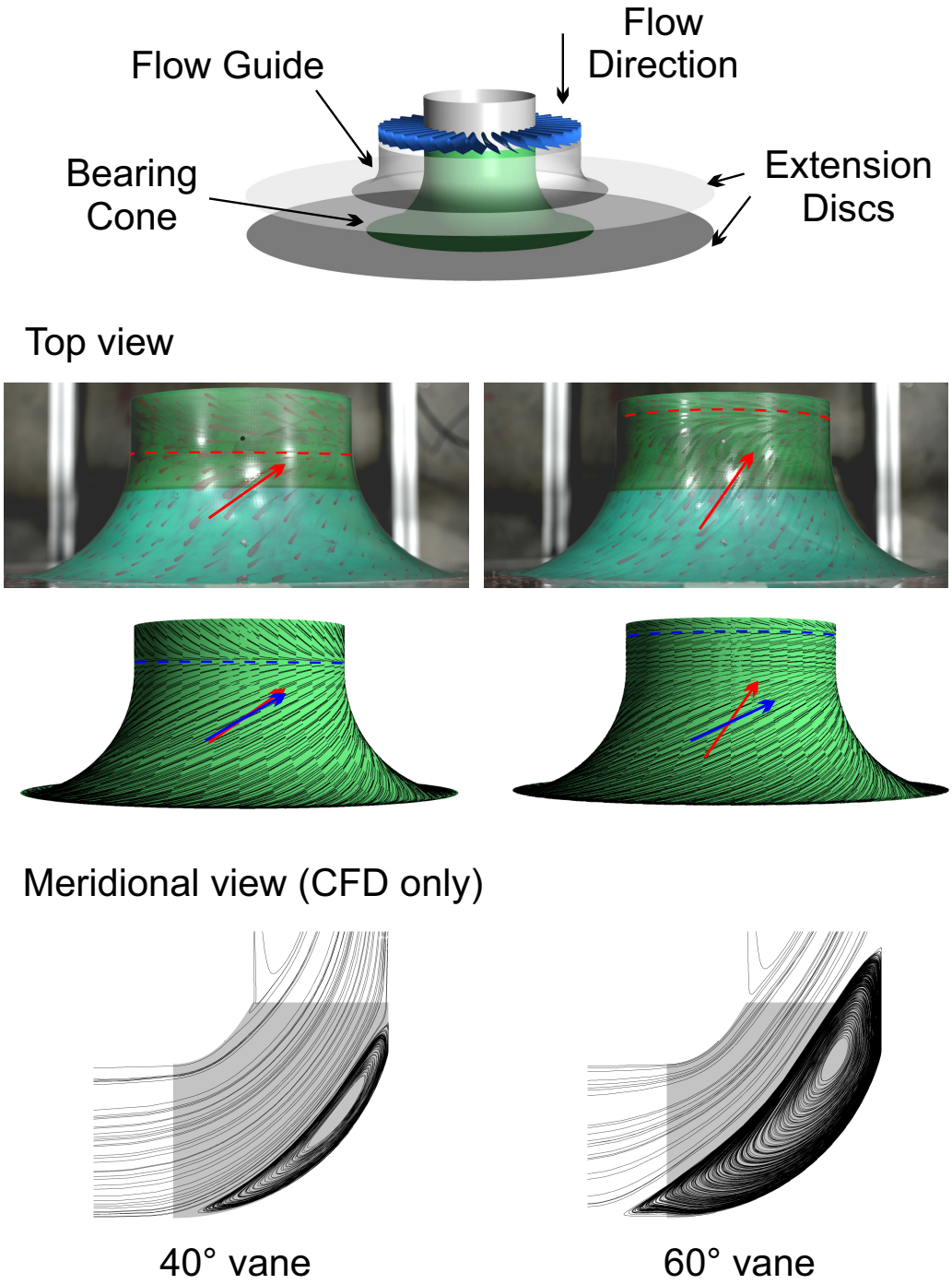

Fig. 3.15 Bearing cone surface streamline comparison and CFD meridional streamlines (axi-symmetric diffuser configuration)

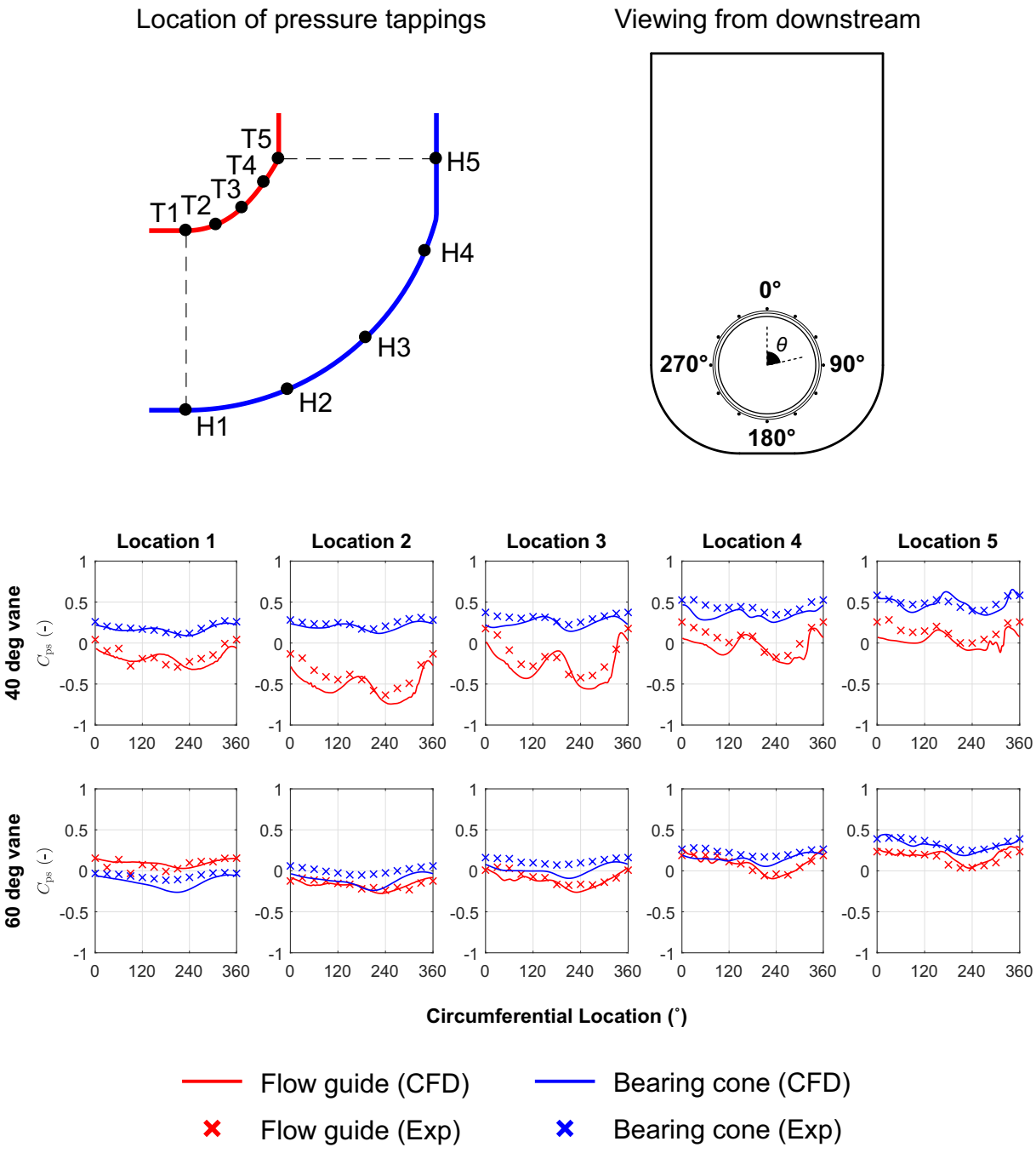

Fig. 3.16 Static pressure distributions on the flow guide and bearing cone for 40° and 60° vanes (full annulus exhaust hood configuration)

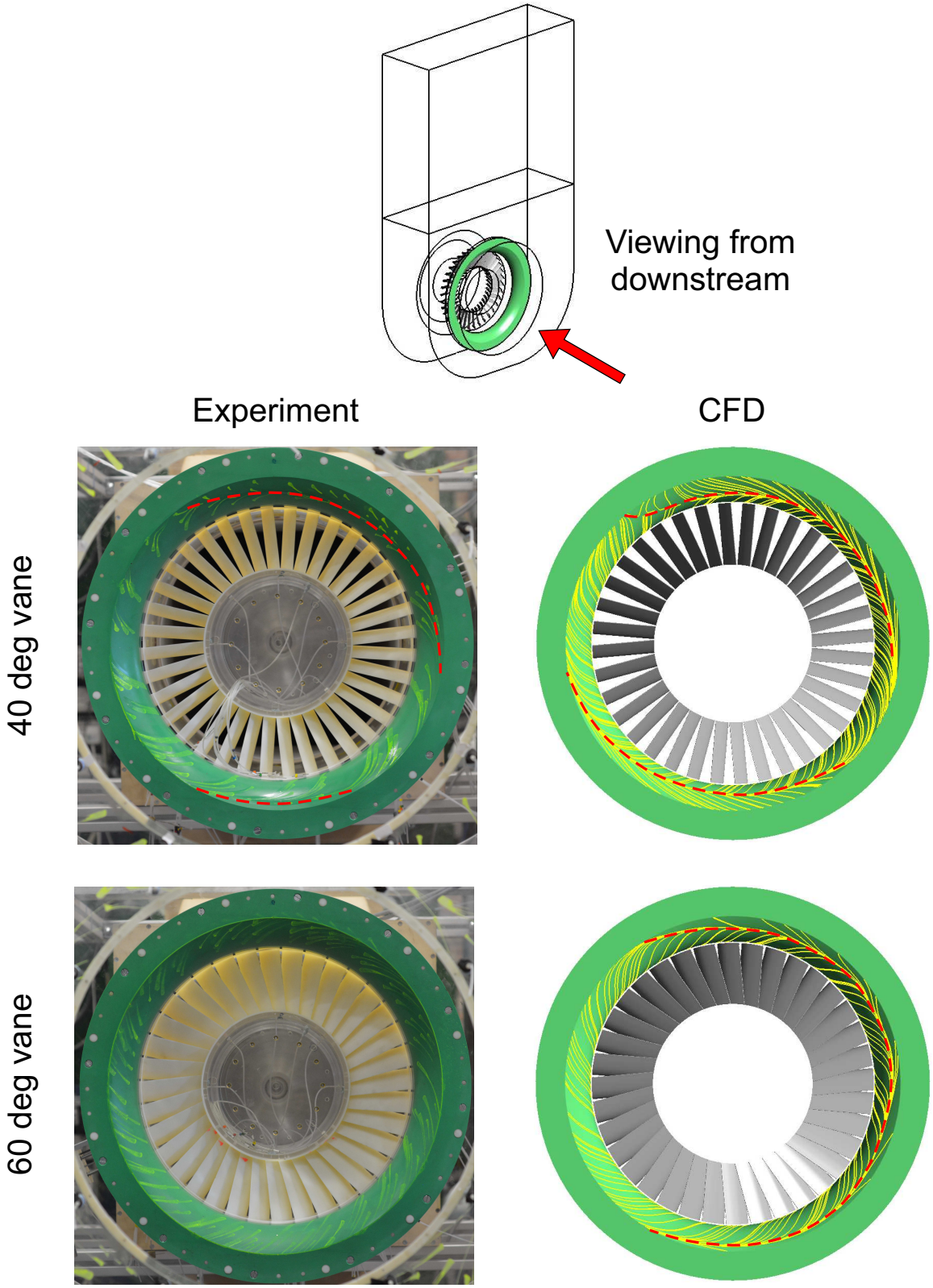

Fig. 3.17 Comparison of surface streamlines on the flow guide (exhaust hood configuration), with red dashed lines indicating separation lines

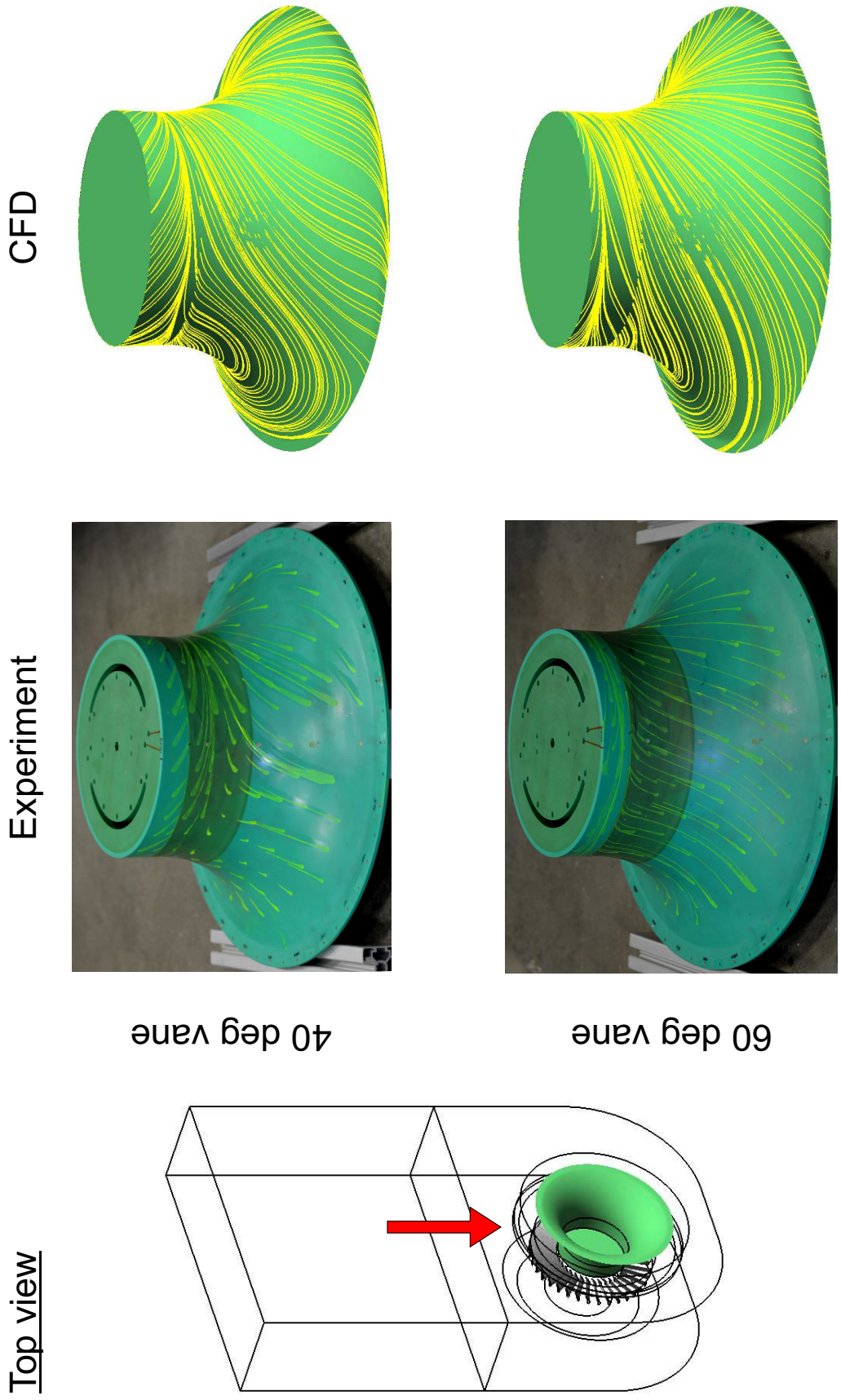

Fig. 3.18 Comparison of surface streamlines on the bearing cone (exhaust hood configuration, viewed from the top)

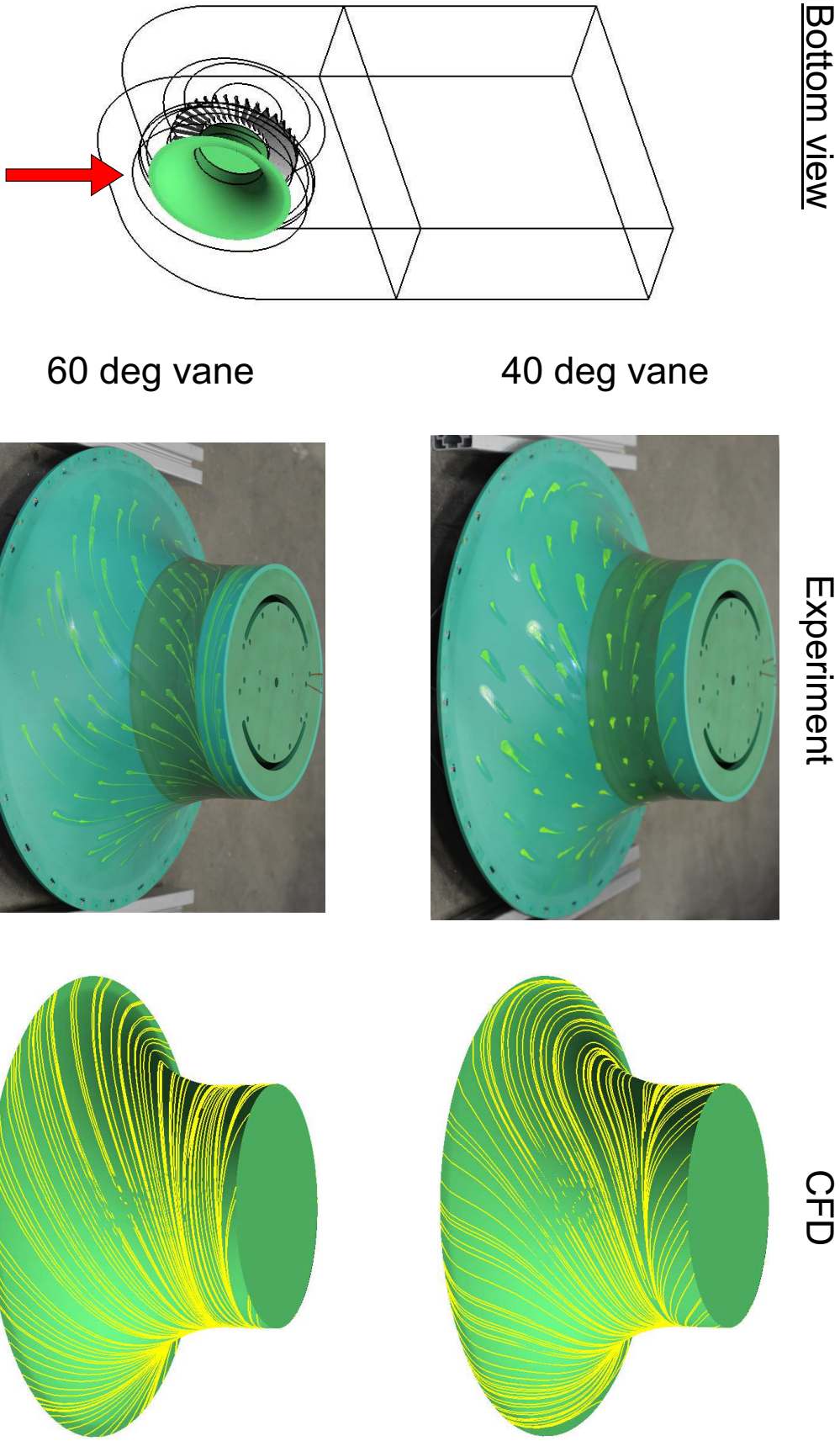

Fig. 3.19 Comparison of surface streamlines on the bearing cone (exhaust hood configuration, viewed from the bottom)

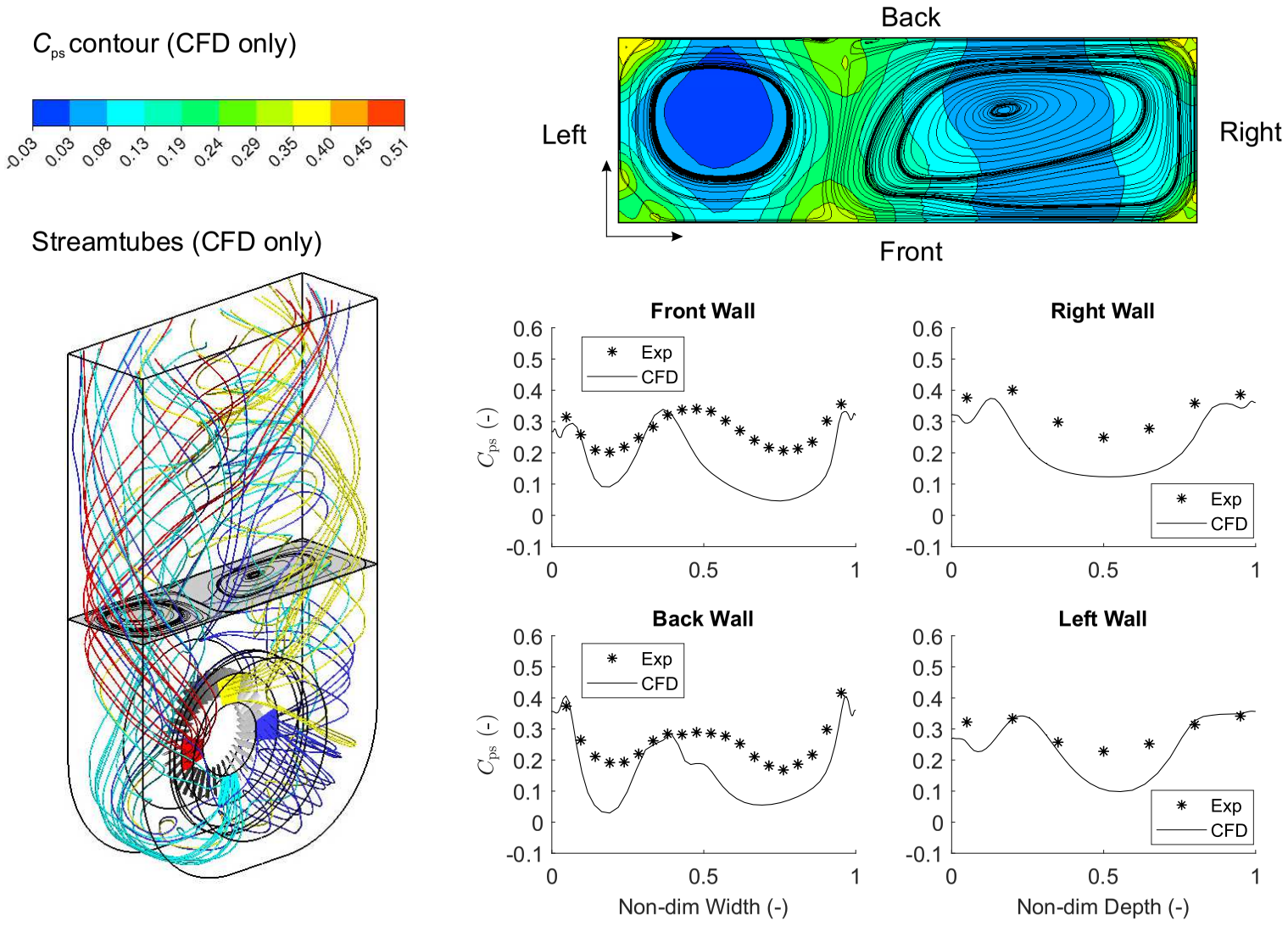

Fig. 3.20 40° vane with exhaust hood. Top: contours of pressure coefficient and streamlines at condenser neck (CFD). Left: 3-D streamtubes originating from different sectors at the diffuser inlet (CFD). Right: pressure coefficient on the side walls of the condenser neck

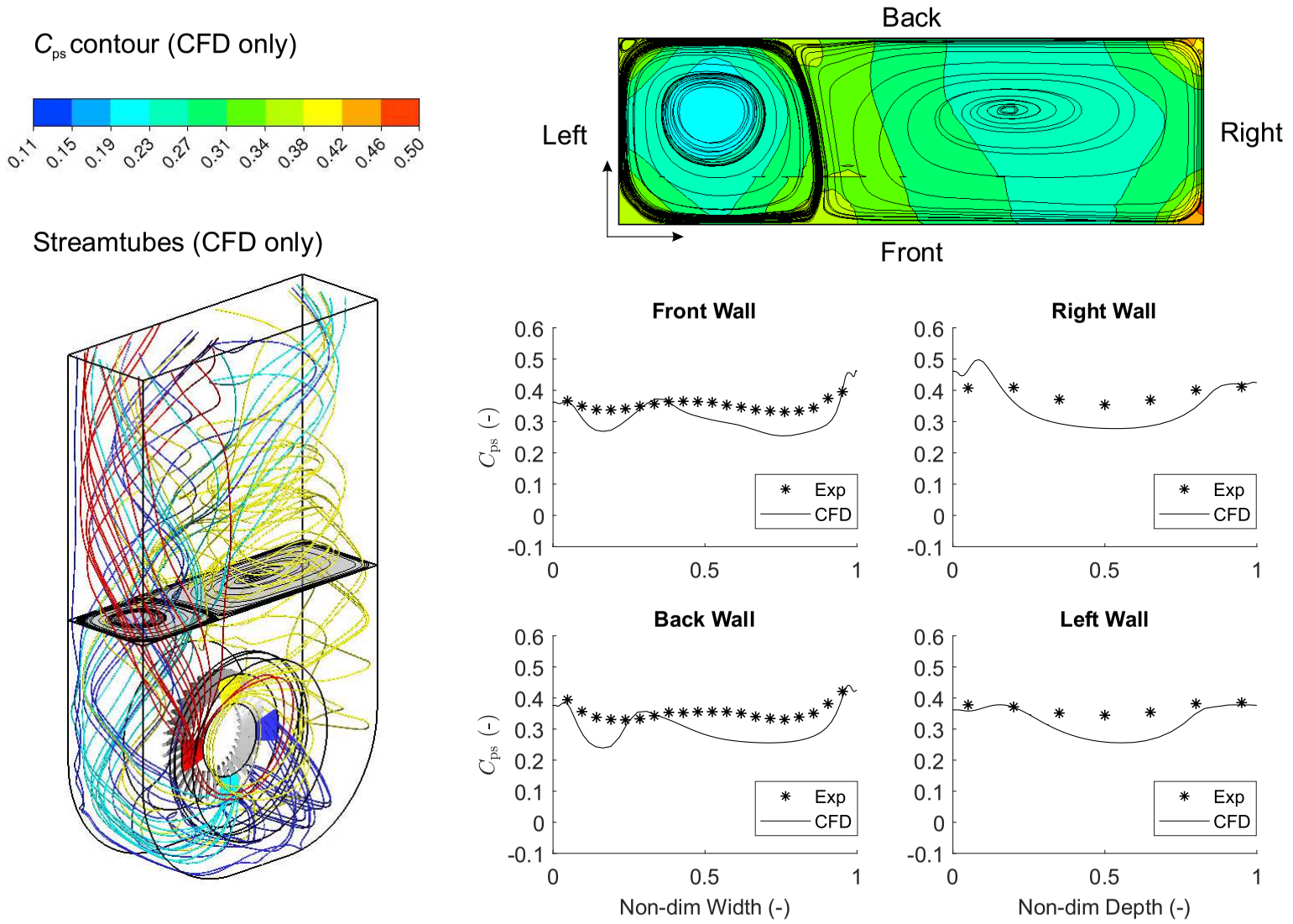

Fig. 3.21 60° vane with exhaust hood. Top: contours of pressure coefficient and streamlines at condenser neck (CFD). Left: 3-D streamtubes originating from different sectors at the diffuser inlet (CFD). Right: pressure coefficient on the side walls of the condenser neck

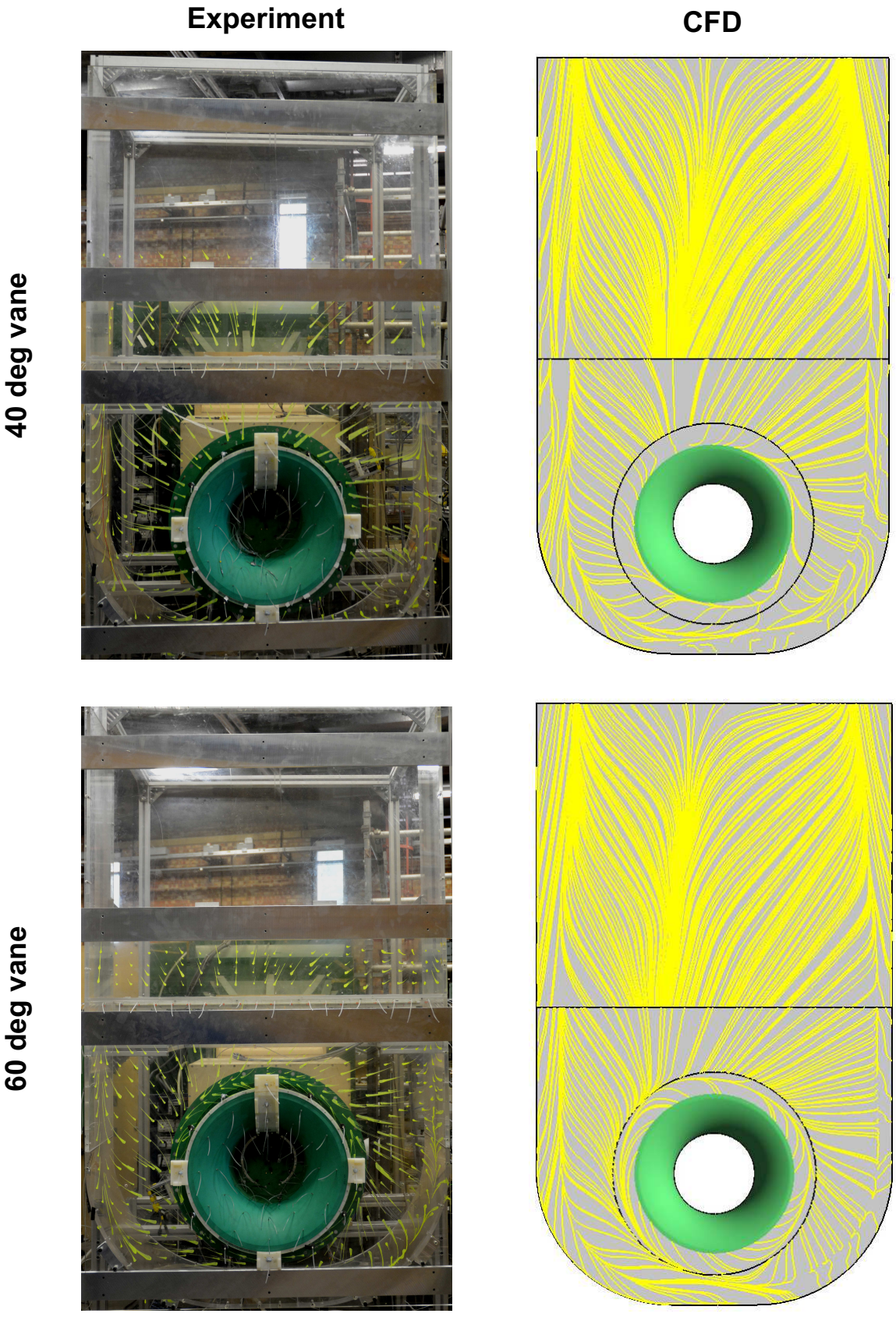

Fig. 3.22 Comparison of exhaust hood front wall surface streamlines

Chapter 4

Numerical Methods for Full-scale LP Exhaust Systems

This chapter will introduce the numerical methods and tools used to investigate the flow fields and performance of full-scale LP exhaust systems. As discussed in the literature survey, high fidelity CFD simulations on detailed blade and exhaust hood geometries have been made possible by improved computational power. Several researchers have performed full annulus unsteady calculations of the last stage coupled with an exhaust hood, *e.g.* [27, 72, 49]. Nevertheless, as Verstraete et al. pointed out, this expensive calculation is for validation rather than a design tool [82].

One of the research objectives in the current study was to identify the most sensitive design parameters in the LP exhaust system. Therefore, a suitable mesh size as well as treatment for rotor-stator and rotor-hood interfaces had to be selected. Such low cost computation will enable the "big picture" of the system performance to be quickly captured, and will pinpoint the most interesting design configurations, for which much finer mesh could be used to study detailed flow physics and loss mechanism. This will be discussed in Chapter 7.

4.1 Geometry and mesh generation

4.1.1 Parametrisation of exhaust hood geometry

Before describing the numerical solver, the exhaust hood geometry it simulates must first be defined. In the current study, eight parameters were used to fully describe exhaust hood geometry, as shown in Fig. 4.1. The last stage casing lines were assumed to be fixed, so that two important dimensional values could be determined: the diffuser inlet height (L_0) and area (A_0), from which other parameters could be derived.

Within the exhaust hood, there are two components: an axial-radial diffuser, and a collector. The inner (or pressure) surface of the diffuser is the bearing cone, while the flow guide refers to the diffuser outer (or suction) surface. To fix the diffuser geometry,

up to six parameters were required. The first three parameters: the diffuser length ratio (L_1/L_0, measured from the start of the flow guide), diffuser area ratio (A_1/A_0, assuming a horizontal diffuser outlet line) and the flow guide height (H_0/L_0) determine the overall diffuser size.

Detailed shapes of flow guide and bearing cone would normally require another four control points or eight parameters (in terms of the $x - r$ coordinates) using cubic Bezier splines. This is impractical for parametric studies or optimisations. To reduce the dimension, a concept of "Minimum Energy Curves" was implemented (discussed in Section 6.3) with which the overall curvature level of the flow guide would be minimised, since flow behaviour is very sensitive to streamline curvature in this region. This way, just two parameters (diffuser turning angle $\Delta\theta$ and tip kink angle $\theta_{\text{kink, tip}}$) were needed to shape the flow guide.

The bearing cone shape determines the cross-sectional area distribution in the diffuser passage. Singh compared frontal, linearly and aft loaded area disributions in the LP exhaust diffuser [68], and found the aft loaded configuration (more diffusion towards the end) provided some slight advantage over the other two, by about 0.02 in pressure recovery coefficient C_p. In manufacturing, however, the bearing cone is typically made of much simpler shapes such as circular arcs and/or straight lines, along with some initial kink angle, such as those used by Taylor et al. [78]. For this study, it was decided to use a circular arc or a cubic Bezier curve (with fixed control point parameters) along with some hub kink angle to fix the bearing cone shape.

Finally, the overall collector size is governed by its vertical height (H_1/L_0) and width (W_1/L_0). It is normally assumed that the distance between the back wall (in Fig. 4.1) and the flow guide, which is effectively half the length of the LP rotor in a double flow cylinder, is fixed. Moreover, the distance between the centreline and the hood exit (condenser neck) is also often assumed to be fixed. This way the hood exit (or exhaust) area is completely determined by the diffuser length ratio and the hood width ratio. In addition, a linear variation in the cross-section length $r(\theta)$ (or effectively, area) is imposed with respect to its angular position θ in the upper part of the collector.

4.1.2 Blade geometry and mesh generation

Two different last stage blading designs were considered in this thesis, and were denoted Stage A and Stage B. Their geometries are provided by the industrial sponsor, and are of typical sizes as those found in 1000 MW units, featured by very long last stage rotor blades (over 1 metre) and low hub-tip ratio (under 0.45). The performance characteristics of the two designs when coupled with an exhaust hood will be presented in Section 5.2 in order to discuss the effect of blading on exhaust system performance.

The structured blade passage mesh was generated in the commercial software NUMECA Autogrid 5, using a "butterfly" type of topology with an O-mesh around the blade surface

and H-mesh elsewhere. As an example, both coarse and fine meshes for Stage B are presented in Fig. 4.2. For the coarse mesh, there were only 0.1 million grid points per row, while there were five times as many in the fine mesh. The average wall distance (y^+) on all viscous surfaces was around 20 and 5 for the two mesh sizes respectively.

4.1.3 *ExhaustGen*: an exhaust system design suite

For the study, a wide range of exhaust hood geometries would need to be investigated. This meant that the mesh generation had to be automated to facilitate numerical simulations. An exhaust system design suite, *ExhaustGen*, has been developed using MATLAB to serve this purpose. It is capable of generating exhaust hood geometries and multi-block hexahedra meshes, preparing definition files for the CFD solver, and post-processing results in batch mode.

The CFD domain of the exhaust hood is illustrated in Fig. 4.3, and consisted of an axial-radial diffuser, a collector, a downward extension and an optional contraction section. The last two domains were used to avoid flow reversal at the CFD exit, a similar configuration to many other publications, *e.g.* [26, 53]. For the diffuser and the collector, two-dimensional multi-block H-meshes were created at each circumferential location, as illustrated in Fig. 4.3. The grid distribution in each direction (axial, radial and circumferential) was controlled by a two-sided strectching function (as described by Vinokur [84]), so that the cell size at each end (especially the wall distance) could be prescribed while the expansion ratio was controlled by varying the number of grid points.

Similar to the blade passage, two mesh sizes were generated for the exhaust hood and a comparison of them is presented in Table 4.1, in terms of the number of grid points in each direction, average wall distance on viscous surfaces, and total mesh size.

Table 4.1 Exhaust hood mesh size comparison

Configuration	$NI_{diffuser}$ (axial)	$NJ_{diffuser}$ (radial)	$NK_{diffuser}$ (circumferential)	$y^+_{avg,\ diffuser}$ (-)	Total (mil)
Coarse	73	57	157	21.2	2.5
Fine	97	81	209	3.4	5.0

4.1.4 Effect of mesh size

Since there were different CFD configurations (scaled test rig vs. full scale exhaust hood, axi-symmetric vs. full annulus, etc.) to consider throughout the study, it was decided to study the effect of mesh size separately in Chapters 5 and 6. Within each chapter, the descriptions of coarse and fine meshes can be found. The purpose of the mesh study was to demonstrate how the CFD solver used can consistently predict the *relative* merit between

different exhaust hood designs, even with a very coarse mesh size. "Coarse" hereby means: approximately 0.1 million grid points per blade row and around 2 to 3 million points in the exhaust hood, leading to around 3 million for a Multiple Mixing Planes configuration, and $10-12$ million for a full annulus calculation, which are computationally affordable for modern workstations. These figures are far lower than those used in steady simulations (*e.g.* Burton used 85 million mesh for her full annulus frozen rotor calculations [10]), but are still in line with recent literature of URANS simulations, *e.g.* [72, 49]. Furthermore, it is important to note that the flow inside the exhaust hood is inherently unsteady. Forcing the CFD solver to simulate an unsteady flow field in a steady fashion will not only slow down the convergence, but also fail to capture the unsteady flow features in the exhaust hood. A balance therefore needs to be struck between achieving grid independence of the solver (by increasing the mesh size) and capturing key flow phenomena, which in this case is the long wavelength unsteadiness inside the hood.

4.2 CFD solver

All simulations in this thesis were performed with the commercial solver ANSYS CFX 17.0, which is widely used in the industry and research community for LP exhaust system simulations, *e.g.* [26, 8, 88, 55].

CFX solves the unsteady Navier-Stokes equations in their conservation form using an element-based finite volume method on a variety of unstructured mesh types [5]. It solves the hydrodynamic equations for velocity components and pressure in a coupled manner, using a fully implicit discretisation approach, and is accelerated by the Algebraic Multigrid (AMG) method. The advection term is calculated using a high resolution scheme summarised by Barth and Jesperson [6]. Both steady and unsteady RANS simulations can be performed using CFX. For the latter, a second order backward Euler scheme is used. It is implicit in time and hence places no limitations on the time step size.

Turbulence closure is a key element in RANS simulations and must be chosen according to the type of flow features. In the exhaust hood, flow is susceptible to separation under adverse pressure gradients. In order to obtain a good prediction of the onset and the amount of separation, Menter's $k-\omega$ based Shear Stress Transport (SST) model was used in this study [50]. Beevers et al. compared different discretisation schemes (upwind and high resolution) and turbulence models ($k-\epsilon$, $k-\omega$ SST and Reynolds stress models) using CFX, along with experiment results from a 1/10 scale test facility [8]. They found no significant difference between the $k-\epsilon$, $k-\omega$ SST models, but did identify the sensitivity of predicted efficiency to numerical schemes.

Finally, the fluid properties of the working fluid (wet steam) was evaluated using look-up tables based on the IAPWS-IF97 database [85]. This approach significantly saves computational cost compared to solving the equations of state at every iteration, and is more accurate than assuming constant specific heat capacities (C_P) and heat ratio (γ)

in a perfect gas formulation. Moreover, equilibrium state of the wet steam was assumed, given that condensation normally occurs before the last two stages.

4.3 Effect of stage-hood interface treatment

As discussed in Section 2.3, the strong coupling between the last stage and the exhaust hood requires both components be included in the CFD simulation. Therefore, the choice of interface treatment between stationary (stator and exhaust hood) and rotating (rotor) frames becomes important, and the computational accuracy and cost should be appropriately balanced. This section details the comparisons between three interface treatments: Multiple Mixing Planes (MMP), full annulus Frozen Rotor (FR) and full annulus sliding planes (*i.e.* URANS).

4.3.1 Choice of stage-hood interface treatments

Table 4.2 presents a comparison of the costs of different stage-hood interface treatments, by assuming an average of $M_\mathrm{b} \approx 0.1 - 0.5$ million grid points per blade row and $M_\mathrm{h} \approx 2.5$ million in the exhaust hood.

Table 4.2 Comparison of different stage-hood interface treatments

Config.	Stator Passages	Rotor Passages	Total Mesh Count	Total Time Steps	Total Cost
Single MP	1	1	$2M_\mathrm{b} + M_\mathrm{h}$	N_step	C
MMP	4	4	$8M_\mathrm{b} + M_\mathrm{h}$	N_step	$1.2 - 2.0 \cdot C$
FR	N_s	N_r	$\approx 80M_\mathrm{b} + M_\mathrm{h}$	N_step	$4 - 12 \cdot C$
URANS	N_s	N_r	$\approx 80M_\mathrm{b} + M_\mathrm{h}$	$\approx 100N_\mathrm{step}$	$200 - 1,000 \cdot C$

At the top of the fidelity hierarchy of stage-hood interface treatment is the full annulus URANS (Fig. 4.4). It requires the modelling of all stator and rotor blade passages, and couples the rotor domain with stator and exhaust hood domains via sliding interfaces. It is considered the most accurate modelling approach within the RANS framework, since it fully accounts for stator-rotor and rotor-hood transient effects, albeit at extremely high computational cost (normally 500 times higher than the MMP configuration). This is predominantly down to the very different time and length scales in the blade passages and the exhaust hood: the former is dominated by the blade passing frequency at $2 - 3$ kHz, whilst the latter is typically lower than one engine order (*i.e.* $\leq 50 - 60$ Hz), due to the very large vortical and separated flows in the exhaust hood. To the author's knowledge, there are only two groups of researchers that have compared steady (mixing plane or frozen rotor) and unsteady (sliding plane) interface treatments in an LP exhaust system. Stanciu et al. stated that around $20 - 50$ turbine revolutions need to be marched to reach

convergence. They found that the single mixing plane method overpredicts the turbine total-total efficiency by around $5 - 10\%$ compared to full annulus URANS, whilst the frozen rotor approach provides a closer agreement [71]. Stein et al. discovered that the MMP approach has some advantage over frozen rotor due to the non-physical modelling in the latter, when compared to URANS simulations, although the numerical setup of the unsteady simulation was not detailed [74].

The full annulus frozen rotor model used in steady calcultations is termed "frozen" because the relative orientation of components across the interface is fixed, while the frame of reference can change [5]. Using this approach, wakes are convected from upstream to downstream in a fixed pattern, which is non-physical. Moreover, the rotor clocking position may have an impact on the numerical solution, although the clocking effect in LP exhaust system simulations has not yet been studied [10]. More recently, Stein et al. reported that a non-physical standing wake structure may lead to incorrect predictions of flow separation in the exhaust diffuser, and hence a deviation from full annulus URANS results [74]. Nevertheless, the model has been widely used in recent publications [88, 81, 53], owing to its capability of simulating flows with circumferential variations larger than the component pitch. This is considered a significant improvement compared to coupling a single passage of stator and rotor blades to the exhaust hood via a mixing plane, at which the flow is circumferentially averaged. Such improvement, however, does come with the cost of simulating the full annulus blade geometry.

To further reduce the computational cost without compromising accuracy, Stein et al. proposed a novel MMP-based coupling method for the stage-hood interface [74]. Instead of coupling one rotor passage to the full annulus hood inlet, they modelled multiple (but not all) stator-rotor passages, and individually coupled each rotor exit (one pitch) to a fraction of the exhaust hood inlet via a mixing plane. For example, with N_{rotor} rotor blades and only four blade passages to be modelled, the hood inlet would be divided into four even sectors so that circumferential averaging is performed locally between each rotor pitch ($2\pi/N_{\text{rotor}}$) and a sector of the hood inlet ($2\pi/4$). This allows the circumferentially non-uniform flow to develop at the exhaust hood inlet, and each blade passage experiences a different back pressure. The accuracy of this model (compared to full annulus simulations) improves with the number of mixing planes used, although four sectors were found to be sufficient [74].

4.3.2 Comparison of interface treatments

The three above-mentioned interface treatments are either readily available or can be easily implemented in CFX. Numerical simulations were thus performed using the blade geometry of Stage A coupled to an exhaust hood of typical design parameters at two operating conditions (100% and 50% of design mass flow rate). Only coarse mesh was used due to limited computational resources. The same numerical setup was applied, apart

from the interface treatment and the number of blade passages modelled. Fig. 4.5 presents the CFD domain for both the full annulus and MMP configurations.

To achieve convergence, URANS simulations were performed for 50 to 80 rotor revolutions before the flow field was deemed to be "converged", followed by another 5 (100% flow rate) or 10 (50% flow rate) revolutions over which time averaging was implemented. Convergence hereby means periodicity in monitored pressure levels in both blade and diffuser passages. Due to the very long physical time to march over, a coarse outer time step (around 5 steps per blade passing) had to be used. There is no doubt that this level of time scale would not fully resolve detailed stator-rotor interactions, but was considered enough when the focus was to be the downstream exhaust hood, where the time scale is much longer.

The objective was to assess the accuracy of low order methods (especially the MMP configurations) compared to both time-averaged URANS results, in terms of 1-D performance metrics (*e.g.* power output), and to circumferential non-uniformity at the stage exit (hood inlet).

Table 4.3 shows the comparison of the stage power output predicted by various interface treatments, referenced to time-averaged URANS values. Two MMP configurations were included: "MMPx4" refers to 4 mixing planes placed at the diffuser inlet, and "MMPx26" refers to 26 mixing planes.

Table 4.3 Predicted power output for different stage-hood interface treatments

Flow Condition	Time-avg URANS	MMPx4	MMPx26	Frozen Rotor
50% $\dot{m}_{\text{design}}$	-	+0.24%	+0.23%	+0.09%
100% $\dot{m}_{\text{design}}$	-	-0.06%	-0.08%	+0.09%

All steady simulations were in very close agreement with the unsteady results, especially at design condition. The level of agreement was closer than the errors of up to 5% that were reported by Stanciu et al. [72]. There are two possible reasons for this: firstly, the very coarse time step (250 steps per rotor revolution) used in this study could not fully resolve the transient stator-rotor interaction and hence may have underpredicted the associated mixing losses; secondly, the time averaging was performed over a much longer period (5 or 10 rather than 1 rotor revolution), to account for the low frequency phenomenon due to the presence of the exhaust hood. Moreover, as far as 1-D performance was concerned, no advantage was observed by placing significantly more mixing planes at the diffuser inlet.

Fig. 4.6 illustrates the circumferential distribution of stage exit (or diffuser inlet) static pressure coefficient

$$C_{\text{ps}} = \frac{p - p_{\text{s, ref}}}{p_{0,\text{ ref}} - p_{\text{s, ref}}}, \tag{4.1}$$

based on mass-averaged total pressure ($p_{0,\,\mathrm{ref}}$) and area-averaged static pressure ($p_{\mathrm{s},\,\mathrm{ref}}$) at the diffuser inlet. For MMP configurations the values were averaged over each individual mixing plane. For full annulus configurations the diffuser inlet was divided into N_{rotor} even sectors, with the averaging performed within each sector. Again, excellent agreement was achieved by all steady interface treatments. At 50% mass flow rates, the circumferential pressure variation level was much lower than the design condition, thought to be associated with the increased amount of mixing through highly swirling flows entering the diffuser, due to the rotor operating at off-design condition (see Section 5.2.4). The shape of the pressure distribution at 50% flow rate was more skewed with the lowest stage exit pressure at $\theta \approx 120°$, but became more or less symmetric at design flow condition. Overall, both distributions were in an approximately sinusoidal form, explaining why a good prediction of turbine back pressure (and hence the power output) could be obtained by using just four mixing planes rather than by modelling *all* blade passages. Therefore, it can be concluded that MMP-based coupling is suitable for assessing 1-D performance of exhaust systems, at a much lower computational cost.

Finally, the circumferentially non-uniform flow field at the diffuser inlet was visualised using contour plots for 100% and 50% flow conditions (Fig. 4.7 and Fig. 4.8 respectively). Again, good qualitative agreement was achieved amongst all interface treatments. In the MMPx4 configuration, discontinuity occurred at the connection lines between mixing planes, similar to what Stein et al. had observed. This was not considered an issue since the flow mixes out quickly downstream of the stage-hood interface [74].

4.4 Concluding remarks

This chapter described the numerical methods and tools used to investigate the flow fields and performance of LP exhaust systems. A design suite *ExhaustGen* was developed to automate exhaust hood geometry and mesh generation, and for the data processing of CFD results. This proved useful for the remainder of the numerical studies presented in this thesis.

Particular attention was directed towards the stage-hood interface treatments and the MMP-based coupling was shown to be in close agreement with the highest fidelity of simulation (full annulus URANS), which would significantly reduce the computational cost for optimisations and parametric studies (see Chapter 7).

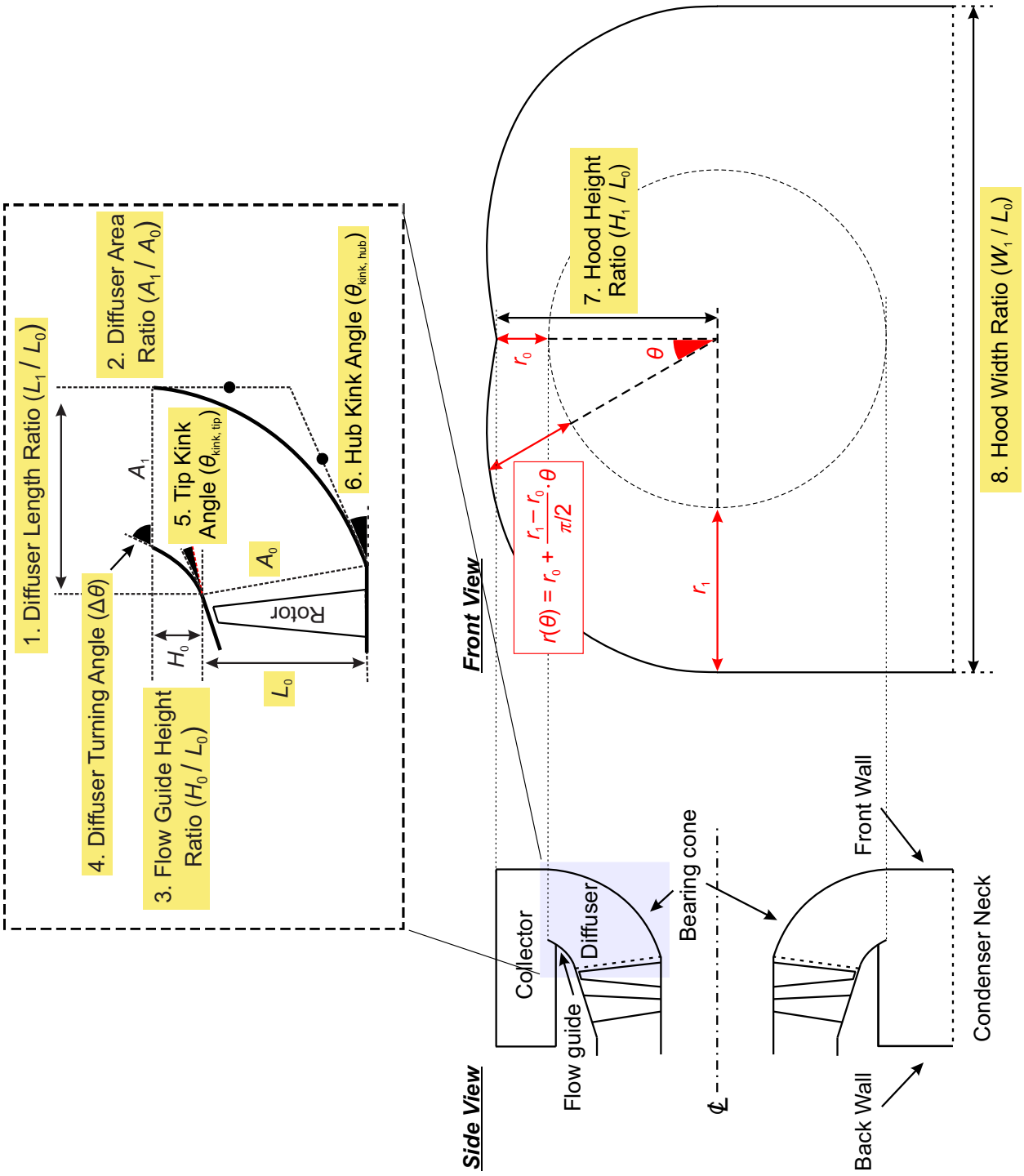

Fig. 4.1 Parametrisation of LP exhaust hood

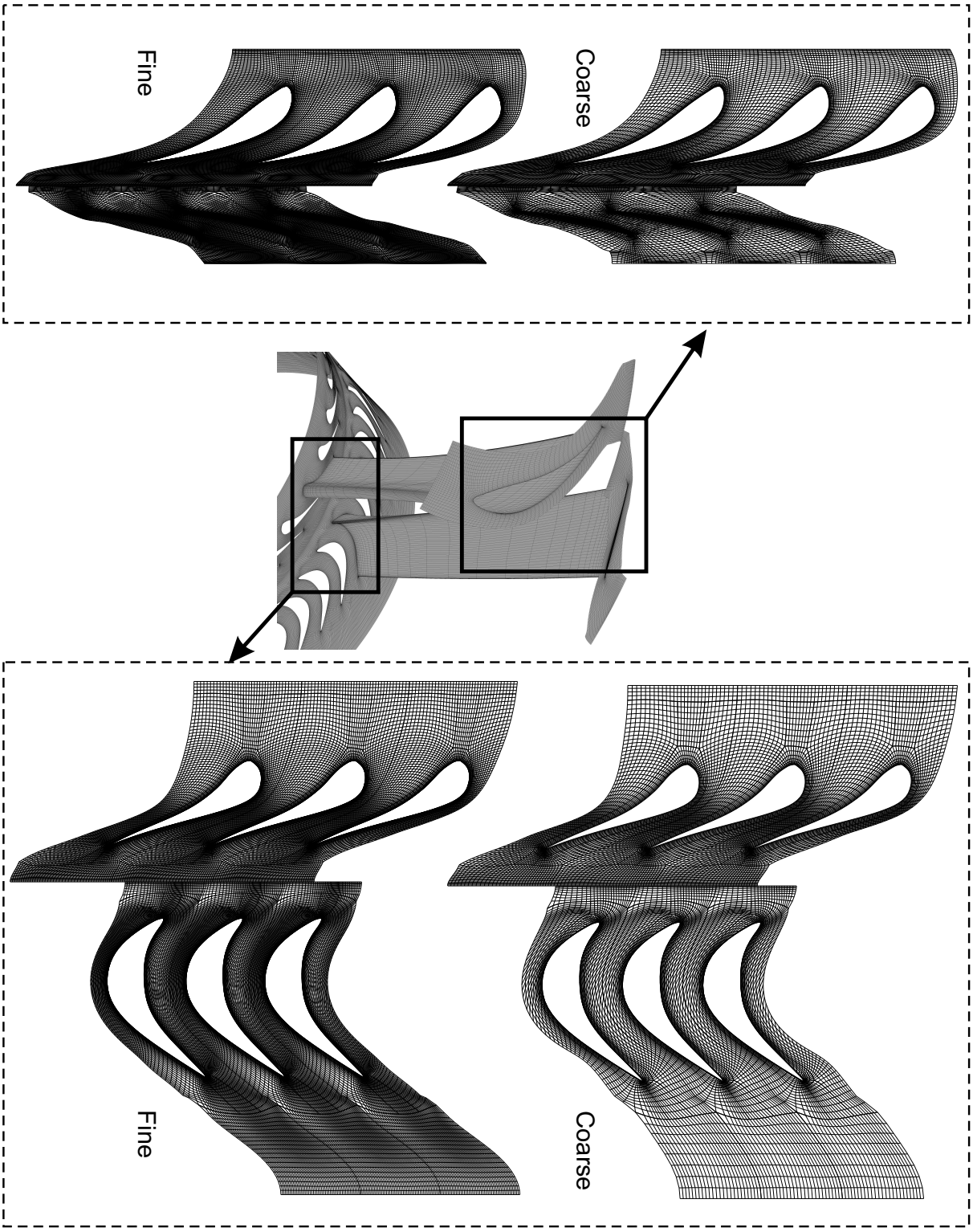

Fig. 4.2 Blade passage meshes of coarse and fine sizes

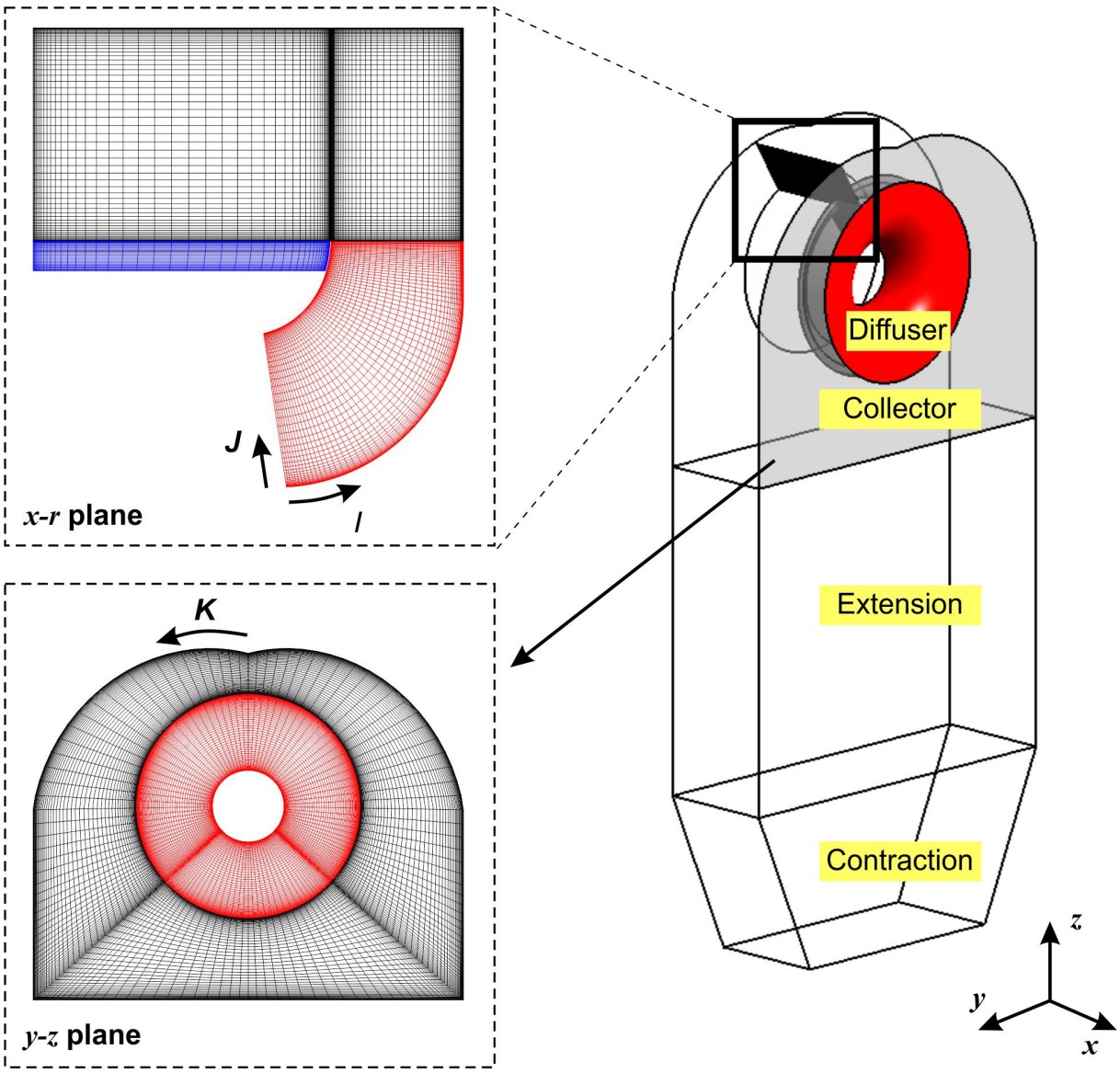

Fig. 4.3 CFD domains and meshes on selected planes

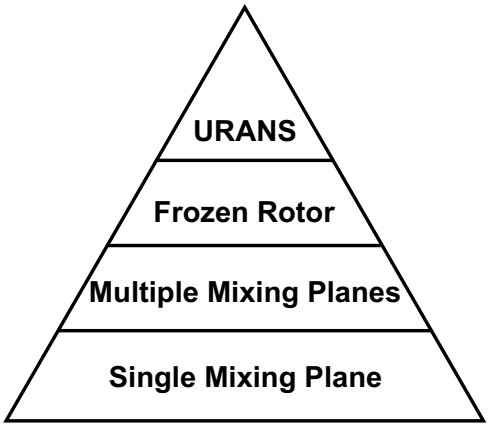

Fig. 4.4 Fidelity hierarchy of stage-hood interface treatment

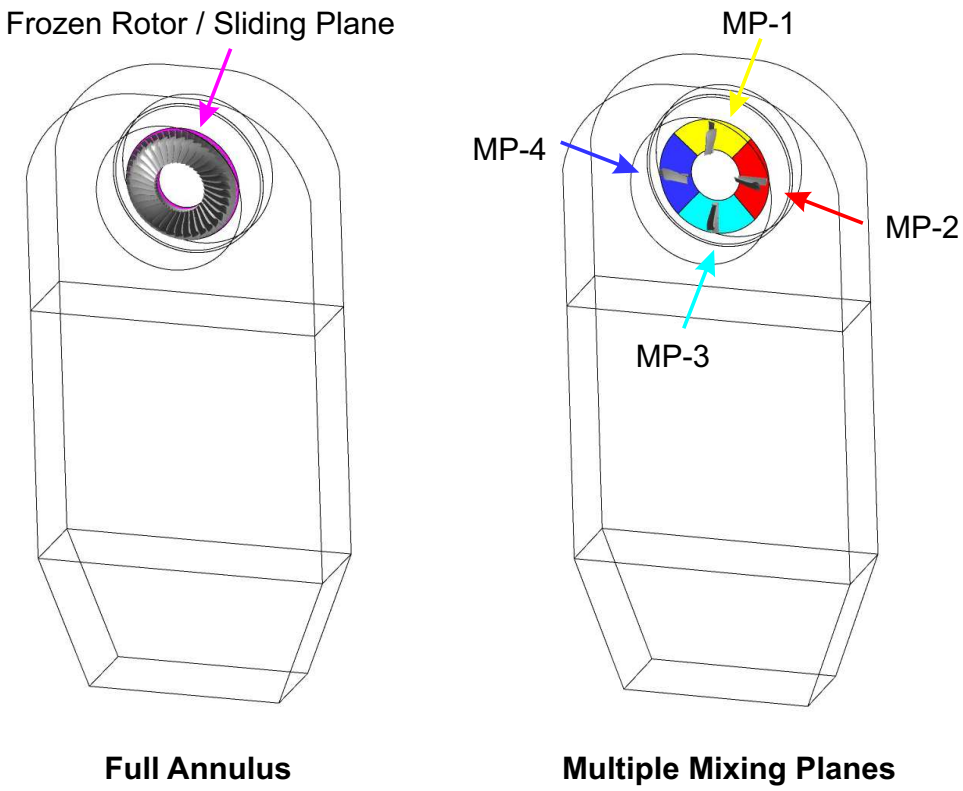

Fig. 4.5 CFD setup for full annulus (left) and multiple mixing plane (right) configurations

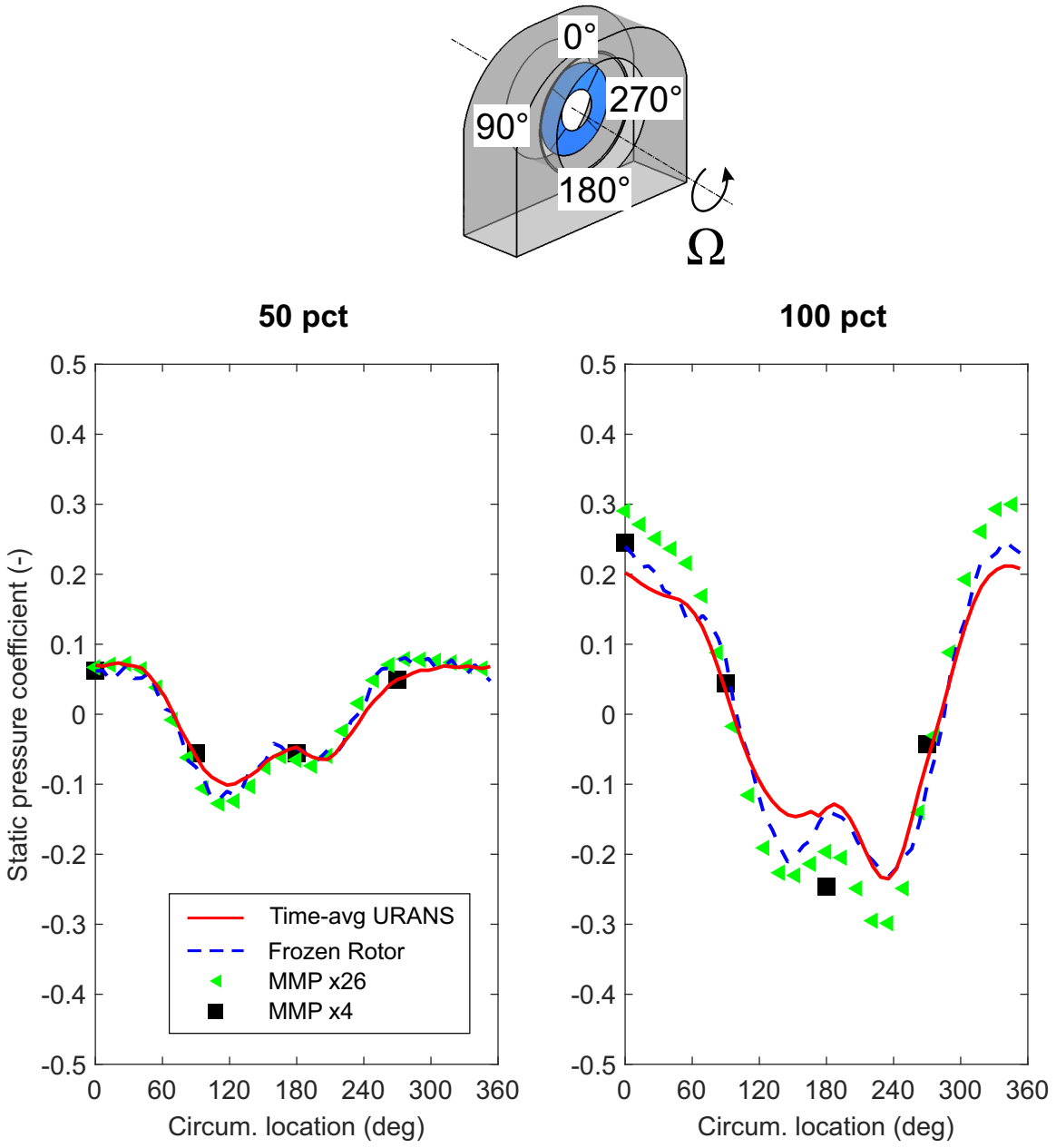

Fig. 4.6 Circumferential variation of diffuser inlet pressure coefficients at 50% (left) and 100% (right) mass flow rates, for different stage-hood interface treatments

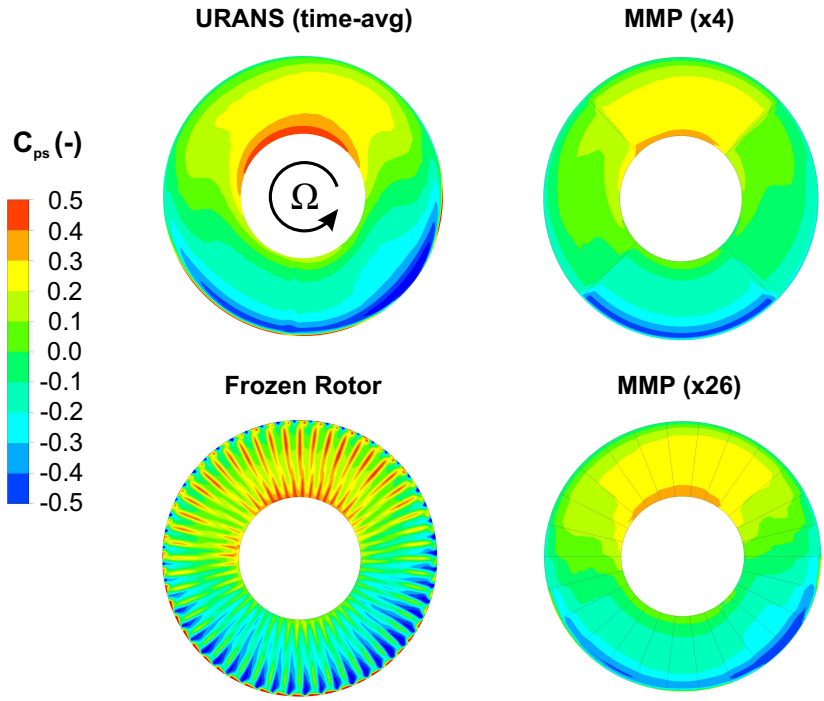

Fig. 4.7 Contours of diffuser inlet static pressure coefficient at 100% mass flow rates for different stage-hood interface treatments, viewed from downstream

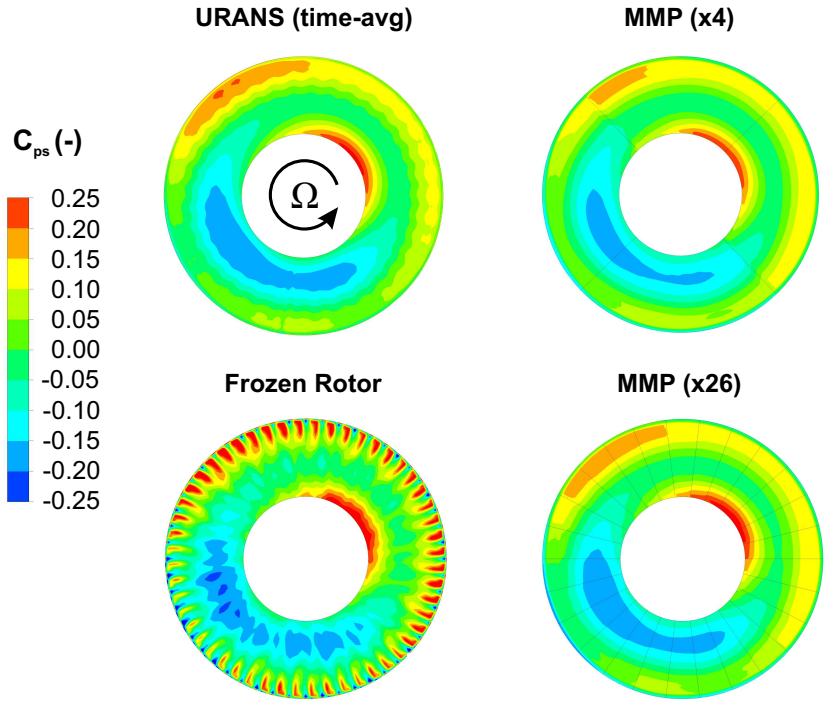

Fig. 4.8 Contours of diffuser inlet static pressure coefficient at 50% mass flow rates for different stage-hood interface treatments, viewed from downstream

Chapter 5

Effect of Stage-Hood Interaction on LP Exhaust System Performance

Although the strong coupling between the last stage and the exhaust hood has been appreciated for a long time, very few items in the literature took blading design into account when designing and/or optimising LP exhaust systems. As commented in Section 1.2, most studies have focused on either the last stage blading or the exhaust hood, but not both. In this chapter, the mechanism of stage-hood interaction will be introduced from an energetic point of view, followed by a discussion of the numerical studies carried out on the flow features and loss mechanisms of two different exhaust systems over a wide operating range. Finally, the investigations into the effect of blading design on system performance will be discussed. This chapter is aimed to answer the following research questions:

1. How much is each component in an LP exhaust system responsible for the loss generation, at different operating conditions?
2. What are the key flow features and corresponding loss mechanisms in an LP exhaust system, as the operating condition changes?
3. How does blading design (*e.g.* rotor blade restaggering) affect LP exhaust system performance, and how much performance gain can be achieved by taking blading design into account?

5.1 An energetic view of the LP exhaust system

The interaction between the last stage and the exhaust hood has been recognised for a long time [28, 45]. The last stage blading design influences the boundary condition experienced by the downstream exhaust hood. The exhaust hood performance is very sensitive to its inlet flow condition, in terms of the spanwise distributions of total pressure and swirl angle [67, 26, 87], and tip leakage flow [7, 12]. Different hood designs, in turn, lead to

different levels of static pressure recovery and total pressure loss, hence influencing the actual flow condition at which the last stage operates. It is therefore important to include both components in the CFD simulation to provide realistic boundary conditions for the exhaust hood.

Although the bi-directionally coupled simulation of last stage and exhaust hood has long been standard practice in the research community [10], it is still unclear as to how much each component in the LP exhaust system (*i.e.* the last stage and the exhaust hood) is responsible for overall system performance, and how their levels of contributions change as the operating condition varies. Without knowing the relative importance of each component, it is difficult to identify areas for further improvement that could lead to higher system efficiency.

For a better understanding of how much each component inside the LP exhaust system contributes to the overall loss generation, an energy based analysis was performed by plotting the thermodynamic process inside the exhaust system. In Fig. 5.1, steam expands from the turbine inlet to its exit ($1 \rightarrow 2$), produces work ($h_{01} - h_{02}$) and diffuses inside the exhaust hood ($2 \rightarrow 3$), ending with some condenser pressure p_3. The system performance ($1 \rightarrow 3$) can be measured using the total-static efficiency, defined as

$$\eta_{\text{sys, t-s}} = \frac{h_{01} - h_{02}}{h_{01} - h_{3s}} = \frac{\text{Actual Work}}{\text{Ideal Work}} \tag{5.1}$$

by assuming that in the ideal case the exhaust loss at hood exit (station 3) should be zero. As commented by Hirschmann et al. [35], zero exhaust loss can only be achieved by an infinite hood exit area ratio, which is not realistic. In an actual exhaust hood, however, the exit area is typically large enough (around 3 times the diffuser inlet area) so that the ideal pressure recovery is over 0.9 for a wide range of inlet Mach numbers. This is based on a study of compressibility effect on ideal pressure recovery [35]. Therefore, the definition in Eq. 5.1 is considered to be an appropriate measure of the system performance.

The total lost work, $h_{02} - h_{3s}$, can be split into various terms:

$$\begin{aligned}
\text{Lost Work} &= h_{02} - h_{3s} && (5.2)\\
&= h_{02} - h_2 + h_2 - h_3 + h_3 - h_{3s} && (5.3)\\
&= (h_{02} - h_2) \cdot (1 - \frac{h_3 - h_2}{h_{02} - h_2}) + h_3 - h_{3s} && (5.4)\\
&= \text{Stage Leaving Loss} \cdot (1 - C_h) + T_3 \cdot (\Delta s_{\text{stage}} + \Delta s_{\text{hood}}) && (5.5)\\
&= \text{Hood Leaving Loss} + T_3 \cdot \Delta s_{\text{total}} && (5.6)
\end{aligned}$$

where

$$C_h = \frac{h_3 - h_2}{h_{02} - h_2} \tag{5.7}$$

is an enthalpy-based recovery coefficient. The two terms on the RHS of Eq. 5.6 are the unrecovered hood leaving loss and total irreversible entropy generation in the system. Such breakdown analysis is similar to that described by Hirschmann et al. [35], although here, all terms are based on energy rather than pressure.

The interaction mechanism between the last stage and the exhaust hood is summarised in Fig. 5.2. Both last stage blading and exhaust hood design influence the overall level of lost work. The blading design should be such that both leaving energy ($LL = \frac{1}{2}V^2$) and loss generation ($T\Delta s_{\text{stage}}$) are minimised, *i.e.* both total-total and total-static efficiencies of the stage should be high. At the same time, the stage exit flow profile (*e.g.* total pressure and swirl angle distributions) should be favourable for the downstream exhaust hood, so that the static pressure recovery coefficient (C_p or equivalently, C_h) is maximised and the loss generation ($T\Delta s_{\text{hood}}$) minimised. On the other hand, the downstream exhaust hood should be designed to achieve the same goal. Clearly there is a balance to strike amongst all these terms. For instance, a blading design that results in higher leaving loss or entropy generation (in the blade passage) does not necessarily lead to lower system performance, so long as the stage exit flow profile is favourable for the exhaust hood. Therefore, it is important to understand how each term in Eq. 5.6 is affected by blading design, and how the level of lost work can be minimised, which is the ultimate goal for design and optimisation.

This suggests a need to include the last stage in the design consideration together with the exhaust hood over a wide operating range. To the author's knowledge, the only related works in public domain that do so are by Musch et al. [56] and Cremanns et al. [18]. The study by Musch et al. [56] was based on a throughflow code coupled with a boundary layer solver, in which the rotor blades were twisted to achieve lower leaving loss at the diffuser exit. The model, however, was unlikely to be able to deal with asymmetric and separated flows in the diffuser, especially at part-load conditions. Moreover, the amount of twist applied was not mentioned and it is questionable if the proposed design could be manufactured at all. In the other work by Cremanns et al. [18], 3-D RANS CFD was used for the optimisation by varying both blading and diffuser designs. It was demonstrated that some 1.8% increase in system efficiency could be achieved through coupled rather than sequential optimisation. Nevertheless, it was not mentioned what flow physics led to such performance improvement.

5.2 Baseline analysis

In this section, two different LP blade geometries are introduced and compared against each other in terms of their overall performance characteristics, detailed flow features and loss mechanisms over a wide operating range. This will not only establish a baseline, but also demonstrate that the conclusions obtained do not just apply to a particular blading.

5.2.1 Datum geometries

Stage design

The two LP turbine geometries for 1000 MW steam plants are called Stage A (last stage) and Stage B (last two stages). Both geometries are provided by the industrial sponsor but are of different design styles. Some geometric and operational information of the last stage for the two designs are summarised in Table 5.1.

Table 5.1 Comparison of two blading designs

	Stage A	Stage B
Rotor blade height	L_0	$1.1 \cdot L_0$
Hub-tip ratio	0.44	0.43
Rotor tip gap size	$0.8\%L_0$	$0.8\%L_0$
Stage design pressure ratio (p_{01}/p_2)	6.2	6.3
Design exit axial Mach number	0.65	0.65

Exhaust hood design

In addition to stage design, datum exhaust hood geometry had to be established. Table 5.2 lists the non-dimensional design parameters of the datum exhaust hood for both stages. The geometry parameterisation has been described in Section 4.1. The choices of these parameters lie within practical engineering limits, and would result in reasonably well-performing exhaust hoods for the baseline analysis.

Table 5.2 Baseline exhaust hood geometric parameters

Parameter	Value
Diffuser axial length ratio (L_1/L_0)	1.3
Diffuser exit area ratio (A_1/A_0)	1.6
Flow guide turning angle ($\Delta\theta$)	75°
Flow guide initial kink angle	0°
Flow guide height ratio (H_0/L_0)	0.6
Bearing cone initial kink angle	0°
Collector height ratio (H_1/L_0)	3.2
Collector width ratio (W_1/L_0)	9.0

5.2.2 Numerical setup

Having established the baseline stage and hood designs, the numerical simulation had to be set up. The requirement was to simulate the circumferentially non-uniform flow in the

exhaust system and to account for the lost work due to each component as accurately as possible. In Section 4.3, the MMP-based approach was found to provide a very close prediction of the asymmetric flow field given by full annulus configurations. Nevertheless, without including all blade passages the loss generation could not be properly calculated. Therefore, it was decided to include the full annulus blade rows and couple them with the exhaust hood via a frozen rotor style of interface, as has been done for many previous studies [10]. As an example, the exhaust hood geometry for Stage B is given in Fig. 5.3 to illustrate the relevant stations for 1-D averaging. Between the nozzle and rotor rows another frozen rotor interface was placed. For Stage B, single blade passages for the penultimate stage were used since the flow becomes more axi-symmetric upstream. Mixing planes were placed between G-1 and L-1, and between L-1 and G-0.

At the turbine inlet, total pressure, total enthalpy and flow angles were prescribed for different operating conditions. The domain outlet had a fixed area ratio ($A_3/A_0 = 2.0$) and average static pressure. Five operating conditions were now considered, corresponding to 50%, 60%, 70%, 85% and 100% of design mass flow rates for each stage design.

Finally, as stated in Section 4.1.4, it is impractical to run full annulus simulations with fine mesh size. All analyses in this chapter are based on a very coarse mesh size ($\sim$ 10 million in total) unless stated otherwise. In order to check the mesh sensitivity, a much finer mesh size was ran for the baseline configuration of Stage A, to ensure that the coarse mesh still captured the same flow features as the fine mesh. The comparison of mesh sizes is summarised in Table 5.3.

Table 5.3 Mesh size comparison

Configuration	Blade passage (per row, in mil)	y^+_{avg} (-)	Exhaust hood (mil)	y^+_{avg} (-)	Total (mil)
Stage A, coarse	0.1	20.7	2.4	21.2	10.2
Stage A, fine	0.5	5.1	5.0	3.4	47.5

5.2.3 Overall performance characteristics

To have an overview of the performance characteristics of the two exhaust systems, some 1-D averaged metrics were plotted against mass flow rate (Fig. 5.4). The system total-static efficiency was defined in Eq. 5.1, and the stage efficiencies were defined as:

$$\eta_{\text{stage, t-t}} = \frac{h_{01} - h_{02}}{h_{01} - h_{02s}} \tag{5.8}$$

and

$$\eta_{\text{stage, t-s}} = \frac{h_{01} - h_{02}}{h_{01} - h_{2s}} \tag{5.9}$$

In addition, stage leaving loss ($h_{02}-h_2$), exhaust hood static pressure recovery coefficient $C_p = (p_3 - p_2)/(p_{02} - p_2)$, and total pressure loss coefficient $Y_p = (p_{02} - p_{03})/(p_{02} - p_2)$ were plotted against mass flow rates for both stages (Fig. 5.4). Note the absolute values are not revealed in these plots.

As shown in Fig. 5.4, the two blading designs had quite distinct stage performance characteristics: Stage A was already optimised with part-load performance in mind, so had a much flatter stage total-total efficiency curve ($\eta_{\text{stage, t-t}}$). The efficiency for Stage B, in contrast, dropped significantly as the mass flow rate reduced, although its peak efficiency was several percentage points higher than Stage A.

As far as overall system performance ($\eta_{\text{sys, t-s}}$) was concerned, the two designs were neck and neck for mass flow rates above 70% of the design value. As the flow rate reduced, the advantage of Stage A became apparent. This can be better seen in Fig. 5.5, where the lost work is broken down into irreversible entropy generation in each component ($T\Delta s$ terms in Eq. 5.6) and the leaving kinetic energy at the hood exit (or condenser neck). All values are normalised by the ideal work and hence represent the lost efficiency. The $T\Delta s$ terms were calculated based on the 1-D mass averaged values of entropy at the inlet and outlet of each domain, *i.e.* stage ($1 \rightarrow 2$), diffuser ($2 \rightarrow 2a$) and collector ($2a \rightarrow 3$), and the temperature at the hood exit (T_3).

At low flow rate (70% and lower), Stage A's system and stage total-static efficiencies were higher than those of Stage B. The irreversible entropy generation for Stage A was lower in both the blade passage and the exhaust hood, the reason for which shall be discussed in the following subsection. In terms of leaving loss at the hood exit, Stage A was actually worse due to its lower level of pressure recovery compared to Stage B. Nevertheless, the overall performance was dominated by the $T\Delta s$ terms rather than pressure recovery. This indicates the importance of using system total-static efficiency rather than pressure recovery coefficient to measure system performance.

It is also worth noting that the loss generated in the exhaust hood (diffuser and collector) surpassed that in the stage when mass flow rate dropped below around 60% of the design value. Therefore, hood design becomes more important at part-load conditions.

Finally, the effect of mesh size can be seen in Fig. 5.6, which shows the contributions to total lost work by various components, comparing between coarse and fine meshes for Stage A at various flow conditions. Very close agreement between the two mesh sizes was observed, especially at part-load conditions. This justified the use of coarse mesh for the remainder of the numerical studies.

5.2.4 Flow features and loss mechanisms in the exhaust hood

Having observed the overall performance characteristics of the exhaust system, it was now appropriate to take a look at the key flow features in the exhaust hood as the operating condition varies, and identify the loss mechanisms associated with such flow behaviours.

Flow features

Fig. 5.7 shows the circumferentially averaged spanwise flow conditions at the diffuser inlet, plotted against absolute total pressure (normalised by the mid-span value at design condition) and absolute swirl angle (90° corresponds to tangential direction). Note the very high total pressure near the tip region is not shown in the plots, in order to make the variations elsewhere more clear. Moreover, only three flow conditions are plotted (50%, 70% and 100% mass flow rates), for clarity. These profiles, passed from the upstream stage(s), are the inlet boundary conditions experienced by the downstream exhaust hood. The dashed lines on the LHS of Fig. 5.7 correspond to results from fine mesh calculations for Stage A, which were almost identical to the coarse mesh results.

At design condition, total pressure was more or less uniform in the radial direction and the flow mostly aligned with the axial direction, except at the tip region where leakage jets with high momentum entered the diffuser at some swirl angle. Stage A had a more hub-strong total pressure distribution and a negative hub swirl (over 90°). This meant that when the flow rate reduced, the absolute level of hub swirl angle would also reduce before increasing, which would affect the bearing cone separation size, as will be explained in the following paragraph.

At part-load condition, the radial gradient of total pressure became more positive as the flow migrated radially outwards, and the absolute swirl angle moves to the right of the plot (Fig. 5.7). This can be understood by the velocity triangles of a typical LP rotor blade (Fig. 5.8). As flow rate decreased, axial momentum decreased and absolute swirl angle increased, especially near the hub region where the blade velocity U was at its lowest. Moreover, flow was susceptible to separation on the bearing cone surface due to two factors. Firstly, it was experiencing an adverse pressure gradient in the diffusing passage. Additionally, the increased hub swirl angle induced a positive radial pressure gradient which further lowered the hub pressure. As shown in Fig. 5.9, the size of the hub separation grew as the flow rate dropped below 70%. For Stage A, a moderate hub separation also existed at design condition, because of the negative swirl at the hub. Stage B performed better at design with almost uniformly axial flow, but was worse off at part-load due to the higher swirl angle. In particular, at 50% flow rate the hub separation commenced upstream of the diffuser inlet, which also explains the higher level of loss in Stage B's blade passage, as shown in Fig. 5.5.

In addition to the bearing cone separation, there was a pair of passage vortices travelling downwards to the condenser neck, initiated from the end of the flow guide, as shown in Fig. 5.9. They can be more clearly viewed in Fig. 5.10, which illustrates 3-D streamtubes originating from four circumferential locations at the diffuser inlet. At design condition, the flow field was close to symmetry with a pair of blocked areas at the hood exit (in black colour), the definition of which will be introduced later in this section. The streamtubes starting from the top of the diffuser inlet (0°) bifurcated into two counter-rotating vortices

on either side of the collector. As the flow rate reduced to 50%, asymmetry grew due to the swirling flow at the diffuser inlet: the yellow streamtubes (staring from 0°) were swept to the left of the collector (viewed from downstream) while blue streamtubes (starting from 270°) occupied a much larger volume inside the collector, which would have led to increased mixing loss. Zhang et al. attributed this passage vortex to the backward-facing-step type of separation behind the flow guide lip [93]. One way to reduce the vortex strength would be to break the large vortex into smaller ones using separation ducts, through which some 12% increase in pressure recovery can be obtained (Mizumi et al. [52]).

Loss mechanisms

The flow features identified above would lead to different loss mechanisms at different flow conditions. As shown in Eq. 5.6 there were two loss sources: irreversible entropy generation ($T\Delta s$) and hood leaving loss ($\frac{1}{2}V^2$), which will be discussed in this subsection.

The entropy rise in each domain, as shown in Fig. 5.5, was the main contributor to the lost efficiency. They helped quantify the overall distribution of loss in the exhaust system, but failed to locate the sources of loss generation. The local entropy generation rate was therefore used instead to visualise loss sources in forms of contour plots.

The rate of change of entropy of a fluid particle, according to Greitzer et al. [29], is:

$$\frac{Ds}{Dt} = \frac{1}{T}\Big(\dot{Q} - \frac{1}{\rho}\frac{\partial q_i}{\partial x_i} + \frac{1}{\rho}\tau_{ij}\frac{\partial u_i}{\partial x_j}\Big) \tag{5.10}$$

with D/Dt referring to material derivative and the heat flux q_i defined as

$$q_i = -\lambda\frac{\partial T}{\partial x_i}, \tag{5.11}$$

where λ is the thermal conductivity. Note that Einstein summation convention is assumed throughout this chapter.

For a turbulent flow with no internal heat sources ($\dot{Q} = 0$), Eq. 5.10 can be used to derive the irreversible entropy generation rate per unit volume $\dot{s}_{\text{gen}}(t)$:

$$\dot{s}_{\text{gen}}(t) = \frac{1}{\rho}\Big(\bar{\Phi}_d + \Phi'_d + \bar{\Phi}_c + \Phi'_c\Big), \tag{5.12}$$

by following the Reynolds decomposition procedure [33, 59]. The RHS of Eq. 5.12 are the irreversible entropy production due to viscous and turbulent dissipations ($\bar{\Phi}_d$ and Φ'_d), and by thermal conduction due to time-averaged and turbulent temperature gradients ($\bar{\Phi}_c$ and Φ'_c). These four terms can be calculated during CFD post-processing.

The entropy production by direct dissipation is

$$\bar{\Phi}_d = \frac{1}{T}\tau_{ij}\frac{\partial u_i}{\partial x_j}. \tag{5.13}$$

The entropy production by turbulent dissipation is modelled as

$$\Phi'_d = \beta^* \cdot \frac{\rho\omega k}{T}, \tag{5.14}$$

where ω and k are the turbulent eddy frequency and turbulent kinetic energy respectively in the $k-\omega$ SST model, and the coefficient β^* is taken to be 0.09 [34].

Next, the entropy production due to mean temperature gradients is

$$\bar{\Phi}_c = \frac{\lambda}{T^2}\big(\nabla T\big)^2. \tag{5.15}$$

Finally, the entropy production due to fluctuating temperature gradients is modelled as

$$\Phi'_c = \frac{\lambda_t}{T^2}\big(\nabla T\big)^2, \tag{5.16}$$

with turbulent thermal conductivity $\lambda_t = C_{\mathrm{P}}\mu_t/Pr_t$. C_{P} is the heat capacity at constant pressure, and the turbulent Prandtl number (Pr_t) is assumed to be 1.

Fig. 5.11 shows the contours of local specific entropy generation rate ($\dot{s}_{\mathrm{gen}}$) at various cross sections of the exhaust hood for the two stages, at 50%, 70% and 100% mass flow rates. Several observations were made regarding entropy generation:

The first source of loss was the flow separation near the bearing cone. As the flow rate reduced to 50% of its design value, the high loss regions near the bearing cone became apparent with increased levels of entropy production in a much enlarged region, due to the viscous mixing between the main stream and the large separation region.

The second region of high levels of entropy generation was identified near the flow guide. Singh investigated the loss mechanisms due to rotor and diffuser casing interaction in detail, and attributed the mixing of the tip leakage flow as one of the main loss sources, in addition to rotor trailing edge shock and wake [68]. Nevertheless, it was noted in Section 6.3.2 that the leakage jet helps suppress or delay the flow separation on the concave upwards surface, meaning there is a balance between reducing mixing loss and preventing flow separation on the flow guide. It is also worth noting that the strength of the mixing loss in this region reduced when the turbine operated at part-load conditions. Therefore, focus should be placed on the bearing cone separation should part-load performance become a major concern.

A final loss generating region was situated within the passage vortex, albeit only visible at design condition (100% $\dot{m}_{\mathrm{design}}$) and weakened at part-load.

In addition to the irreversible entropy generation, the hood exit leaving energy was the other source of loss, since it could not be recovered any more. The level of this leaving energy was determined by the stage exit leaving energy ($LL = h_{02} - h_2$) and static pressure (or enthalpy) recovery (C_p or C_h). As shown in Fig. 5.2, stage exit leaving energy very much depended on the blading design, while the pressure recovery was influenced by both

blading design (via its influence on the diffuser inlet flow profile) and exhaust hood design. For the latter, a key parameter was the effective exhaust area, through which the flow travelled *downwards* rather than upwards, at the condenser neck (station 3).

Fig. 5.12 illustrates the 3-D streamtubes starting from and ending at the blocked area at the condenser neck (Fig. 5.10). The colours refer to the time (in seconds) on the streamtube and are clipped to the $[0.0, 1.0]$ range for clarity. Blue colour thus means the streamtube has not arrived at the blocked area yet, while other colours refer to streamtubes departing from the blocked area. From Fig. 5.12 it can be clearly seen that the passage vortex reduces the effective area the rest of the flow could travel through, occupying much greater volume as the flow rate reduces, for both stages investigated.

Furthermore, a closer look at the origin of the streamtubes unveils the effect of swirl as the operating condition changes. At 100% flow rate, the streamtubes that landed at the blocked area mostly originated from the top of the diffuser inlet (near 0°), and formed a symmetric pair of counter-rotating vortices. This created two symmetric spots of blocked area, with a third one situated towards the back wall (Fig. 5.10). As the flow rate reduced to 50%, the middle spot gradually disappeared and the asymmetry of the pair intensified (Fig. 5.10). This was because the origin of the streamtubes moved clock-wise (viewed from downstream) towards the bottom of the diffuser inlet (near 200°), explaining the greater blocked area on the right hand side.

The effect of large blockage area on the pressure recovery can be seen in Fig. 5.13 where pressure recovery coefficient C_p is plotted against the effective exhaust area ratio (unblocked area over diffuser inlet area), *i.e.*

$$\bar{A}_{\text{eff}} = \frac{A_{\text{hood exit}} - A_{\text{blocked}}}{A_{\text{dif inlet}}} \tag{5.17}$$

Despite the slight difference in slopes, both stages experienced declining pressure recovery due to reduced effective exhaust area. As shall be seen in Chapter 7, the performance of the exhaust hood is positively affected by its width (and hence the hood area) ratio, especially at part-load conditions.

5.3 Effect of blading design on system performance

The previous section discussed the flow features and loss mechanisms inside the LP exhaust system, suggesting that both blading and hood designs influence system performance, as shown in Fig. 5.2. In this section, blading redesign in terms of rotor blade restaggering is proposed and a numerical study of its effect on the exhaust system performance is presented. Compared to re-cambering the rotor blade sections and re-stacking the stator blades, rotating the rotor blade is considered one of the simplest ways to study the stage-hood coupling effect and to demonstrate the benefits of system-based design. It also helps to provide general design guidance, which can be directly applied to existing blade designs.

A more extensive exploration of full design options would certainly be worthwhile, and shall become the focus in future work.

The other component in the exhaust system, the exhaust hood, also influences system performance. However, the associated numerical studies would require much greater computational resources due to the high dimensionality of the exhaust hood design space. The issue with high dimensionality will be addressed in Chapter 6, and the results of the hood geometry effect will be presented in Chapter 7.

5.3.1 Proposed blading redesign

As stated in Section 5.2.4, bearing cone separation is the main contributor to the loss generation at part-load condition, primarily caused by low axial momentum and high swirl angle at the hub. Quite a few people have studied the effect of diffuser inlet flow profiles on its performance, *e.g.* [26, 36]. The consensus is that swirl is beneficial for flow near the outer casing (*i.e.* flow guide) and detrimental for the hub (*i.e.* bearing cone), and that a hub-strong total pressure profile helps delay the flow separation. Nevertheless, it is unclear how these spanwise flow profiles can be realised in an actual LP exhaust system.

One of the ways to modify the diffuser inlet flow profile is to simply restagger the rotor blade, as illustrated in Fig. 5.14. Restaggering the rotor blade has two effects. Firstly, it modifies the stage exit swirl angle through changes to the blade exit angle. Secondly, it influences the radial distribution of mass flow and total pressure through radial equilibrium, due to the change in the throat area and swirl angle distribution. For instance, opening the hub would redistribute the flow from the upper to the lower part of the blade passage, and hence increase the axial momentum in the hub region. The resulting change to the rotor exit flow profile would consequently affect the exhaust hood and hence also system performance.

Although rotor structural integrity was not the focus of this study, it was felt that the maximum restagger should not exceed 10°, and that the top half of the span should be kept unchanged, given the sensitivity of supersonic aerofoils to incidence. The rotor hub section was opened by 5° around the centroid, with a linear variation to 0° at mid span. As an example, the datum and modified stagger angle distributions of Stage B are presented in Fig. 5.14.

5.3.2 Results and discussions

The same exhaust hood geometries introduced in Section 5.2 were now coupled to the restaggered rotor blades. Similar to Section 5.2, Fig. 5.15 illustrates the comparison of 1-D averaged performance metrics of the datum and restaggered blade geometries, while Fig. 5.16 shows a breakdown of the lost efficiency into different components.

Stage A's system performance improved at all operating conditions, simply by opening the rotor hub section by 5°. In particular, at 70% mass flow rate the system total-static

efficiency increased by 1.5%. This can be understood by comparing the diffuser inlet profiles plotted in Fig. 5.17, along with the meridional streamline plots in Fig. 5.18. At 70% and 100% flow rates, hub total pressure increased while the absolute swirl angle decreased. This helped suppress the flow separation on the bearing cone. At low flow rate (50%), although hub total pressure was still stronger compared to the baseline, the overall swirl angle increased, explaining the lower performance gain. It is also worth pointing out that the stage total-total efficiency did not change much compared to the baseline. This is again suggestive of the fact that the system, rather than stage efficiency, should be used as the optimisation goal.

For Stage B, there was a very limited level of performance improvement apart from 60% and 70% flow rates, at which the bearing cone separation was suppressed (Fig. 5.18). Two reasons can explain this. Firstly, the hub swirl angle of Stage B was higher than that in Stage A. As the rotor hub was opened up, the absolute swirl level increased further, which counteracted the benefits brought by higher hub axial momentum. Secondly, Stage B's blading was not optimised for part-load operation, meaning the entropy generation in the redesigned blade passage would be greater than the datum, as demonstrated by the $T\Delta s_{\text{blade}}$ term in Fig. 5.16.

Overall, restaggering the rotor blade had two effects on the exhaust system. Firstly, it changed the level of leaving energy (which became lower at design condition and higher at part-load) through changes to the overall swirl angle at stage exit. This helped to alleviate the detrimental impact from the reduction of pressure recovery (especially for Stage B). Secondly, it changed the system's pressure recovery capability as well as irreversible entropy generation through changes to the spanwise flow profile experienced by the downstream exhaust hood. The effect of rotor blade restaggering on the stage performance was rather small, but it could positively impact the exhaust hood and the overall system, the extent of which are dependant on the datum blade design.

5.4 Concluding remarks

In this chapter, an energy-based analysis showed that hood exit leaving loss and irreversible entropy generation in both blade passages and the exhaust hood contributed to the lost work in an LP exhaust system. The contribution of each component (blade, diffuser and collector) to the total loss is dependant on the blading design as well as the operating condition. Despite the difference in design intents and styles, the same trend was observed in terms of loss breakdown and mechanisms for both stages investigated, over a wide operating range. In particular, the loss generated in the exhaust hood surpassed that in the blade passages at around 60% mass flow rate. Therefore, both the blading and exhaust hood should be carefully designed to minimise the entropy generation inside the exhaust hood, should the system be expected to operate frequently at part-load.

Detailed flow visualisations (2-D and 3-D streamlines) of the CFD results revealed key flow features in the exhaust hood, namely the bearing cone separation and passage vortex, the relative strength of which were dependant on the operating condition. As the flow rate reduced, the asymmetry and the size of the passage vortex grew, which created larger blockage at the hood exit and reduced pressure recovery level; at the same time, the bearing cone separation size also grew, further increasing blockage and loss.

Local entropy generation rate was used to pinpoint the sources of loss. At high flow rate, the loss was dominated by the mixing between the tip leakage jet and the main flow, as well as mixing through the passage vortex that travelled downwards to the condenser neck. At low flow rate, the strength of the leakage jet and the passage vortex weakened, whilst the bearing cone separation intensified and occupied a greater volume, leading to increased levels of entropy generation.

Restaggering the last stage rotor blade near the hub is an effective way of adjusting the spanwise flow profile at the stage exit, which can be designed to be more favourable for the exhaust hood. Stage A benefited more from opening the hub section, through an increase in system efficiency of 1.5% at 70% flow rate. With full optimisation, further improvement should be expected. Stage B did not enjoy as much improvement due to the higher swirl level and lower total pressure at the hub for the baseline design. Further redesign would be required for Stage B to achieve better part-load performance.

Last but not least, restaggering the rotor blade is just one of the ways to improve system performance. Other methods such as re-cambering the rotor blade sections (*i.e.* re-distributing blade loading along the span) and 3-D stacking of stator blade ([30, 31]) shall be the candidates in future work. It is important to bear in mind the ultimate goal, which is to improve the performance of the entire system rather than individual components.

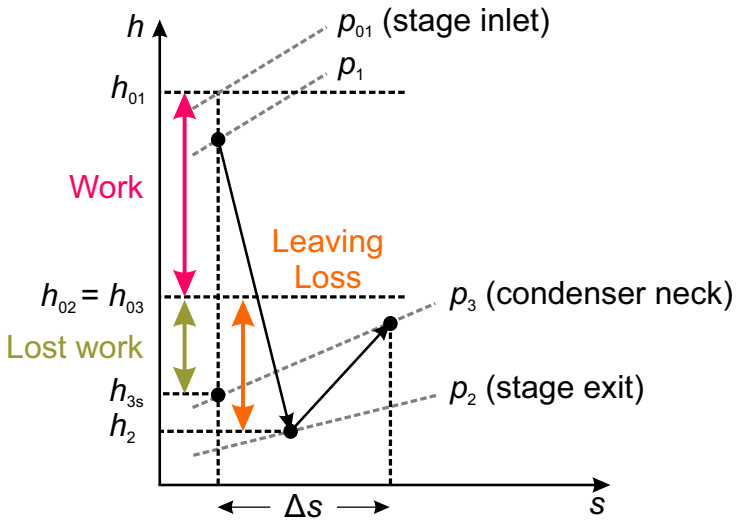

Fig. 5.1 Thermodynamic process in an LP exhaust system

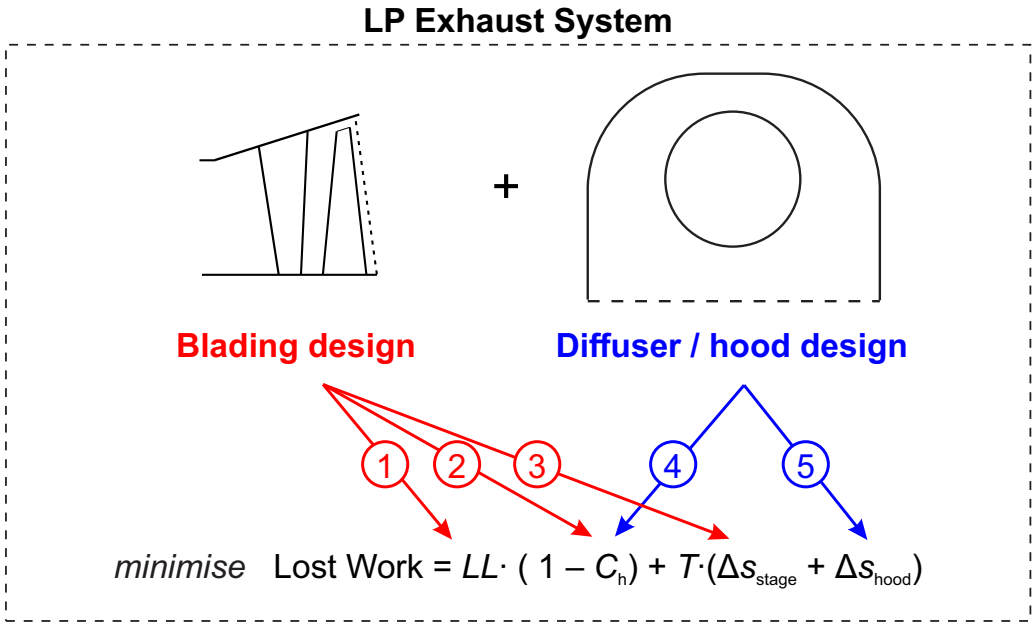

1. Minimise stage exit leaving loss
2. Provide favourable inlet flow profile for the diffuser
3. Minimise entropy generation in the last stage
4. Suitable choice of diffuser / hood design parameters
5. Minimise entropy generation in the diffuser / hood

Fig. 5.2 Interaction mechanism in an LP exhaust system

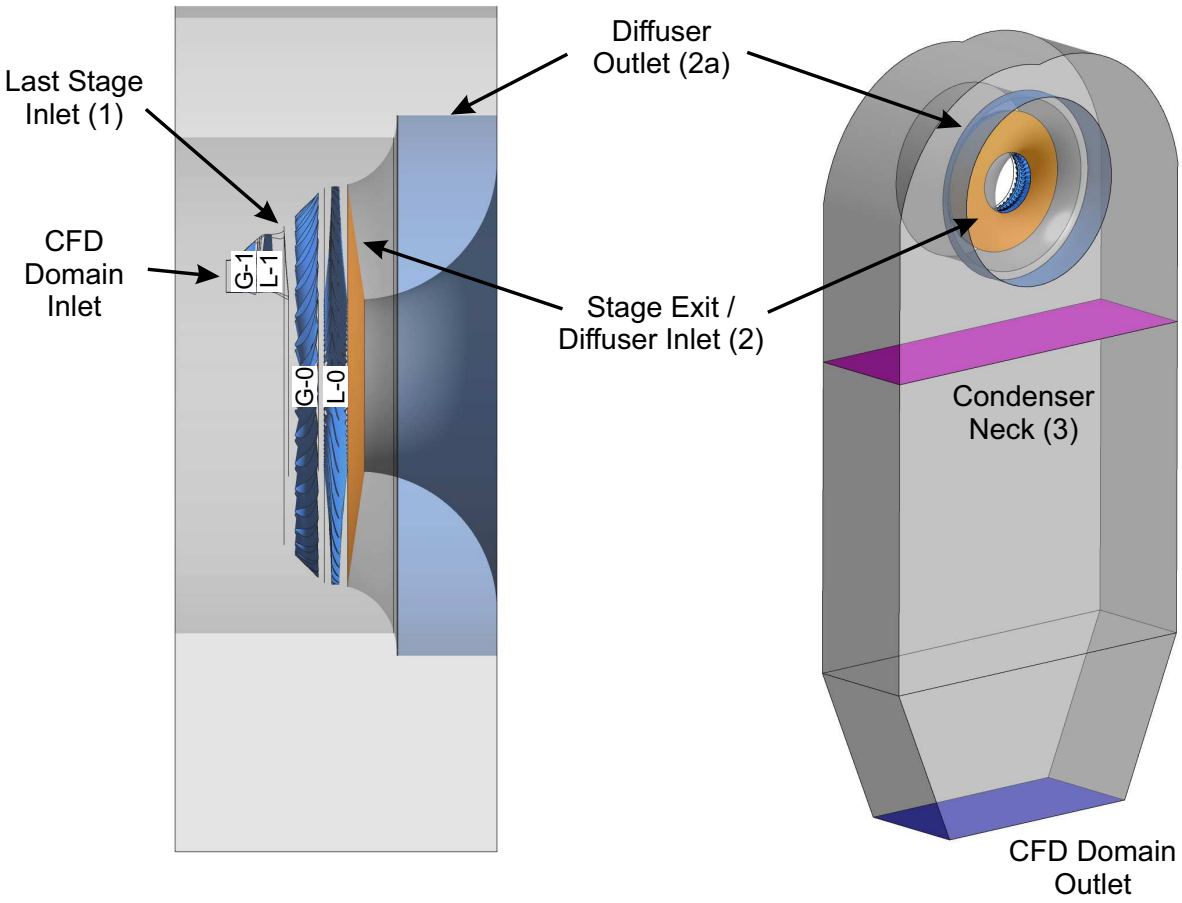

Fig. 5.3 CFD setup for Stage B. Left: side view. Right: 3-D view

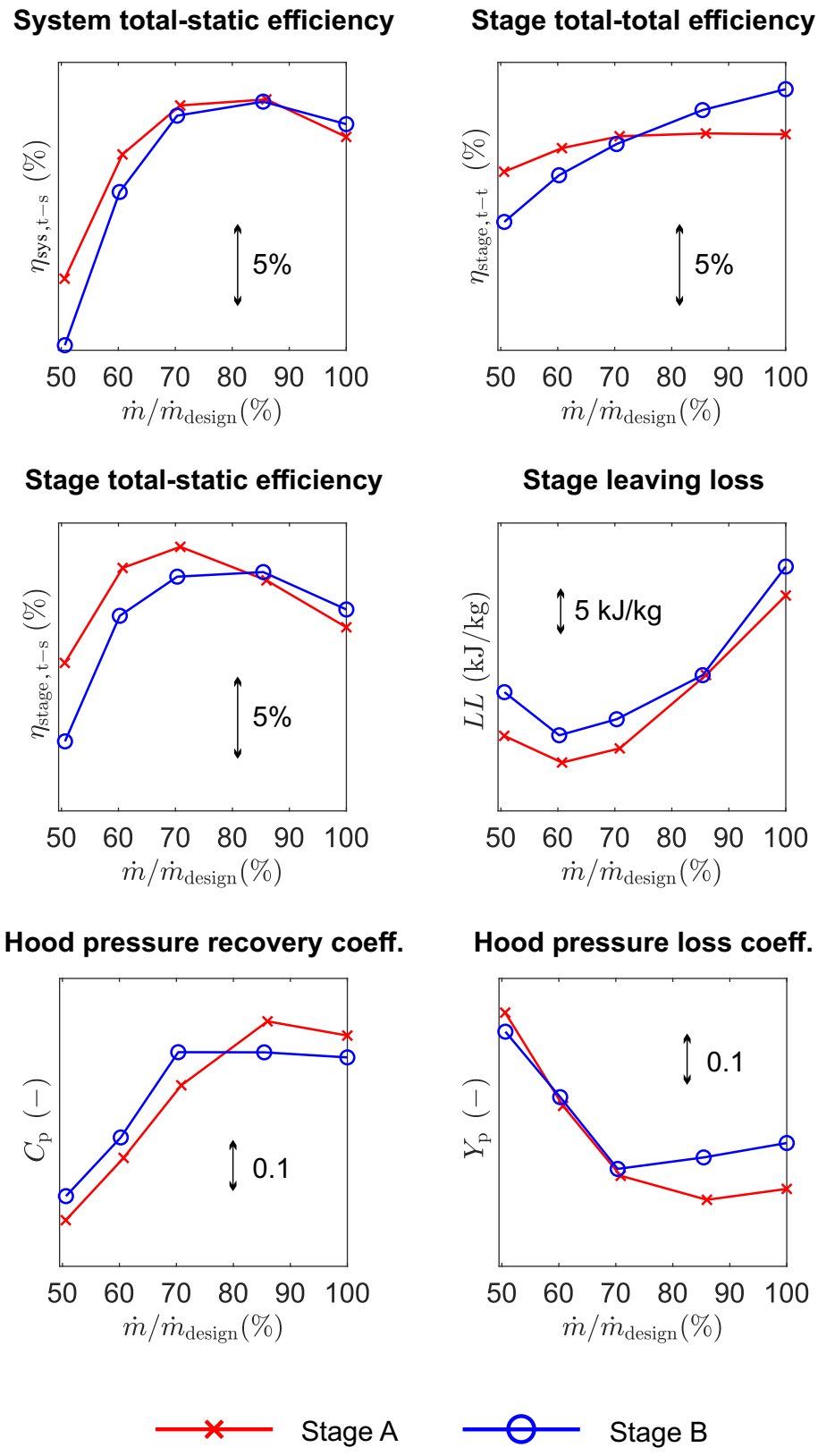

Fig. 5.4 1-D performance metrics for baseline Stage A (red) and Stage B (blue) against mass flow rates

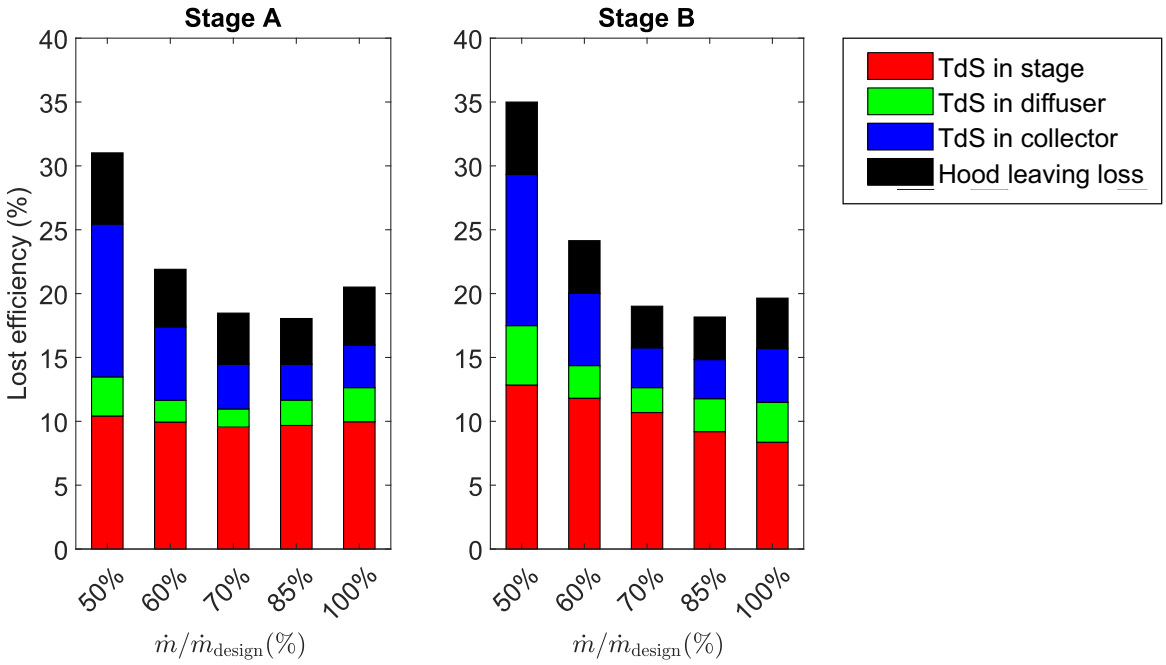

Fig. 5.5 Exhaust system loss breakdown for baseline Stage A (left) and Stage B (right)

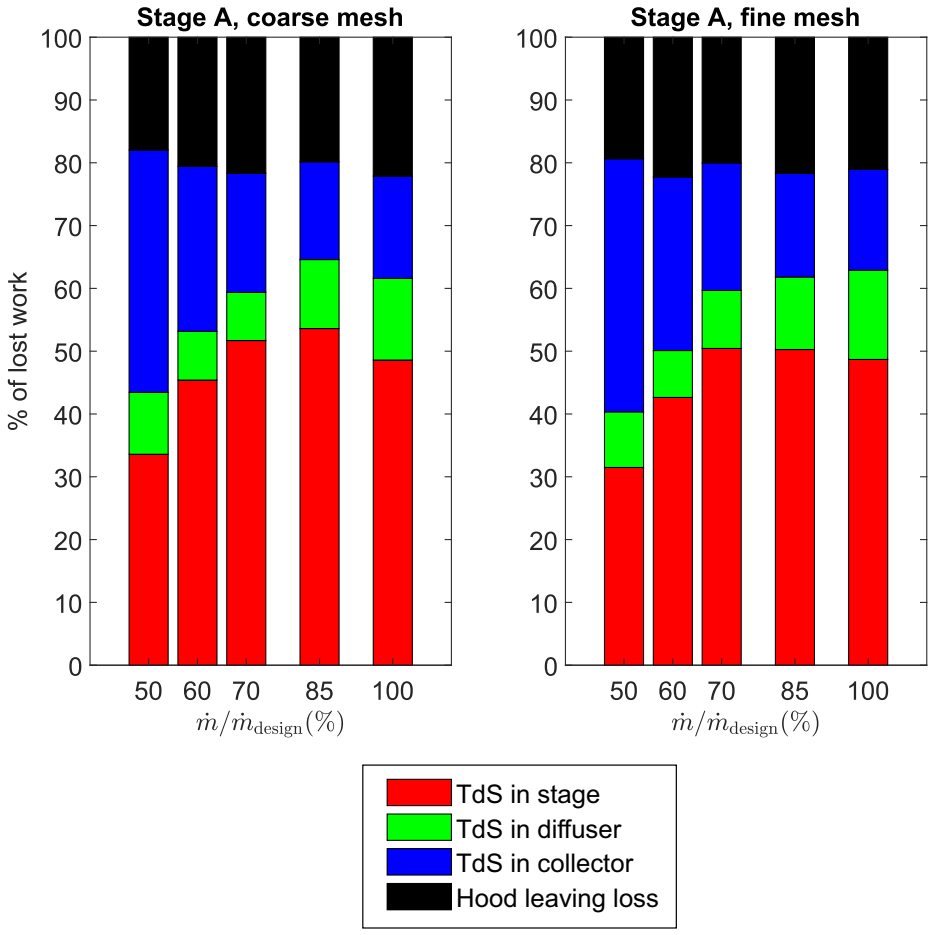

Fig. 5.6 Contributions to total lost work by various components for Stage A using coarse (left) and fine (right) mesh sizes

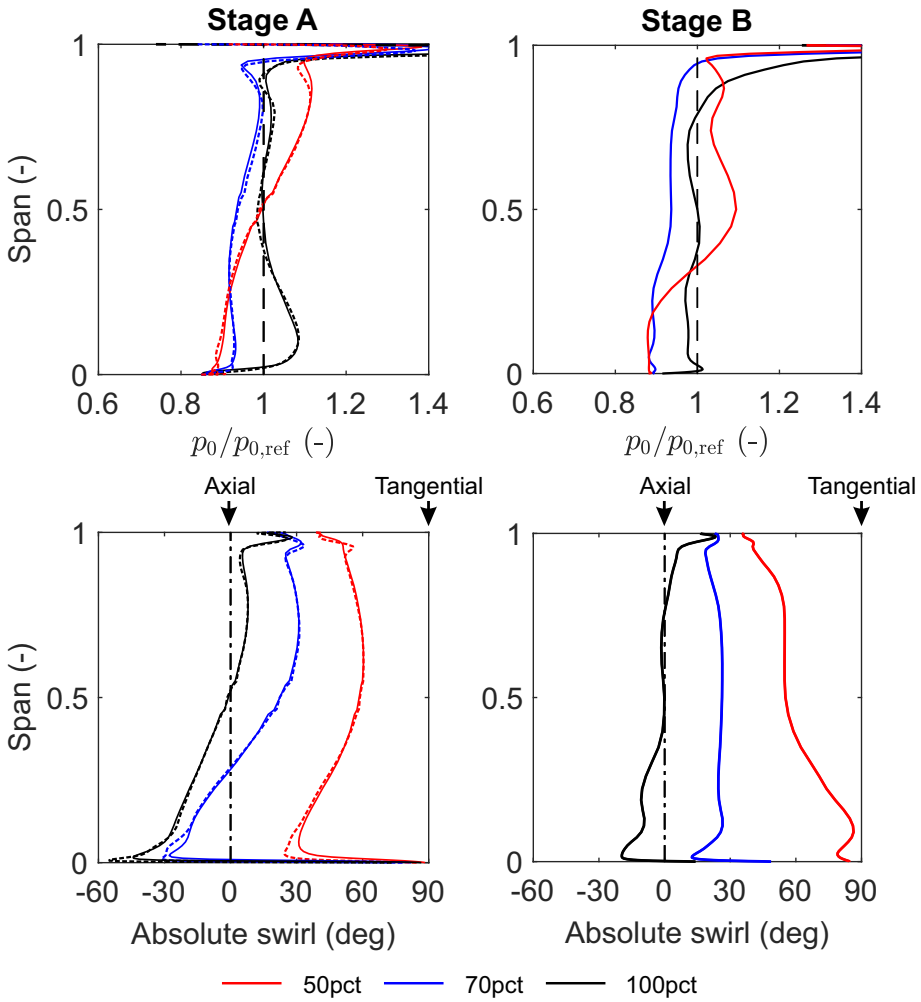

Fig. 5.7 Stage exit spanwise flow profile for Stage A (left) and Stage B (right). Top: total pressure scaled by $p_{0,\text{ mid-span}}$ at design flow rate. Bottom: absolute swirl angle. Dashed: fine mesh for Stage A only

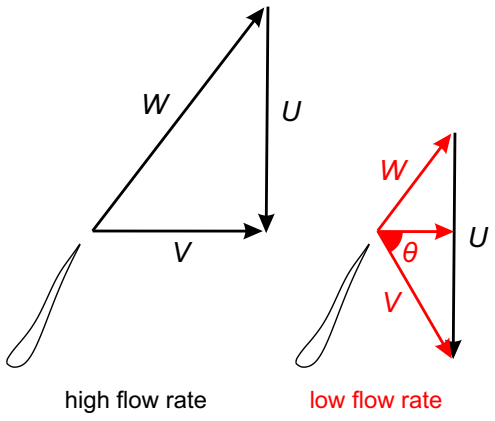

Fig. 5.8 Velocity triangle of the blade section at mid-span (meanline analysis)

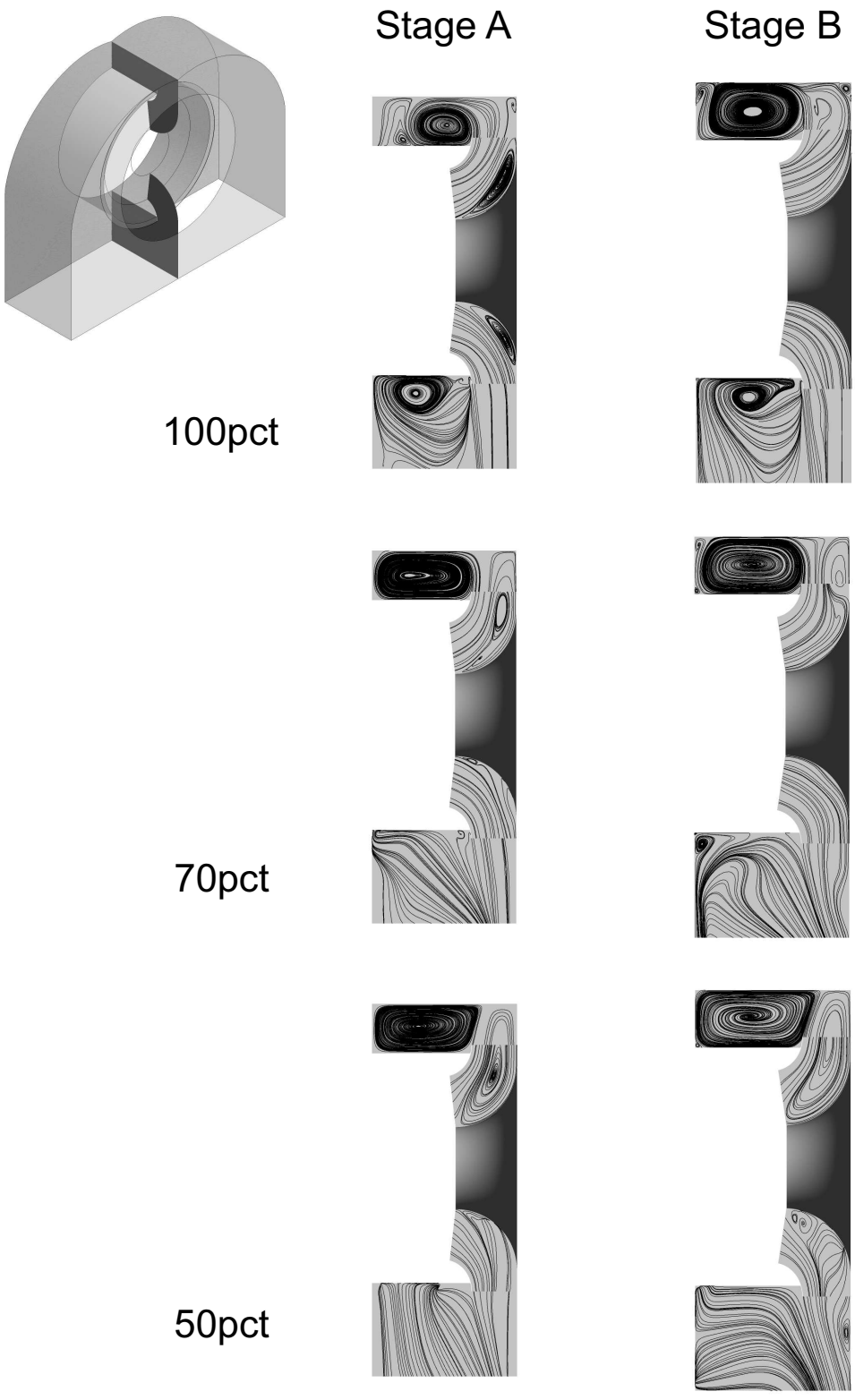

Fig. 5.9 Meridional streamlines of the exhaust hood at various flow conditions

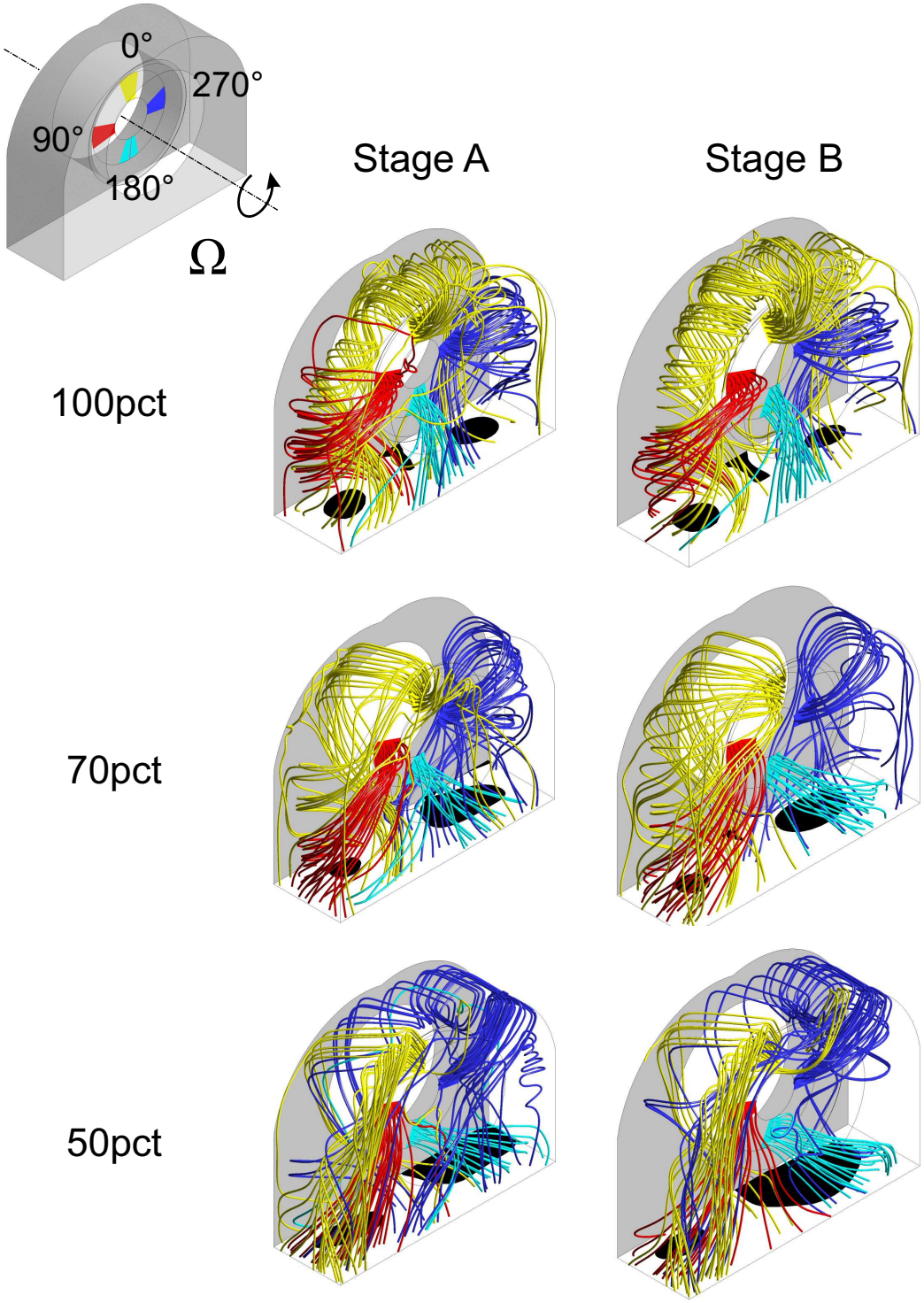

Fig. 5.10 Streamtubes originating from different sectors at diffuser inlet, with black regions indicating blocked area at the hood exit of Stage A (left) and Stage B (right)

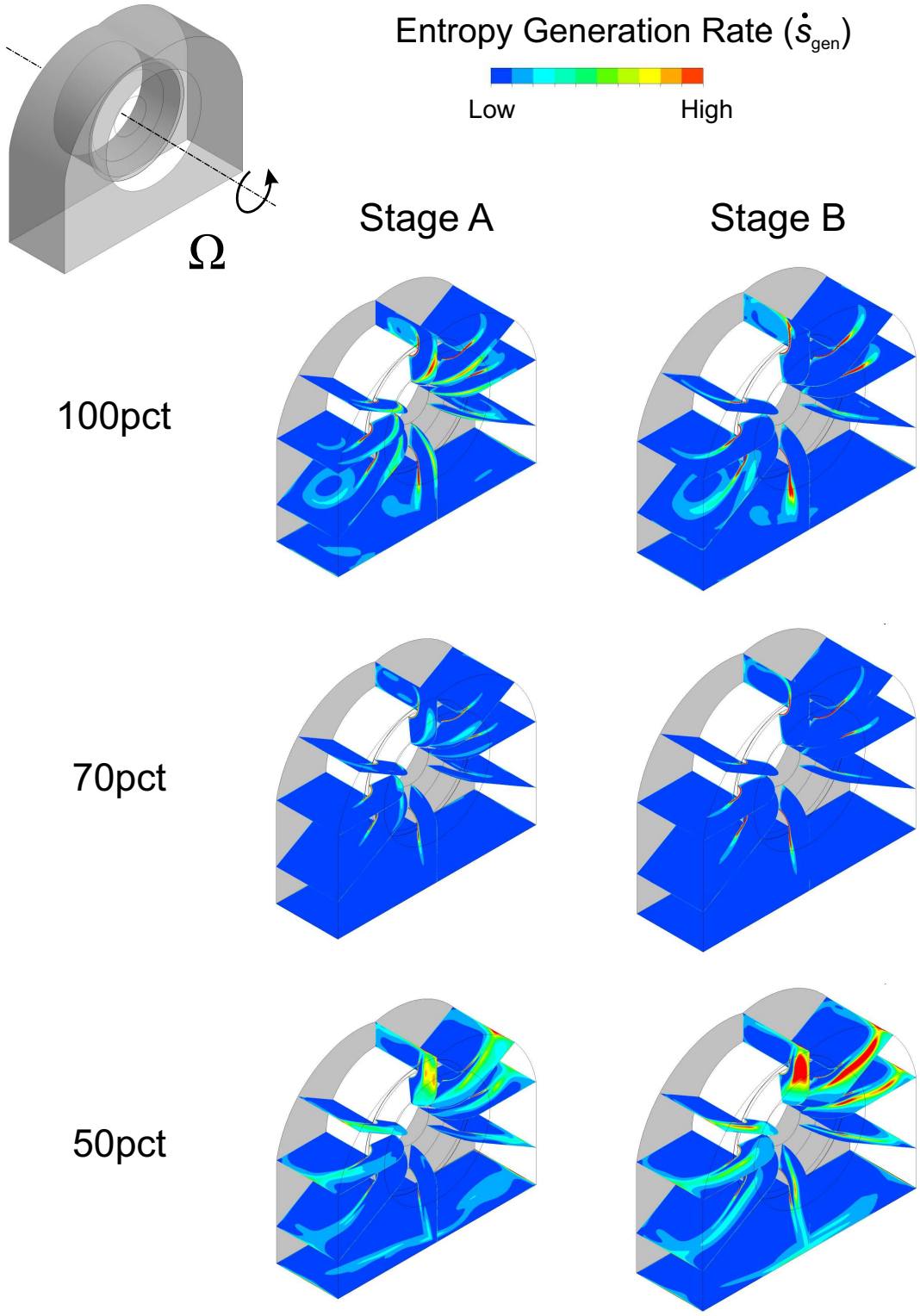

Fig. 5.11 Contours of entropy generation rate for Stage A (left) and Stage B (right) at various flow conditions

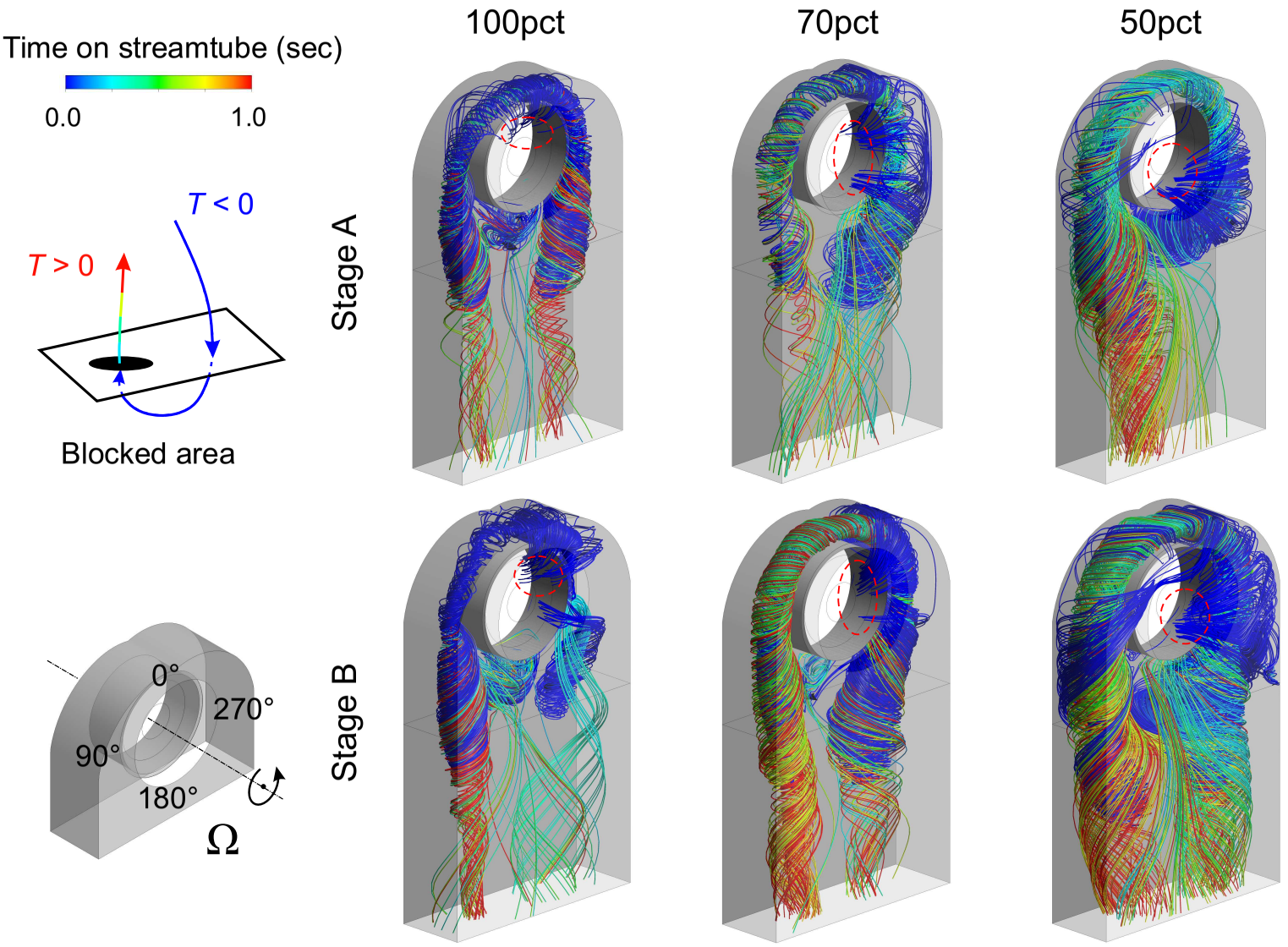

Fig. 5.12 Streamtubes originating from and ending at the blocked area (in black) at the condenser neck for Stage A (top) and Stage B (bottom). Note the downward extension is included. Colours refer to the time (clipped to $0-1$ sec) on the streamtubes, with blue colour meaning the streamtube has not arrived at the blocked area yet

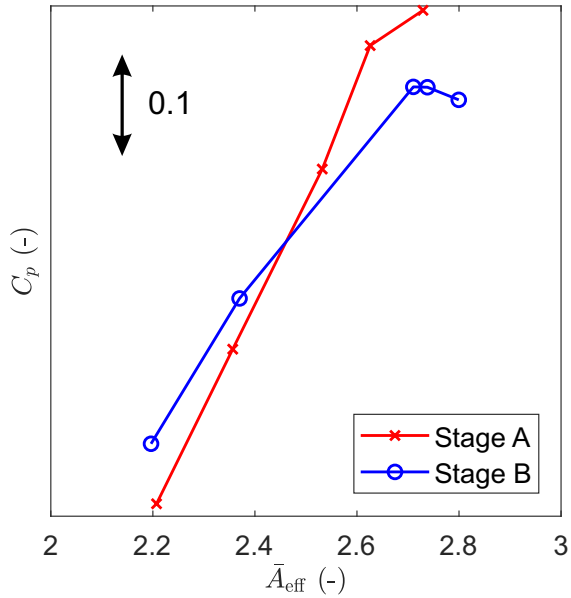

Fig. 5.13 Static pressure recovery coefficient against effective exhaust area ratio

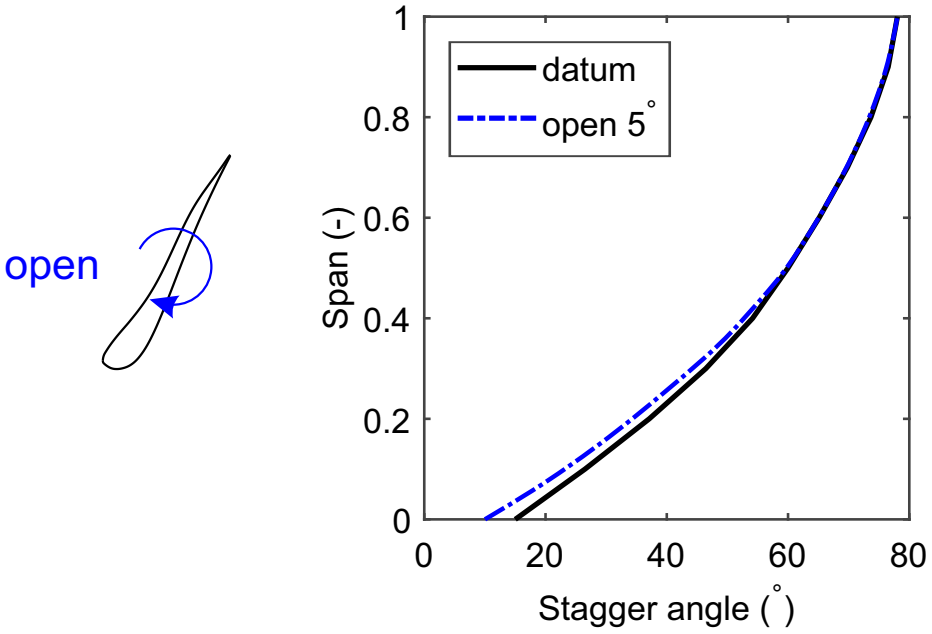

Fig. 5.14 Rotor blade stagger angle variations for Stage B

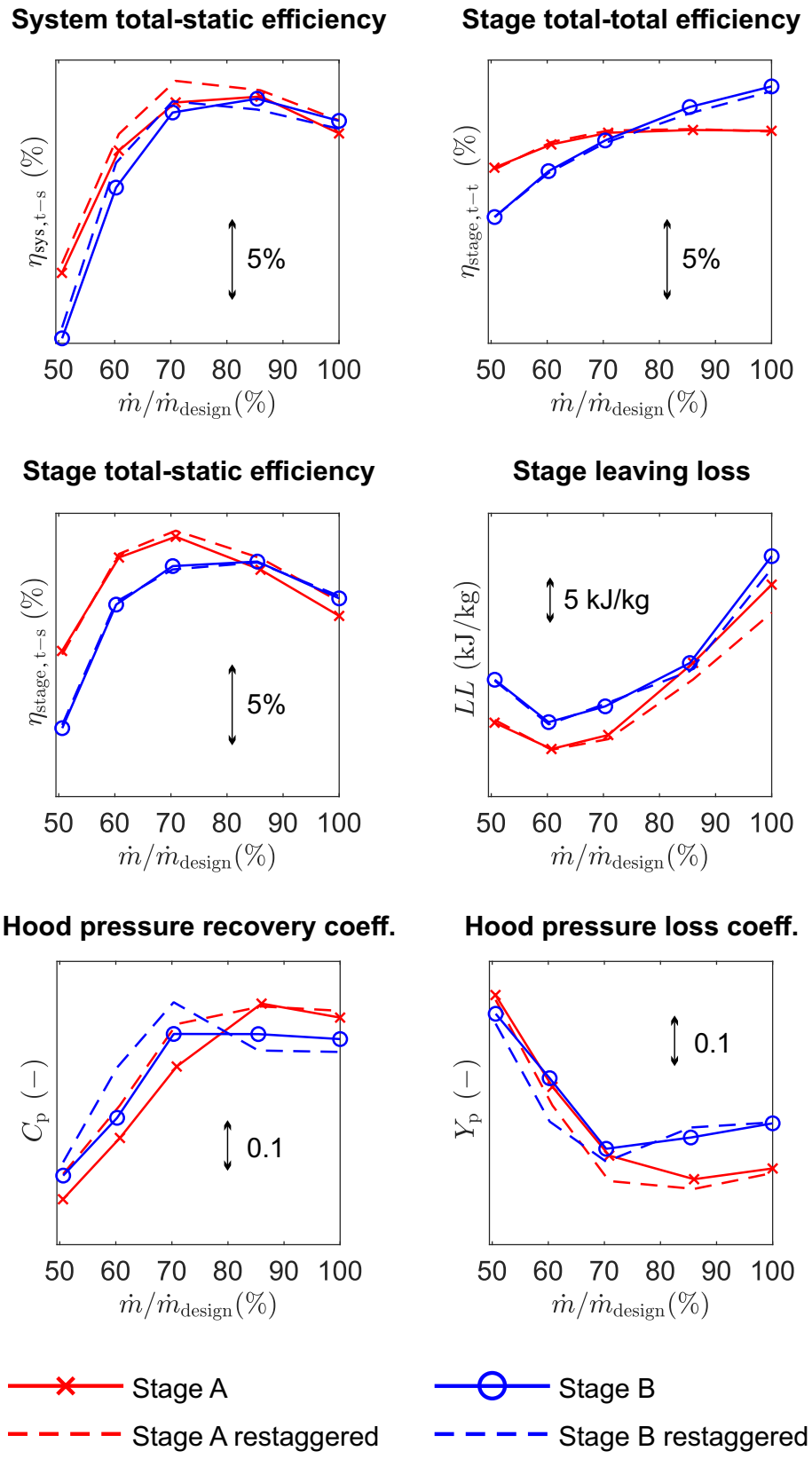

Fig. 5.15 1-D performance metrics for Stage A (red) and Stage B (blue). Solid: datum geometry. Dashed: rotor blade hub section opened by 5°

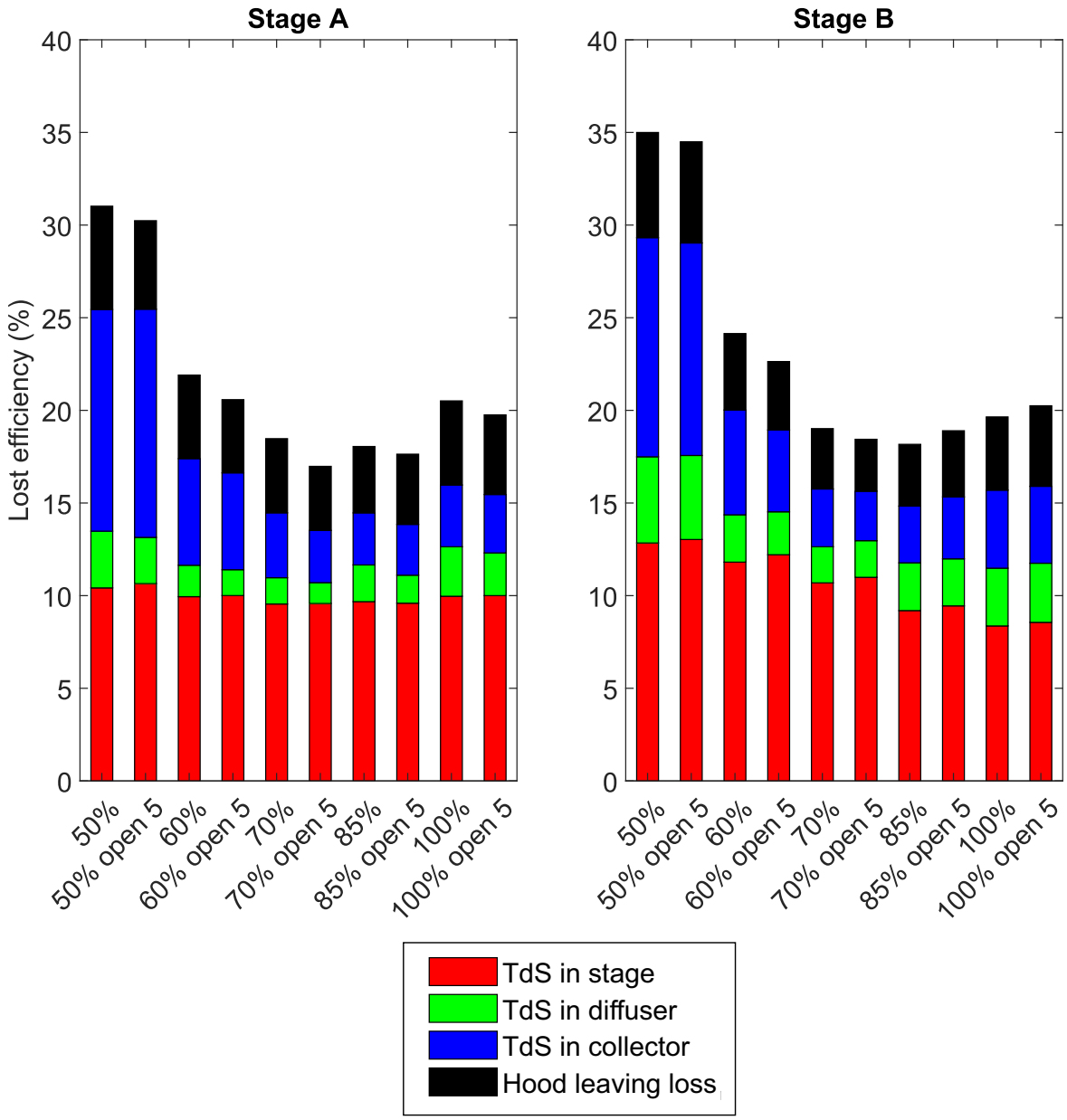

Fig. 5.16 Exhaust system loss breakdown for Stage A (left) and Stage B (right) with datum and redesign (hub section opened by 5°) rotor blades

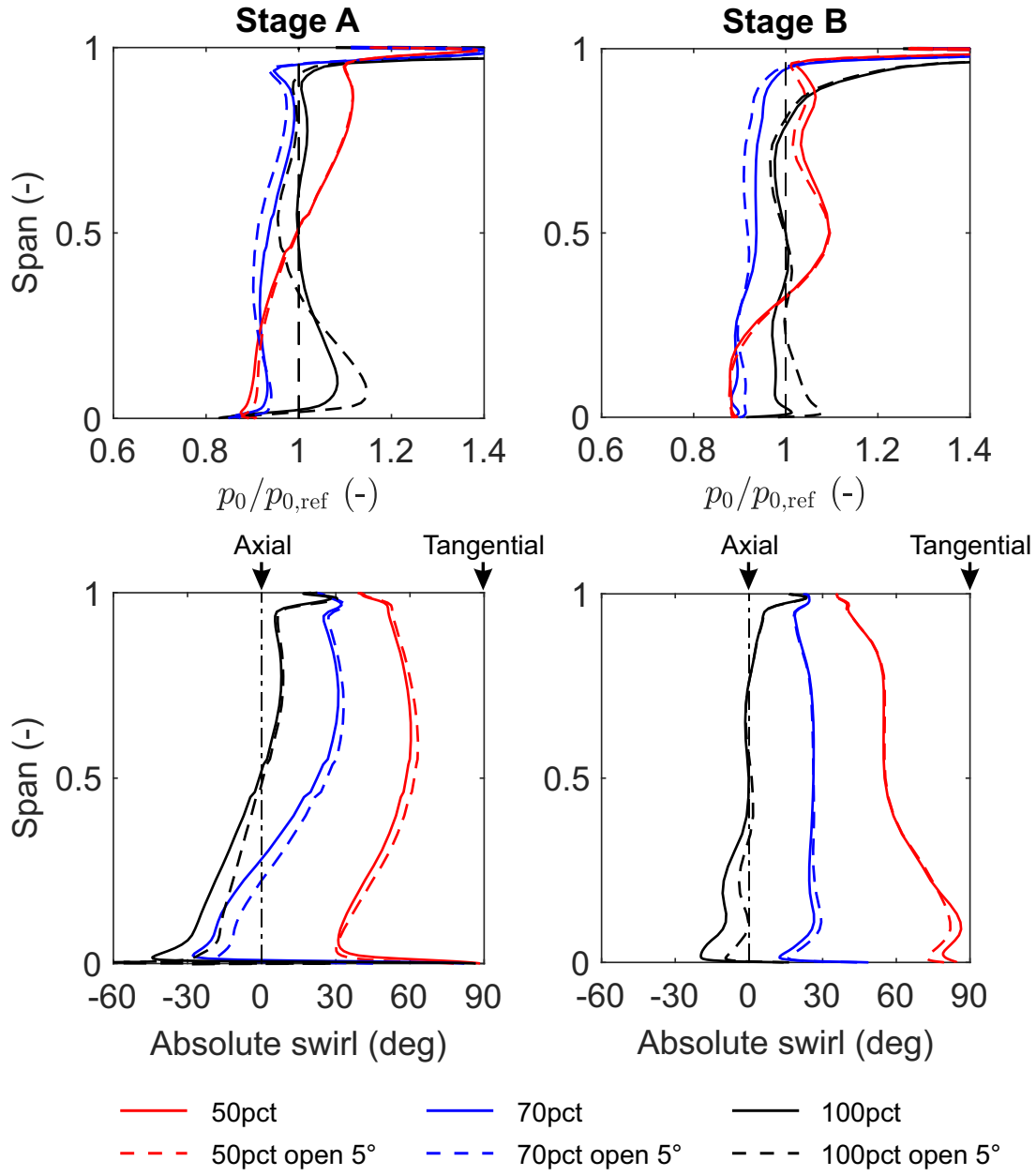

Fig. 5.17 Stage exit spanwise flow profile for Stage A (left) and Stage B (right) with datum (solid) and restaggered (dashed) rotor blades. Top: total pressure scaled by $p_{0,\text{ mid-span}}$ at design condition. Bottom: absolute swirl angle

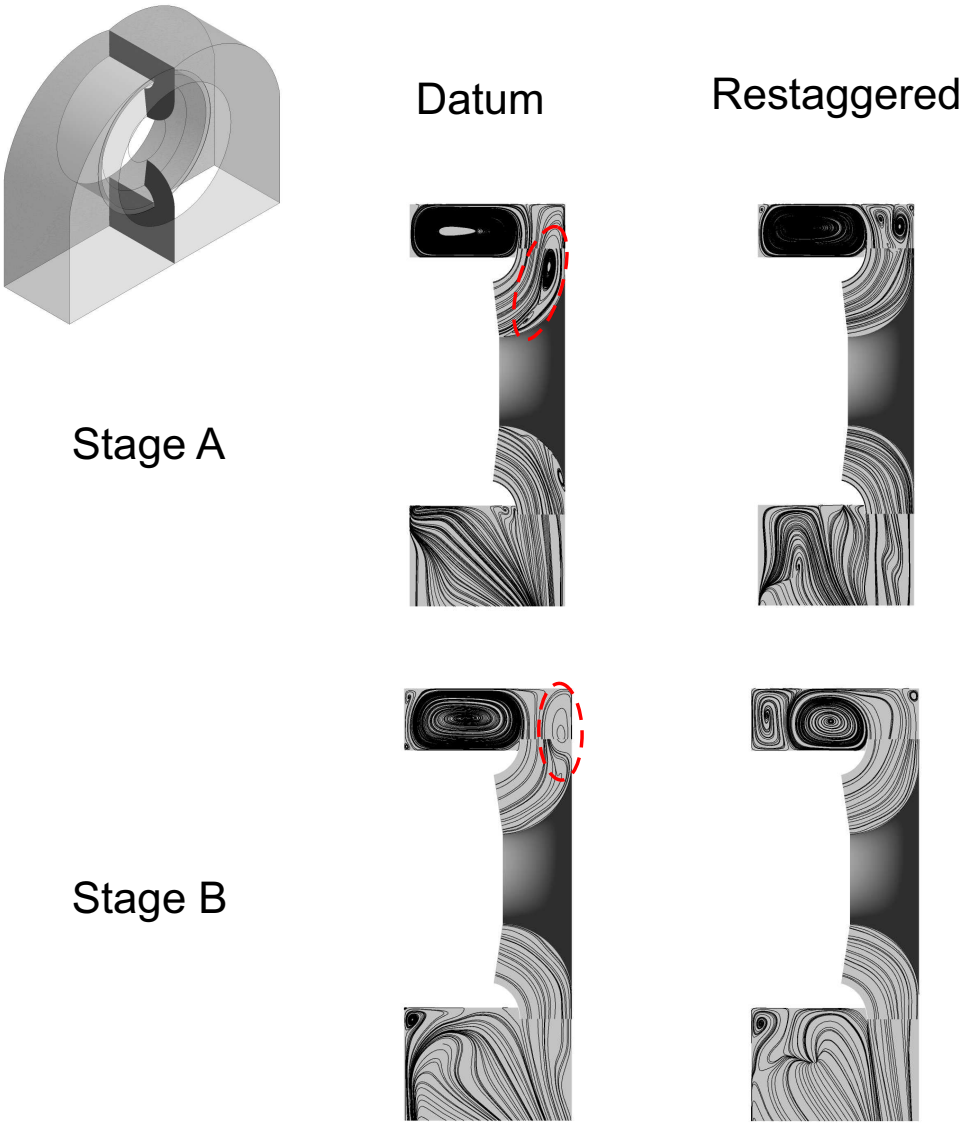

Fig. 5.18 Meridional streamlines of the exhaust hood with datum (left) and restaggered (right) rotor blades at 70% mass flow rate

Chapter 6

Dimension Reduction of the Exhaust Hood Parameter Space

In Chapter 4, different treatments of stage-hood interface were compared. The "Multiple Mixing Plane" method was shown to be capable of simulating circumferentially non-uniform flow inside the exhaust hood with much reduced computational cost (approximately five times lower cost than full annulus Frozen Rotor simulations). This chapter will discuss the effort made to further speed up the design cycle through dimension reduction of the exhaust hood parameter space.

There are many design parameters to consider when determining the exact shape of the exhaust diffuser or hood. For researchers, the "curse of dimensionality" prohibits comprehensive studies into the effect of parameter variation and hence the construction of response surfaces [15]. For design engineers, high dimensionality leads to a longer design cycle and is thus economically unfavoured. It is important, therefore, to reduce the dimension of the parameter space whilst still attaining near-optimum geometry.

As an example, this chapter details the reduction of the parameter space dimension of the exhaust diffuser flow guide (*i.e.* the outer casing), using the concept of "Minimum Energy Curves" (MEC), which minimises the overall curvature distribution along the flow guide. Compared to optimised flow guides parametrised by the state-of-art cubic Bezier curves, MEC-based flow guides perform similarly well, whilst reducing the computational cost by up to 100 times. Such cost saving shortens the design cycle, and makes the generation of diffuser performance maps and optimisation possible within reasonable time.

Moreover, analysis of the flow field near the flow guide provides insight into the effect of geometric properties (curvature distribution) on the aerodynamics in LP exhaust diffusers. The presence of the rotor tip leakage jet was also found to have a strong impact on the optimised shape of the flow guide, which must be taken into account in numerical simulations.

6.1 LP exhaust diffuser flow guide

A flow guide refers to the outer casing of the exhaust diffuser in an LP exhaust system. It is used to guide the flow from an axial to a radial direction within a short distance, typical axial length being less than half the last stage blade height.

Throughout the literature, the axi-symmetric flow guides are often parametrised in two ways. They can either be a combination of straight lines and/or circular arcs when viewed in the meridional plane (Fig. 6.1), or be parametrised using cubic Bezier curves, as shown in Fig. 6.2. For the latter, a greater flexibility is allowed when controlling the amount of turning through the flow guide, although two control points are required to fully define the curve, which makes optimisation expensive and unsuitable for normal design cycles.

On the convex downward surface of the flow guide, a diffusing flow is susceptible to separation. The diffuser performance drops considerably should such separation occur and hence requires careful design [40]. Although extensive experimental studies have been carried out for exhaust diffusers [70, 19], most of them have not considered the presence of the upstream stage and its effect on the downstream diffuser. For unshrouded rotor blades, in particular, the leakage jet over the rotor tip contains high momentum which can energise the boundary layer flow near the flow guide and delay separation. The effect of tip leakage jet on the optimised flow guide shape will be presented in Section 6.4.

6.2 The importance of curvature control for flow guide

It is well known, through theoretical and experimental investigations [42], that the curvature distribution of aerodynamic shapes has a strong impact on boundary layer development and aerodynamic performance. For the diffuser flow guide especially, the importance of curvature control can be explained by the radial equilibrium equation and by learning from the geometry and flow features of Controlled Diffusion Airfoils (CDA).

6.2.1 Radial equilibrium in an exhaust diffuser

The radial equilibrium equation with streamline curvature terms (*e.g.* [20]), as illustrated in Fig. 6.3, is:

$$-\frac{1}{\rho}\frac{\partial p}{\partial r} = V_m \frac{\partial V_m}{\partial m}\sin\psi + \frac{V_m^2}{r_c}\cos\psi - \frac{V_\theta^2}{r}, \tag{6.1}$$

On the LHS of Eq. 6.1 is the pressure gradient along the radial direction r. The three terms on the RHS are the components in the r direction of acceleration along the meridional direction, acceleration due to streamline curvature, and acceleration due to swirl. In the last stage of LP steam turbines, hub-to-tip ratio is usually very low (between 0.4 and 0.5), which means the impact of the swirl term is relatively small when the region of interest is near the tip (i.e. when $r = r_{\text{tip}}$). Moreover, at the inlet of the diffuser, the streamline turning angle ψ is very low (usually below 20°), which leaves the streamline

curvature term to be the most dominant. This streamline curvature is strongly influenced by the curvature of the flow guide. As such, by reducing the curvature level (or increasing the magnitude of r_c), the negative impact on the pressure gradient due to the streamline curvature term can be reduced, which tends to prevent or delay separation.

6.2.2 Lessons from CDA

The importance of curvature control can also be illustrated by the development of CDA. For instance, in the optimised subsonic compressor airfoil designed by Köller et al. [41], the blade is front loaded and quickly turns the flow close to the leading edge, followed by slow turning and diffusion towards the trailing edge in a controlled fashion. This can be seen in the isentropic Mach number plot in Fig. 6.4. The suction side peak Mach number of the optimised profile moves upstream compared to the starting profile. Furthermore, the boundary layer shape factor on the same surface remains close to, but stays below, 2 after the transition point. This is considered to demonstrate good balance between maintaining low surface shear stress while keeping the flow attached.

Such a healthy boundary layer integral parameter distribution is achieved by a sharp turning near the leading edge (the curvature being below –5 m^{-1}) followed by a monotonically decreasing curvature (in magnitude) until the middle of the chord, which then stays more or less constant towards the end. This idea of monotonically decreasing curvature will be shown to have importance when considering the flow guide design and the control of boundary layer separation.

6.3 Minimum energy curves

To control the curvature distribution of a flow guide, a parameterisation of its geometry is needed. For CFD optimisations performed in the literature, cubic Bezier curves have been the most popular choice which involve at least two control points and five design parameters (see Fig. 6.2), with the bearing cone shape kept fixed. Although this provides a flexible way to generate geometries, it is still computationally expensive. The present study aimed to seek a functional form of the curve which minimises its overall curvature distribution, cumulative over the whole arc.

The idea for the method used in this study originates from work in computer graphics [37], for which the objective was to maximise the smoothness of a two-dimensional curve $\mathcal{C}$ with constraints on the coordinates and the slopes at the two endpoints. To quantify the level of smoothness, the strain energy of a curve, $\mathcal{E}$, was first used as the cost function of the optimisation problem. It was simply the square of the curvature integrated along the whole curve [37]. Later, a modified, non-dimensional strain energy was introduced [9] and this was used in this study. Here, $\mathcal{E}$ is the total arc length multiplied by the integral

of curvature squared:

$$\mathcal{E} = L \cdot \int_{\mathcal{C}} \kappa^2 ds \tag{6.2}$$

The fact that the strain energy defined in Eq. 6.2 is non-dimensional means MEC can be scaled without changing the level of smoothness, and be applied in generic forms [9]. Moreover, it allows one to take total arc length L to be unity, so that this strain energy takes the same form as in the original work [37]. The derivation of the analytical solution using Euler-Lagrange formulation may be found in Horn's original paper [37] and is thus not included here. The functional form of the curve of least energy is:

$$\psi'(s) = \pm\sqrt{A\sin\psi + B\cos\psi} \tag{6.3}$$

where $\psi(s)$ is the angle relative to the axial direction when the arc length is s, and $\psi'(s)$ is, by definition, the local curvature. From here onwards, only the positive sign in Eq. 6.3 is retained since the flow guide shape is always in an upward concave fashion. The two constants of integral, A and B, are to satisfy the boundary conditions imposed by the end points' coordinates and slopes. If $\psi(0) = 0$, *i.e.* the initial slope of the curve is zero, the kink angle vanishes in Fig. 6.5 and we have:

$$\psi'(0) = \sqrt{B} \tag{6.4}$$

which means B controls the initial curvature level if the slope of the curve is continuous at the beginning ($G1$ continuity). The effect of A will be explained later.

It was shown in the original work that Eq. 6.3 can be solved after being converted to an elliptic integral form [37]. Simple as it seems, the elliptic integral is of little practical use if one wishes to obtain the shape of the entire curve. Instead it is proposed to use the accompanying look-up table method: the shape of the curve $\psi(s)$, along with its effective aspect ratio ($AR = H_{\text{eff}}/L_{\text{eff}}$ - see Fig. 6.5) and the total turning angle ($\Delta\theta = \theta_1 - \theta_0$) for given values of (A, B), are computed and stored in a database. To find the shape of the MEC for given AR and $\Delta\theta$, one can simply look up the database using whichever interpolation method is desired.

In Fig. 6.6 a sample database is illustrated with contours of $\Delta\theta$, AR and $\mathcal{E}$. Note that for a given B, there exists a lower bound for A, the calculation of which can be found in [22]. Normally there is no upper limit for A. However, to avoid a monotonically increasing curvature, which is aerodynamically undesirable, one should select a less positive or even negative A based on the form of Eq. 6.3.

Compared to cubic Bezier curves that require at least five design parameters, MEC only need three: the coordinate (x, r) of the end point (which can be fixed by the diffuser area ratio A_1/A_0, and the flow guide's height ratio H_{dif}/L_0) and the total turning angle $\Delta\theta$. From a designer's point of view, a saving of two design parameters would significantly reduce the time and effort of a typical design cycle. Moreover, the geometry generation of

MEC-based flow guides can still be quite flexible: for a given AR, one can travel along its contour in Fig. 6.6 by varying A or $\Delta\theta$, and obtain different curvature distributions. As an example, the blue and red symbols in Fig. 6.6 both lie on the $AR = 0.8$ contour, but have different levels of turning (by 15°) and curvature distributions, as shown in Fig. 6.7. The curve with less turning ($\Delta\theta = 65°$) is featured with a monotonically decreasing curvature, and almost 30% reduction of the strain energy.

6.3.1 Numerical setup

The effects of MEC must be numerically checked to demonstrate its effectiveness and flexibility. Two types of steady simulations were used in the current study. The first type involved only the exhaust diffuser, as shown in Fig. 6.8. Upstream of the diffuser, it was extended by $0.1L_0$ to allow for some boundary layer development. A uniform total pressure and total enthalpy distribution was specified at the domain inlet, with no swirl and linearly varied pitch angle, based on the angles at the hub and casing. The stagnation quantities at the inlet were the averaged values at the last stage exit for a typical 1000 MW steam turbine at design condition. The second type of simulation replaced the upstream extension with the last stage to account for stage-diffuser interactions, with the presence of a tip leakage jet over the last stage rotor blades. This type of simulation will be discussed in Section 6.4.

In all simulations, the diffuser exit was extended radially by a length $L_2/L_0 \approx 4$, and the cross-sectional area reduced to the diffuser's inlet area A_0 at the exit, so that reverse flows at the CFD exit were avoided. An average static pressure was specified at the exit. 80 cells were used in the spanwise direction of the diffuser, with y^+ between 2 to 5 on the flow guide surface. The grid expansion ratio was kept under 1.2 everywhere inside the diffuser domain. For a 4° segment of axi-symmetric diffuser, around 200,000 grid points were considered an acceptable balance of grid quality and computational effort, given there were a large number of calculations to be performed.

6.3.2 Generating diffuser performance maps using MEC

Given the fact that the number of design parameters had been reduced (by two), the generation of the diffuser performance maps was now possible. In this study, clean flow conditions were specified at the inlet without the last stage, as described above. For each combination of (L_1/L_0, A_1/A_0), the turning angle $\Delta\theta$ was iterated (typically five times) to find the optimum diffuser with the highest pressure recovery coefficient defined as:

$$C_p = \frac{p_2 - p_1}{p_{01} - p_1} \tag{6.5}$$

i.e. the ratio of static pressure rise between diffuser inlet and outlet over its inlet dynamic head. The ranges of the design parameters used are listed in Table 6.1, which are all typical for large steam turbines.

Table 6.1 Ranges of the diffuser design parameters

Parameter	Nomenclature	Range
Axial length ratio	L_1/L_0	$1.2 - 1.7$
Diffuser area ratio	A_1/A_0	$1.2 - 1.7$
Total turning angle	$\Delta\theta$	$30 - 75°$

As seen in Fig. 6.9, the performance map obtained for optimum diffusers using MEC was very similar to those of the optimum conventional diffusers from experimental studies [70]. The optimum diffusers for a given length or area ratio fell within a narrow band that centred closely to the diagonal $L_1/L_0 = A_1/A_0$ (indicated by the coloured band in Fig. 6.9), based on the balance of sufficient diffusion and avoidance of flow separation. This seemed to suggest a "one for one" rule of thumb for good diffuser design.

To take a closer look at the effect of flow guide turning angle ($\Delta\theta$) on its performance, the C_p values of optimum diffusers (for which $L_1/L_0 = A_1/A_0$) are plotted (Fig. 6.10). It is first worth noting the similarity in the shape of the plots, when optimum length and area ratios were chosen. Moreover, for a given L_1/L_0, it is preferred to have a small total turning angle $\Delta\theta$, so that the overall curvature is monotonically decreasing, as indicated in Fig. 6.11 when $L_1/L_0 = A_1/A_0 = 1.4$.

Furthermore, the curvature effect could be illustrated by the flow guide's boundary layer development. The curvature distribution and the boundary layer shape factor H along the flow guide for given length ratio ($L_1/L_0 = 1.4$) and area ratio ($A_1/A_0 = 1.4$) are plotted against turning angles $\Delta\theta$ in Fig. 6.11. With a low level of turning ($\Delta\theta = 50°$) and monotonically decreasing curvature, the shape factor grew gradually to just below 2 and remained almost constant thereafter, not only delaying flow separation, but also minimising the skin friction to the maximum extent possible. In contrast, any further increase in $\Delta\theta$ resulted in earlier flow separation, indicated by the sharp increase in the shape factor. In the case where $\Delta\theta$ was slightly lower than the optimum choice ($\Delta\theta = 45°$), the shape factor started to decrease after it reached around 2.2, resulting in a performance very close to the optimum case. Nevertheless, it was felt to be safer to keep the shape factor below 2 to avoid any flow separation. The curvature and shape factor distribution for the optimum geometry appeared similar to those of the optimised CDA in Fig. 6.4, suggesting that MEC-based flow guides do perform well aerodynamically owing to the control of curvature distribution and boundary layer thickness growth.

Lastly, the performance map in Fig. 6.6, based on around 600 steady CFD calculations, took less than 3 days to generate on a 16-core workstation, which means it is now possible

to generate many such performance maps based on the operating conditions and geometric constraints *a priori*, so that designers may use them for a fast and simple estimate of diffuser sizing and performance prediction in the actual design.

6.4 Comparison with Bezier curves

The Minimum Energy Curves introduced in the previous section helped reduce the dimension of the design parameter space. It was hoped that MEC-based flow guides would perform well aerodynamically in comparison to Bezier curves. This section concerns the comparison between MEC-based flow guides and cubic Bezier curves, which are optimised with the Genetic Algorithm (GA) in MATLAB's Global Optimisation Toolbox [2].

6.4.1 Problem setup

The GA setup is summarised in Table 6.2. The parameterisation using Bezier curves was the same as in a previous study [81], except that the parameters controlling the distances, d_1 and d_2, were normalised based on the maximum distance allowed, while the flow guide end point (x, r) and the bearing cone shape were fixed by other design parameters such as the diffuser axial length ratio (L_1/L_0) and area ratio (A_1/A_0). More details regarding the Bezier curves and the control parameters (d_1 and d_2) can be found in Appendix B.

Table 6.2 Genetic algorithm parameters

GA Parameters	Range
Population size	20
No. of generations	25
Crossover fraction	0.8
Mutation rate	10%

In the author's previous study [22], the MEC and cubic Bezier curves were compared with clean flow conditions at the diffuser inlet, without the presence of the last stage. Here, it was decided that the last stage was to be included in the simulation to provide more realistic boundary conditions for the diffuser. The objective of the optimisation was the last stage specific power output (Δh_0), which was considered a more direct measure of the system performance, compared to the diffuser's pressure recovery (C_p).

Axi-symmetric simulations were performed, coupling the single passage last stage (Stage A as introduced in Section 5.2) and an axial-radial diffuser via mixing planes. A recent work by Singh [68] compared two different rotor-diffuser interface treatments (with or without mixing plane). It was suggested the mixing loss levels are similar, should it occur across the mixing plane or within the diffuser.

This study focused only on the stage and diffuser performance at design condition. At the turbine inlet, total pressure, total enthalpy and flow directions were prescribed. At the domain exit (the area of which was fixed), the averaged exit pressure was fixed for all simulations. Four parameters were varied: diffuser area ratio (A_1/A_0), total turning angle ($\Delta\theta^* = \Delta\theta/\Delta\theta_{\max}$, normalised by the maximum value allowed), and normalised lengths of the two control points (d_1 and d_2). The axial length ratio was fixed to some typical value $L_1/L_0 = 1.3$. The parameters that were varied and their ranges are summarised in Table 6.3.

Table 6.3 Parameter range for GA optimisation

Design Parameter	Nomenclature	Range
Diffuser area ratio	A_1/A_0	$1.2 - 1.7$
Normalised turning angle	$\Delta\theta^*$	$0.0 - 1.0$
Bezier curve control parameter 1	d_1	$0.0 - 1.0$
Bezier curve control parameter 2	d_2	$0.0 - 1.0$

Tip gaps, typically of $\sim 1\%$ of the blade height, existed at the top of the free-standing rotor blades, which resulted in a strong leakage jet entering the diffuser. It is known that the leakage jet energises the flow near the flow guide and delays flow separation, owing to the Coanda effect [60, 25]. This means there is a balance between improving diffuser performance (allowing aggressive flow guide turning and diffusion without separation), increasing rotor efficiency (reducing tip gap size and leakage flow rate), and reducing mixing loss between tip leakage jet and the bulk flow, as commented by Finzel et al. [24] and Burton [10]. Here, a tip gap of approximately 0.8% of the rotor blade height was used for unshrouded rotor configuration. To study the effect of the tip leakage jet, the tip gaps were removed in a second configuration. This reduced the leakage loss and increased stage efficiency, although the less energised tip flow was more likely to separate on the flow guide and hence a more gentle turning would be expected for the optimised flow guide shape.

Finally, all calculations were carried out using very coarse mesh size, with ∼0.1 million grid points per blade row and 56 cells in the spanwise direction. Selected calculations with much finer mesh size (∼1 million grid points per blade row and 80 cells in the spanwise direction) were also performed to check the effect of mesh size.

6.4.2 Results and discussions

Optimised flow guide shapes

The parameters for the respective optimised flow guides and associated performance are shown in Table 6.4. To optimise MEC-based flow guides, a coarse sweep was performed in the range of $A_1/A_0 = 1.2 - 1.7$ and $\Delta\theta = 45 - 75°$.

Table 6.4 Parameter selection for optimised flow guides

	A_1/A_0	$\Delta\theta$	d_1	d_2	% difference in Δh_0
Bezier, with tip gap	1.382	68.0°	0.119	0.259	-
MEC, with tip gap	1.4	65°	-	-	-0.09%
Bezier, no tip gap	1.245	49.7°	0.439	0.500	-
MEC, no tip gap	1.2	50°	-	-	-0.06%

The first observation from Table 6.4 is that the MEC-based flow guides performed well even compared to those parametrised using Bezier curves and optimised using GA, the difference in terms of last stage specific power output being less than 0.1%. Moreover, the choices of area ratio (A_1/A_0) and total turning angle ($\Delta\theta$) were very close for the two parametrisation methods. This suggests MEC could be used in the initial stage of "coarse" optimisation, in order to quickly determine the combination of area ratio and turning angle. Should time and computational resources permit, more detailed optimisations using Bezier curves may follow.

The effect of curvature on the diffuser performance was determined by comparing the geometric and aerodynamic features of the four flow guides listed in Table 6.4. Fig. 6.12 displays a plot of the curvature distribution along the non-dimensional arc length of the flow guides. All curves exhibit high turning at the beginning followed by slow diffusion, which is very similar to that on the suction surface of CDA in Fig. 6.4. The optimised Bezier curves have much higher initial curvature and turning. This creates a kink angle, which has previously been used to achieve better blade exit flow uniformity in the blade-diffuser interaction region [43]. For MEC-based flow guides, the mathematical form in Eq. 6.3 demands that the curvature distribution must obey the square root of sinusoidal functions, and hence does not allow sharp initial turning.

Fig. 6.13 shows Mach number contours in the meridional plane of the optimised diffusers, using either Bezier or MEC-based flow guides, with or without rotor tip gaps. The surface pressure distributions were also plotted (Fig. 6.14), where pressure was normalised by the averaged total and static pressure at the diffuser inlet.

When the rotor tip gap was present, high speed leakage jet from the rotor tip entered the diffuser and energised the flow near the flow guide so that separation was avoided, as shown in Fig. 6.13. There was also an accelerated region at the front of the flow guide due to high curvature. For Bezier curves, the peak curvature location was further upstream compared to MEC, explaining the lower static pressure near the rotor tip. Moreover, curvature starts to pick up from as early as 25% of the arc length, along with an almost flat pressure distribution afterwards, shown in Fig. 6.14. For MEC-based flow guides, there is actually a slight increase in curvature at the beginning before it falls, explaining the very high initial pressure level compared to the optimised Bezier curve, although there was continuous diffusion following the pressure drop.

When there was no tip gap, the optimised exhaust diffuser had a much smaller area ratio (≈ 1.245) and lower turning angle ($\approx 50°$) in order to delay flow separation and to reduce skin friction. For the Bezier curves, curvature only starts to increase from around 50% of the arc length, which suggests that curvature control at the beginning of the flow guide becomes more important should there be no leakage jet. The pressure distribution in Fig. 6.14 shows very similar trend between the two curves. However, MEC had a slightly lower level of pressure recovery, which was due to the lower value of diffuser area ratio (1.2) and a more aft loaded curvature distribution.

Effect of mesh size

The optimised flow guides were recalculated using a much finer mesh, with around 1 million grid points per blade row and 80 cells in the spanwise direction. Total mesh count was approximately 10 times higher than that used in the optimisation.

Fig. 6.14 shows that, although the level of pressure coefficients only shifted upwards slightly, the overall trends were in good agreement between coarse and fine meshes. Table 6.5 summarises the difference in last stage specific power output for both mesh sizes.

Table 6.5 Performance comparison for optimised flow guides

	% difference in Δh_0 (coarse mesh)	% difference in Δh_0 (fine mesh)
Bezier, with tip gap	-	-
MEC, with tip gap	-0.11%	-0.09%
Bezier, without tip gap	-	-
MEC, without tip gap	-0.01%	-0.06%

When tip gaps were present, the predicted percentage differences in Δh_0 were very close (-0.09% for coarse mesh and -0.11% for fine mesh), although the wavy pressure distributions on the flow guide were different. When there was no tip leakage jet, the viscous effect on the flow guide dominated, and the pressure distribution for MEC-based flow guides seemed to be more sensitive to mesh resolution. This may explain the bigger difference in the predicted performances of the two types of flow guide (-0.06% for coarse mesh and -0.01% for fine mesh). Nevertheless, the coarse mesh was found to be able to provide a good prediction of the relative merit between different geometries and the correct trend in surface pressure distributions, and was therefore considered appropriate for optimisation purposes.

Effect of curvature distribution on diffuser performance

A simple parametric study was also performed with regard to the choice of Bezier curve control parameters, d_1 and d_2, in order to understand what kind of curvature distribution

is preferred, and how MEC-based flow guides compare with all the Bezier curves. To do so, d_1 and d_2 were varied in the range of [0.05, 0.95] in steps of 0.05, so that 100 calculations were performed in each 2-D sweep. L_1/L_0 was again fixed at 1.3. The combination of $(A_1/A_0, \Delta\theta)$ was fixed at (1.4, 65°) when there was a tip gap, and at (1.2, 50°) when there was no gap.

In order to find out the effect of curvature distribution on diffuser performance, contour plots were produced in Fig. 6.15, of percentage change in last stage power output (relative to the optimised MEC-based flow guide) and the non-dimensional strain energy that was defined in Eq. 6.2. The difference in specific power output between the worst flow guide and the MEC-based flow guide was around 0.5% when there was no tip gap, and over 1.5% when there was tip gap.

Firstly, it is evident that the MEC-based flow guides outperformed all Bezier curves tested, when the same area ratio and total turning angle were chosen for both parametrisation methods. Moreover, without the tip gap, the best performing Bezier curves had lower levels of strain energy $\mathcal{E}$, *i.e.* the overall curvature distribution. These curves, in terms of (d_1, d_2) coordinates, were situated below the diagonal in the bottom left subplot in Fig. 6.15. With the presence of rotor tip gaps, the optimum region lies closer to the origin in the d_1-d_2 plane, although curves below the diagonal still have relatively good performance.

Absolute Mach number contour plots were generated for selected designs (A, B and C as indicated in Fig. 6.15) with and without tip gaps in Fig. 6.16 and Fig. 6.17 respectively. It is clear that when the overall curvature level was controlled (MEC and design A), flow separation could be avoided even without the tip leakage jet. For design B, the very large initial kink angle induced flow separation despite the tip leakage jet, and resulted in over 1.5% reduction in power output. Finally, the very high turning in the middle of the flow guide for design C resulted in a shock-induced boundary layer separation, which was suppressed by the tip leakage flow to some extent.

6.5 Concluding remarks

This chapter detailed how the concept of Minimum Energy Curves (MEC) could be used to help reduce the dimension of the exhaust diffuser parameter space and to control the overall curvature distribution of the flow guide for good aerodynamic performance.

Compared to the state-of-art cubic Bezier curves, the method used here had two fewer design parameters, allowing for a quick generation of flow guide geometry. The remaining control parameters such as $(AR, \Delta\theta)$ have clear physical and geometrical meanings and are thus easy to use. It is also possible to generate diffuser performance maps within reasonable time, thanks to the reduced parameter space dimension.

The simplicity of the method does come at a price. The optimised Bezier curves still outperform MEC-based flow guides, owing to a sharp turning and high level of curvature at

the diffuser inlet, a feature that can be found in CDA profiles. The MEC-based flow guide is relatively inflexible given its functional form derived from mathematical optimisation. Nevertheless, the method is still recommended in the initial design stage, so that key design parameters can be quickly determined at a much lower cost.

Finally, the rotor tip arrangement (unshrouded or shrouded) must be taken into account in numerical simulations, given its impact on the flow field and performance of the diffuser. Further, according to Musch et al. [80], the interaction between the tip leakage jet and the flow guide has an impact on the mechanical integrity of the last stage rotor blade. A balance therefore needs to be struck between improving diffuser performance and suppressing the "diffuser humming effect" due to self-excited shock oscillations. This was beyond the scope of this study, but will become relevant in future work.

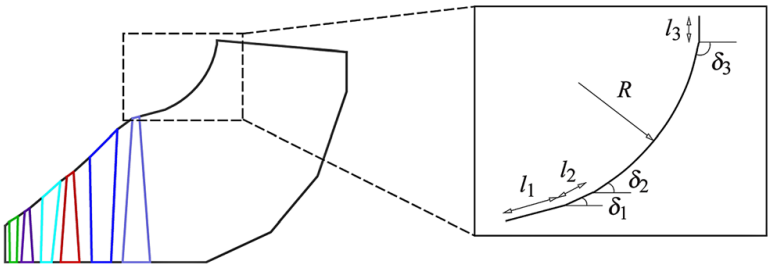

Fig. 6.1 Parameterisation of the flow guide using lines and circular arcs [56]

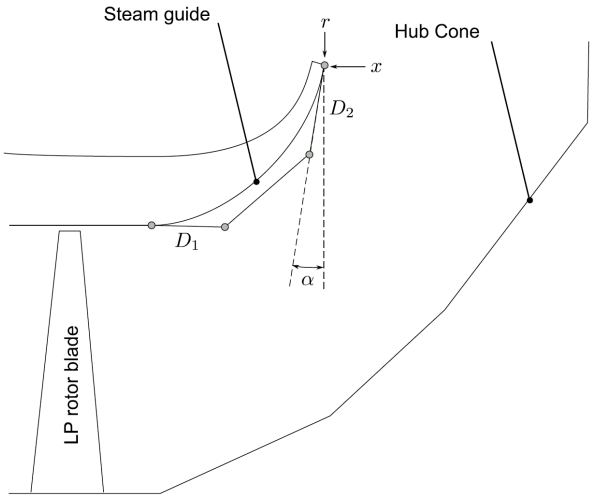

Fig. 6.2 Parameterisation of the flow guide using Bezier curve [81]

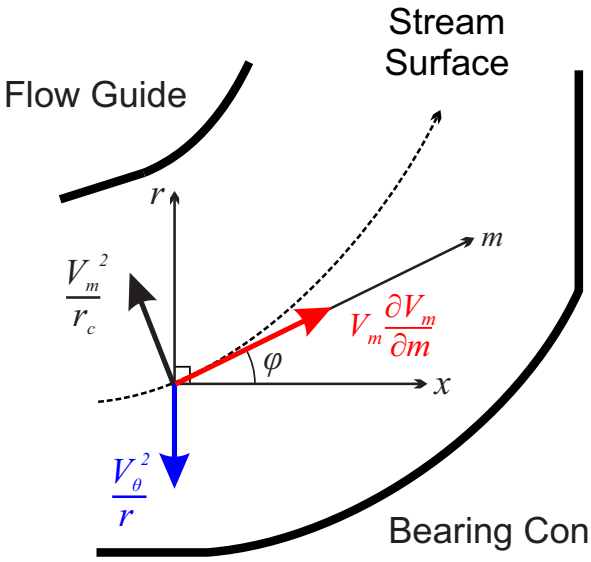

Fig. 6.3 Radial equilibrium in an exhaust diffuser

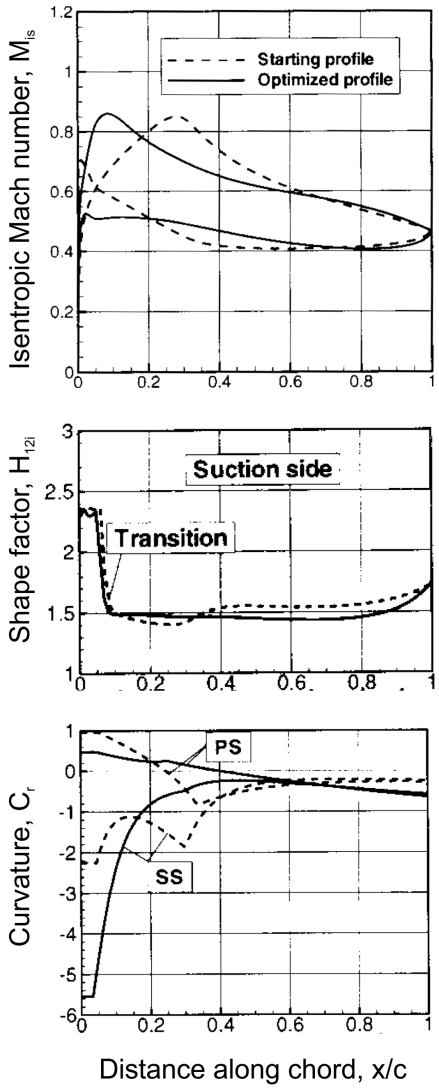

Fig. 6.4 Mach number, shape factor and surface curvature distributions of a CDA profile, adapted from Köller et al. [41]

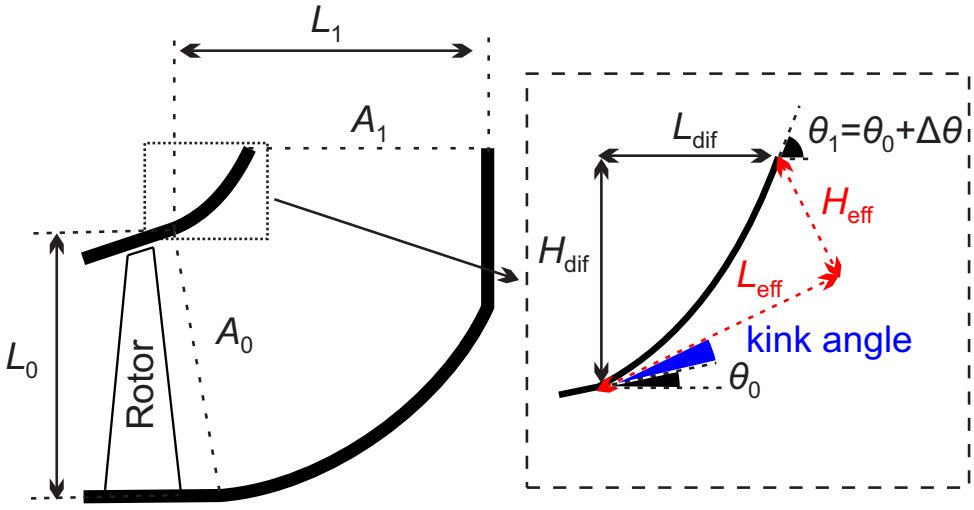

Fig. 6.5 Parameterisation of the exhaust diffuser (left) and flow guide (right) using MEC

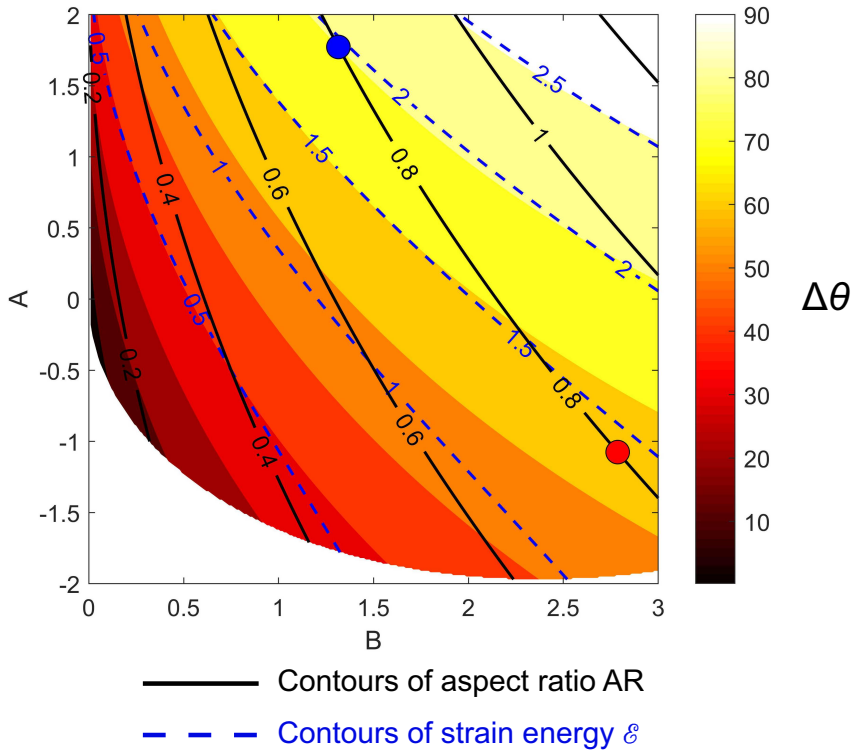

Fig. 6.6 Contours of total turning angle (filled), aspect ratio (solid lines, black) and non-dimensional strain energy (dashed lines, blue) for Minimum Energy Curves parametrised by (A, B). Blue circle: $AR = 0.8$, $\Delta\theta = 80°$. Red circle: $AR = 0.8$, $\Delta\theta = 65°$

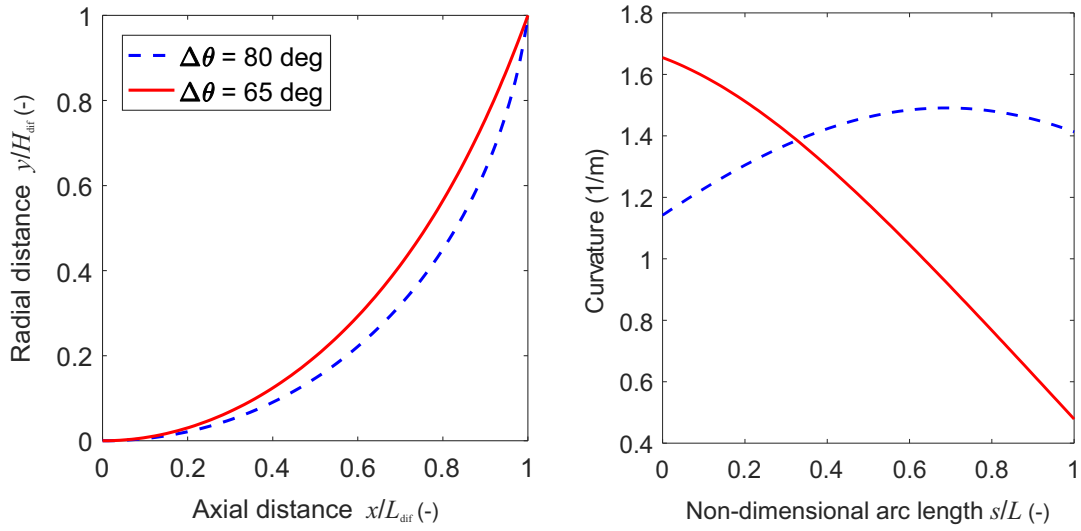

Fig. 6.7 Examples of Minimum Energy Curves in terms of shape (left) and curvature distribution (right). Solid red: $AR = 0.8$, $\Delta\theta = 65°$. Dashed blue: $AR = 0.8$, $\Delta\theta = 80°$

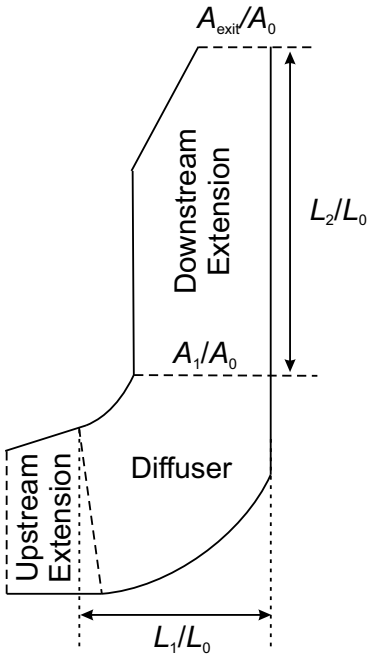

Fig. 6.8 CFD domain and design parameters for the standalone diffuser (not to scale)

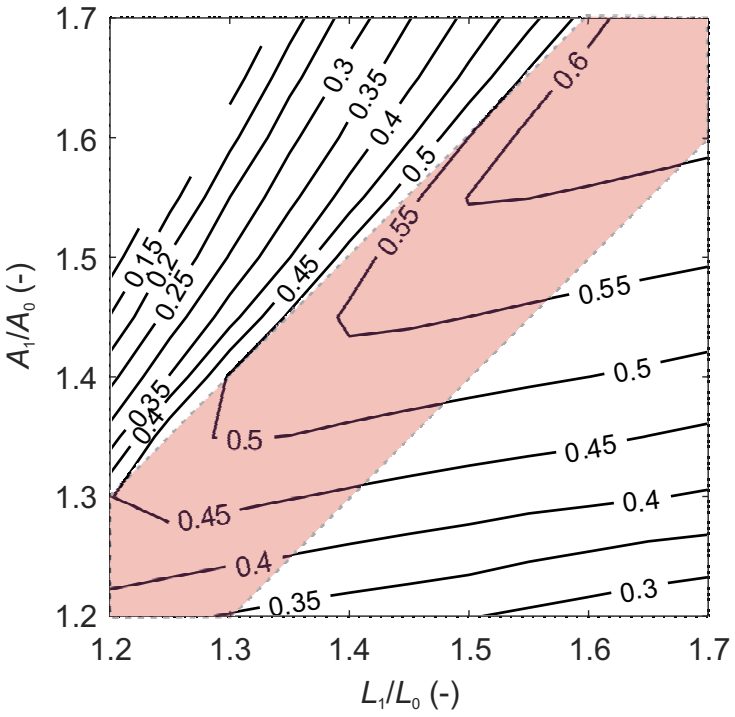

Fig. 6.9 Performance map of MEC-based diffusers in terms of C_p contours against diffuser length ratio (L_1/L_0) and area ratio (A_1/A_0)

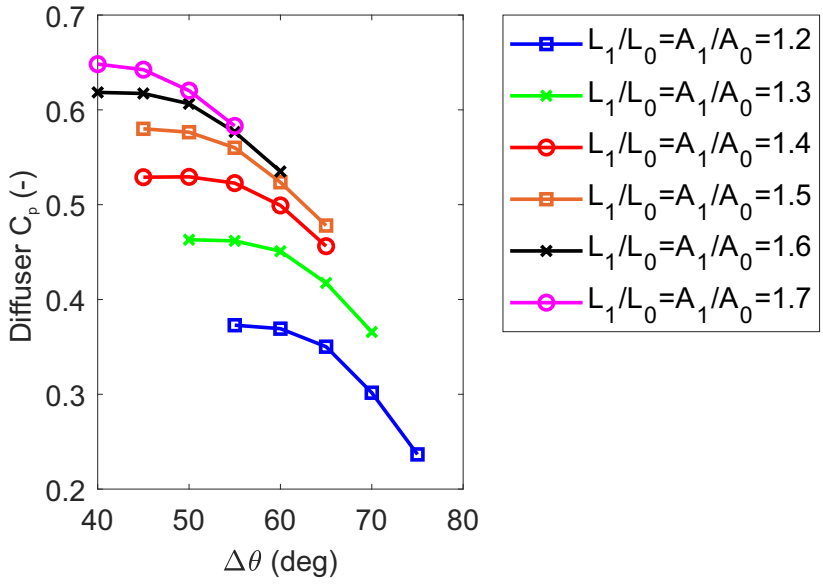

Fig. 6.10 Diffuser C_p against total turning angles for flow guides with $L_1/L_0 = A_1/A_0$

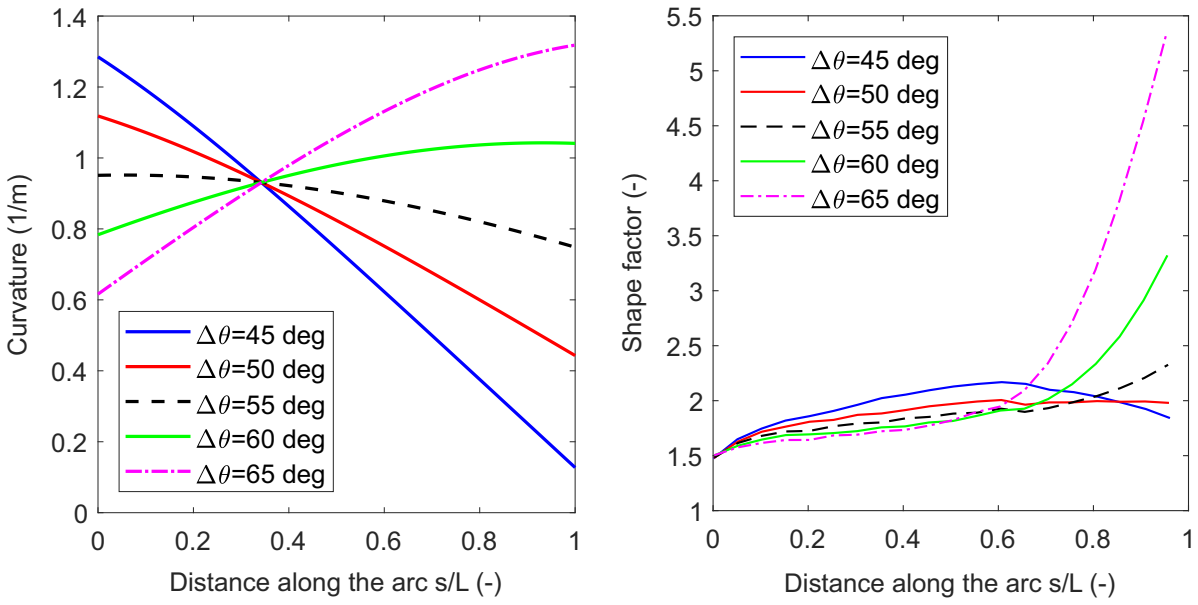

Fig. 6.11 Curvature (left) and boundary layer shape factor (right) distributions along the flow guide ($L_1/L_0 = A_1/A_0 = 1.4$, $45° \leq \Delta\theta \leq 65°$)

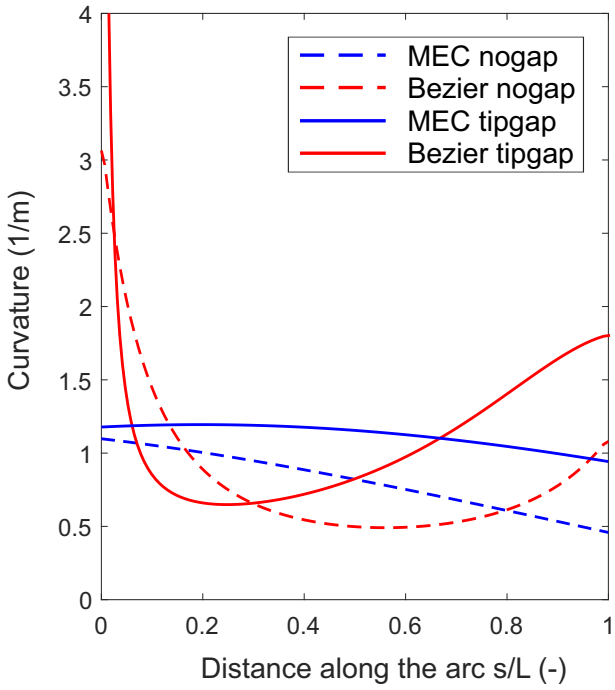

Fig. 6.12 Curvature distributions of optimised diffusers using MEC and cubic Bezier curves

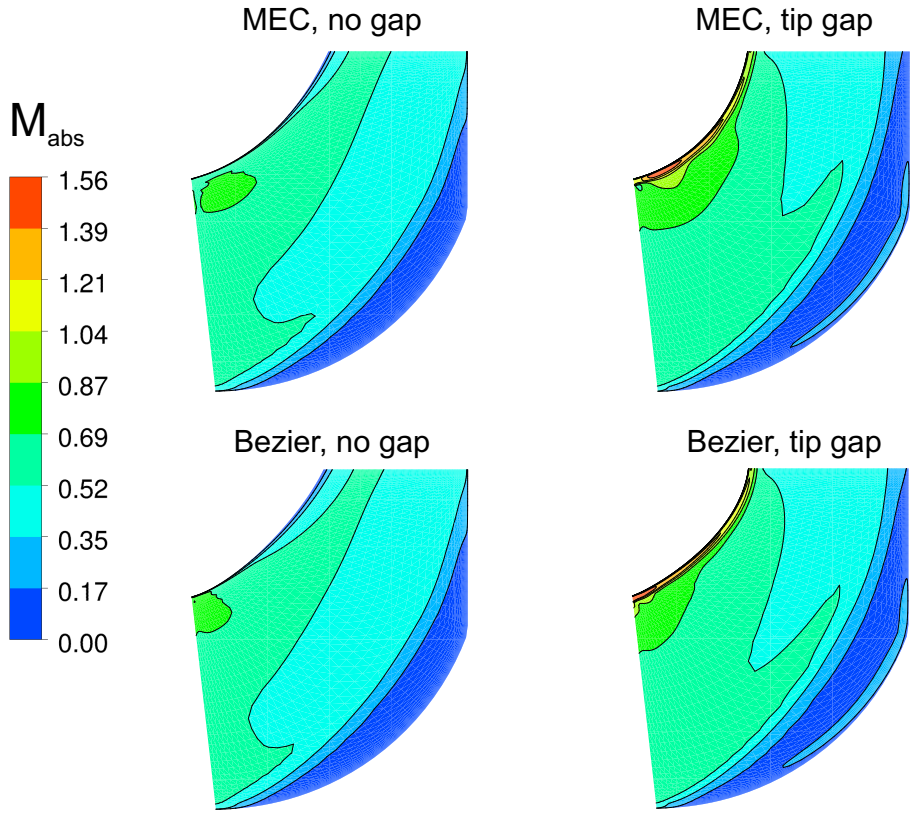

Fig. 6.13 Absolute Mach number contours of optimised diffusers

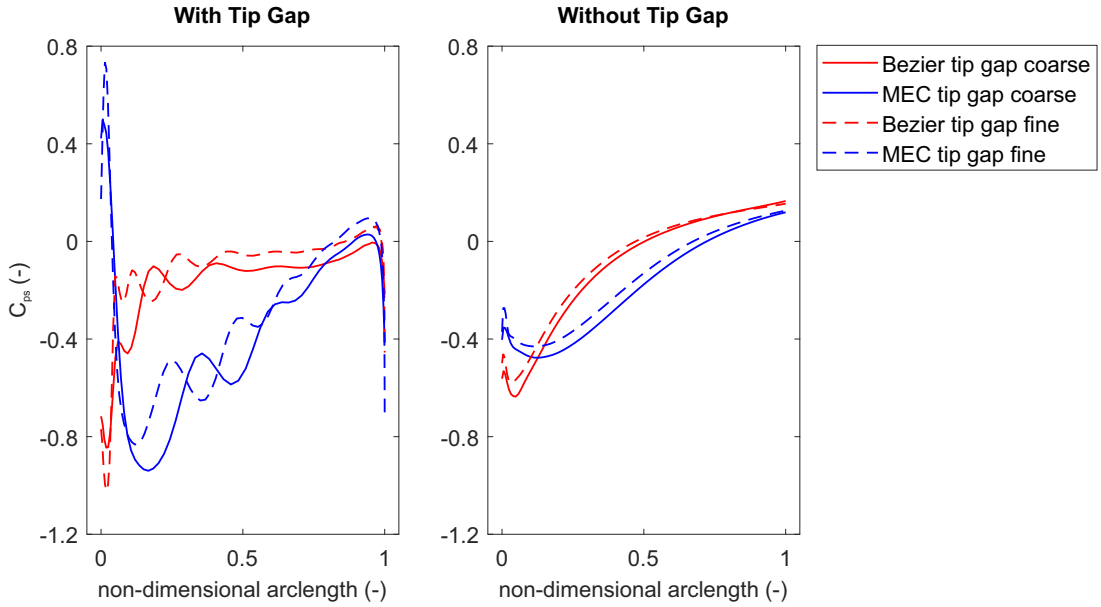

Fig. 6.14 Flow guide pressure distributions with (left) and without (right) rotor tip gap

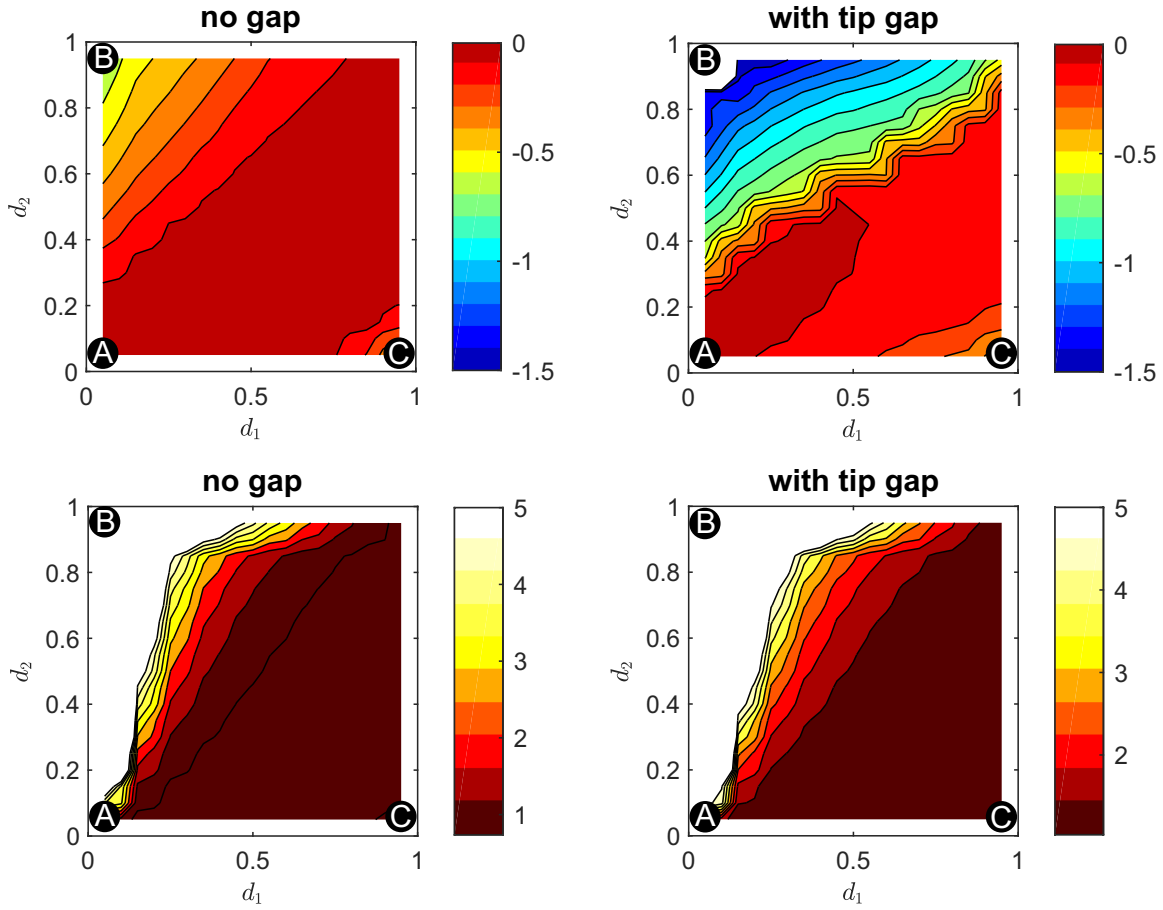

Fig. 6.15 Contours of last stage specific power output (percentage change compared to MEC-based flow guides, top row) and non-dimensional strain energy (bottom row) against Bezier curve control points (d_1, d_2) with and without rotor tip gaps. White-coloured region refer to out-of-range data. Design A: $d_1 = 0.05, d_2 = 0.05$. Design B: $d_1 = 0.05, d_2 = 0.95$. Design C: $d_1 = 0.95, d_2 = 0.05$

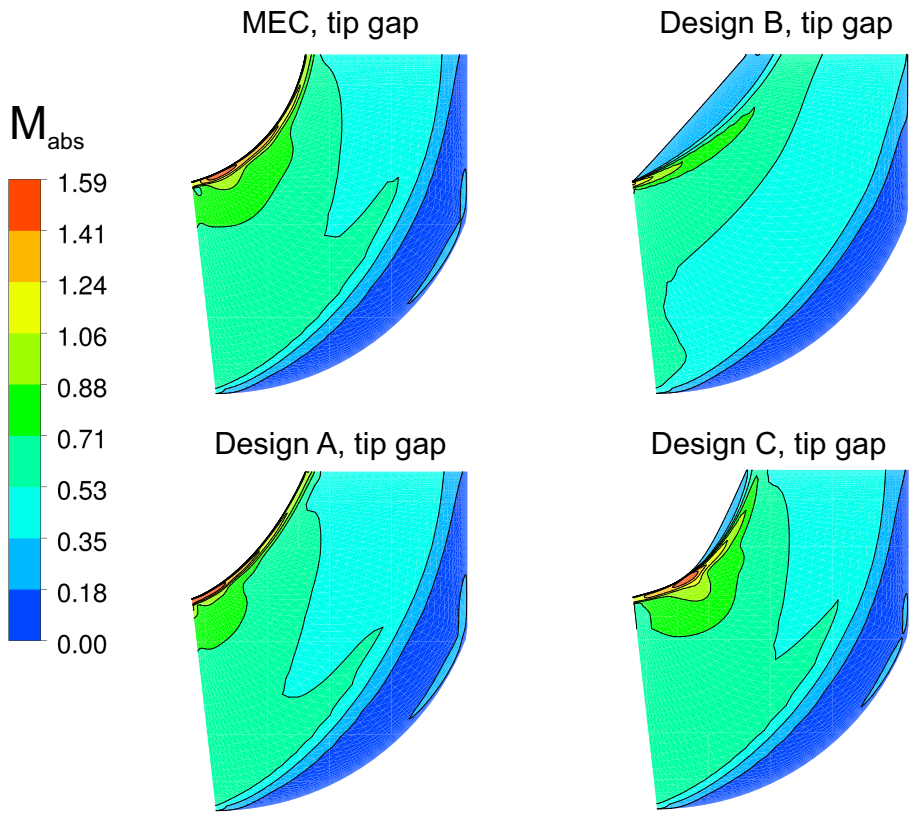

Fig. 6.16 Absolute Mach number contours for selected flow guides (with rotor tip gaps)

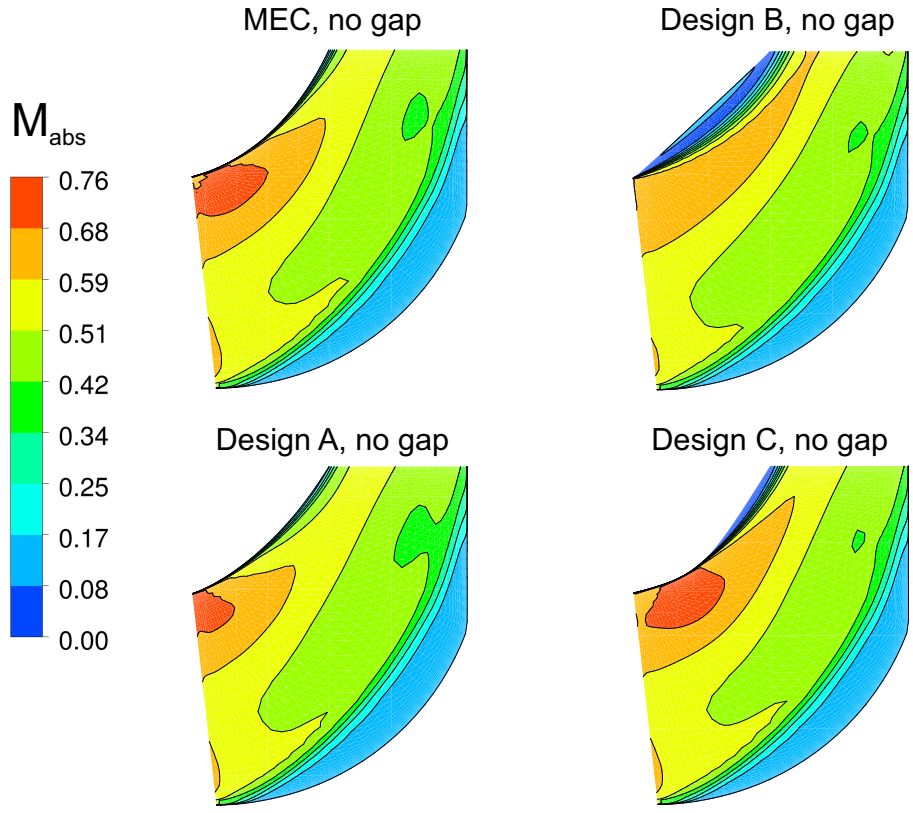

Fig. 6.17 Absolute Mach number contours for selected flow guides (without rotor tip gaps)

Chapter 7

Global Sensitivity Analysis of LP Exhaust Systems

Previous chapters have discussed how the computational cost (Chapter 4) and the parameter space dimension (Chapter 6) for LP exhaust system studies can be reduced, while new design parameters (*e.g.* rotor blade stagger distribution) were also identified (Chapter 5). This final result chapter details how attempts were made to assess the global sensitivity of the LP exhaust system design parameters numerically with relatively low computational cost, so that the most influential variables could be unveiled.

As demonstrated in Section 4.1, at least eight parameters are required to describe the exhaust hood geometry. Such high dimensionality prohibits the performance of typical sensitivity studies with limited computational resources. Recently, the so-called "active subspaces" have gained popularity for sensitivity studies, and was recently implemented in turbomachinery design [64]. The tool is useful in reducing the high dimensional parameter space to the most important one or two directions, in forms of linear combinations of original design variables, and can be thought of an output-based Principal Component Analysis (PCA) as commented by Seshadri et al. [64].

In this chapter, the concept of active subspaces will first be introduced, followed by the setup for the current study of LP exhaust systems. A 1-D active subspace was constructed for the two blading designs described in Chapter 5, over a wide operating range. The active subspace obtained revealed that the most influential variables are the **diffuser axial length ratio** and **area ratio**, the **flow guide turning angle**, and the **exhaust hood width ratio**. Finally, exhaust hood performance maps were constructed in terms of diffuser axial length and area ratio at different operating conditions, and recommendations were made concerning LP exhaust system design.

7.1 Active subspaces

The objective of most turbomachinery design practices, as is true for many other disciplines, is to select a parametrised geometry to achieve a certain desired outcome, be it maximised turbine stage efficiency, extended compressor operating range, or prolonged blade life. The design variables and their ranges are often determined by engineering requirements and limitations, and can be abstracted to an input vector $\mathbf{x} = (x_1, x_2, .., x_n)$ where n is the number of design variables. The output of interest can be a scalar y (as found in single-objective optimisations) or a vector $\mathbf{y}$ (for multi-objective optimisations). The outcome y can be obtained by performing experiments or simulations based on physical models such as the Navier-Stokes equations on geometries parametrised by $\mathbf{x}$, which construct a mapping $y = f(\mathbf{x})$ from the design space (some subset in $\mathbb{R}^n$) to the output space (some subset in $\mathbb{R}$, for scalar output). If a semi-analytic form of f can be found, optimisations and sensitivity analysis can be carried out with a much reduced computational cost, compared to expensive rig tests and 3-D CFD.

The biggest challenge to such input-output-based analysis, however, is the high dimensionality of the parameter space. Designers may have some knowledge about which parameters are more sensitive based on experience and explorations in a small subset of the design space. To assess the parameter sensitivity in the global sense, the dimension must be reduced in some way.

The recently emerged idea of "active subspaces", developed by Constantine [16], suits this task. This chapter describes how the simplest, 1-D active subspace was sought for the LP exhaust system. The general algorithm is as below, taken from Constantine et al. [16]:

1. Draw m independent samples $\mathbf{x}_j = (x_{j1}, x_{j2}, .., x_{jn})$ with $j = 1, 2, .., m$ from the n-dimensional parameter space with some sampling density ρ.

2. Perform simulations (such as CFD) on geometries parametrised by each sample $\mathbf{x}_j$, and obtain the output of interest, $y_j = f(\mathbf{x}_j)$.

3. Perform linear regression (least squares fit) on $\mathbf{x}_j$ and y_j, and find the linear coefficients c and $\mathbf{b}$ such that

$$y_j \approx c + \mathbf{b}^T \mathbf{x}_j,\ j = 1, 2, .., m.$$

4. Compute the normalised gradient of the linear model

$$\hat{\mathbf{w}} = \mathbf{b}/||\mathbf{b}||.$$

The algorithm above assumes a global linear model. The vector of normalised linear coefficients $\hat{\mathbf{w}}$ is termed the 1-D *active subspace*. By multiplying $\hat{\mathbf{w}}$ to the left of $\mathbf{x}_j$, the n-dimensional parameter space is reduced to just one *active variable* $\hat{\mathbf{w}}^T \mathbf{x}$.

Quadratic models can also be used to construct 2-D active subspaces, an example of which can be found in Seshadri et al. [64]. A key limitation of high-order active subspaces is the lack of physical interpretability of the active variables. For instance, if active variable 1 is equal to $(0.2 \times \text{length ratio} + 0.4 \times \text{area ratio} - 0.9 \times \text{width ratio})$ and active variable 2 is equal to $(0.5 \times \text{length ratio} - 0.3 \times \text{area ratio} + 0.8 \times \text{width ratio})$, designers would find it very difficult to understand the influence of each design variable.

This study has assumed a global linear model, so that the linear coefficients obtained from the above algorithm can be interpreted as the global sensitivity for each parameter. The question was whether the performance of LP exhaust systems could be approximated using a linear model at all, which will be addressed later in this chapter.

7.2 Problem setup

7.2.1 Exhaust hood design parameters

The first step of the global sensitivity study was to introduce the design parameters and their typical ranges. The parametrisation of the LP exhaust hood can be found in Fig. 4.1 from Chapter 4, where the eight design variables are highlighted. The design parameters and their typical ranges are summarised in Table 7.1. Other design parameters were fixed to values recommended by the industrial sponsor.

Table 7.1 Typical ranges of LP exhaust hood design parameters

No.	Design Parameter	Typical Range
1	Diffuser axial length ratio (L_1/L_0)	$0.9 - 1.7$
2	Diffuser exit area ratio (A_1/A_0)	$1.2 - 2.0$
3	Flow guide height ratio (H_0/L_0)	$0.55 - 0.95$
4	Flow guide turning angle ($\Delta\theta$)	$60 - 90°$
5	Flow guide initial kink angle	$0 - 15°$
6	Bearing cone initial kink angle	$0 - 30°$
7	Hood height ratio (H_1/L_0)	$2.85 - 3.55$
8	Hood width ratio (W_1/L_0)	$8.0 - 10.0$

The parametrisation was almost the same as that in Chapter 6. The only exception is the bearing cone, which was shaped using simple cubic Bezier curves with control parameters $d_1 = d_2 = 0.5$, as defined in Section 6.4. This was because the curvature distribution on the bearing cone was less important compared to the flow guide which was shaped using the Minimum Energy Curves (MEC) introduced in the previous chapter, and that a spline-based curve definition is more flexible compared to circular arcs. Moreover, flow guide and bearing cone initial kink angles (parameters 5 and 6 respectively) were included, so that their relative importance could be determined. Finally, the cross-sectional

length $r(\theta)$ of the collector (Fig. 4.1) was represented as a linear function with respect to the angular position θ, *i.e.*

$$r(\theta) = r_0 + \frac{r_1 - r_0}{\pi/2} \cdot \theta, \tag{7.1}$$

so that the cross-sectional area varied linearly inside the collector.

7.2.2 Sampling in the parameter space

Having defined the design parameters, the next step was to carry out independent sampling in the parameter space. Before doing so, the ranges of all design variables had to be normalised to $[-1, 1]$, so that the conclusions of the sensitivity study were not affected by the nominal values taken by each parameter. For a design variable x in the range of $[x_{\min}, x_{\max}]$, the normalisation was achieved by setting

$$\hat{x} = \frac{2x - (x_{\max} + x_{\min})}{x_{\max} - x_{\min}} \tag{7.2}$$

Following the approach by Seshadri et al. [64], Latin Hypercube Sampling (LHS) was chosen to generate samples in the $[-1, 1]^8$ space. In practice this was realised by using the built-in function *lhsdesign* in MATLAB [3]. LHS is commonly used for generating near-random multi-dimensional samples, and details of this method can be found in the original work by McKay et al. [47].

Fig. 7.1 demonstrates the wide range of geometries covered by the sampling in the parameter space.

7.2.3 CFD pre- and post-processing

In order to reduce the computational cost without much compromise to accuracy compared to full annulus simulations, the Multiple Mixing Planes (MMP) approach introduced in Section 4.3 was used to model the stage-hood interface using four equidistantly placed mixing planes between the rotor exit and the diffuser inlet. Moreover, very coarse mesh ($\sim$ 0.1 mil per blade row and $\sim$ 2.7 mil in the exhaust hood) was used, since it was the relative merit between designs that was the principal concern.

Both Stage A and Stage B, introduced in Chapter 5, were considered to investigate the effect of blading design. The modelled geometry included the last stage (or last two stages for Stage B), the exhaust hood and a vertical extension from the condenser neck. This was the same as that in Fig. 5.3, except that the final contraction section was omitted. Thereby, the effect of diffuser length ratio on the hood area ratio could be appreciated (*i.e.* a longer diffuser also leads to a greater hood exit area), and this was considered a more fair configuration when the entire parameter space was explored.

For each blade design around 80 hood geometries were sampled, which was considered enough for linear models (in theory, only $n + 1$ samples are required for an n-dimensional

parameter space). Structured mesh was then automatically generated using the exhaust system design suite *ExhaustGen* introduced in Chapter 4, followed with batch runs on the High Performance Computing (HPC) clusters at Cambridge University, at three different operating conditions (50%, 70% and 100% mass flow rates). In total, around 500 steady RANS calculations were performed, which took about 9 days to finish on three 32-core Intel Skylake CPU nodes.

With the computations completed, post-processing scripts were run in batch mode to extract the exhaust system performance for each geometry configuration. The performance metric used, or the output of interest, was the system total-static efficiency defined in Eq. 5.1. This was the y_j value in the 1-D active subspace algorithm introduced at the beginning of this chapter, following which linear regressions could be performed to study the effect of geometry on system performance.

7.3 1-D active subspace

The first section of the following results concerns the global linear model, based on the least squares fit on the samples. The following questions were raised and the results will be presented in accordance with these questions:

1. How accurate is the linear model?
2. Of the eight design parameters studied, which ones are more effective than the others?
3. How do blading and operating condition influence system performance?

7.3.1 Accuracy of the linear model

In a previous study by Seshadri et al. [64], 150 samples were drawn from the 25-dimensional parameter space, representing an oversampling factor of 6. In this study, around 80 hood geometries were sampled for each blading design, so that some of the samples could be used as the training set, while the rest were used to test the accuracy of the linear model. An oversampling factor of 5 was chosen for the training set size, so that each time $8 \times 5 = 40$ samples were picked randomly out of the entire sampling set. These training data was then fitted using least squares to obtain the corresponding linear coefficients. Comparisons could then be made between the actual and the predicted system performances for the test dataset. For each blading design and operating condition, this process was carried out 100 times to obtain an estimate of the distribution of errors.

System total-static efficiency was plotted against the active variable $\hat{\mathbf{w}}^T\hat{\mathbf{x}}$ (*i.e.* some linear combination of normalised design parameters), for both blade designs at three operating conditions (Fig. 7.2). All plots have the same range on the vertical axis,

although the nominal values are hidden. On the same figure the least squares fit lines are also plotted with a ±1% band, showing the trend of the scatter plots. The results are based on *all* samples obtained (around 80 in total).

Overall, a clear trend of linearity could be observed from the scatter plots, with most points falling within the band of ±1 percentage point of efficiency at all flow conditions. As the flow rate reduced, the gradient of the least squares fit lines increased, indicating a greater sensitivity of the system performance to its design variables at part-load conditions. This could also be observed in a 2-D hood performance map, which will be discussed in the next section.

The level of accuracy could also be visualised by plotting the distribution of root mean square (RMS) errors, defined as

$$\Delta\eta_{\text{rms}} = \sqrt{\frac{1}{n_{\text{test}}} \sum_{i=1}^{n_{\text{test}}} (\eta_{\text{i, lin}} - \eta_i)^2}, \tag{7.3}$$

n_{test} being the size of the test dataset. The predicted efficiency $\eta_{\text{i, lin}}$ was defined as

$$\eta_{\text{i, lin}} = c + b_1 \cdot x_{i1} + b_2 \cdot x_{i2} + .. + b_8 \cdot x_{i8}, \tag{7.4}$$

where c and $\mathbf{b}$ are the linear coefficients obtained from least squares fit on the training dataset, and $\mathbf{x}$ are the design variables from the test dataset. $\Delta\eta_{\text{rms}}$ were calculated 100 times, each time based on a random sampling of training and test data out of the entire dataset. From the histograms in Fig. 7.3, it can be seen that the level of accuracy dropped as the flow rate decreased, with increased level of spread (or variance), albeit all within 1 percentage point of efficiency. Moreover, the levels of accuracy of the two stage designs were similar, at most operating conditions.

7.3.2 Sensitivities of design parameters

The sensitivity of each design parameter was quantified using the normalised coefficients ($\hat{\mathbf{w}}$) introduced in Section 7.1, assuming a global linear model. The coefficients for each design parameter were plotted together with error bars based on 100 evaluations of linear regressions on 70 out of all samples each time (Fig. 7.4). Despite the uncertainties in the actual coefficient levels, the rank of parameter sensitivities could still be observed on a qualitative basis. The most sensitive parameters were:

- Variable 1: diffuser axial length ratio (L_1/L_0)
- Variable 2: diffuser area ratio (A_1/A_0)
- Variable 4: flow guide turning angle ($\Delta\theta$)
- Variable 8: exhaust hood width ratio (W_1/W_0)

For both stage designs, higher values in diffuser area ratio, flow guide turning angle and exhaust hood width ratio led to a higher system efficiency, at all operating conditions. The main difference between the two stages was the coefficient for diffuser length ratio at design condition: Stage A favoured a shorter diffuser while Stage B preferred a longer diffuser. This could be understood from the diffuser inlet conditions in Fig. 5.7 and the streamline plots in Fig. 5.9 from Chapter 5. At design condition, Stage A had a negative hub swirl angle, resulting in bearing cone separation. To suppress this separation, a shorter diffuser should be used. As the flow rate reduced, the level of diffuser inlet swirl increased and the size of the bearing cone separation grew, explaining the drop in diffuser length coefficients for both stages.

Turning to the other influential factors, the coefficients in diffuser area ratio reduced as the machine operated further off-design, in accordance with the reduction in flow rates. The coefficients for turning angle also reduced as the flow rate decreased: at design condition, the tip leakage jet ensured the flow remained attached to the outer casing (flow guide), allowing a higher turning angle without flow separation, as well as a larger diffuser exit area; at part-load condition the strength of the leakage jet weakened, and a lower turning angle or curvature level would be preferred.

Finally, it is worth noting the positive effect of hood width ratio, or effectively the hood area ratio, on exhaust system performance. In particular, the coefficients increased as the flow rate reduced, which is thought to be associated with the increase in the blocked area at the condenser neck, as previously illustrated in Fig. 5.12. Therefore, whenever possible, designers should maximise the hood width.

Overall, the relation between system performance and the design parameters can be approximated with a global linear model with good accuracy (under 1 percentage point). Designers can use such a model to identify the most sensitive parameters to focus on during the initial design process, followed by optimisations for the remainder of the parameters.

7.4 Exhaust hood performance maps

7.4.1 Performance map construction process

In the previous section, the four most influential design variables were identified. To corroborate these findings and to better understand the flow physics behind them, exhaust hood performance maps were constructed, by varying the **diffuser length ratio** and **area ratio** alone and plotting the contours of system total-static efficiencies. The exhaust hood width ratio was fixed to some typical value, while the flow guide turning angle was set to the maximum value for each combination of diffuser length and area ratios. The ranges and the values of the parameters are summarised in Table 7.2. Different ranges of diffuser length and area ratios were sought for the two stages, since Stage B was in favour of longer diffusers.

Table 7.2 Ranges and values of LP exhaust hood design parameters

No.	Design Parameter	Stage A	Stage B
1	Diffuser axial length ratio (L_1/L_0)	$1.1 - 1.5$	$1.2 - 1.7$
2	Diffuser exit area ratio (A_1/A_0)	$1.2 - 1.7$	$1.3 - 1.8$
3	Flow guide height ratio (H_0/L_0)	0.75	
4	Flow guide turning angle ($\Delta\theta$)	90° or maximally allowed	
5	Flow guide initial kink angle	$0 - 10°$	
6	Bearing cone initial kink angle	0°	
7	Hood height ratio (H_1/L_0)	3.2	
8	Hood width ratio (W_1/L_0)	9.0	

The procedure to generate the performance maps was as follows. First, a 2-D sweep was carried out in the (L_1/L_0, A_1/A_0) space, in steps of 0.05. At each point, 90° or maximally allowed flow guide turning angle (from axial direction to the end of the flow guide) was sought by adjusting the initial kink angle in the $0 - 10°$ range. This was to alleviate the restrictions imposed by the MEC formulation introduced in Section 6.3. For short diffusers, there was an upper limit on the diffuser area ratio imposed by both the MEC formulation, and the degradation in performance due to separation for highly loaded diffusers. At the same time, a lower limit of area ratio was also imposed, to save the computational cost of those ineffective diffusers. The upper and lower limits would lead to a slanted band in the 2-D parameter space. With other parameters fixed, the exhaust hood geometry was uniquely determined, and corresponding CFD calculations could then be performed.

7.4.2 Results and discussions

In this study, performance maps for both stages at three operating conditions were generated (Fig. 7.5), in the form of contours of system total-static efficiencies as defined in Eq. 5.1. Note that different ranges of colour maps were used for each operating condition, since the efficiency levels varied significantly as the flow rate reduced. The following observations could be made from the performance maps.

Firstly, the sensitivity to design variables increased as flow rate reduced, which was clear from the greater number of contour levels (same distance of 0.5% of efficiency was used in all subplots). This was consistent with the increased gradient in the least squares fit lines shown in Fig. 7.2.

Secondly, the overall shapes of the performance maps for the two stages and their associated exhaust hoods are similar to each other at high flow rates, namely 100% and 70% of design mass flow rates. As the flow rate reduced to 50%, discrepancies started to appear. Stage A was more tolerant of part-load operation: for instance, at point "a" ($L_1/L_0 = 1.3, A_1/A_0 = 1.55$) in Fig. 7.5, the system efficiency is at the top of its range at all operating conditions. For Stage B, however, an optimised hood design (point "b"

for which $L_1/L_0 = 1.55, A_1/A_0 = 1.7$) at design condition performed badly at off-design conditions. This can be visualised in the contour plots of absolute Mach number (Fig. 7.6). For Stage B, the bearing cone separation was larger in exhaust hood "b" which had a longer diffuser and consequently larger hood exit area (by 15%), compared to the shorter exhaust hood "a".

Furthermore, it is interesting to note that the contours for Stage B at 50% flow rate are almost straight. This can be understood from the linear coefficient levels in Fig. 7.4: at 50% flow rate, the coefficient of flow guide turning angle ($\Delta\theta$) for Stage B becomes much smaller in absolute value, compared to Stage A and also other operating conditions. With the hood width ratio fixed, we are left with just two dominant parameters (diffuser length ratio and area ratio), and thus can approximate the system performance using some linear combination of these two parameters, which explains the straight patterns in Fig. 7.5. By contrast, the turning angle remains important for Stage A at the lowest flow rate, resulting in the wavy patterns in the contour plots.

Finally, the benefits of choosing suitable diffuser sizes (in terms of length and area ratios) and redesigning the blade (by opening the rotor hub section by 5°) were quantified by the averaged last stage power output, weighted by the time spent on each operating condition. Three operating scenarios for a typical 1000 MW steam power plant are presented in Fig. 7.7 and also summarised in Table 7.3, where w_i is the proportion of time the power plant operates at flow condition i over the course of one year. Note that five operating conditions (50%, 60%, 70%, 85% and 100% mass flow rate) were considered, for each stage and hood configuration.

Table 7.3 Weight factor in different operating scenarios

Scenario	$w_{50\%}$	$w_{60\%}$	$w_{70\%}$	$w_{85\%}$	$w_{100\%}$
1	0%	5%	15%	30%	50%
2	5%	15%	30%	35%	15%
3	10%	30%	40%	15%	5%

In Scenario 1, the power plant operates near the design condition most of the time. Scenario 2 is considered a representative operating profile for today's large steam turbine plants. With further increase in renewable energy use, Scenario 3 may become a reality, with the turbine operating at part-load conditions much more frequently. The weighted average power output, P_{avg}, is defined as

$$P_{\text{avg}} = \sum_i P_i \cdot w_i, \tag{7.5}$$

where P_i is the total power output (in MW) at operating condition i.

To quantify the effect of blade redesign, exhaust hood design "a" ($L_1/L_0 = 1.3, A_1/A_0 = 1.55$, shown in Fig. 7.5) is coupled to both datum and restaggered Stage A. The weighted average power output in each scenario is presented in Table 7.4.

Table 7.4 Weighted average power output for Stage A

Scenario	Stage A datum + Hood a	Stage A restaggered + Hood a	Effect of restaggering
1	$1.2543P_{\text{avg, A}}$	$1.2553P_{\text{avg, A}}$	+0.1%
2	$1.0000P_{\text{avg, A}}$	$1.0043P_{\text{avg, A}}$	+0.4%
3	$0.8065P_{\text{avg, A}}$	$0.8151P_{\text{avg, A}}$	+1.1%

The table above shows that the benefits of restaggering the rotor hub section (even just by 5°) can be as much as a 0.4% increase in averaged power output based on a realistic operating profile (Scenario 2), despite that hood design "a" is already a near-optimum geometry based on the performance maps in Fig. 7.5. Moreover, the level of benefits grows as more time is spent at part-load conditions (1.1% in Scenario 3), again demonstrating the importance of including blade design in the exhaust system design process.

The effect of hood geometry on exhaust system performance can be studied by comparing the averaged power output for Stage B coupled with two different exhaust hoods (design "a" and "b" in Fig. 7.5), as summarised in Table 7.5.

Table 7.5 Weighted average power output for Stage B

Scenario	Stage B datum + Hood a	Stage B datum + Hood b	Effect of hood resizing
1	$1.2680P_{\text{avg, B}}$	$1.2705P_{\text{avg, B}}$	-0.2%
2	$1.0048P_{\text{avg, B}}$	$1.0000P_{\text{avg, B}}$	+0.5%
3	$0.8115P_{\text{avg, B}}$	$0.8006P_{\text{avg, B}}$	+1.4%

Although hood "b" is an optimised geometry at design condition for Stage B, hood "a" should be favoured when a wide range of operating condition is considered. From Table 7.5 it can be seen that choosing a shorter diffuser with smaller area ratio leads to an increase of 0.5% in averaged power output for Scenario 2 and 1.4% in Scenario 3. Therefore, designers must bear in mind the most frequent flow condition the steam turbine is expected to operate over in the early design stage.

7.5 Concluding remarks

This chapter detailed how the recently emerged idea of active subspace was used to identify the most important direction ("active variable") in the parameter space, in the form of

linear combinations of original design variables. The coefficients of the active variable revealed that the most sensitive parameters are the **diffuser axial length ratio** and **area ratio**, the **flow guide turning angle**, and the **exhaust hood width ratio**. For the two blading designs studied (Stage A and Stage B), similar conclusions could be drawn with regard to the sensitivities of most parameters, apart from the diffuser axial length ratio at design condition. The sensitivities also changed as the operating condition varied, highlighting the importance of determining the most frequent operating condition of the power plant during the design process. Finally, exhaust hood performance maps based on the diffuser axial length and area ratios enabled the visualisation of parameter sensitivities, especially when the operating condition changed. For a typical operating profile of the power plant, the benefits of choosing a suitable exhaust hood size can be around 0.5% in terms of weighted average power output throughout the year, while restaggering the rotor blade can bring a similar level of improvement in performance. Should the power plant operate more frequently at part-load conditions, the benefits quoted above can be more than doubled.

Based on the findings in this chapter, the following recommendations are made for the design process:

1. During the design process, initial focus should be placed on low order parameters, *i.e.* the blading design, diffuser axial length ratio (L_1/L_0) and area ratio (A_1/A_0), flow guide turning angle ($\Delta\theta$), and exhaust hood width ratio (W_1/L_0). Other design variables can be fixed to reasonable values based on design experience.

2. Subject to practical engineering limits, the exhaust hood width ratio (W_1/L_0) should be as large as possible, as the associated linear coefficients in Fig. 7.4 indicated that a wider exhaust hood would lead to higher system efficiency, at all operating conditions.

3. The flow guide's total turning angle ($\Delta\theta$) should also be maximised, for the same reason above. This can be realised by applying the concept of Minimum Energy Curves (MEC) introduced in Chapter 6, in order to maximise the turning angle whilst keeping the overall curvature level low.

4. The designer can then just focus on two key design parameters ($L_1/L_0, A_1/A_0$), the optimum combination of which can be found by performing searches with coarse steps in the 2-D design space, or by referring to previously generated hood performance maps, at the most frequent operating condition.

5. Finally, if permitted, some variation to the rotor blade stagger distribution may further improve system performance.

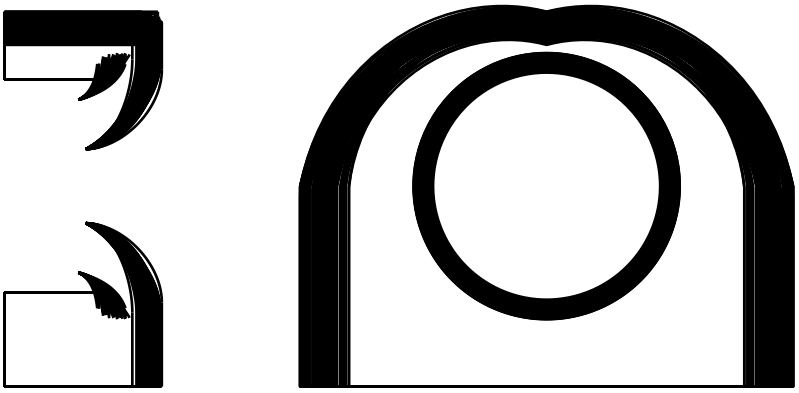

Fig. 7.1 All LP exhaust hood geometries generated using Latin Hypercube Sampling. Left: side view. Right: front view

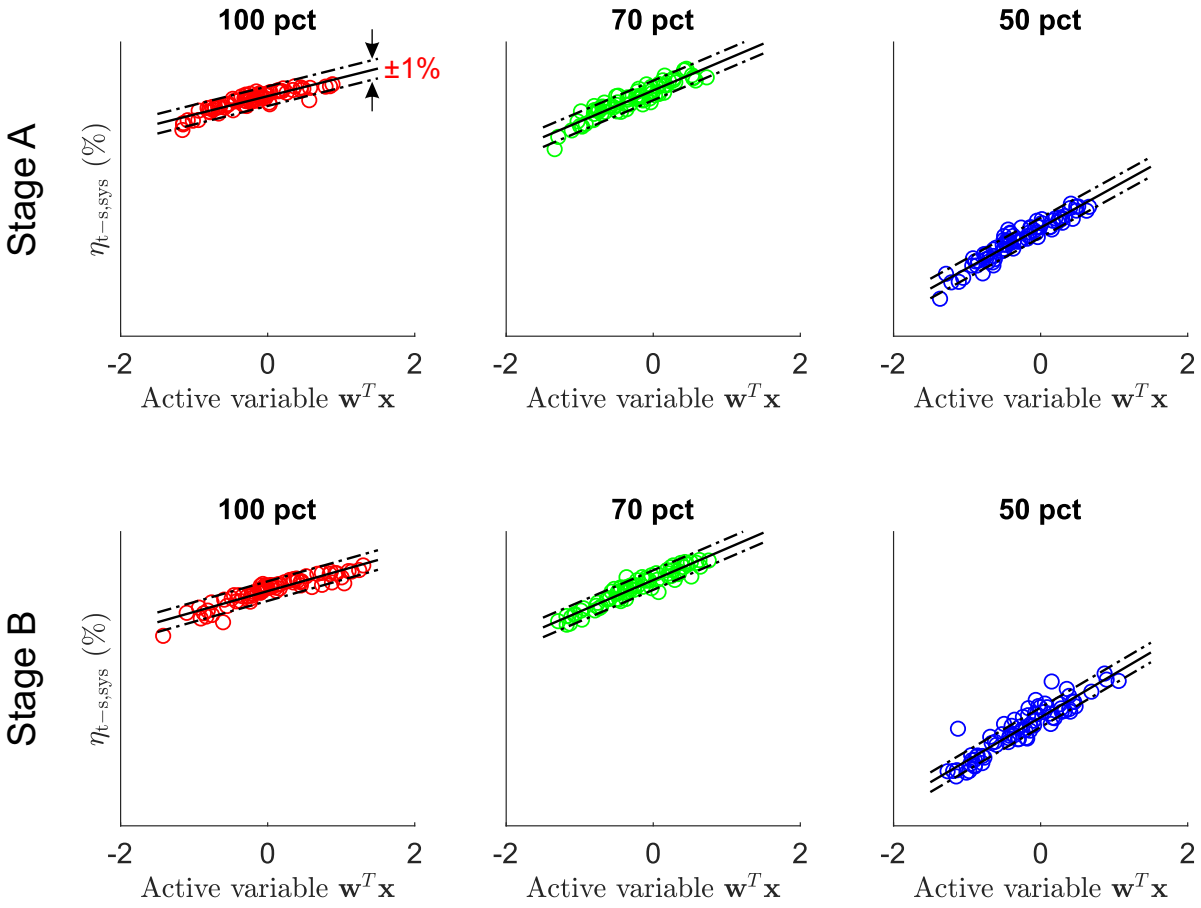

Fig. 7.2 Scatter plots of system total-static efficiency against active variables at different operating conditions for Stage A (top) and Stage B (bottom), along with least squares fit lines and ±1% error bands based on all samples obtained

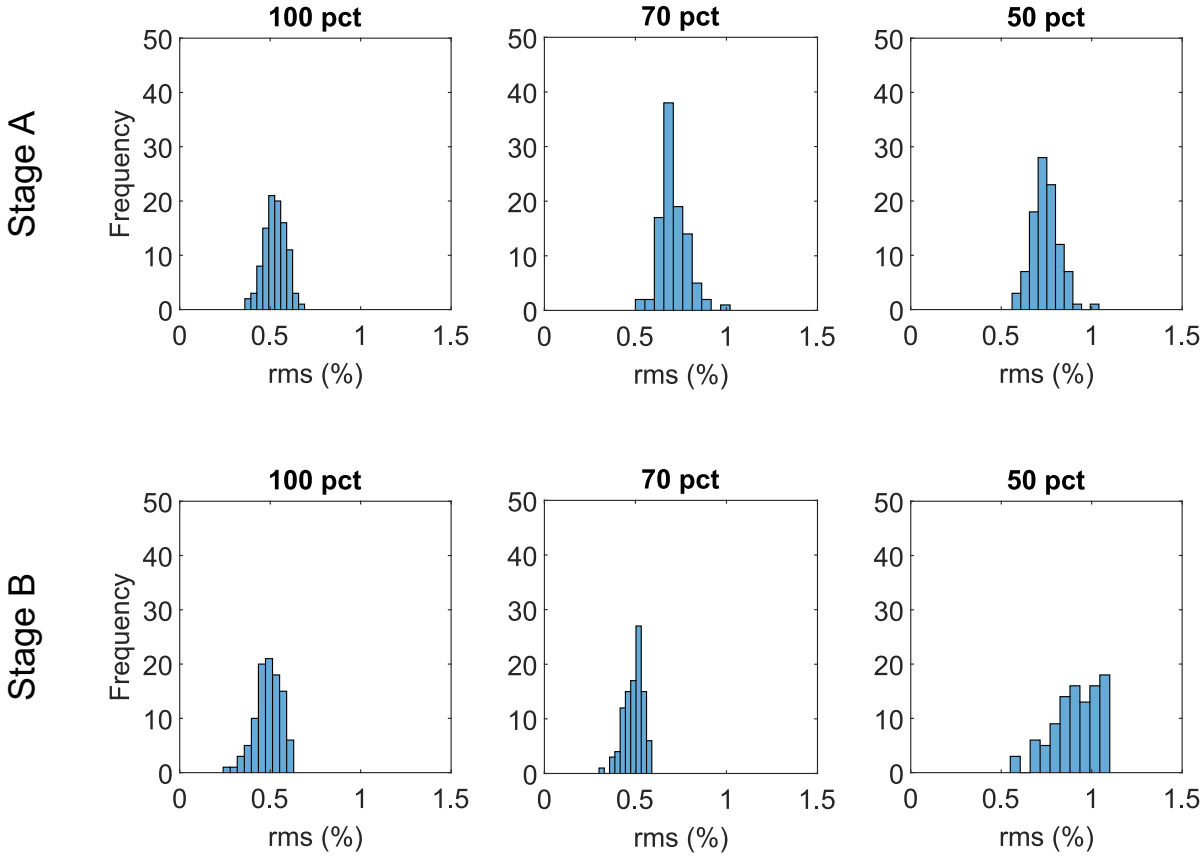

Fig. 7.3 Histogram of root mean square errors of predicted system efficiency in percentage points for Stage A (top) and Stage B (bottom) at different operating conditions, with 10 bins

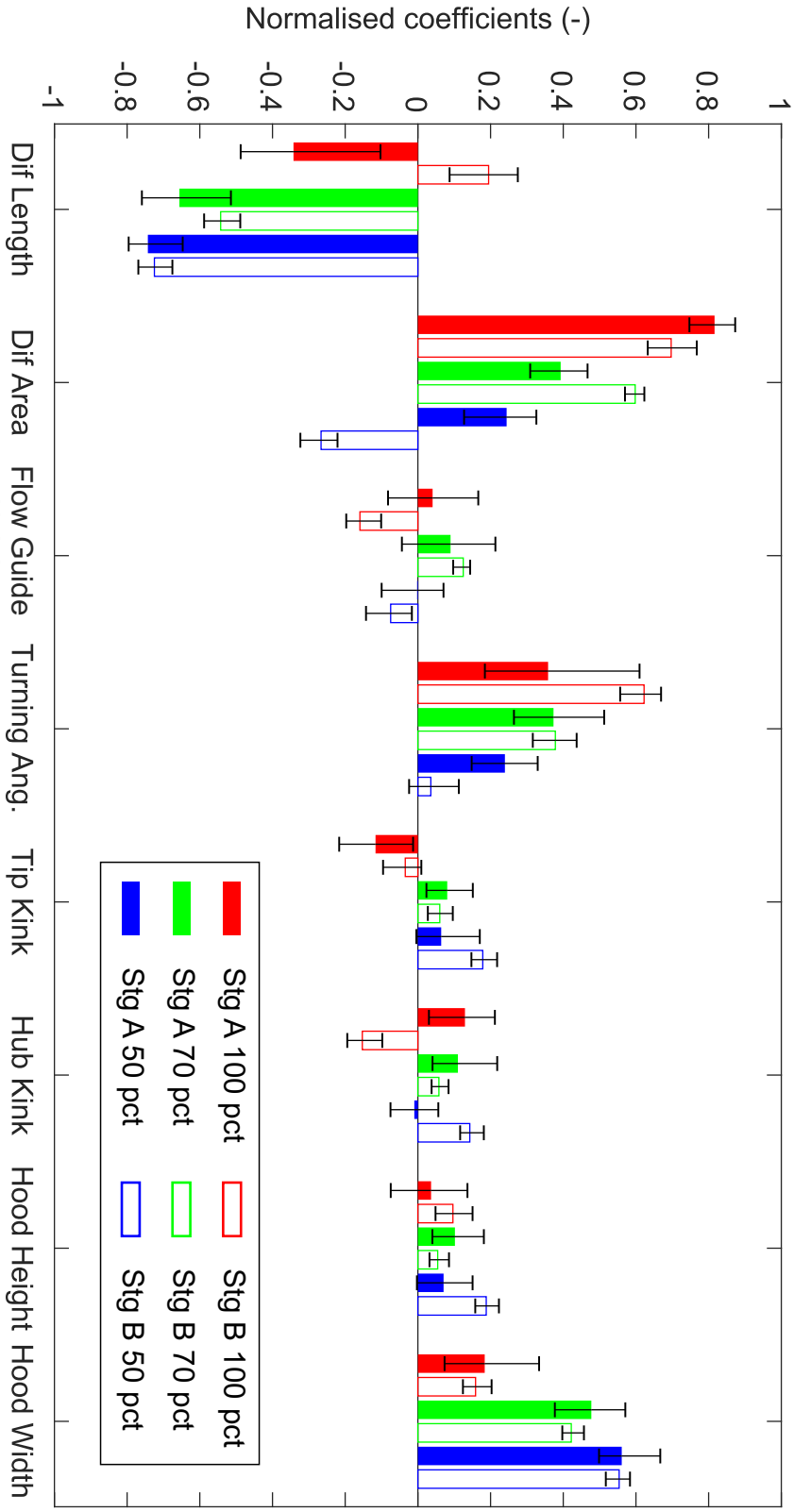

Fig. 7.4 Normalised coefficients of design parameters in the system efficiency active variable for Stage A (solid) and Stage B (hollow) at different operating conditions. Mean values (bar heights) and error bars are based on 100 evaluations of 70 samples

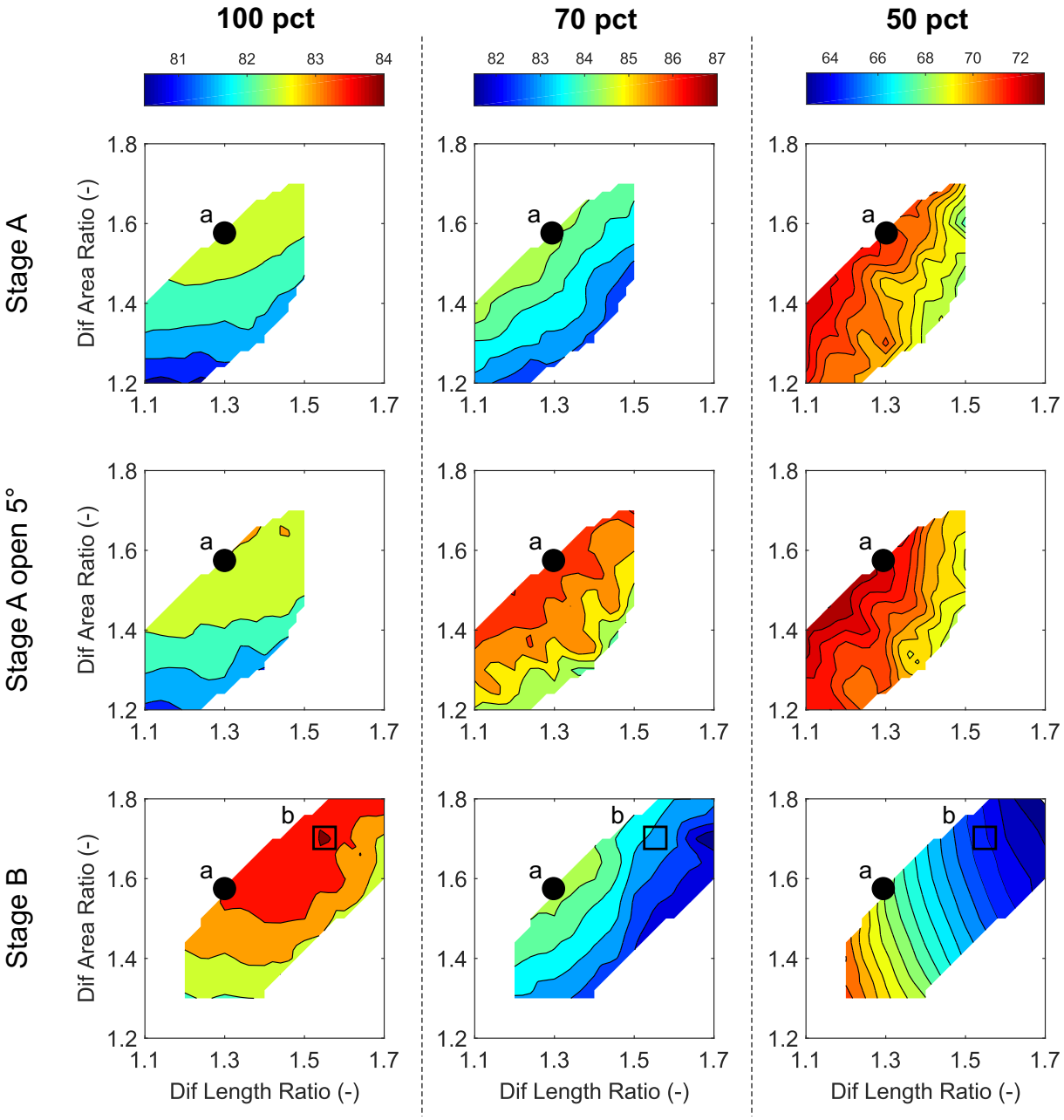

Fig. 7.5 Exhaust hood performance maps for Stage A (top), Stage A with rotor hub opened by 5° (centre) and Stage B (bottom) at various operating conditions, in terms of system total-static efficiencies with 0.5% difference between adjacent contour levels. Point a: $L_1/L_0 = 1.3, A_1/A_0 = 1.55$. Point b: $L_1/L_0 = 1.55, A_1/A_0 = 1.7$. Note: a different range of color maps is used for each operating condition

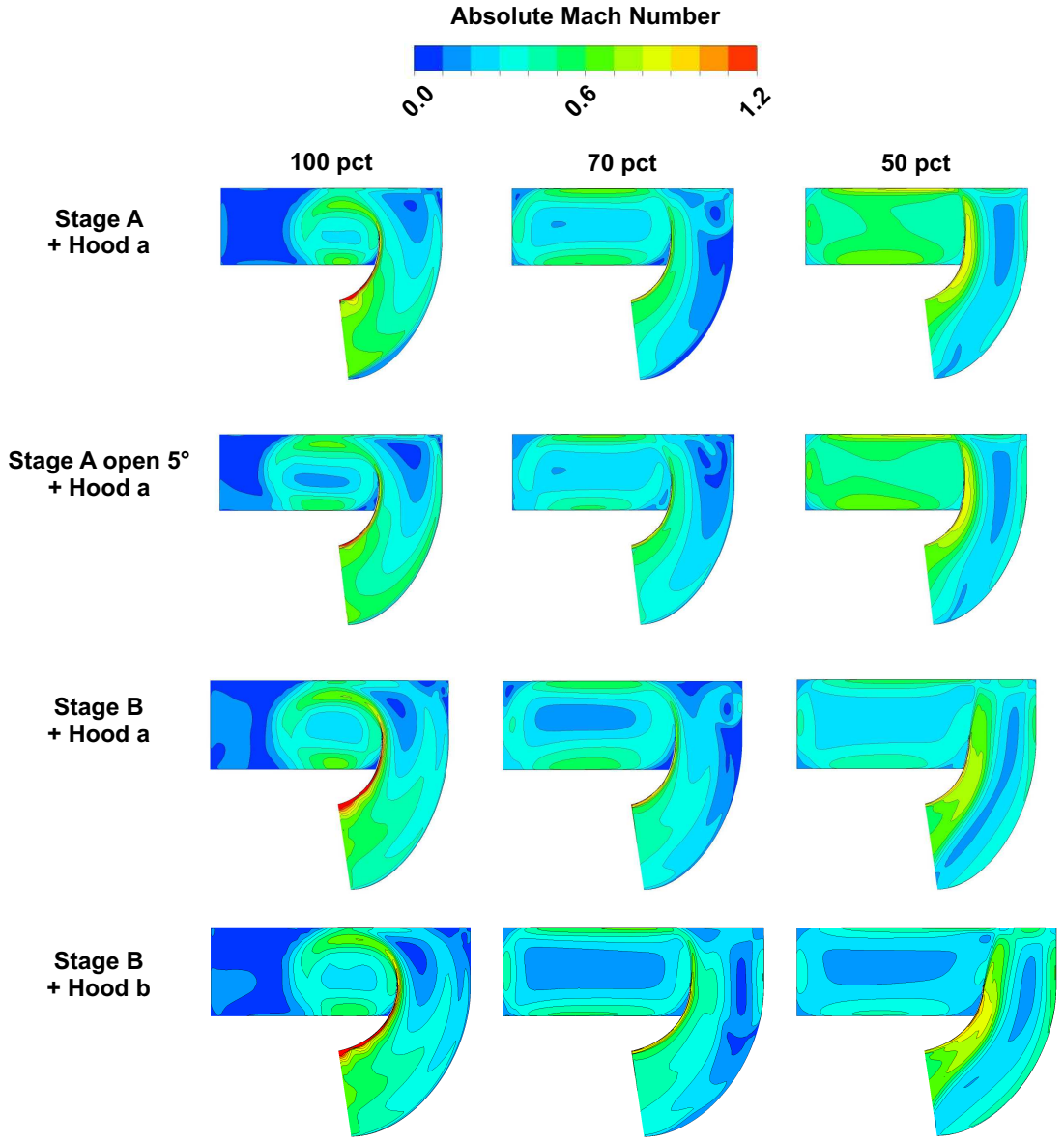

Fig. 7.6 Contours of absolute Mach number in the upper vertical plane of the exhaust hood for different stage and hood configurations at various operating conditions. Note: the range of color maps is clipped to $[0, 1.2]$ for clarity

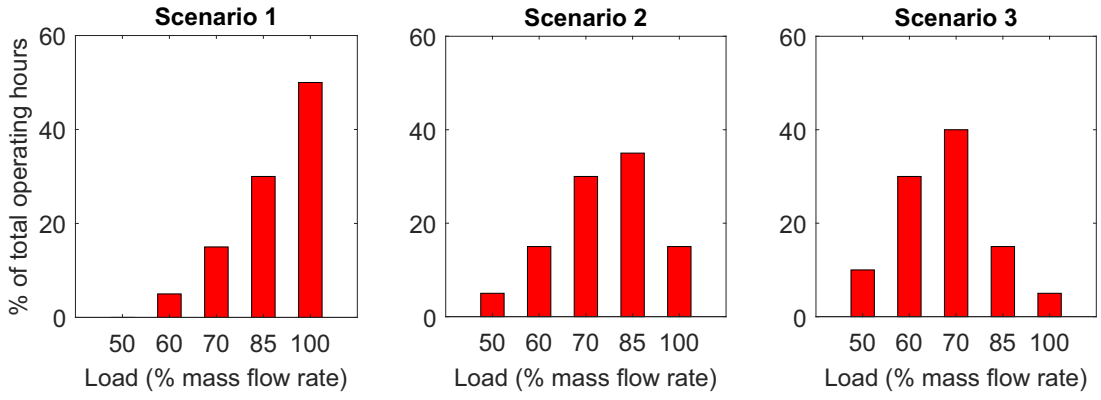

Fig. 7.7 Operating profiles of typical 1000 MW steam plants over the course of one year

Chapter 8

Conclusions and Recommendations

Although the LP exhaust system has long been recognised as one of the most promising components when considering further improvement to a large steam turbine, it still remains a challenge to design a good exhaust system, especially when the power plants are now required to operate much more flexibly due to the rise of renewable energies. The challenges are two-fold. From an aerodynamic perspective, there has been very little experimental validation of numerical tools at part-load conditions. Furthermore, the flow features and loss mechanisms in the exhaust system have not been well understood, particularly at off-design conditions. From an engineering point of view, designers are faced with many geometric parameters to consider, while very few exhaust system design guidances are publicly available. Through this project, the author aimed to gain a better understanding of the flow physics and loss mechanisms in the LP exhaust system, with a particular focus on part-load conditions, and to identify the most influential design parameters as the operating condition varies.

To achieve these research objectives, a validated CFD solver was required. In Chapter 3, the commercial RANS solver ANSYS CFX was validated against a 1/10 scale air test rig, under flow conditions representative of an actual steam turbine at part-load, characterised by highly swirling flows entering the diffuser inlet. In addition, tools were developed to facilitate subsequent numerical studies: the design suite *ExhaustGen* described in Chapter 4 allowed automation of geometry generation and CFD pre- and post-processing, while the concept of Minimum Energy Curves introduced in Chapter 6 helped to reduce the parameter space dimension to facilitate numerical studies. These tools enabled the investigations into the effect of stage-hood interaction on both aerodynamic performance and design of the exhaust system (Chapter 5), and on the global sensitivities of exhaust hood design parameters (Chapter 7).

8.1 Major findings

The major findings that contributed to this thesis are summarised as follows:

1. Through the experiments performed on the scaled test rig, it was established that the numerical uncertainties in CFD would grow with the size of the separation region. In the axi-symmetric diffuser configuration, the CFD solver agreed with the experiment when there was moderate level of swirl (around 40°). For higher swirl angles and consequently larger separation regions, CFD overpredicted the reattachment radius on the bearing cone, whilst underpredicting the pressure loss and level of mixing inside the diffuser. In the configuration with full annulus exhaust hood, similar conclusions could be drawn for the diffuser domain. Nevertheless, when the entire exhaust hood was considered, a closer agreement in C_p was observed between experiment and CFD for the 60° vane instead, due to a much more uniform pressure field at the condenser neck and a smaller separation region on the flow guide compared to the 40° vane. Overall, for higher flow rates and lower swirl angles, CFD can be used at least qualitatively to study the flow physics in the exhaust hood.

2. The Multiple Mixing Planes (MMP) approach [74] to couple the last stage and the exhaust hood can achieve close agreement with full annulus steady and unsteady simulations, at a much reduced computational cost (∼5 times lower than frozen rotor and ∼500 times lower than URANS). It is therefore recommended as a cost-effective option for parametric studies and optimisations with reasonable level of accuracy.

3. Similar trends can be observed in the flow physics and loss breakdown for different stage designs over a wide range of operating conditions. In particular, loss generated in the exhaust hood surpasses that in the blade passages as the flow rate reduces, due to increased size of bearing cone separation (mixing loss) and passage vortex in the collector (blockage). It is therefore important to minimise the entropy generation in the exhaust hood, should the system be expected to operate frequently at part-load.

4. Restaggering the last stage rotor blade (near the hub) adjusts the spanwise flow profile at the stage exit, which can be designed to be more favourable for the exhaust hood. The benefits from opening the hub section can be seen through a 1.5% increase in the *system* efficiency at part-load conditions, while the *component* (stage) efficiency stays more or less the same. This makes the system total-static efficiency a more suitable measurement of performance compared to component-based metrics, and demonstrates the importance of system-based rather than component-based design and optimisation.

5. The geometry parameter space of the exhaust diffuser can be reduced using "Minimum Energy Curves" by minimising the overall curvature level of the flow guide, which not only allows for quick geometry generation, but also provides a similar performance compared to optimised cubic Bezier curves. The diffuser performance is also found to be sensitive to the tip leakage jet, which must be taken into account in the design and optimisation processes.

6. The recently emerged idea of "active subspaces" can be used to identify the most important direction in the parameter space, in the form of linear combinations of design variables. The linear coefficients revealed that the most sensitive parameters are the diffuser axial length and area ratios, the flow guide turning angle, and the exhaust hood width ratio. For the two blading designs studied, similar conclusions could be drawn regarding the sensitivities of most of the parameters. The sensitivities change as the flow condition varies, which makes it important to determine the most frequent operating condition of the power plant in the design process.

7. Finally, exhaust hood performance maps based on the diffuser axial length and area ratios enable the visualisation of parameter sensitivities, especially when the flow condition changes. For a realistic operating profile (Scenario 2 in Fig. 7.7), choosing a suitable exhaust hood size results in a 0.5% increase in weighted average last stage power output throughout the year, compared to a hood geometry that is optimised for performance at design condition only. In addition, redesigning the last stage exit flow profile (by restaggering the rotor blade) can bring a similar level of improvement. Should the power plant operate more frequently at part-load conditions, the benefits quoted above can be more than doubled.

8.2 Recommendations for future work

The major findings presented in this thesis lead to the following recommendations for future work.

8.2.1 Effect of the tip leakage flow

In an actual LP exhaust system, especially with unshrouded rotor blades, the leakage jet from the rotor tip helps to suppress the flow separation on the diffuser flow guide due to the Coanda effect. On the other hand, the mixing between the tip leakage jet and the main flow has been identified as one of the main loss sources in the LP exhaust system, both by Singh [68] and by the author's numerical investigations in Chapter 5. It is therefore recommended to add the tip leakage jet to the current test rig to further improve the representativeness of the flow conditions. Moreover, experimental and numerical parametric studies regarding the strength and the swirl angle of the leakage jet will be useful to help formulate design guidance for the last stage tip section. As commented in Section 6.4, a balance needs to be struck between improving diffuser performance (allowing aggressive flow guide turning and diffusion without separation), increasing rotor efficiency (reducing tip gap size and leakage flow rate), and reducing mixing loss between the tip leakage jet and the bulk flow, as commented by Finzel et al. [24] and Burton [10].

8.2.2 High fidelity measurement and numerical simulations

In Chapter 3, it was established that the numerical uncertainties in RANS CFD would grow with the size of the separation region, which were induced by the swirling flow at the diffuser inlet. The turbulence models widely used by the industry are known to have difficulty dealing with large scale separations. Measuring unsteady flow using fast-response pressure probes, and Reynolds stress components using hotwire and/or Particle Image Velocimetry (PIV) techniques, will provide much more information to help identify the weak spots of (eddy-viscosity-based) turbulence models and hopefully shed some light on how the existing models can be improved for LP exhaust system simulations.

On the other hand, the increase in computational power will make high fidelity numerical simulations such as hybrid RANS-LES and LES more affordable in the near future. For instance, the hybrid approach Scale-Adaptive Simulation (SAS) implemented in ANSYS CFX has recently been applied by Megerle to study unsteady aerodynamics of LP steam turbines under very low flow rate conditions, with very encouraging outcomes when compared to experiment results [49]. Such simulations will not only help with the study of detailed flow physics, but also assist to calibrate and improve RANS CFD, which is now widely used by the industry.

8.2.3 Integrated design of LP exhaust systems

The strong coupling of the last stage and the exhaust hood, and the demonstrated benefits from rotor blade restaggering suggests that the two components (last stage and exhaust hood) should be designed together as a system. Some researchers have demonstrated successes in coupled optimisation of LP exhaust systems in recent years [18], although the computational cost is still too high (one month on a modern workstation). By making use of the numerical tools developed or applied in this thesis (*e.g.* Multiple Mixing Planes, Minimum Energy Curves, and Active Subspaces), system design and optimisation can be performed with much reduced cost. These tools will enable the industrial sponsor to establish databases of LP exhaust systems, and to improve the system performance by focusing on the most sensitive design parameters in a much shortened design cycle.

8.2.4 Wetness effects

The last stage has over 10% wetness. The condensed water is likely to accumulate on the blade and diffuser surfaces. How variation of surface water affects the diffusion, and thus the last stage performance, is not clear and needs to be addressed in order to reduce the modelling uncertainties. This requires further investigation on both experimental and numerical fronts.

References

[1] Bezier curve. https://en.wikipedia.org/wiki/Bezier_curve.

[2] Genetic algorithm. https://uk.mathworks.com/discovery/genetic-algorithm.html.

[3] Latin hypercube sample. https://uk.mathworks.com/help/stats/lhsdesign.html.

[4] Abernethy, R., Benedict, R., and Dowdell, R. (1985). ASME measurement uncertainty. *Journal of Fluids Engineering*, 107(2):161–164.

[5] ANSYS (2011). ANSYS CFX-solver theory guide.

[6] Barth, T. and Jespersen, D. (1989). The design and application of upwind schemes on unstructured meshes. In *27th Aerospace sciences meeting*, page 366.

[7] Becker, S., Gretschel, E.-C., and Casey, M. (2005). Influence of a tip clearance jet on a swirling flow in an axial-radial diffuser. In *Proceedings of the 6th European Turbomachinery Conference, Lille, France, March*, pages 7–11.

[8] Beevers, A., Congiu, F., Pengue, F., and Mokulys, T. (2010). An analysis of the merits of CFD for the performance prediction of a low pressure steam turbine radial diffuser. In *ASME Turbo Expo 2010: Power for Land, Sea, and Air*, pages 563–574. American Society of Mechanical Engineers.

[9] Bruckstein, A. M. and Netravali, A. N. (1990). On minimal energy trajectories. *Computer Vision, Graphics, and Image Processing*, 49(3):283–296.

[10] Burton, Z. (2014). *Analysis of low pressure steam turbine diffuser and exhaust hood systems*. PhD thesis, Durham University.

[11] Burton, Z., Ingram, G., and Hogg, S. (2013a). A novel method of coupling the steam turbine exhaust hood and the last stage blades using the non-linear harmonic method. In *ASME Turbo Expo 2013: Turbine Technical Conference and Exposition*, pages V05BT25A006–V05BT25A006. American Society of Mechanical Engineers.

[12] Burton, Z., Ingram, G., and Hogg, S. (2014). The influence of condenser pressure variation and tip leakage on low pressure steam turbine exhaust hood flows. In *Proceedings of the Institution of Mechanical Engineers, Part A: Journal of Power and Energy*, volume 228, pages 370–379.

[13] Burton, Z., Ingram, G., and Hogg, S. (2015). Efficient methods for predicting low pressure steam turbine exhaust hood and diffuser flows at design and off-design conditions. *Journal of Engineering for Gas Turbines and Power*, 137(8):082601.

[14] Burton, Z., Ingram, G. L., and Hogg, S. (2013b). A literature review of low pressure steam turbine exhaust hood and diffuser studies. *Journal of Engineering for Gas Turbines and Power*, 135(6):062001.

[15] Constantine, P., Dow, E., and Wang, Q. (2014). Active subspace methods in theory and practice: applications to kriging surfaces. *SIAM Journal on Scientific Computing*, 36(4):A1500–A1524.

[16] Constantine, P. G. (2015). *Active subspaces: emerging ideas for dimension reduction in parameter studies*, volume 2. SIAM.

[17] Conti, J., Holtberg, P., Diefenderfer, J., LaRose, A., Turnure, J. T., and Westfall, L. (2016). International energy outlook 2016 with projections to 2040. Technical report, USDOE Energy Information Administration (EIA), Washington, DC (United States). Office of Energy Analysis.

[18] Cremanns, K., Roos, D., and Graßmann, A. (2014). Sequential vs multidisciplinary coupled optimization and efficient surrogate modelling of a last stage and the successive axial radial diffuser in a low pressure steam turbine. In *ASME Turbo Expo 2014: Turbine Technical Conference and Exposition*, pages V02BT45A006–V02BT45A006. American Society of Mechanical Engineers.

[19] Deich, M. and Zaryankin, A. (1970). *Gas Dynamics of Diffusers and Exhaust Pipes of Turbomachines*. Energiya Press, Moscow.

[20] Denton, J. (1978). Throughflow calculations for transonic axial flow turbines. *Journal of Engineering for Power*, 100(2):212–218.

[21] Denton, J. D. (1990). The calculation of three dimensional viscous flow through multistage turbomachines. In *ASME 1990 International Gas Turbine and Aeroengine Congress and Exposition*, pages V001T01A009–V001T01A009. American Society of Mechanical Engineers.

[22] Ding, B. and Xu, L. (2017). Designing steam turbine exhaust diffusers using Minimum Energy Curves. In *Proceedings of Shanghai 2017 Global Power and Propulsion Forum, 30 Oct – 1 Nov. Paper No. GPPS2017-0060*.

[23] Fan, T., Xie, Y., Zhang, D., and Sun, B. (2007). A combined numerical model and optimization for low pressure exhaust system in steam turbine. In *ASME 2007 Power Conference*, pages 349–358. American Society of Mechanical Engineers.

[24] Finzel, C., Schatz, M., Casey, M. V., and Gloss, D. (2011). Experimental investigation of geometrical parameters on the pressure recovery of low pressure steam turbine exhaust hoods. In *ASME 2011 Turbo Expo: Turbine Technical Conference and Exposition*, pages 2255–2263. American Society of Mechanical Engineers.

[25] Finzel, C.and Casey, M. V. (2011). Experimental and CFD investigations on the influence of a wall jet flow on the performance of a curved diffuser. In *Proceedings of the 9th European Conference on Turbomachinery*.

[26] Fu, J.-L. and Liu, J.-J. (2008). Influences of inflow condition on non-axisymmetric flows in turbine exhaust hoods. *Journal of Thermal Science*, 17(4):305–313.

[27] Fu, J.-L., Liu, J.-J., and Zhou, S.-J. (2012). Unsteady interactions between axial turbine and nonaxisymmetric exhaust hood under different operational conditions. *Journal of Turbomachinery*, 134(4):041002.

[28] Gray, L., Sandhu, S., Davids, J., and Southall, L. (1989). Technical considerations in optimizing blade-exhaust hood performance for low pressure steam turbines. *Latest Advances in Steam Turbine Design, Blading, Repairs, Condition, Assessment, and Condenser Interactions*, 7:89–97.

[29] Greitzer, E. M., Tan, C. S., and Graf, M. B. (2007). *Internal flow: concepts and applications*. Cambridge University Press.

[30] Havakechian, S. and Denton, J. (2016a). Three-dimensional blade-stacking strategies and understanding of flow physics in low-pressure steam turbines—Part I: three-dimensional stacking mechanisms. *Journal of Engineering for Gas Turbines and Power*, 138(5):052603.

[31] Havakechian, S. and Denton, J. (2016b). Three-dimensional blade stacking strategies and understanding of flow physics in low-pressure steam turbines—Part II: stacking equivalence and differentiators. *Journal of Engineering for Gas Turbines and Power*, 138(6):062601.

[32] He, L. and Ning, W. (1998). Efficient approach for analysis of unsteady viscous flows in turbomachines. *AIAA journal*, 36(11):2005–2012.

[33] Herwig, H. and Kock, F. (2006). Local entropy production in turbulent shear flows: A tool for evaluating heat transfer performance. *Journal of Thermal Science*, 15(2):159.

[34] Herwig, H. and Schmandt, B. (2014). How to determine losses in a flow field: A paradigm shift towards the second law analysis. *Entropy*, 16(6):2959–2989.

[35] Hirschmann, A., Volkmer, S., Casey, M., and Montgomery, M. (2012a). Hub extension in an axial gas turbine diffuser. In *ASME Turbo Expo 2012: Turbine Technical Conference and Exposition*, pages 1229–1238. American Society of Mechanical Engineers.

[36] Hirschmann, A., Volkmer, S., Schatz, M., Finzel, C., Casey, M., and Montgomery, M. (2012b). The influence of the total pressure profile on the performance of axial gas turbine diffusers. *Journal of Turbomachinery*, 134(2):021017.

[37] Horn, B. K. (1983). The curve of least energy. *ACM Transactions on Mathematical Software (TOMS)*, 9(4):441–460.

[38] Hoznedl, M., Tajc, L., Krejcik, J., Bednar, L., Sedlak, K., and Linhart, J. (2009). Exhaust hood for steam turbines-single-flow arrangement. *Frontiers of Energy and Power Engineering in China*, 3(3):321–329.

[39] Hoznedl, M., Živnỳ, A., Macálka, A., Kalista, R., Sedlák, K., Bednář, L., and Tajč, L. (2018). The pressure field at the output from a low pressure exhaust hood and condenser neck of the 1090 MW steam turbine: Experimental and numerical research. In *ASME Turbo Expo 2018: Turbomachinery Technical Conference and Exposition*, pages V008T29A006–V008T29A006. American Society of Mechanical Engineers.

[40] Keller, H. (1986). Low pressure turbine exhaust system design. In Moore, M. J. and Sieverding, C., editors, *Aerothermodynamics of low pressure steam turbines and condensers*. Hemisphere Publishing, New York, NY.

[41] Köller, U., Mönig, R., Küsters, B., and Schreiber, H.-A. (1999). Development of advanced compressor airfoils for heavy-duty gas turbines: Part I—design and optimization. In *ASME 1999 International Gas Turbine and Aeroengine Congress and Exhibition*, pages V001T03A021–V001T03A021. American Society of Mechanical Engineers.

[42] Korakianitis, T. and Papagiannidis, P. (1992). Surface-curvature-distribution effects on turbine-cascade performance. In *ASME 1992 International Gas Turbine and Aeroengine Congress and Exposition*, pages V001T01A044–V001T01A044. American Society of Mechanical Engineers.

[43] Kreitmeier, F. and Greim, R. (2003). Optimization of blade—diffuser interaction for improved turbine performance. *Proceedings of the Institution of Mechanical Engineers, Part A: Journal of Power and Energy*, 217(4):443–451.

[44] Liu, B., Yang, J., Zhou, D., Zhu, X., and Du, Z. (2015). Numerical investigations of flow features in a low pressure steam turbine last stage under different mass flow rates. In *ASME Turbo Expo 2015: Turbine Technical Conference and Exposition*, pages V008T26A022–V008T26A022. American Society of Mechanical Engineers.

[45] Liu, J. J., Cui, Y. Q., and Jiang, H. D. (2003). Investigation of flow in a steam turbine exhaust hood with/without turbine exit conditions simulated. *Journal of Engineering for Gas Turbines and Power*, 125(1):292.

[46] McBean, I., Havakechian, S., and Masserey, P.-A. (2010). The development of long last stage steam turbine blades. In *ASME Turbo Expo 2010: Power for Land, Sea, and Air*, pages 2245–2256. American Society of Mechanical Engineers.

[47] McKay, M. D., Beckman, R. J., and Conover, W. J. (2000). A comparison of three methods for selecting values of input variables in the analysis of output from a computer code. *Technometrics*, 42(1):55–61.

[48] McNeil, I. (2002). *An encyclopedia of the history of technology*. Routledge.

[49] Megerle, B. (2014). *Unsteady aerodynamics of low-pressure steam turbines operating under low volume flow conditions*. PhD thesis, EPFL.

[50] Menter, F. R. (1994). Two-equation eddy-viscosity turbulence models for engineering applications. *AIAA journal*, 32(8):1598–1605.

[51] Menter, F. R. (2012). Best practice: scale-resolving simulations in ANSYS CFD. *ANSYS Germany GmbH*, pages 1–70.

[52] Mizumi, S., Ishibashi, K., and Sawamura, Y. (2012). Steam turbine exhaust hood with swirl flow separation ducts. In *ASME Turbo Expo 2012: Turbine Technical Conference and Exposition*, pages 385–393. American Society of Mechanical Engineers.

[53] Munyoki, D., Schatz, M., and Vogt, D. M. (2017). Detailed numerical study of the main sources of loss and flow behavior in low pressure steam turbine exhaust hoods. In *ASME Turbo Expo 2017: Turbomachinery Technical Conference and Exposition*, pages V008T29A004–V008T29A004. American Society of Mechanical Engineers.

[54] Munyoki, D., Schatz, M., and Vogt, D. M. (2018). Numerical investigation of the influence of hood height variation on performance of low pressure steam turbine exhaust hoods. In *ASME Turbo Expo 2018: Turbomachinery Technical Conference and Exposition*, pages V008T29A031–V008T29A031. American Society of Mechanical Engineers.

[55] Musch, C., Cremanns, K., S, H., and Penkner, A. (2017). Combined optimisation of the last stage and diffuser in a steam turbine using meta-model. In *Proceedings of 12th European Conference on Turbomachinery Fluid dynamics & Thermodynamics*.

[56] Musch, C., Stüer, H., and Hermle, G. (2013). Optimization strategy for a coupled design of the last stage and the successive diffuser in a low pressure steam turbine. *Journal of Turbomachinery*, 135(1):011013.

[57] Nicol, K. (2015). *Application and development prospects of double-reheat coal-fired power units*. IEA Clean Coal Center, London, UK.

[58] Owczarek, J., Warnock, A., and Malik, P. (1989). A low pressure turbine exhaust end flow model study. *Latest Advances in Steam Turbine Design, Blading, Repairs, Condition, Assessment, and Condenser Interactions, DM Rasmussen, ed., ASME, New York*, pages 77–88.

[59] Palenschat, T., Newton, P., Martinez-Botas, R. F., Müller, M., and Leweux, J. (2017). 3-D computational loss analysis of an asymmetric volute twin-scroll turbocharger. In *ASME Turbo Expo 2017: Turbomachinery Technical Conference and Exposition*, pages V008T26A016–V008T26A016. American Society of Mechanical Engineers.

[60] Panitz, T. and Wasan, D. (1972). Flow attachment to solid surfaces: the Coanda effect. *AIChE Journal*, 18(1):51–57.

[61] Pfau, A., Schlienger, J., Kalfas, A. I., and Abhari, R. S. (2002). Virtual four sensor fast response aerodynamic probe (FRAP). In *16th Symposioum on Measuring Techniques in Transonic and Supersonic Flow in Cascades and Turbomachines, Cambridge, UK, Sep 23-24. Paper No.5-1.*

[62] Piegl, L. and Tiller, W. (2012). *The NURBS book*. Springer Science & Business Media.

[63] Rogers, H. (2011). *The impact of import dependency and wind generation on UK gas demand and security of supply to 2025*. Oxford Institute for Energy Studies.

[64] Seshadri, P., Shahpar, S., Constantine, P., Parks, G., and Adams, M. (2018). Turbomachinery active subspace performance maps. *Journal of Turbomachinery*, 140(4):041003.

[65] Shao, S., Deng, Q., Shi, H., Feng, Z., Cheng, K., and Peng, Z. (2013). Numerical investigation on flow characteristics of low pressure exhaust hood under off-design conditions for steam turbines. In *ASME Turbo Expo 2013: Turbine Technical Conference and Exposition*, pages V05BT25A031–V05BT25A031. American Society of Mechanical Engineers.

[66] Sigg, R., Heinz, C., Casey, M. V., and Sürken, N. (2009). Numerical and experimental investigation of a low-pressure steam turbine during windage. *Proceedings of the Institution of Mechanical Engineers, Part A: Journal of Power and Energy*, 223(6):697–708.

[67] Simoyu, L., Lagun, V., Gudkov, N., and Kirillov, V. (1997). Influence of the inlet steam flow on the operation of the turbine hood. *Thermal engineering*, 44(1):25–30.

[68] Singh, G. (2014). *The study of the interactions between a low pressure steam turbine and axial-radial diffuser*. PhD thesis, Queen Mary University of London.

[69] Singh, G., Wheeler, A. P., and Singh, G. (2017). The effect of rotor casing on low-pressure steam turbine and diffuser interactions. *Journal of Engineering for Gas Turbines and Power*, 139(2):022607.

[70] Sovran, G. and Klomp, E. (1967). Experimentally determined optimum geometries for rectlinear diffusers with rectangular, conical or annular cross section. *Fluid Mechanics of Internal Flow*, pages 270–319.

[71] Stanciu, M., Fendler, Y., and Dorey, J. (2011). Unsteady stator-rotor interaction coupled with exhaust hood effect for last stage steam turbines. In *Proceedings of the 9th European Turbomachinery Conference, Istanbul, March*, pages 21–25.

[72] Stanciu, M., Marcelet, M., and Dorey, J.-M. (2013). Numerical investigation of condenser pressure effect on last stage operation of low pressure wet steam turbines. In *ASME Turbo Expo 2013: Turbine Technical Conference and Exposition*, pages V05BT25A003–V05BT25A003. American Society of Mechanical Engineers.

[73] Štastnỳ, M., Tajc, L., Kolár, P., and Tucek, A. (2000). Effects of inlet swirl on the flow in a steam turbine exhaust hood. *Journal of Thermal Science*, 9(4):327–333.

[74] Stein, P., Pfoster, C., Sell, M., Galpin, P., and Hansen, T. (2015). CFD modeling of low pressure steam turbine radial diffuser flow by using a novel Multiple Mixing Plane based coupling—simulation and validation. In *Proceedings of ASME Turbo Expo 2015. Paper No. GT2015-42632*.

[75] Stüer, H., Truckenmüller, F., Borthwick, D., and Denton, J. D. (2005). Aerodynamic concept for very large steam turbine last stages. In *ASME Turbo Expo 2005: Power for Land, Sea, and Air*, pages 673–687. American Society of Mechanical Engineers.

[76] Takehira, A., Tanaka, M., Kawashima, T., and Hanabusa, H. (1977). An experimental study of the annular diffusers in axial-flow compressors and turbines. In *Tokyo Joint Gas Turbine Congress, Tokyo, Japan*, page 1977.

[77] Tanuma, T., Sasao, Y., Yamamoto, S., Takada, S., Niizeki, Y., Shibukawa, N., and Saeki, H. (2011). Numerical investigation of exhaust diffuser performances in low pressure turbine casings. In *Proceedings of ASME Turbo Expo 2011. Paper No. GT2011-45677*.

[78] Taylor, D., Singh, G., Hemsley, P., and Claridge, M. (2016). Parametric experimental and numerical study of LP diffuser and exhaust hoods. In *Proceedings of ASME Turbo Expo 2016. Paper No. GT2016-56640*.

[79] Tindell, R. H., Alston, T. M., Sarro, C. A., Stegmann, G. C., Gray, L., and Davids, J. (1996). Computational fluid dynamics analysis of a steam power plant low-pressure turbine downward exhaust hood. *Journal of Engineering for Gas Turbines and Power*, 118(1):214–224.

[80] Tusche, J. and Musch, C. (2018). A novel evaluation procedure for the prediction and assessment of diffuser humming in steam turbines. In *Proceedings of ASME Turbo Expo 2018. Paper No. GT2018-75499*.

[81] Verstraete, T., Prinsier, J., and Cosi, L. (2014). Design and off-design optimization of a low pressure steam turbine radial diffuser using an evolutionary algorithm and 3D CFD. In *Proceedings of ASME Turbo Expo 2014. Paper No. GT2014-26850*.

[82] Verstraete, T., Prinsier, J., Di Sante, A., Della Gatta, S., and Cosi, L. (2012). Design optimization of a low pressure steam turbine radial diffuser using an evolutionary algorithm and 3D CFD. In *ASME Turbo Expo 2012: Turbine Technical Conference and Exposition*, pages 603–613. American Society of Mechanical Engineers.

[83] Vilmin, S., Lorrain, E., Hirsch, C., and Swoboda, M. (2006). Unsteady flow modeling across the rotor/stator interface using the nonlinear harmonic method. In *ASME Turbo Expo 2006: Power for Land, Sea, and Air*, pages 1227–1237. American Society of Mechanical Engineers.

[84] Vinokur, M. (1983). On one-dimensional stretching functions for finite-difference calculations. *Journal of Computational Physics*, 50(2):215–234.

[85] Wagner, W. and Kretzschmar, H.-J. (2008). IAPWS industrial formulation 1997 for the thermodynamic properties of water and steam. *International Steam Tables: Properties of Water and Steam Based on the Industrial Formulation IAPWS-IF97*, pages 7–150.

[86] Xu, X., Kang, S., and Hirsch, C. (2001). Numerical simulation of the 3D viscous flow in the exhaust casing of a low-pressure steam turbine. In *ASME Turbo Expo 2001: Power for Land, Sea, and Air*, pages V001T03A071–V001T03A071. American Society of Mechanical Engineers.

[87] Xue, S., Guillot, S., Ng, W. F., Fleming, J., Lowe, K. T., Samal, N., and Stang, U. E. (2016). An experimental investigation of the performance impact of swirl on a turbine exhaust diffuser/collector for a series of diffuser strut geometries. *Journal of Engineering for Gas Turbines and Power*, 138(9):092603.

[88] Yang, J., Chen, T., Li, J., and Feng, Z. (2014). Aerodynamic optimization design of exhaust hood diffuser for steam turbine with three-dimensional Reynolds-Averaged Navier-Stokes solutions. In *ASME Turbo Expo 2014: Turbine Technical Conference and Exposition*, pages V01BT27A007–V01BT27A007.

[89] Yin, M., Yang, C., Meng, L., Yan, W., Zhuhai, Z., Li, J., and Feng, Z. (2016). Numerical analysis on the swirl flows in the exhaust hood of steam turbine and optimization design. In *ASME Turbo Expo 2016: Turbomachinery Technical Conference and Exposition*, pages V008T26A002–V008T26A002. American Society of Mechanical Engineers.

[90] Yoon, S., Stanislaus, F. J., Mokulys, T., Singh, G., and Claridge, M. (2011). A three-dimensional diffuser design for the retrofit of a low pressure turbine using in-house exhaust design system. In *Proceedings of ASME Turbo Expo 2011. Paper No. GT2011-45466*.

[91] Zhang, L., Congiu, F., Gan, X., and Karunakara, D. (2016). Performance prediction and optimisation of LP steam turbine radial diffuser at design and off-design conditions using streamline curvature method. In *ASME Turbo Expo 2016: Turbomachinery Technical Conference and Exposition*, pages V008T26A021–V008T26A021. American Society of Mechanical Engineers.

[92] Zhang, L., He, L., and Stüer, H. (2013). A numerical investigation of rotating instability in steam turbine last stage. *Journal of turbomachinery*, 135(1):011009.

[93] Zhang, W., Paik, B. G., Jang, Y. G., Lee, S. J., Lee, S. E., and Kim, J. H. (2007). Particle image velocimetry measurements of the three-dimensional flow in an exhaust hood model of a low-pressure steam turbine. *Journal of Engineering for Gas Turbines and Power*, 129(2):411–419.

Appendix A

Multiple Mixing Planes

The Multiple Mixing Planes (MMP) approach was first proposed by Stein et al. and applied to simulate the circumferentially non-uniform flow field at the stage-diffuser interface [74]. A typical MMP setup is illustrated in Fig. A.1, in which a radial cut of the stage-diffuser domain is unwrapped and four mixing planes are placed at the stage-diffuser interface.

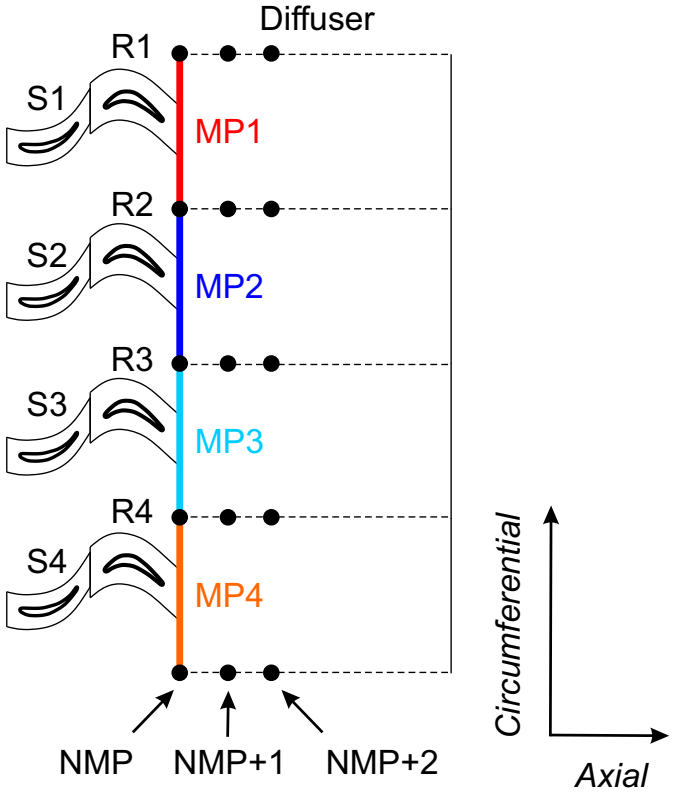

Fig. A.1 Multiple mixing planes

In Fig. A.1, each stage (S1-R1, S2-R2, etc.) is isolated from the others, *i.e.* rotational periodicity is only applied within the stage itself. Between the stator and rotor in each stage (*e.g.* S1 and R1), a mixing plane interface is employed (*e.g.* Denton [21]). So far the stator-rotor interface treatment has been set up.

The rotor-diffuser interface (on the diffuser side) is then divided evenly into four sectors. Each of these sectors covers 90° and is coupled to the outlet of the nearest rotor blade, again via a mixing plane interface. For instance, the very top sector of the diffuser inlet (Fig. A.1) is coupled to rotor R1 via mixing plane MP1, at which mixed-out calculations and circumferential averaging are carried out.

The black dots in Fig. A.1 refer to the grid points at the connection face between sectors in the diffuser domain. Location "NMP" is situated at the rotor-diffuser interface, while locations "NMP+1" and "NMP+2" are one and two grid points downstream of the interface. At location "NMP", a slight discontinuity would occur at the black dots (*i.e.* the connection lines between the sectors), as demonstrated in Fig. 4.7 and Fig. 4.8 in Chapter 4. This is because circumferential averaging is only performed within each independent mixing plane (MP1, MP2, etc.). From location "NMP+1" onwards, discontinuity starts to be washed out and disappears in a short distance downstream of the rotor-diffuser interface.

Appendix B

Bezier Curves

Bezier curves are a group of parametric curves that are widely used in fields such as computer graphics, animation and fonts [1]. A general nth degree Bezier curve $\mathbf{C}(u)$, according to Piegl and Tiller [62], is defined by

$$\mathbf{C}(u) = \sum_{i=0}^{n} B_{i,n}(u)\mathbf{P}_i, \quad 0 \leq u \leq 1, \tag{B.1}$$

where the basis functions $B_{i,n}(u)$ are given by

$$B_{i,n}(u) = \frac{n!}{i!(n-i)!}u^i(1-u)^{n-i}, \tag{B.2}$$

the classical nth degree Bernstein polynomials. $\mathbf{P}_i$ are the coordinates of the control points. When $n = 3$, we have the cubic Bezier curves which are defined by

$$\mathbf{C}(u) = (1-u)^3\mathbf{P}_0 + 3u(1-u)^2\mathbf{P}_1 + 3u^2(1-u)\mathbf{P}_2 + u^3\mathbf{P}_3. \tag{B.3}$$

Fig. B.1 presents a cubic Bezier curve parametrised by its four control points.

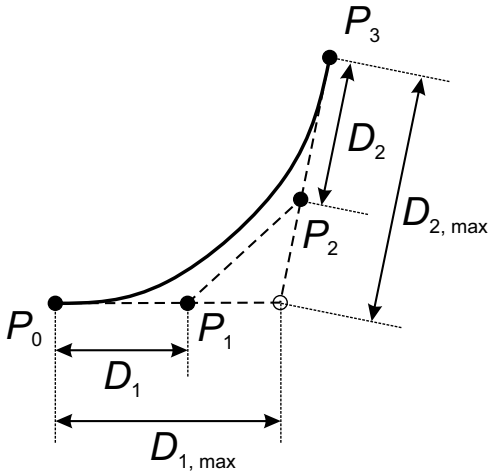

Fig. B.1 Cubic Bezier curves

In Fig. B.1, the end point tangent directions are parallel to $\mathbf{P}_1 - \mathbf{P}_0$ and $\mathbf{P}_3 - \mathbf{P}_2$. The two tangents intersect and hence define the distances $D_{1,\,\max}$ and $D_{2,\,\max}$. In Chapter 6 of this thesis where the diffuser flow guide was described using the cubic Bezier curves, the two endpoints $\mathbf{P}_0$ and $\mathbf{P}_3$ and their associated tangents were fixed by other geometric parameters. Therefore only two control points, $\mathbf{P}_1$ and $\mathbf{P}_2$, need to be varied. In a previous study by Verstraete et al. [81], such variations were achieved by moving $\mathbf{P}_1$ and $\mathbf{P}_2$ along the respective tangents, *i.e.* by varying the dimensional control point distances D_1 and D_2 (Fig. 6.2). In the current study, the control point distances were non-dimensionalised as

$$d_i = \frac{D_i}{D_{\mathrm{i},\,\max}}, \quad i = 1, 2 \tag{B.4}$$

so that d_i is always in the $[0, 1]$ range, which is useful for the optimisation setup.